University of Florida
Civil and Coastal Engineering

University of Florida
Civil and Coastal Engineering

Final Report **October 2009**

VALIDATION OF STRESSES CAUSED BY THERMAL GRADIENTS IN SEGMENTAL CONCRETE CONSTRUCTION

Principal investigators:
H. R. Hamilton
G. R. Consolazio

Research assistants:
Farouk Mahama
David C. Walter
Nathan Currier

Department of Civil and Coastal Engineering
University of Florida
P.O. Box 116580
Gainesville, Florida 32611

Sponsor:
Florida Department of Transportation (FDOT)
Marcus H. Ansley, P.E. – Project Manager

Contract:
UF Project No. 00030906
FDOT Contract No. BD 545-10

DISCLAIMER

The opinions, findings, and conclusions expressed in this publication are those of the authors and not necessarily those of the State of Florida Department of Transportation.

Technical Report Documentation Page

1. Report No.	2. Government Accession No.	3. Recipient's Catalog No.

4. Title and Subtitle	5. Report Date
Validation of Stresses Caused by Thermal Gradients in Segmental Concrete Construction	October 2009
	6. Performing Organization Code

7. Author(s)	8. Performing Organization Report No.
Farouk Mahama, David C. Walter, Nathan Currier, H. R. Hamilton, and G. R. Consolazio	00030906

9. Performing Organization Name and Address	10. Work Unit No. (TRAIS)
University of Florida Department of Civil & Coastal Engineering P.O. Box 116580 Gainesville, FL 32611-6580	11. Contract or Grant No. BD545-10

12. Sponsoring Agency Name and Address	13. Type of Report and Period Covered
Florida Department of Transportation Research Management Center 605 Suwannee Street, MS 30 Tallahassee, FL 32399-0450	Final Report 8/21/03-10/28/09
	14. Sponsoring Agency Code

15. Supplementary Notes

16. Abstract

Segmental bridges experience not only uniform temperature changes, but also nonlinear distributions of temperature (thermal gradient) through the depth of the superstructure. Nonlinear temperature distributions lead to internal self-equilibrating thermal stresses that cannot be relieved through adjustment of support conditions.

Part One of this report presents the results of a series of tests and analytical work aimed at quantifying the self-equilibrating thermal stresses caused by American Association of State Highway and Transportation Officials (AASHTO) design nonlinear positive (deck warmer than web) and negative (deck cooler than web) thermal gradients in segmental concrete bridges. To experimentally quantify thermal gradient stresses in this study, a 20 ft long 3 ft deep segmental T beam externally post-tensioned with four high-strength steel bars was constructed. By embedding rows of copper tubing into two of the beam segments, and passing heated water through the tubes, the desired thermal gradients were imposed on the heated segments. Thermal and mechanical loads were imposed. Two independent methods were used to measure stresses at the joint. Good agreement was found between the measurement techniques. Furthermore the maximum stresses (measured at a distance 0.5 in. below the extreme top flange fibers) were about 10% to 20% less than stresses predicted using the AASHTO method, for the positive thermal gradient and negative thermal gradient, respectively. Measurements on the top surface of the flanges of the segments were significantly less than predicted by the AASHTO method due to differential shrinkage and a likely discontinuity in the shape of thermal gradients in the top 0.5 in. of the flange of the beam.

Part Two of this report covers component testing of prestressed concrete specimens and a final test to cracking on the beam used for the research reported in Part One. The component testing consisted of prestressed concrete specimens constructed to replicate the top 8 in. of a segmental concrete bridge deck where the self-equilibrating stresses from the negative thermal gradient causes net tension. A series of six test sets were performed during which the specimens were initially prestressed and then loaded in tension until a crack formed. The objective was to determine the effect of an applied nonlinear thermal gradient on the cracking stress and behavior of the concrete specimen relative to a specimen that had no thermal gradient applied. A negative nonlinear thermal gradient was applied to one specimen from each test set using an open-channel flow of chilled water. The specimens were each loaded to failure and the results of each test set compared. The net tensile stress (or net tensile load) at the initiation of microcracking and the net tensile stress at cracking were determined using measured strain data and cumulative acoustic emission energy. The net tensile stress at the initiation of microcracking and the net tensile stress at visible cracking were compared between specimens within each test set to determine the effect of the self-equilibrating stresses on the cracking behavior. Based on the measurements, the thermal gradient appeared to have no significant effect on the cracking behavior in these tests.

17. Key Word	18. Distribution Statement
Concrete, prestressed, temperature effects, thermal stresses, bridges, thermal gradient	No restrictions. This document is available to the public through the National Technical Information Service, Springfield, VA, 22161

19. Security Classif. (of this report)	20. Security Classif. (of this page)	21. No. of Pages	22. Price
Unclassified	Unclassified	262	

Form DOT F 1700.7 (8-72) Reproduction of completed page authorized

ACKNOWLEDGMENTS

The authors would like to acknowledge and thank the Florida Department of Transportation for funding this research project. The authors would especially like to thank Mr. Marc Ansley of the FDOT Structures Research Center, Tallahassee, for his invaluable support and suggestions during the course of this project. Sincere thanks to Mr. Frank Cobb, Mr. David Allen, Mr. Steve Eudy, Mr. Tony Johnston, and Mr. Paul Tighe also of the FDOT Structures Research Center, Tallahassee, for their help in constructing and transporting the laboratory specimen from Tallahassee to Gainesville, Florida. Thanks are extended to DYWIDAG Systems Incorporated (DSI) for donating the post-tensioning bars which were used to post-tension the laboratory specimen. In addition, the authors would like to thank Mr. Richard M. DeLorenzo of the FDOT Materials Laboratory, Gainesville, for his assistance in determining material properties of the test specimen. Finally, the authors would like to express their sincere gratitude to Mr. Chuck Broward of the University of Florida Structures Laboratory, Mr. Hubert "Nard" Martin, George Fernandez and Robert Gomez for their various contributions towards the successful execution of experiments in the laboratory.

EXECUTIVE SUMMARY

Segmental bridges experience not only uniform temperature changes, but also variation of temperature through the depth of the superstructure (thermal gradient). Bridge deformations due to uniform temperature changes are well understood and accounted for in design by providing sliding joints and flexible piers, among other methods, to accommodate such movements. Thermal gradients, however, present a more complex engineering problem. In simply-supported spans, the nonlinear portion of the thermal gradient will cause internal self-equilibrating thermal stresses that cannot be relieved through adjustment of support conditions. In continuous spans, the linear portion of the thermal gradient leads to continuity stresses due to restraint to curvature in addition to self-equilibrating thermal stresses caused by the nonlinear portion of the thermal gradient.

Design gradients are based on field measurement of temperature variations on both a seasonal and diurnal basis. There are, however, little data in which actual self-equilibrating stresses have been isolated and measured during these peak gradients to verify that the stresses are indeed as high as predicted by analysis. One reason for this is the difficulty of stress measurement in concrete. Stress is generally estimated by measuring strain, which is then converted to stress by applying an elastic modulus. This works well for homogeneous elastic materials but there is less confidence in this procedure when applied to concrete due to material variability at the scale of the strain gauge.

Part One of this report presents the results of a series of tests and analytical work aimed at quantifying the self-equilibrating thermal stresses caused by American Association of State Highway and Transportation Officials (AASHTO) design nonlinear positive (deck warmer than web) and negative (deck cooler than web) thermal gradients in segmental concrete bridges. The negative gradients can cause significant tensile stresses to develop in the top few inches of bridge decks, perhaps leading to requirements for excessive prestressing forces to counteract this tension.

To experimentally quantify thermal gradient stresses in this study, a 20-ft long 3-ft deep segmental T beam externally post-tensioned with four high-strength steel bars was constructed. By embedding rows of copper tubing into two of the beam segments, and passing heated water through the tubes, the desired thermal gradients were imposed on the heated segments. These segments were also instrumented with thermocouples to monitor concrete temperatures during the application of thermal loads. The beam was supported on one end and at midspan. Mechanical loads were applied at the cantilevered end with the objective of creating a known (zero) stress state at the dry joint (at midspan) between the two heated segments from which the effects of thermal gradients could be determined.

Two independent methods were used to measure stresses at the joint. The first was to convert measured strains using the elastic modulus of the concrete, referred to as elastic modulus derived stresses (E stress). The second method was a more direct measure of stress using the known stress state at incipient joint opening, and is referred to as joint opening derived stresses (J stress). Linear elastic behavior was assumed for both methods.

Good agreement was found between E stresses and J stresses in the top 4 in. of the flange, where the maximum stresses caused by the thermal gradients were expected to occur (maximum J stresses were within 10% of maximum E stresses for both positive and negative thermal gradient cases). Maximum J and E stresses (measured at a distance 0.5 in. below the

extreme top flange fibers) were on average about 10% and 20% less than stresses predicted with the AASHTO method, for the positive thermal gradient and negative thermal gradient, respectively. E stresses on the top surface of the flanges of the segments were significantly less than predicted by the AASHTO method due to differential concrete shrinkage and a likely discontinuity in the shape of thermal gradients in the top 0.5 in. of the flange of the beam.

Part Two of this report covers component testing of prestressed concrete specimens and a final test to cracking on the beam used for the research reported in Part One. The component testing consisted of prestressed concrete specimens constructed to replicate the top 8 in. of a segmental concrete bridge deck where the self-equilibrating stresses from the negative thermal gradient causes net tension. A series of six test sets were performed during which the specimens were initially prestressed and then loaded in tension until a crack formed. The objective was to determine the effect of an applied nonlinear thermal gradient on the cracking stress and behavior of the concrete specimen relative to a specimen that had no thermal gradient applied. A negative nonlinear thermal gradient was applied to one specimen from each test set using an open-channel flow of chilled water. The specimens were each loaded to failure and the results of each test set compared.

The net tensile stress (or net tensile load) at the initiation of microcracking and the net tensile stress at cracking were determined using measured strain data and cumulative acoustic emission energy. The net tensile stress at the initiation of microcracking and the net tensile stress at visible cracking were compared between specimens within each test set to determine the effect of the self-equilibrating stresses on the cracking behavior. Based on the measurements, the thermal gradient appeared to have no significant effect on the cracking behavior in these tests.

TABLE OF CONTENTS

1 INTRODUCTION

Thermal stresses are the result of restraint to deformations caused by temperature changes. In general, stresses are generated in bridges when the temperature of all or part of the superstructure varies significantly from the temperature at which it was constructed. Seasonal and diurnal variations in temperature are usually the cause of these temperature changes. Bridge superstructures will generally experience not only uniform temperature changes, but also variations of temperature through the depth of the superstructure (thermal gradients). Bridge deformations due to uniform temperature changes are well understood and easily accounted for in design by providing sliding joints and flexible piers, among other methods, to accommodate such movements. Thermal gradients over the depth of the cross section, however, present a more complex engineering problem. In simply-supported spans, the nonlinear portion of the thermal gradient will cause internal self-equilibrating thermal stresses that cannot be relieved through adjustment of the support conditions. In continuous spans, the linear portion of the thermal gradient causes continuity stresses due to restraint to curvature in addition to self-equilibrating thermal stresses caused by the nonlinear portion of the thermal gradient.

Designing continuous segmental concrete bridges for stresses due to thermal gradients is typically accomplished by making use of the American Association of State Highway and Transportation Officials (AASHTO) Load and Resistance Factor Design (LRFD) Specifications and the AASHTO *Guide Specifications for Design and Construction of Segmental Concrete Bridges* (1999). These specifications require the consideration of a nonlinear thermal gradient load case when analyzing a segmental bridge for serviceability. Gradients that must be considered are positive (deck warmer than web) and negative (deck cooler than web). Stresses due to thermal gradients are analytically determined using concepts from classical mechanics. The magnitudes of thermal stresses determined in this manner can sometimes equal those due to live loads. This is of particular concern in the negative gradient case, which causes high tensile stresses to develop in the top few inches of the bridge deck. Due to limitations on the allowable tensile stress in segmental bridges, as stipulated by design codes, excessive prestress forces may be needed to counteract the tension generated by the negative gradient. From the perspective that nonlinear thermal gradients are considered only in serviceability checks, and do not affect the ultimate strength condition of a bridge, designing for thermal stresses as high as those determined analytically can produce overly-conservative and costly structures.

Past research leading to the determination of design thermal gradients for segmental concrete bridges has focused mainly on collection of temperature data over varying periods of time, and selection of the maximum observed gradients as design gradients. Little data, however, are available that indicate, whether the design thermal gradients produce stresses that are as high as those predicted analytically. One reason for this is the difficulty of stress measurement in concrete. Stress is generally estimated by measuring strain, which is then converted to stress by applying an elastic modulus. This works well for homogeneous elastic materials but there is less confidence in this procedure when applied to concrete due to material variability at the scale of the strain gauge.

2 SCOPE AND OBJECTIVES

This research focused on two primary objectives. The first was to determine whether experimentally determined self-equilibrating thermal stresses caused by application of the AASHTO nonlinear thermal gradients are as severe as predicted by analysis. To this end an experimental program was carried out to quantify self-equilibrating stresses caused by the thermal gradients. The details of this work are described in Part One of this report. The second objective of this research focused on evaluating the effect that self-equilibrating thermal stresses have on cracking and the necessity of considering superposition of the full self-equilibrating stresses for serviceability design checks. The details of this work are described in Part Two of this report.

3 BACKGROUND

3.1 THERMAL GRADIENTS

Thermal gradients in concrete bridges are largely the result of the low thermal conductivity of concrete. By convention, a positive gradient is defined as a condition in which the temperature of the top deck is higher than the temperature of the webs. A negative gradient exists when the temperature of the web is warmer than that of the top deck and bottom flange.

Climate, bridge material, and the shape of the cross section all affect the shape and magnitude of thermal gradients. Climatic factors of importance include solar radiation, ambient temperature, wind speed, and precipitation. Climatic conditions leading to the development of positive and negative thermal gradients in concrete bridges are illustrated in Figure 1 and Figure 2, respectively. Material properties such as thermal conductivity, density, absorptivity, and specific heat influence thermal gradients in concrete. The effect of cross sectional shape on the development of thermal gradients is highly complicated and has not been the focus of extensive research, however, from thermocouple data taken from existing segmental box-girder bridges it is known that in addition to vertical temperature gradients, box girder sections experience transverse temperature gradients due to the effects of differential temperature inside and outside the section (see points A and B in Figure 1 and Figure 2). Furthermore, the effect of enclosed air inside concrete box girders causes slightly different temperatures between the deck above the cavity and the exposed (cantilevered) deck overhang (points C and D in Figure 1 and Figure 2).

AASHTO specifications for the design of bridges for thermal gradients were first introduced in 1989. In 1983 Potgieter and Gamble developed a two-dimensional finite difference program to calculate the distribution of temperature in a concrete section using weather station data from around the United States. From the studies conducted, they determined conditions at each site that would produce the maximum temperature differences, shapes, and magnitudes of nonlinear (positive) temperature gradients. The analytical model was validated with data taken from the Kishwaukee River Bridge in Illinois. In 1985 the National Cooperative Highway Research Program (NCHRP) published Report 276, *Thermal Effects in Concrete Bridge Superstructures* (Imbsen et al. 1985), which provided guidelines for the consideration of thermal gradients in the design of concrete bridges. The recommendations in NCHRP Report 276 were based largely on the work by Potgieter and Gamble (1983). In 1989 AASHTO published their *Guide Specifications, Thermal Effects in Concrete Bridge Superstructures* (AASHTO 1989a), which was based on NCHRP Report 276. The AASHTO *Guide Specifications for Design and Construction of Segmental Concrete Bridges* (AASHTO 1989b), a derivative of the AASHTO (1989a) specifications, required the consideration of thermal gradients in the design of all segmental bridges.

In the AASHTO *Guide Specifications, Thermal Effects in Concrete Bridge Superstructures* (AASHTO 1989a), the United States is divided into four solar radiation zones (see Figure 3), and a positive and negative gradient magnitude is specified for each zone. At the time of publication of the AASHTO (1989a) Guide Specifications very little field data were available to substantiate the nonlinear thermal gradients utilized by the specifications. Since then, several field studies have been conducted on existing segmental bridges in the United States (e.g. Shushkewich 1998) that generally agree with the positive gradients stipulated by AASHTO.

Negative gradients in the AASHTO (1989a) Guide Specifications were based on the British Standard BS 5400 (1978). The shape of negative thermal gradients has since been modified and the magnitudes reduced to simplify the design process. The AASHTO *Guide Specifications for Design and Construction of Segmental Concrete Bridges* (AASHTO 1999), and the AASHTO *LRFD Bridge Design Specifications* (AASHTO 1998a) specify the negative gradient as a fractional multiple of the positive gradient (-0.30 for plain concrete surfaces and -0.20 for surfaces with 2-in. asphalt topping). Magnitudes of the negative gradients in each geographic zone depend on categorization into one of two superstructure surface conditions: plain concrete surface, and 2-in. asphalt topping. Asphalt toppings tend to reduce loss of heat from the flanges of bridge superstructures, thus increasing the surface temperature and algebraic maximum magnitude of the thermal gradient. Thermal gradient shapes are essentially the same for all cross sections.

Thermal gradients in the AASHTO *Guide Specifications, Thermal Effects in Concrete Bridge Superstructures* (AASHTO 1989b) are applicable only to superstructure depths greater than 2 ft. Thermal gradients in the AASHTO *Guide Specifications for Design and Construction of Segmental Concrete Bridges* (AASHTO 1999), and the AASHTO *LRFD Bridge Design Specifications* (AASHTO 1994a), which are derivatives of the AASHTO (1989b) Guide Specifications, are not restricted to superstructure depths greater than 2 ft. (see Figure 4 for a comparison of AASHTO gradients). Instead, different superstructure depths are taken into account by means of a vertical dimension, "A" (see Figure 5). The dimension "A" is taken as 12 in. for superstructure depths greater than 16 in. For superstructures with depth less than 16 in., "A" is taken as 4 in. less than the depth of the superstructure.

Magnitudes of T_1 and T_2 for the four solar radiation zones into which the United States is divided (see Figure 3) are shown in Table 1 (Florida is located in zone 3). The AASHTO (1999) Guide Specifications specify the value of T_3 as zero, unless a site-specific study is conducted to determine an appropriate value. Furthermore, should a site-specific study be conducted, the maximum value of T_3 as required by the specifications is 5 ^{o}F. It is worth mentioning that T_3 is usually taken as zero in design since it is unlikely that design engineers will have the necessary site data to determine otherwise.

Nonlinear thermal gradients in AASHTO specifications published after 1999 are identical to the gradients in the AASHTO (1999) Guide Specifications. The AASHTO (1999) thermal gradients were therefore used in this study since are currently being used in the design of segmental concrete bridges.

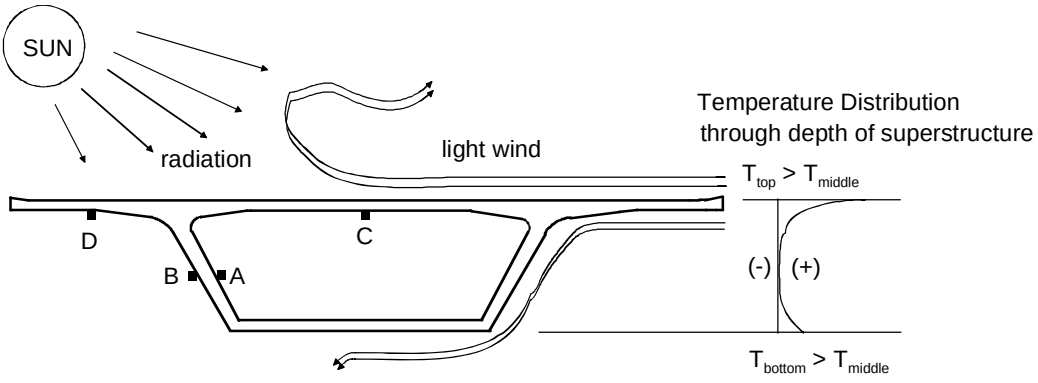

Figure 1 – Conditions for the development of positive thermal gradients

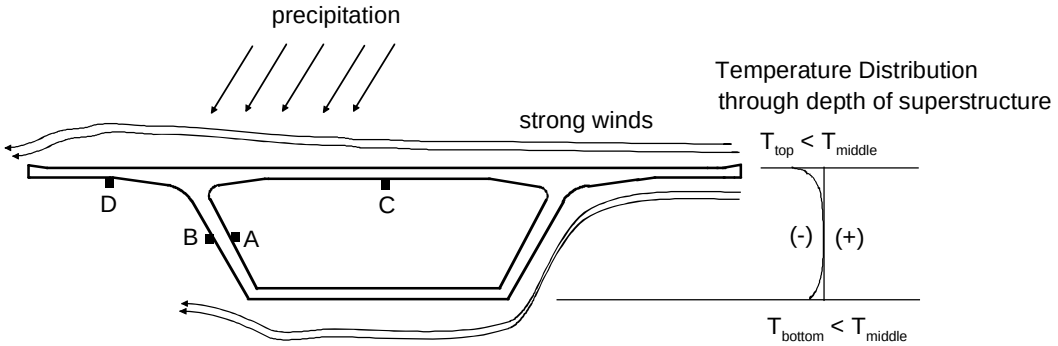

Figure 2 – Conditions for the development of negative thermal gradients

Figure 3 – Solar radiation zones for the United States (AASHTO 1989b)

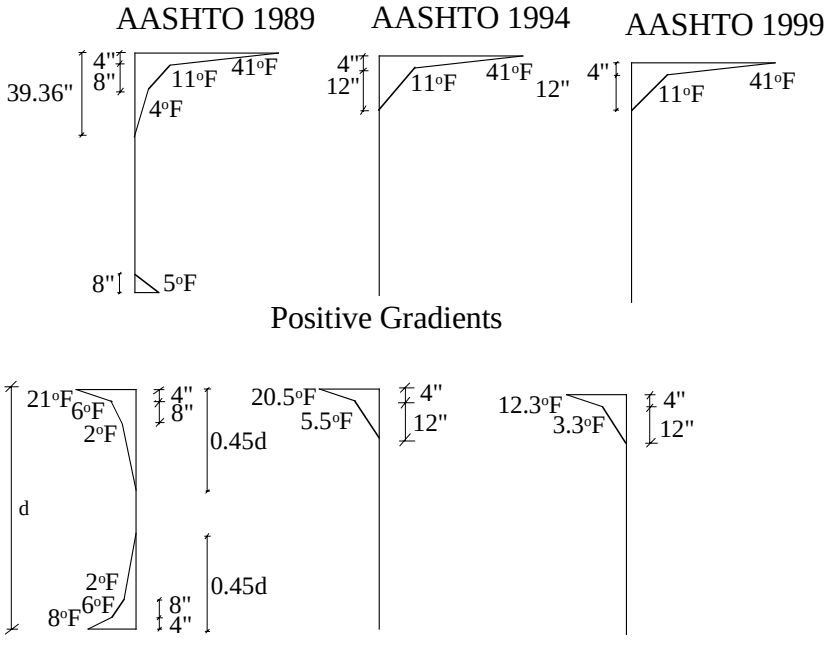

d = superstructure depth

Figure 4 – Comparison of AASHTO gradients for zone 3 (for superstructure depths greater than 2 ft)

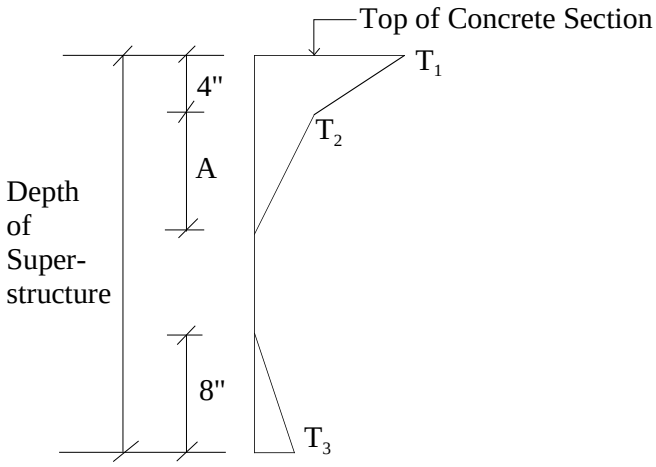

Figure 5 – Positive vertical temperature gradient for concrete superstructures (after AASHTO (1999))

Table 1 – Positive temperature differentials (after AASHTO (1999))

Plain Concrete Surface or Asphalt Topping		
Zone	**T_1 (^oF)**	**T_2 (^oF)**
1	54	14
2	46	12
3	41	11
4	38	9

3.2 STRUCTURAL RESPONSE TO THERMAL GRADIENTS

Nonlinear thermal gradients are usually divided into three components for analysis purposes (Figure 6): uniform temperature, linear thermal gradient and, self-equilibrating temperature distribution. The uniform temperature component causes uniform expansion or contraction of the unrestrained superstructure. If the structure is restrained against this deformation, axial forces may develop. A linear temperature gradient causes uniform curvature in the unrestrained superstructure. If the structure is restrained against curvature (restraints from vertical supports, e.g. bridge piers) then secondary moments develop as the result of a linear gradient.

The self-equilibrating temperature gradient, as the name implies, leads to the development of self-equilibrating stresses in the structure. The resultant force and moment due to these stresses are both zero because the stresses are developed as the result of inter-fiber compatibility and are not associated with external forces and moments. The development of self-equilibrating thermal stresses is discussed in the following paragraphs.

Consider the beam cross section shown in Figure 7 and assume the fibers of the section are free to deform independently. Under the action of a nonlinear positive thermal gradient the section fibers would deform in the shape of the gradient with the top fibers undergoing greater elongations than the middle and bottom fibers. In a real beam, however, inter-fiber bonds tend to resist the free deformation of section fibers. If the cross section of the beam is able to resist

out-of-plane flexural distortion (which is the case for a beam made of a homogeneous isotropic material undergoing uniform bending), the fibers of the beam will undergo a uniform elongation and uniform curvature. For deformations of the fibers to be consistent with the resistance of the cross section to out-of-plane flexural distortion, stresses are developed. These stresses, which are self-equilibrating, are compressive in the top and bottom fibers and tensile in the middle fibers of the cross section.

The development of self-equilibrating thermal stresses under the action of a nonlinear negative thermal gradient is illustrated in Figure 8. In this case, if the fibers of the section are free to deform independently, they would shorten with the top fibers undergoing greater shortening than the middle and bottom fibers. For deformations of the fibers of the beam to be consistent with the resistance of the cross section to out-of-plane flexural distortion, self-equilibrating stresses are developed. These stresses are tensile in the top and bottom fibers and compressive in the middle fibers of the beam.

The AASHTO approach to calculating stresses due to thermal gradients is based on one-dimensional Bernoulli beam theory. The procedure is outlined in the AASHTO *Guide Specifications, Thermal Effects in Concrete Bridge Superstructures* (AASHTO 1989b). The following assumptions regarding material behavior (for segmental box girder bridges, the construction material typically used is concrete) are made in the calculations:

1. Concrete is homogeneous and isotropic.
2. The material properties of concrete are independent of temperature.
3. Concrete has linear stress-strain and temperature-strain relationships.
4. The Navier-Bernoulli hypothesis; that initially plane sections remain plane after bending, is valid.
5. Temperature varies vertically with depth, but is constant at all points of equal depth.
6. Longitudinal and transverse thermal stress fields are independent of each other.

The shape of box-girder sections leads to the development of transverse thermal gradients because of differential temperatures between parts of the section that are inside and outside the box. Analysis for the effects of transverse thermal gradients is generally considered unnecessary (AASHTO 1999). For relatively shallow bridges with thick webs, however, such an analysis may be necessary. The AASHTO 1999 specifications recommend a plus or minus 10 ^{o}F transverse temperature differential in such cases. Generally, the primary stresses of interest in design are usually longitudinal stresses. To determine self-equilibrating longitudinal stresses using the AASHTO approach, a sectional analysis is performed. The structure is first assumed to be fully restrained against rotation and translation and the thermal stresses determined (see Equation 1). Axial force and bending moment required to maintain full restraint are then determined from the resulting stresses (see Equation 2 and Equation 3). Stresses due to the axial force and bending moment are then subtracted from the fully restrained thermal stresses to give self-equilibrating thermal stresses (see Equation 4). In statically determinate structures, this superposition yields the complete internal stress state. The strain and curvature of the structure are given by Equation 5 and Equation 6, respectively. Strains the structure does not undergo (i.e. strains corresponding to self-equilibrating thermal stresses) are calculated from Equation 7. In statically indeterminate (continuous) structures, additional continuity stresses must be determined by first performing a structural analysis using the negative of the restraining axial force and bending moment as loads at the ends of the continuous structure. This is usually done

using structural analysis software. Stresses computed from the structural analysis are then superimposed on stresses due to the restraining axial force and bending moment in the primary (sectional) analysis to give continuity stresses. Alternatively, the indeterminate structure can be allowed to undergo continuity deformations due to the nonlinear gradient (which can be obtained from Equation 5) by removing enough redundant supports to make the structure statically determinate. Reactions necessary to enforce displacement compatibility and accompanying continuity stresses can then be subsequently determined (e.g. using the flexibility method). The sum of the self-equilibrating stresses (determined previously via sectional analysis) and continuity stresses gives the total stress state in the continuous structure due to the nonlinear thermal gradient.

If the thermal gradient varies through the depth and width of the cross section, self-equilibrating thermal stresses are determined using Equation 8 through Equation 12, which are two-dimensional versions of Equation 1 through Equation 4, respectively.

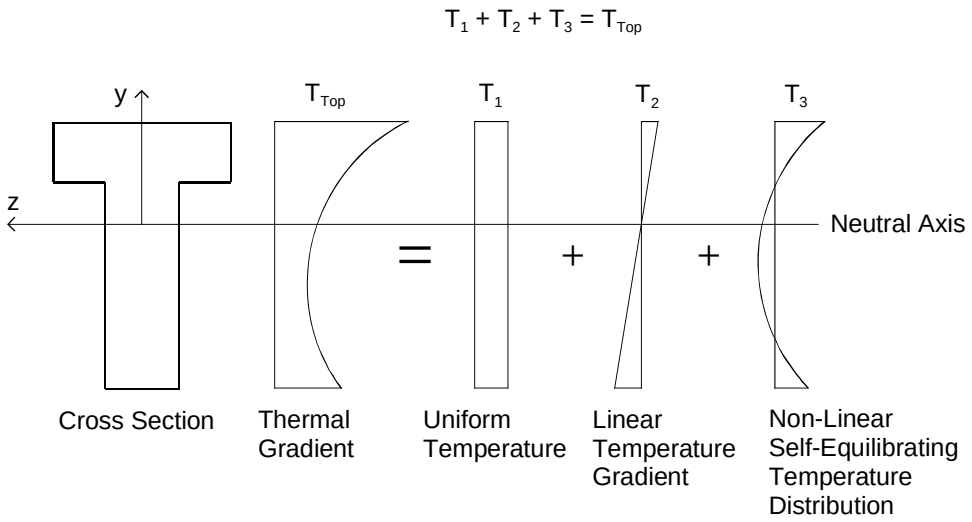

Figure 6 – Decomposition of a nonlinear thermal gradient

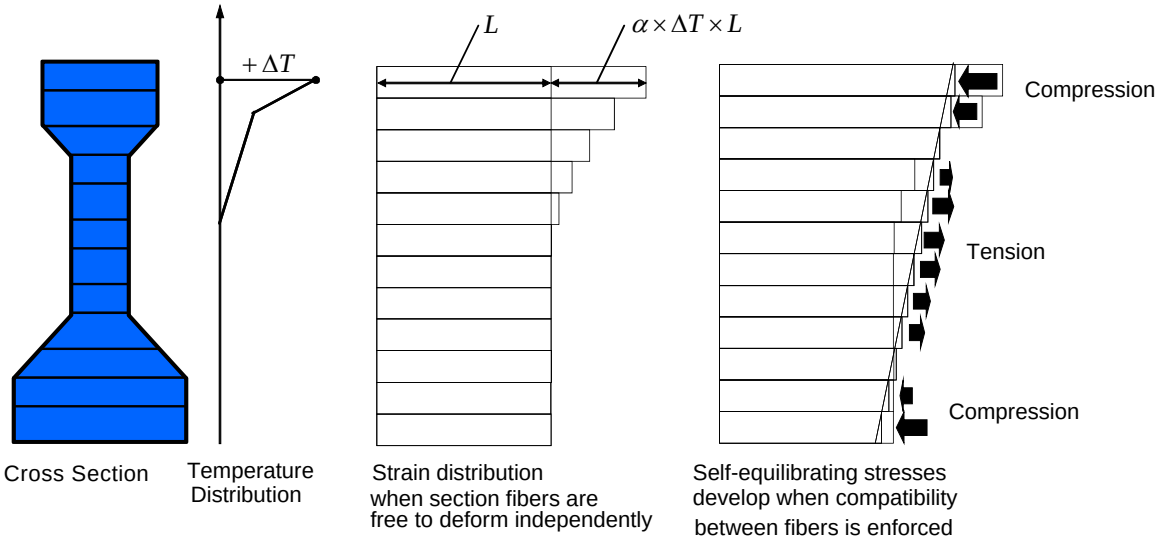

Figure 7 – Development of self-equilibrating thermal stresses for positive thermal gradient

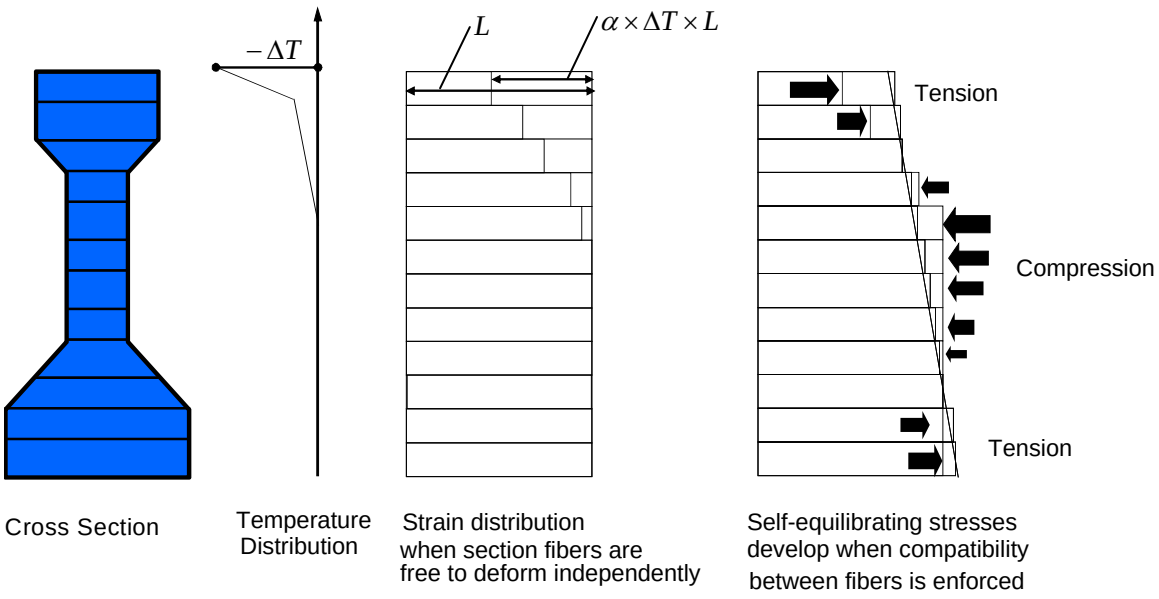

Figure 8 – Development of self-equilibrating thermal stresses for negative thermal gradient

$$f_{RT}(y) = -1 \cdot (E \cdot \alpha \cdot TG(y)) \qquad \text{Equation 1}$$

$$N_R = \int f_{RT}(y) \cdot b(y) dy \qquad \text{Equation 2}$$

$$Mz_R = \int f_{RT}(y) \cdot b(y) \cdot y dy \qquad \text{Equation 3}$$

$$f_{SE}(y) = f_{RT}(y) - \frac{N_R}{A} - \frac{Mz_R \cdot y}{I_z} \qquad \text{Equation 4}$$

$$\varepsilon(y) = \frac{-1}{E} \cdot \left(\frac{N_R}{A} + \frac{Mz_R \cdot y}{I_z} \right) \qquad \text{Equation 5}$$

$$\phi = -\frac{Mz_R}{E \cdot I_z} \qquad \text{Equation 6}$$

$$\varepsilon_{SE}(y) = \varepsilon(y) - \alpha \cdot TG(y) \qquad \text{Equation 7}$$

$$f_{RT}(z, y) = -1 \cdot (E \cdot \alpha \cdot TG(z, y)) \qquad \text{Equation 8}$$

$$N_R = \int_z \int_y f_{RT}(z, y) dz dy \qquad \text{Equation 9}$$

$$Mz_R = \int_z \int_y f_{RT}(z,y) \cdot y dz dy \qquad \text{Equation 10}$$

$$My_R = \int_z \int_y f_{RT}(z,y) \cdot z dz dy \qquad \text{Equation 11}$$

$$f_{SE}(z,y) = f_{RT}(z,y) - \frac{N_R}{A} - \frac{Mz_R \cdot y}{I_z} - \frac{My_R \cdot z}{I_y} \qquad \text{Equation 12}$$

where:

y	=	vertical distance from z axis
z	=	horizontal distance from y axis
$TG(y)$, $TG(z,y)$	=	thermal gradient in cross section
E	=	elastic modulus
$f_{RT}(y)$, $f_{RT}(z,y)$	=	thermal stresses assuming a fully restrained structure
N_R	=	restrained axial load
Mz_R	=	restrained moment about z axis
My_R	=	restrained moment about y axis
I_z	=	moment of inertia of section about z axis
I_y	=	moment of inertia of section about y axis
$f_{SE}(y)$, $f_{SE}(z,y)$	=	self-equilibrating thermal stress
$\varepsilon(y)$	=	thermal strains developed in structure
$\varepsilon_{SE}(y)$	=	strain corresponding to self-equilibrating thermal stress
ϕ	=	section curvature due to thermal gradient

3.3 Selected Field Studies on Thermal Gradients

Past studies on thermal gradients in continuous concrete segmental bridges have focused on determining the magnitude and shape of positive and negative thermal gradients. The frequencies at which the maximum positive and negative gradients occur, due to variations in environmental heating, have also been investigated. The studies vary in location, duration, number and type of thermocouples, and placement of thermocouples. Bridge cross sections most frequently considered were of the box-girder type. Three such field studies are discussed here.

3.3.1 The North Halawa Valley Viaduct Project

The North Halawa Viaduct consists of twin prestressed concrete segmental bridges on the island of Oahu in Hawaii. As part of the instrumentation set up to measure various bridges responses, two sections along a five-span unit were heavily instrumented with thermocouples (Shushkewich, 1998). One section, E, with 26 gauges, was near midspan. The other section, F, with 32 gauges, was near a support.

Thermocouple readings were first recorded in late 1994 and were to be recorded through the end of 1999. Initially readings were taken at 2-hour intervals but this was increased to 6-hour intervals when it was felt that too much data was being gathered. When it became apparent that

the critical positive thermal gradient was being underestimated the recording interval was again reduced to 2 hours (for design gradients in Hawaii, see Figure 5 and Table 1, zone 3). According to Shushkewich (1998), negative gradient readings were not as sensitive to the time interval as positive gradient readings. Thus, all the negative gradient readings were considered useful. Positive gradient readings taken during the period when the time interval between readings was 6 hours were considered unreliable. A 2-in. thick concrete topping was later placed on the instrumented sections. The topping was instrumented with thermocouples at the top, middle, and bottom.

Monthly and daily positive thermal gradient data were seen to be slightly higher for Section E than they were for Section F. Shushkewich (1998) attributed this to the higher thermal inertia of Section F (larger depth). Critical positive and negative thermal gradient profiles determined during the study were plotted for gauges along the centerlines of the web, top and bottom slabs. The gradients were also compared to design gradients in the then-proposed AASHTO (1998b) Segmental Guide Specifications. Because construction traffic interfered with the gauge at the top of the deck, Shushkewich (1998) considered readings from that gauge unreliable and suggested that readings at the deck surface be obtained by extrapolating data from a gauge 2.5 in. from the deck surface. Considering the positive and negative thermal gradient profiles, it was clear that in general, the slab readings were very close to the design gradients. The same could not be said for the web readings. The overall measured positive thermal gradient profile matched the design gradient more than the negative gradient profile matched the design negative gradient. The results of this study substantiated the reduction of the negative thermal gradient from -0.5 (AASHTO 1994a) to -0.3 times the positive gradient: the value used in the AASHTO Segmental Guide Specifications (AASHTO 1998b) and the AASHTO *LRFD Bridge Design Specifications* (AASHTO 1998a).

3.3.2 The San Antonio "Y" Project

As part of a field study (Roberts et al. 2002), four segments of a three-span continuous unit in the extensive upgrade to the intersection of interstate highways I-35 and I-10 in downtown San Antonio, Texas (the San Antonio "Y" project) were heavily instrumented with thermocouples. The instrumented segments were part of elevated viaducts comprised of precast segmental concrete box girders constructed using span-by-span techniques. Thermocouples in a web of one instrumented segment (Figure 9) were connected to a data logger. Temperatures were recorded every 30 minutes for 2 years and 6 months. There were gaps in the data due to limited memory of the data logger.

Maximum positive and negative temperature differences were determined for each day that thermocouple readings were recorded. Maximum positive temperature differences were computed from the difference between the largest top thermocouple reading (located 1 inch from the deck surface) and the coolest web thermocouple reading. Maximum negative temperature differences were computed from the difference between the coolest top thermocouple reading and the warmest web thermocouple reading.

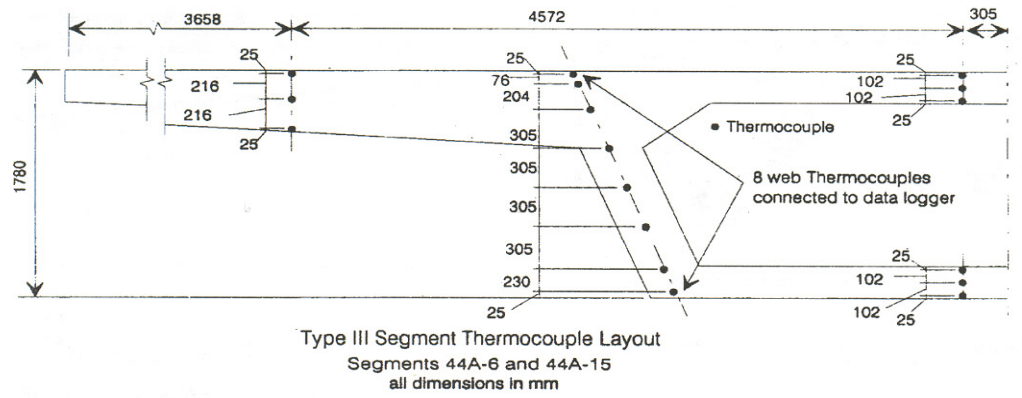

Figure 9 – Thermocouple locations (Roberts et al. 2002)

Measured positive thermal gradient magnitudes were found by Roberts et al. (2002) to be smaller than the design gradients in the AASHTO (1994a) LRFD specifications and the AASHTO (1999) segmental guide specifications (for design gradients in Texas, see Figure 5 and Table 1, zone 2). The gradient shapes were found to be similar to the older tri-linear shape in the *Guide Specifications for Thermal Effects in Concrete Superstructures* (AASHTO 1989b). Measured maximum negative thermal gradients were also compared to the design gradient. It was found that the field measured magnitudes were less than the AASHTO (1994b) LRFD specifications but slightly greater than the AASHTO (1999) segmental specifications. Figure 10 shows a comparison between design gradient magnitudes and the recorded maximum positive and negative temperature difference for each day in the data record, respectively. Data from the top most thermocouple (1 in. below the deck surface) were extrapolated to estimate deck surface temperatures using a fifth order polynomial equation based on earlier work by Priestley (1978).

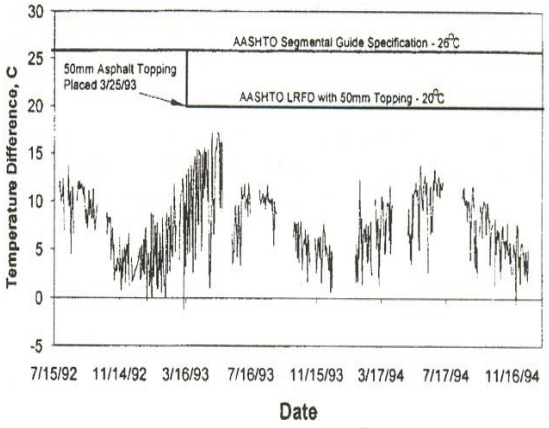

(Positive gradient)

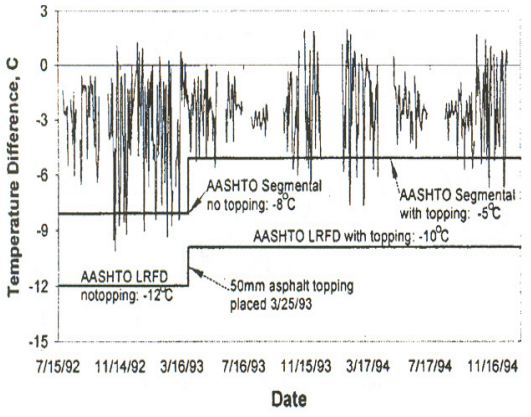

(Negative gradient)

Figure 10 – Comparison of maximum daily positive and negative temperature differences with design gradients (Roberts et al. 2002)

3.3.3 NORTHBOUND IH-35/NORTHBOUND US 183 FLYOVER RAMP PROJECT

Results from a field study conducted by Thompson et al. (1998) on a five-span continuous precast segmental horizontally curved concrete bridge erected in balanced cantilever are discussed. The bridge was part of a flyover ramp between interstate highway I-35 and US highway 183 in Austin, Texas. Three segments designated P16-2, P16-10, and P16-17 in one span of the structure were instrumented with thermocouples (see Figure 11). Segment P16-2 was at the base of the cantilever where the maximum negative moment (tension in the top fiber of the section) occurred during construction. Segment P16-10 was near the quarter point of the completed span where an inflection point in the load moment diagram was expected to occur. Segment P16-17 was located near the midpoint of the completed span where the maximum moment from gravity load was expected to occur. Response of the structure was studied under the actions of daily thermal gradients that occurred over a 9-month period.

From the temperature data gathered during the course of monitoring the bridge, daily temperature gradients were evaluated. The average temperature at the junction between the webs and the top flange was used as baseline reference and deducted from the measured average top and bottom temperatures. These resulting temperatures were taken as the basis for determining the thermal gradients.

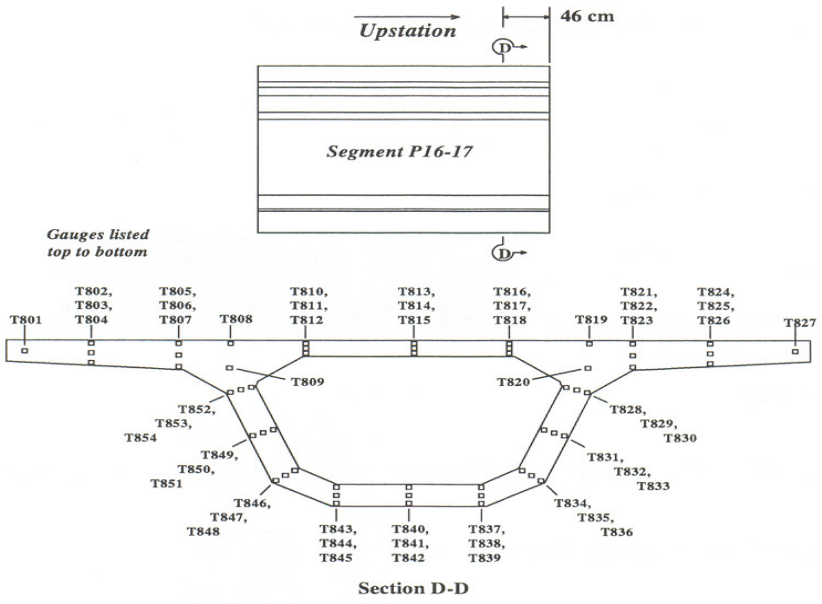

Figure 11 – Thermocouple locations (Thompson et al. (1998))

Longitudinal stresses from the design gradients and stresses from the maximum measured thermal gradients were calculated. The calculations were based on the technique recommended in the AASHTO *LRFD Bridge Design Specifications* (1994a). The calculated stresses were compared to *measured thermal gradient stresses*. The measured stresses were determined by making use of measured concrete strains (from strain gauges), a determined coefficient of thermal expansion, and elastic modulus determined from concrete test cylinders. To make calculated stresses comparable to measured stresses, calculated stress results were adjusted by adding a uniform temperature to the nonlinear AASHTO gradients. According to the

investigators, measured stresses came from readings taken between the time of peak gradient occurrence and some baseline time when the temperature distribution in the section was fairly uniform. Since a uniform change in temperature occurred within this time, the adjustment was necessary to make comparisons between measured and calculated stresses reasonable. Average values of elastic modulus and coefficient of thermal expansion determined during the course of the field study are shown in Table 2 and Table 3, respectively. Table 4 compares measured stresses with stresses calculated from the measured thermal gradients (tension is positive and compression is negative). Table 5 compares measured stresses with stresses calculated from application of the design gradients. It can be seen that measured stresses for P16-10 and P16-17 are high compared to those at P16-2. Furthermore, they do not compare well with the stresses determined using the AASHTO design technique. Thompson et al. (1998) attributed this to warping of the box girder. Of the three sections, P16-2 was the only one restrained by an anchorage diaphragm from section distortion. Since the AASHTO design specifications assume plane sections remain plane, stresses at P16-10 and P16-17, which were free to undergo out-of-plane distortion, could not be expected to match stresses computed using the AASHTO recommended design technique.

In spite of the observed high stresses, Thompson et al. (1998) did not observe any distress in the structure that could be attributed to thermal effects. The maximum and minimum top flange stresses, under load combinations of dead load, prestress, live load, and thermal gradient were computed. The field load combinations were not necessarily the same for each segment. From the computations, it was clear that no tension existed in the bridge under the load combinations considered. A design 28-day concrete compressive strength, f'_c, of 6.5ksi was used in the design of the bridge. However, compressive strength tests revealed that concrete strengths of 10 ksi were common. The maximum allowable compressive stress, $0.45f'_c$, was exceeded in P16-10 and P16-17 under full service loads. The approximate limit of elastic behavior in concrete, $0.7f'_c$, was also exceeded in a small (about 1-ft wide) part of P16-10. Based on the range of compressive strengths obtained from tests, the investigators felt the true compressive strength of concrete in the segments was probably much greater than the average design compressive strength. They therefore decided the stress distributions needed no adjustment.

Table 2 – Modulus of elasticity values for selected Ramp P segments

(after Thompson et al. (1998))

Test Date	**P16-2 (Cast 5/24/96)**	**P16-10 (Cast 6/4/96)**	**P16-17 (Cast 6/10/96)**
9/24/1996	6350 ksi	5900 ksi	5950 ksi
6/17/1997	6080 ksi	5470 ksi	5570 ksi

Table 3 – Coefficient of thermal expansion values for selected Ramp P segments (after Thompson et al. (1998))

	P16-2	**P16-10**	**P16-17**	**Average**
Coefficient of Thermal Expansion (α)	(5.0E-6/^{o}F) 9.0E-6/^{o}C	(5.4E-6/^{o}F) 9.7E-6/^{o}C	(5.2E-6/^{o}F) 9.4E-6/^{o}C	(5.2E-6/^{o}F) 9.4E-6/^{o}C

Table 4 – Comparison of Measured and Calculated Stresses from Measured Thermal Gradients (after Thompson et al. (1998), tension is negative)

Segment	Positive Thermal Gradient			Negative Thermal Gradient		
	Average Measured	**Average Calculated**	**Measured/ Calculated**	**Average Measured**	**Average Calculated**	**Measured/ Calculated**
P16-2	(368 psi) 2.54 MPa	(441 psi) 3.04 MPa	0.836	(-251 psi) -1.73 MPa	(-220 psi) -1.52 MPa	1.138
P16-10	(669 psi) 4.61 MPa	(458 psi) 3.16 MPa	1.459	(-466 psi) -3.21 MPa	(-225 psi) -1.55 MPa	2.071
P16-17	(609 psi) 4.20 MPa	(451 psi) 3.11 MPa	1.350	(-316 psi) -2.18 MPa	(-219 psi) -1.51 MPa	1.444
	Peak Measured	**Peak Calculated**	**Measured/ Calculated**	**Peak Measured**	**Peak Calculated**	**Measured/ Calculated**
P16-2	(584 psi) 4.03 MPa	(624 psi) 4.30 MPa	0.937	(-426 psi) -2.94 MPa	(-292 psi) -2.01 MPa	1.463
P16-10	(1874 psi) 12.92 MPa	(640 psi) 4.41 MPa	2.930	(-1144 psi) -7.89 MPa	(-297 psi) -2.05 MPa	3.849
P16-17	(1291 psi) 8.90 MPa	(627 psi) 4.32 MPa	2.060	(-483 psi) -3.33 MPa	(-287 psi) -1.98 MPa	1.682

Table 5 – Comparison of Measured and Design Stresses (after Thompson et al. (1998), tension is negative)

Segment	Positive Thermal Gradient			Negative Thermal Gradient		
	Peak Measured	**Design Calculated**	**Measured/ Design**	**Peak Measured**	**Design Calculated**	**Measured/ Design**
P16-2	(584 psi) 4.03 MPa	(518 psi) 3.57 MPa	1.129	(-426 psi) -2.94 MPa	(-264 psi) -1.82 MPa	1.615
P16-10	(1874 psi) 12.92 MPa	(518 psi) 3.57 MPa	3.619	(-1144 psi) -7.89 MPa	(-263 psi) -1.81 MPa	4.359
P16-17	(1291 psi) 8.90 MPa	515 psi (3.55 MPa)	2.507	(-483 psi) -3.33 MPa	(-260 psi) -1.79 MPa	1.860

PART ONE – VALIDATION OF SELF-EQUILIBRATING THERMAL STRESSES

4 OVERVIEW – PART ONE

A 20-ft long, 3-ft deep segmental concrete T-beam was constructed and laboratory-tested for this portion of the study. In-situ tests utilizing non-stress-inducing temperature profiles (uniform and linear temperature distributions) were performed on selected simply supported segments of the beam, to determine coefficients of thermal expansion. The post-tensioned beam was initially tested under the action of mechanical loads to establish a baseline condition from which the effect of thermal loads could be determined. Data from these tests were also used to evaluate the most suitable method of determining loads at which the dry joint at the midspan of the beam opened at specified depths. Accurate determination of loads at which the joint opened was important in quantifying stresses at the joint caused by nonlinear thermal gradients. A uniform temperature increment was imposed to investigate the expansion behavior of the beam under thermal loading. Though the beam was statically determinate with respect to support conditions, expansion or contraction of the concrete segments relative to the post-tensioning bars was expected to lead to the development of additional stresses that had to be accounted for in quantifying self-equilibrating thermal stresses. Subsequently a combination of AASHTO nonlinear thermal gradients and mechanical loads were applied to the beam. Self-equilibrating thermal stresses determined with results from these tests were then compared with corresponding thermal stresses determined using the AASHTO recommended method for calculating stresses caused by nonlinear thermal gradients.

5 BEAM DESIGN

5.1 CROSS-SECTION DESIGN

The Santa Rosa Bay (SRB) Bridge, located near Milton, Florida, was used as a prototype for design of the laboratory segmental beam. Laboratory space and equipment constraints ruled out the use of a full scale replica of the cross-section of the bridge (see Figure 12) as the test specimen. A scaled model of the box-girder section was considered. This, however, required scaling of the AASHTO design thermal gradients such that self-equilibrating thermal stresses in the model, determined using the AASHTO recommended procedure, matched those in the full size bridge. The logistics of imposing scaled AASHTO thermal gradients on a scaled model of the bridge (e.g. difficulties of scaling aggregates, steel reinforcements, etc.) eliminated this as a viable option.

Past research constituting the basis of thermal gradients in the design codes were conducted mainly on segmental box girder bridges. The design codes, however, do not restrict the use of the gradients to box girder bridges. Furthermore, the codes assume that the gradients vary only through the depth of the section. This means two cross-sections of different shapes, with the same depths, section properties, and material properties will experience identical self-equilibrating thermal stresses due to a nonlinear thermal gradient (from classical Bernoulli beam theory). For the purpose of determining longitudinal stresses due to bending about the weak axis, the cross-section of the SRB Bridge can be simplified to that of an un-symmetric I-section (see Figure 13) with the same cross sectional area and flexural stiffness about the weak axis as the box-girder section. The results of an analysis on the simplified section for self-equilibrating thermal stresses under the action of the AASHTO positive and negative design thermal gradients (for Florida) are shown in Figure 14 and Figure 15, respectively. The positive gradient leads to the development of compressive stresses (negative) in the top and bottom fibers of the section while tensile stresses (positive) develop in intermediate parts of the section. The negative gradient leads to the development of tensile stresses in the top and bottom fibers of the section and compressive stresses in the intermediate parts of the section. Throughout this document tensile stresses will be considered positive and compressive stresses negative. Of primary interest in this study were the tensile stresses created in the top few inches of the section by the negative thermal gradient. Consequently, a segmental T-beam with cross sectional geometry matching the top portion of the modified SRB Bridge section (illustrated by the hatching in Figure 14 and Figure 15) was constructed. Analytically determined self-equilibrating thermal stresses developed in the T-section by the AASHTO design gradients are also shown in the figures. The key aspects of the thermal stress profile in the SRB Bridge are captured in the laboratory segmental beam, including stress magnitudes in the top four inches of the flange, where the thermal gradient is steepest. Details of the cross-section of the laboratory beam together with analytically determined self-equilibrating thermal stresses due to the AASHTO design gradients are shown in Figure 16.

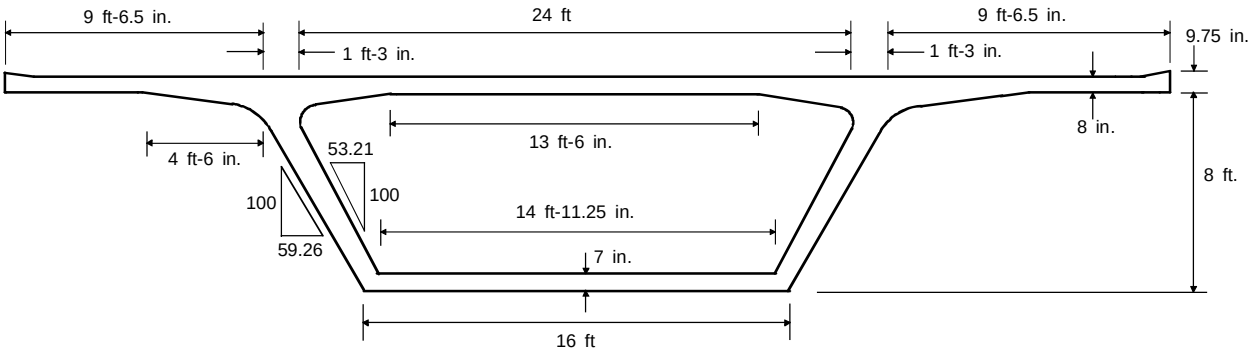

Figure 12 – Cross-section of Santa Rosa Bay Bridge

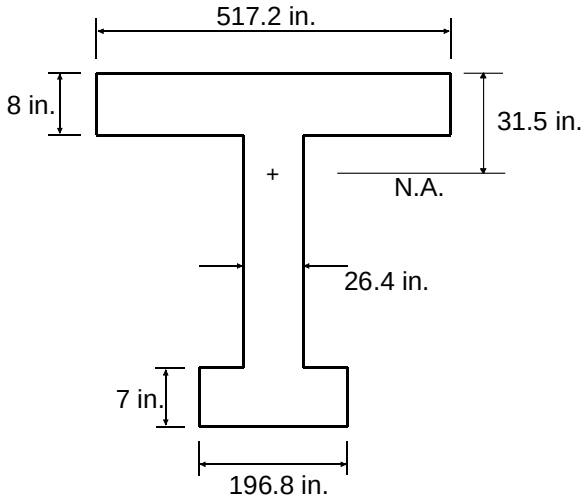

Figure 13 – I-section representation of SRB bridge cross section

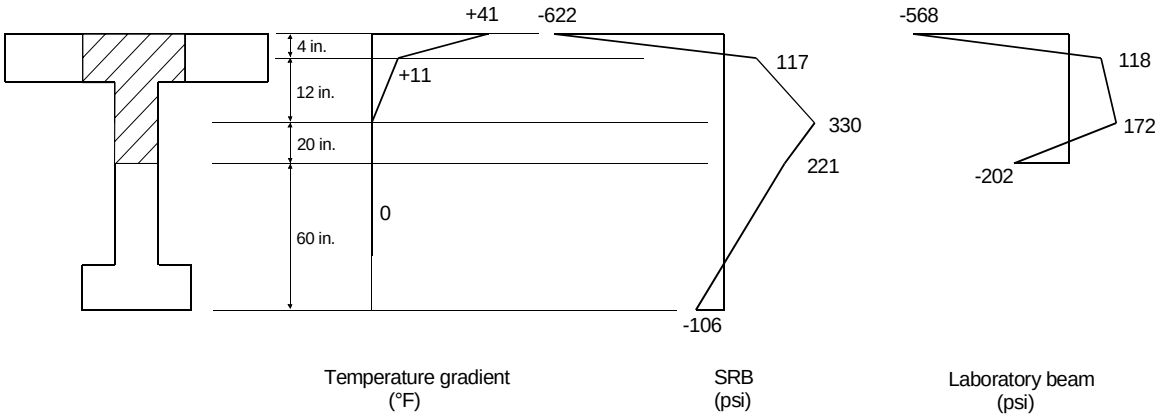

Figure 14 – Self-equilibrating stresses due to AASHTO positive thermal gradient

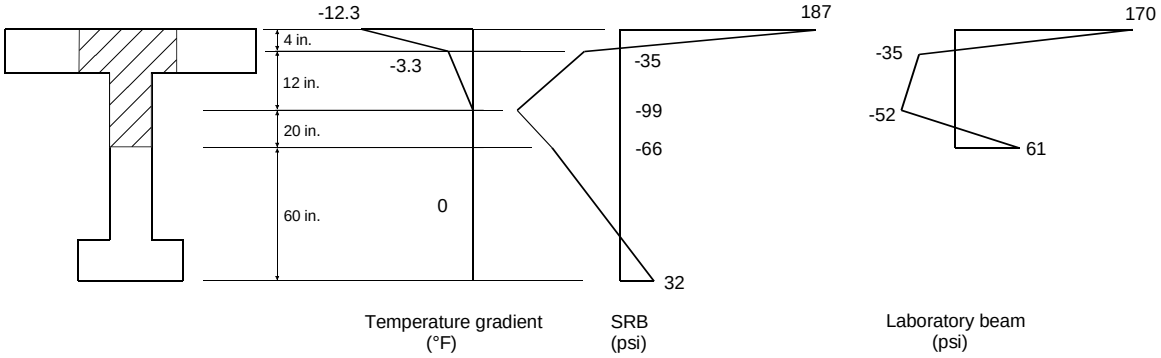

Figure 15 – Self-equilibrating stresses due to AASHTO negative thermal gradient

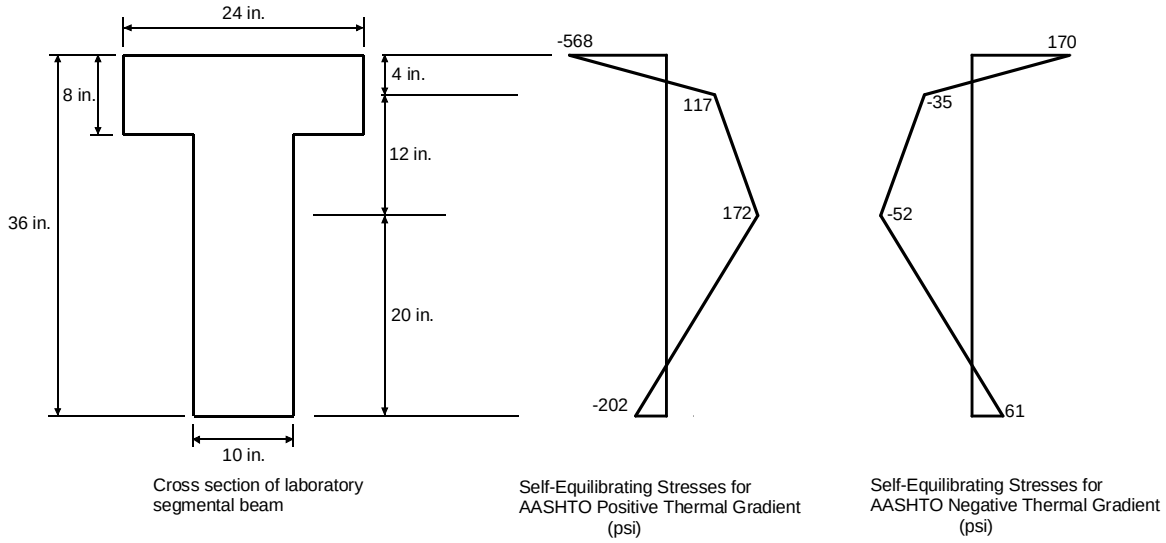

Figure 16 – Cross section of laboratory beam with analytically determined self-equilibrating thermal stresses due AASHTO design gradients

The flange width of the laboratory test beam was chosen based on recommendations in the AASHTO *LRFD Bridge Design Specifications* (AASHTO 2004), which are similar to recommendations in the ACI Committee 318, *Building Code Requirements for Structural Concrete and Commentary* (ACI 318-02). In prestressed beams with very wide flanges, shear deformations tend to relieve extreme fibers in the flange of longitudinal compressive stress, leading to a non-uniform distribution of stress. Therefore, for simplicity in design calculations it is recommended that an effective flange width, which may be smaller than the actual flange width, be used together with the assumption of uniform stress distribution in the flange. For symmetrical T-beams it is recommended that the width of slab effective as a T-beam flange not exceed one-quarter of the span length of the beam, and the effective overhanging flange width on each side of the web not exceed eight times the slab thickness nor one-half the clear distance to the next web. A width of 2 ft was chosen so that the entire flange of the beam could be considered effective in resisting the prestress force. Heating time and thermal energy required to impose the AASHTO nonlinear thermal gradients on the beam were also considered in limiting the width of the flange to 2 ft.

5.2 SEGMENT DESIGN

A 20-ft long segmental beam was designed for use in laboratory testing. The length of the beam was chosen based on the length of a typical segment of the Santa Rosa Bay Bridge. The beam was constructed as four 5 ft segments post-tensioned together. Equal segment lengths allowed a single set of forms to be used in casting the segments. The design of the segments included shear keys (see Figure 17), which were used to fit the segments together and prevent relative vertical sliding during load tests. Details of shear keys on each segment can be found in Appendix A. Figure 18 shows the segments as designed to fit together for laboratory testing. Two of the segments (segments 1 and 4) were designated "ambient" segments because they remained at the ambient laboratory temperature throughout testing. These segments were reinforced with steel to resist the high prestress forces arising in the anchorage zones. The remaining two segments (segments 2 and 3) were designated "heated" segments because they were thermally controlled during tests that involved the application of thermal loads. The heated segments contained copper tubes for thermal control but did not contain steel reinforcement, except for three thermocouple positioning steel cages.

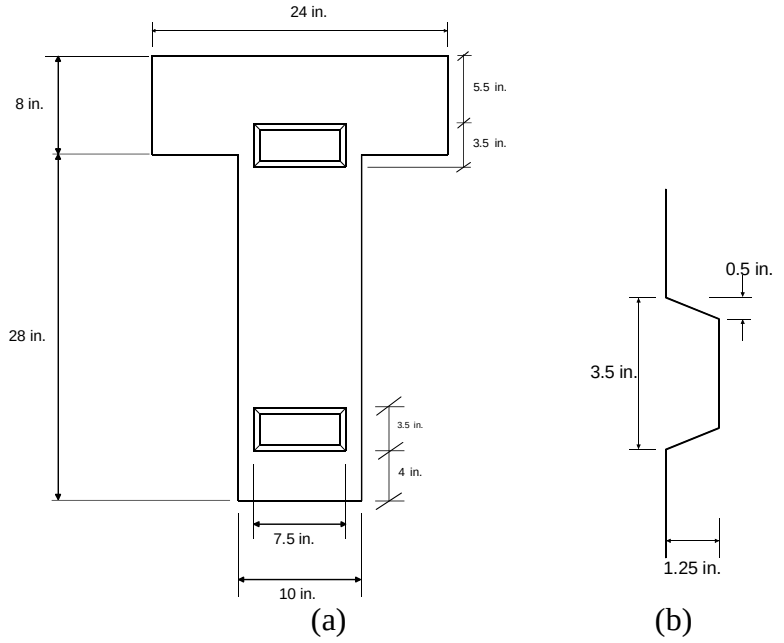

Figure 17 – (a) Location of shear keys on beam cross section; (b) Detailed elevation view of shear key

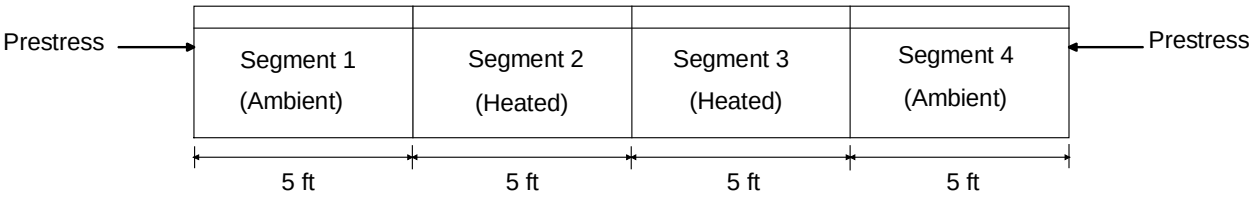

Figure 18 – Beam segments

5.3 SEGMENT HEATING SYSTEM DESIGN

Thermal control was achieved by passing varying temperature water through layers of copper tubes embedded in the heated segments of the beam. The number of copper tubes in each layer was minimized to reduce any reinforcing effect and reduction in concrete cross-sectional properties. Tests were first conducted on a 5 ft long, 2 ft deep prototype beam to optimize the number of copper tubes used in the laboratory segmental beam. AASHTO positive and negative design thermal gradients were imposed on the prototype beam using a varying number of copper tubes in each layer. The number of tubes in each layer that minimized piping while not sacrificing the ability to achieve the gradients in a reasonable amount of time, was chosen for the laboratory segmental beam. Copper tube layouts in the prototype and laboratory beam are shown in Figure 19 (a) and (b), respectively. As shown in Figure 20, layers 1, 2, and 4 were located near the slope changes in the AASHTO design thermal gradients. Additional layers of tubes were positioned to aid in heating the entire beam and in shaping the AASHTO gradients. The top layer of tubes was placed as close to top of the flange of the segments as possible while retaining adequate concrete cover (1 in.). This resulted in a slight nonlinearity of the thermal gradients near the top surface of the beam. Test results indicated that this may have affected the magnitude of measured strains caused by the AASHTO nonlinear thermal gradients in the extreme top flange fibers of the heated segments (see Chapter 14 and Chapter 15 for a complete discussion).

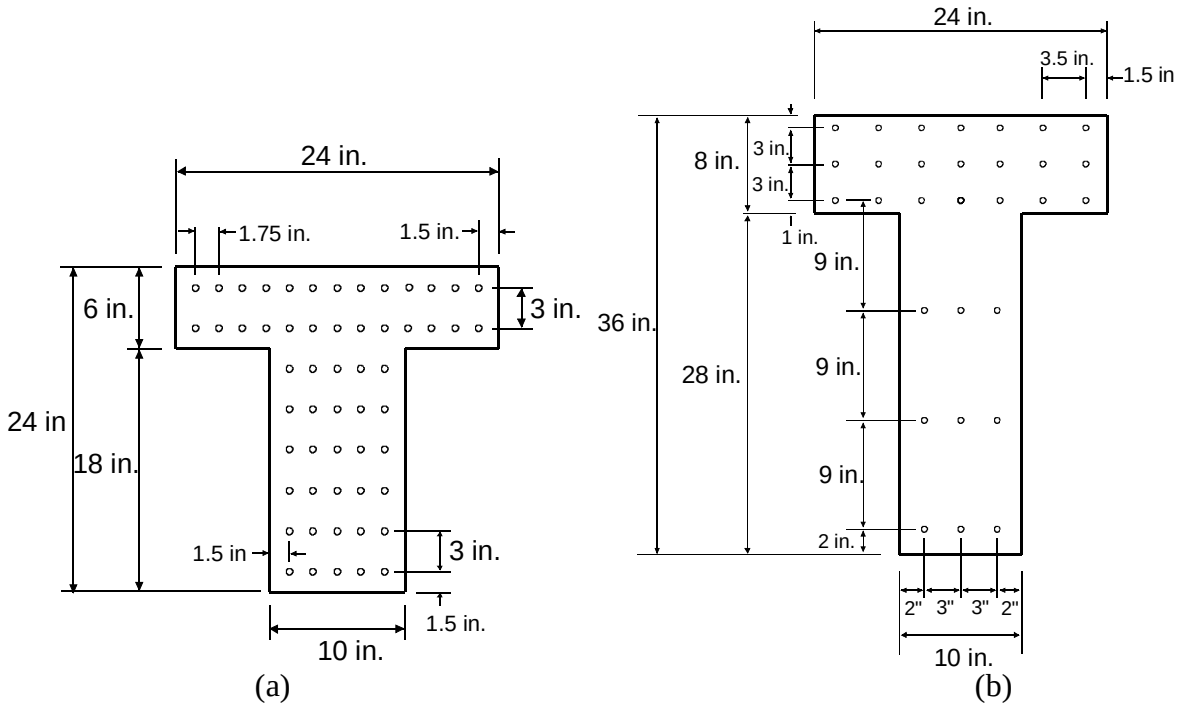

Figure 19 – Copper tube layouts for (a) Prototype beam and (b) Laboratory segmental beam

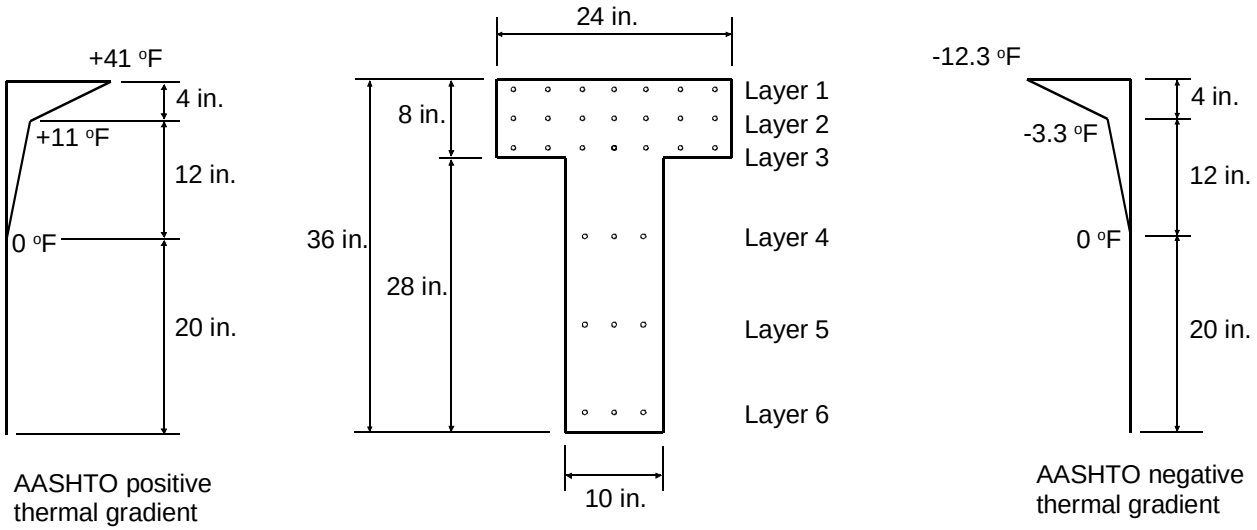

Figure 20 – Copper tube layouts in relation to shape of AASHTO design thermal gradients

Manifold systems were designed to distribute approximately equal flow to each pipe, which was key in achieving a uniform distribution of temperature across the width of the beam. Typical manifolds in the flange and web of the heated segments are shown in Figure 21 and Figure 22, respectively. The web manifolds consisted of constant-diameter inlet and outlet pipes. The flange manifolds required the use of varying-diameter inlet and outlet pipes due to the significant number of tubes in each layer in the flanges. Typical flow rates through the manifolds in the web and flange of the heated segments are shown in Figure 23 and Figure 24, respectively. Tests conducted on the manifolds showed that they were adequate in uniformly distributing heat across the web and along the length of the heated segments.

Heat energy was supplied to the beam by pumping water through on-demand electrical water heaters (see Figure 25). The heating system comprised of two S-H-7 Seisco electric heaters and one DHC-E Stiebel Eltron. The Seisco heaters (referred to as Heaters 1 and 2) could deliver water at temperatures as high as135 ^{o}F. The Stiebel Eltron heater (referred to as Heater 3) could instantly deliver water at temperatures as high as 125 ^{o}F. Pressurized water was supplied to the heaters (and beam) by 0.5 horsepower Depco submersible pumps. The pumps were able to operate at temperatures as high as 200 ^{o}F, which was required to re-circulate hot water through the beam. Hoses used with the pumps and the heaters were flexible plastic braided tubing, which could also operate at high temperatures.

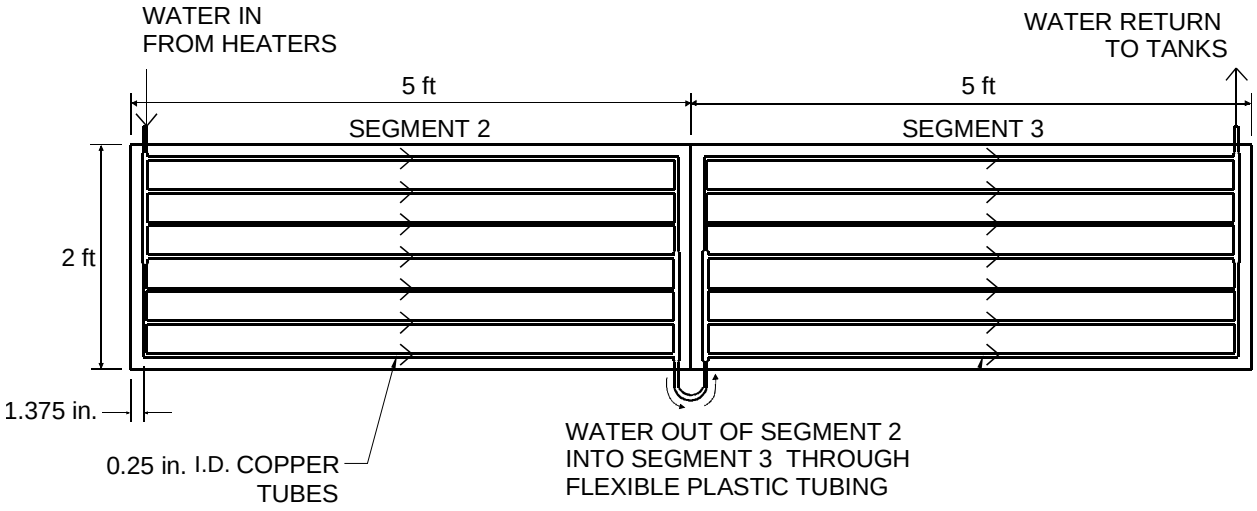

Figure 21 – Typical manifold in flange

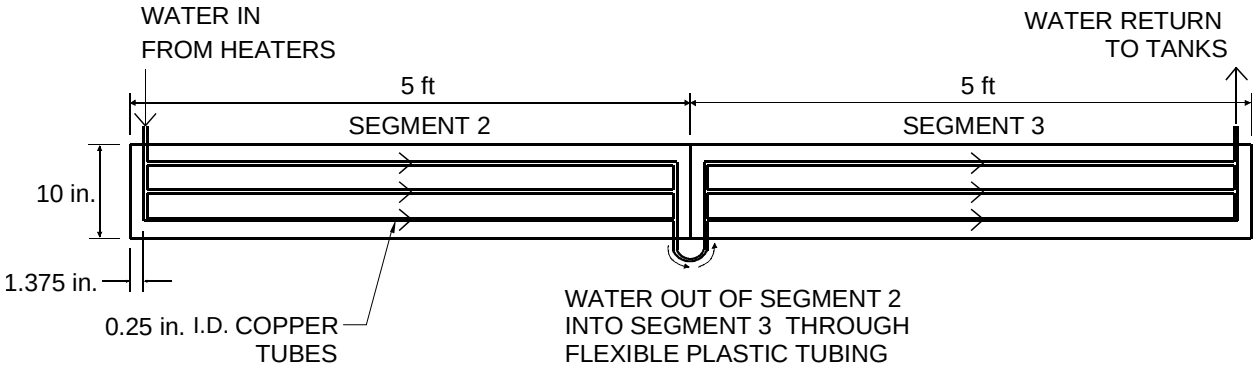

Figure 22 – Typical manifold in web

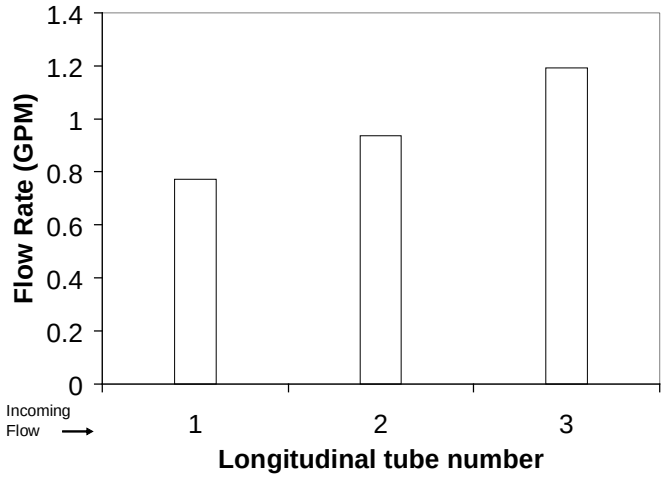

Figure 23 – Typical flow rates through web manifolds

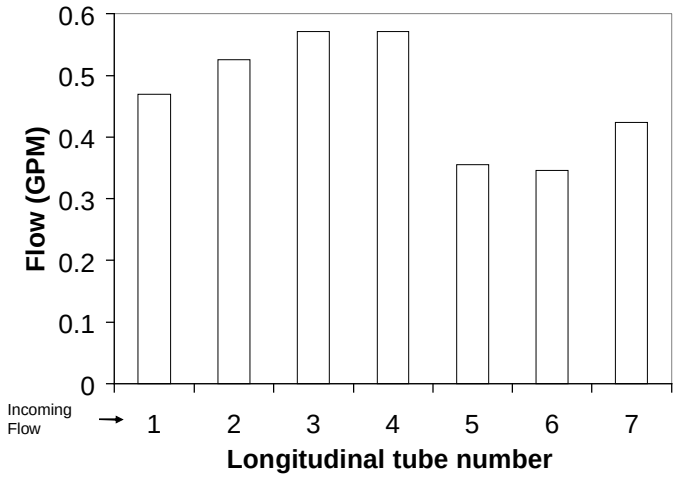

Figure 24 – Typical flow rates through flange manifolds

Figure 25 – Heating system

5.4 *PRESTRESS DESIGN*

An external post-tensioning system was designed for prestressing the segmental beam. This was done to avoid problems with concrete void space and interference with internal instrumentation. Stress levels considered in the design of the post-tensioning system were Service I stresses at the midspan and first interior support of a typical five-span unit of the Santa Rosa Bay Bridge (see Table 6). The Santa Rosa Bay Bridge was designed using HS20-44 vehicular loads, however, HL-93 vehicular loads (LRFD) were considered in the prestress design of the laboratory beam. In Table 6, M/S_t and M/S_b refer to stresses in the extreme top and bottom fibers of the cross section of the Santa Rosa Bay Bridge, respectively.

Four 1 3/8 in.-diameter high-strength DYWIDAG threaded bars were used to apply prestress to the beam. An anchorage system fabricated from structural steel shapes was designed to hold the bars in place during post-tensioning (see Figure 26 and Figure 27). Steel channels were placed back-to-back with sufficient space to allow for passage of the DYWIDAG bars. A

pair of back-to-back channels was used for the top and another pair for the bottom bars. Stiffeners were welded to the channels under the bar bearing plates. The design of the channel systems allowed the prestress force to be evenly distributed over the web of the beam.

Table 6 – Approximate Service I stresses in Santa Rosa Bay Bridge

	Effective Prestress (psi)						Dead + Live Load (psi)			
	Support			Midspan			Support		Midspan	
	P/A	M/S_t	M/S_b	P/A	M/S_t	M/S_b	M/S_t	M/S_b	M/S_t	M/S_b
HS20-44	-700	-338	680	-700	460	-940	810	-1630	-610	1230
HL-93	-700	-338	680	-700	460	-940	810	-1735	-684	1380

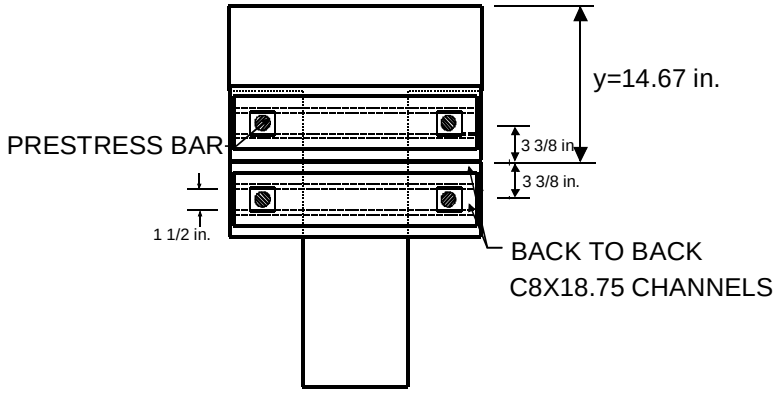

Figure 26 – Cross section view of prestress assembly

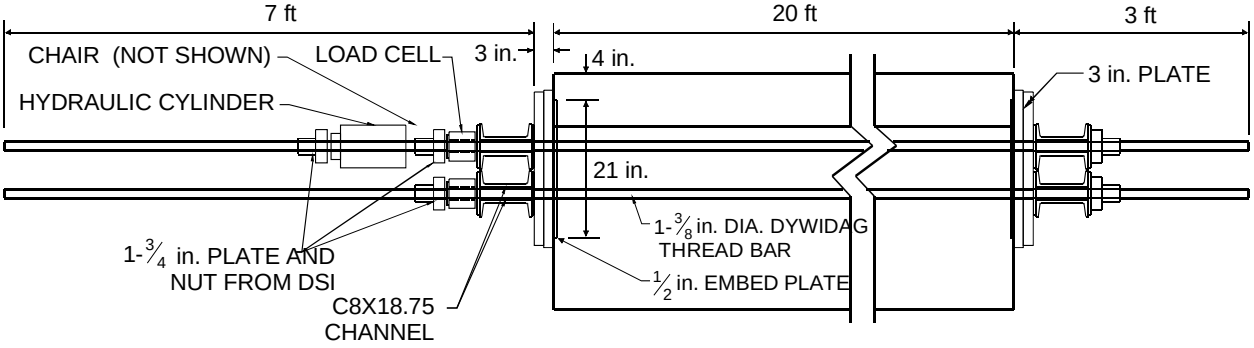

Figure 27 – Elevation view of prestress assembly

Steel reinforcement was required to resist the high post-tensioning forces in segments 1 and 4, where the post-tensioning systems were anchored. The AASHTO *LRFD Bridge Design Specifications* (AASHTO 2004a) was used in the design of reinforcement in the prestress anchorage zones. Number 3 vertical stirrups were placed 1.75 in. on center to resist principal tensile stresses that developed in the general anchorage zones. This reinforcement was placed within 27 in. from the bearing ends of the segments. The approximate method, which is permitted by the LRFD specifications, was the basis of the design. Outside the anchorage zone vertical stirrups were placed 12 in. on center. Stresses in the local zones were determined using guidelines from the AASHTO 2004a specifications. A set of three confinement spirals were

used to resist the high local zone stresses. The reinforcement design is shown in Figure 28 and Figure 29.

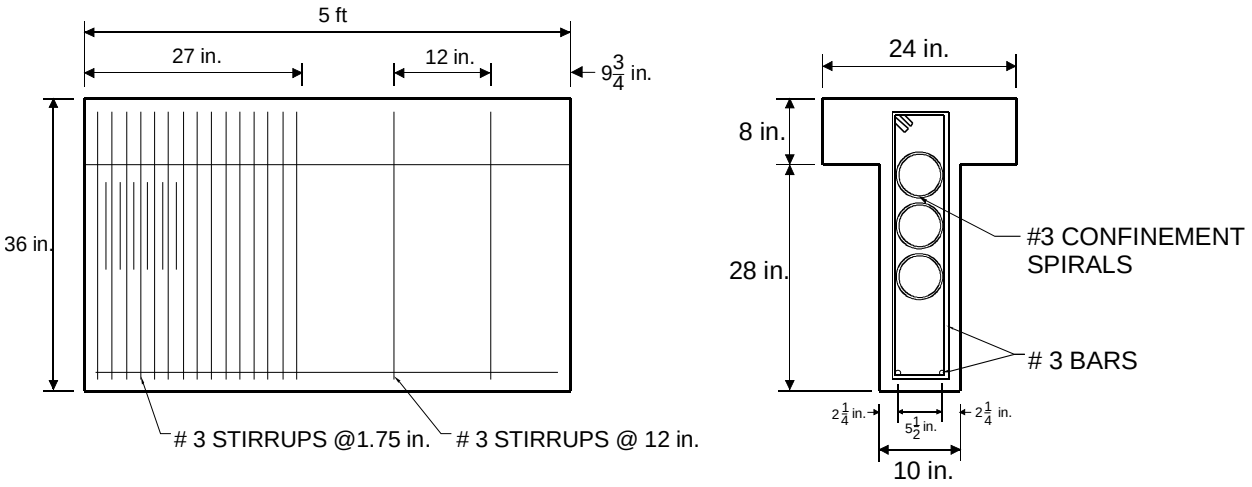

Figure 28 – Mild steel reinforcements in Segments 1 and 4

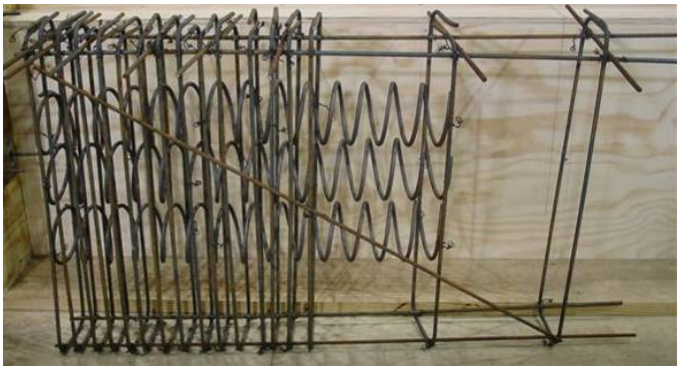

Figure 29 – Mild steel reinforcement

6 BEAM CONSTRUCTION

The segmental beam was constructed at the Florida Department of Transportation (FDOT) Structures Research Center in Tallahassee, Florida. Beam design plans (see Appendix A) prepared by the research team at the University of Florida, Gainesville, were submitted to the FDOT personnel in the summer of 2005. Construction began in December, 2005 and was completed in February, 2006. Formwork, reinforcement, and thermocouple cages were fabricated by FDOT personnel. After the segments were cast and cured, they were transported to the University of Florida Civil Engineering Structures Laboratory in Gainesville.

6.1 PLACEMENT OF STEEL REINFORCEMENT, THERMOCOUPLE CAGES, AND COPPER TUBES

Because the segments were of equal length, a single set of re-usable wooden forms was used to cast each of the four segments of the beam. Segments 1 and 4 contained a steel bearing plate to distribute the anchorage force to the prestress anchorage zones, which contained mild steel confinement reinforcement (Figure 30 (a)). Two steel lifting hooks were placed 1 ft from each end of the segments as shown in Figure 30 (b). The segment joints contained two shear keys to assist in alignment during prestressing and to transfer shear during load tests (Figure 31). The heated segments (Segment 2 and 3) each contained three thermocouple positioning steel cages (Figure 32). In addition, six copper tube manifolds were tied to the thermocouple cages to ensure that their positions were maintained during concrete placement. Three manifolds were placed in the flange and three were placed in the web.

Figure 30 – (a) Open form with mild steel reinforcement; (b) Closed form with mild steel reinforcement and lifting hooks

Figure 31 – Form for shear keys

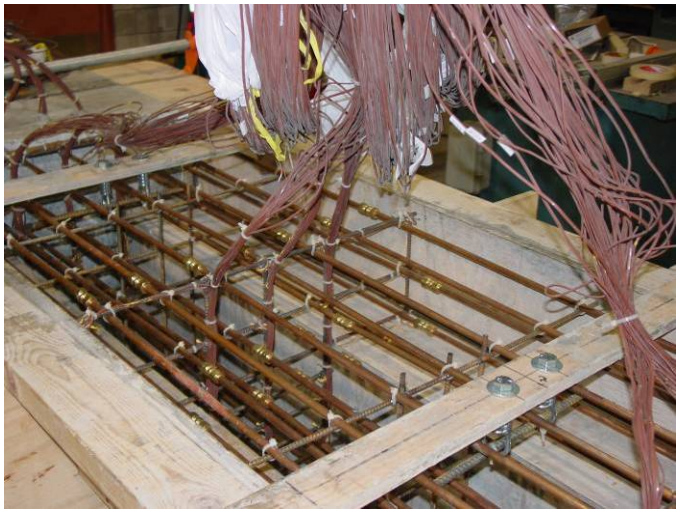

Figure 32 – Heated segment with copper tubes, thermocouple cages and thermocouples

6.2 CONCRETE PLACEMENT

The casting sequence of the segments of the laboratory beam is shown in Figure 33 and in Table 7 in ascending order. The ambient segments (1 and 4) were cast first so that the heated segments (2 and 3) could be match cast against them.

A 7000-psi concrete pump mix was used for all four segments. The design mix proportions are shown in Table 8. Delivery tickets for each mix are provided in Appendix B. Although the slump of the concrete is listed as 5 in. in Table 8, the mix was delivered with a slightly lower water content and slump to allow for adjustments prior to casting. Each segment was left in the forms for a week in the FDOT research laboratory before being removed and re-positioned for match-casting the next segment (see Figure 34). Finished pours for Segments 1 through 4 are shown in Figure 35 (a) through (d), respectively.

SEGMENT 1 December 1, 2005	SEGMENT 2 January 19, 2006	SEGMENT 3 February 2, 2006	SEGMENT 4 December 12, 2005

Figure 33 – Beam layout with casting sequence

Table 7 – Segment cast dates

Segment Number	**Date Cast**
1	12/01/2005
4	12/12/2005
2	01/19/2006
3	02/02/2006

Table 8 – Concrete pump mix proportions

Mix Number			**FC82JC**
Strength (psi)			7000
W/C Ratio			0.31
Slump (in)			5 +/- 1”
Air Content (%)			4.5 +/- 1.5%
Plastic Unit Weight (lbs/cf)			140.1 +/- 1.5
Material	ASTM	Type	
Cement	C 150	I/II	820
Cement	C 618	F. Ash	160
Water	--	--	304
Fine Aggregate	C 33	Sand	1095
Aggregate	C 33	#89STONE	1400
Admixture	C 260	AIR	Dosage rates vary with manufacturers recommendations
Admixture	C 494	W/Reducer	

Figure 34 – Match-casting of segment

(a)

(b)

(b)

(d)

Figure 35 – Finished concrete pours for (a) Segment 1, (b) Segment 2, (c) Segment 3, and (d) Segment 4

6.3 MATERIAL TESTS AND PROPERTIES

During the casting of each segment, fifteen 6 in. diameter by 12 in. long cylinders were cast for later use in determining material properties. The material properties determined for the ambient segments (1 and 4) were the compressive strength and modulus of elasticity (MOE). For the heated segments (2 and 3), the coefficient of thermal expansion (CTE) was determined in addition to the compressive strength and elastic modulus. The test setup for compressive strength and elastic modulus tests are shown in Figure 36 (a) and Figure 36 (b), respectively.

Compressive strength tests were conducted in accordance with the Standard Test Method for Compressive Strength of Cylindrical Concrete Specimens (ASTM C 39-01). Modulus of elasticity tests were conducted in accordance with the *Standard Test Method for Static Modulus of Elasticity and Poisson's Ratio of Concrete in Compression* (ASTM C 469-94). Coefficient of thermal expansion tests were conducted on each heated segment under laboratory conditions (in-situ CTE) and on 4 in. diameter by 8 in. long cylinders in accordance with the *Standard Method of Test for Coefficient of Thermal Expansion of Hydraulic Cement Concrete* (AASHTO TP 60-00). The in-situ CTE tests are discussed in Chapter 10. Unfortunately, cylinders meeting the specifications of the AASHTO TP 60-00 test method were not taken for Segment 2 therefore results from this test are only available for Segment 3. The AASHTO TP 60-00 test setup is shown in Figure 37. Tests were conducted in the FDOT Materials Testing Laboratory in Gainesville, Florida.

(a) (b)

Figure 36 – (a) Compressive strength test setup; (b) Elastic modulus test setup

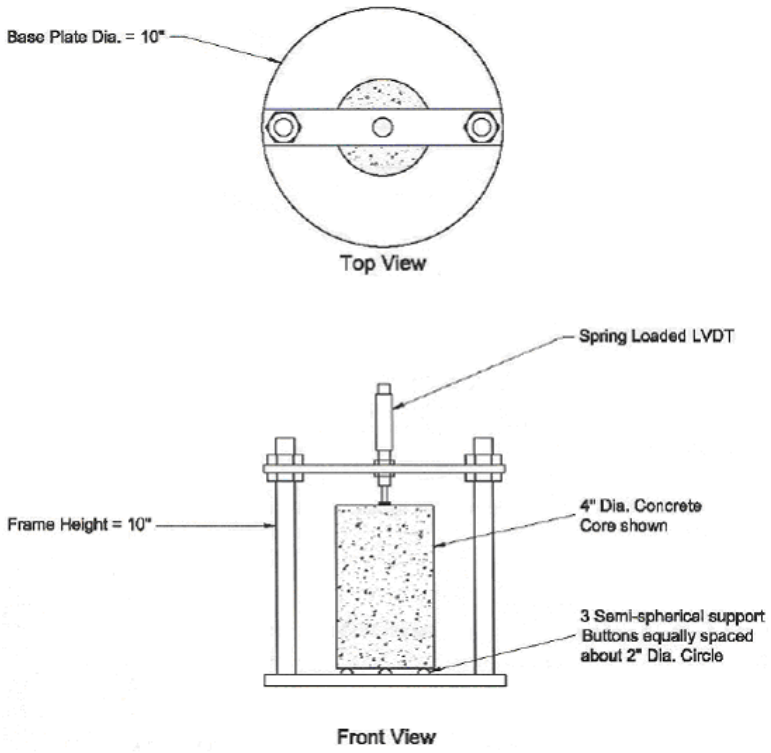

Figure 37 – AASHTO TP 60-00 test setup

The results of compressive strength and modulus of elasticity tests for each segment are shown in Table 9. Three sets of compressive strength and elastic modulus tests were conducted for all segments except for Segment 3, the last segment to be cast. The first two sets of tests were conducted in early 2006 soon after the cylinders were transported from Tallahassee to Gainesville. The last set of tests was conducted in late 2006 during the course of conducting experiments on the laboratory segmental beam. In each test, one cylinder from each segment was used to determine the compressive strength and two cylinders were used for determining the elastic modulus. The elastic modulus values shown in the table are the average of elastic moduli determined from two cylinders. Because of scheduling conflicts, the ages of cylinders at the times tests were conducted were generally not the same. However, test results for segments 1 and 4 which were cast 11 days apart, match closely (maximum difference of 2% and 6% in compressive strength and modulus of elasticity values, respectively). The same is true for segments 2 and 3, which were also cast 11 days apart (maximum difference of 12% and 5% in compressive strength and modulus of elasticity values, respectively).

The coefficient of thermal expansion (CTE) of Segment 3 was determined using the AASHTO TP 60-00 test method. The focus of the test method is the measurement of the change in length of a fully saturated concrete cylinder over a specified temperature range. The length change is then divided by the product of the original length of the specimen and the temperature change to give the CTE.

The AASHTO TP 60-00 test procedure is conducted as follows. The tests specimens consist of concrete cylinders that are 7.0 ± 1 in. long and 4 in. in diameter. The specimens are submerged in saturated limewater at 73 ± 4 ^{o}F for at least two days. After the cylinders are fully saturated, they are wiped dry and their lengths measured at room temperature to the nearest 0.004 in. The specimens are then placed in the measuring apparatus shown in Figure 37, which

is positioned in a prepared water bath. The temperature of the water bath is set to 50 ± 2 °F. The bath is allowed to remain at this temperature until the specimen reaches thermal equilibrium, which is indicated by consistent readings of a linear variable displacement transducer (LVDT) to the nearest 0.00001 in. taken every 10 minutes over a half hour time period. The temperature of the water bath and the consistent LVDT readings are taken as initial readings. The temperature of the water bath is then set to 122 ± 2 °F. The bath is allowed to remain at this temperature until the specimen reaches thermal equilibrium in the same manner as for the initial readings. The temperature of the water bath and LVDT readings are taken as the second readings. The temperature of the water bath is finally set back to 50 ± 2 °F. After thermal equilibrium is reached the temperature of the water bath and LVDT readings are taken as final readings.

The CTE is calculated using Equation 13 through Equation 15 below. The correction factor, C_f, in Equation 15 is usually taken as 9.6E-6/°F, the coefficient of thermal expansion of stainless steel. CTEs are determined from the expansion (initial and second readings) and contraction (second and final readings) segments of the test. The two CTE values thus obtained are averaged to give the CTE of the test specimen, provided the values are within 0.5E-6/°F of each other. If the CTEs obtained from the expansion and contraction phases are not within 0.5E-6/°F of each other, the test is repeated until this criterion is satisfied. Results for the coefficient of thermal expansion of Segment 3 determined using the AASHTO TP 60-00 test procedure are given in Table 10. Three cylinders were used for the test. Recent unpublished FHWA research has shown that the correction factor, C_f, used to correct for the stainless steel frame may be incorrect. Consequently, the thermal analyses in this report use the in situ CTE as reported in Chapter 10.

$$\text{CTE} = \left(\Delta L_a / L_o\right) / \Delta T \qquad \text{Equation 13}$$

$$\Delta L_a = \Delta L_m + \Delta L_f \qquad \text{Equation 14}$$

$$\Delta L_f = C_f \times L_o \ \Delta T \qquad \text{Equation 15}$$

where:

ΔL_a = actual length change of the specimen during temperature change
L_a = measured length of specimen at room temperature
ΔT = measured temperature change (increase is positive, decrease is negative)
ΔL_m = measured length change of specimen during temperature change (increase is positive, decrease is negative)
ΔL_f = length change of the measuring apparatus during temperature change
C_f = correction factor accounting for the change in length of the measurement apparatus with temperature

Table 9 – Compressive strengths and moduli of elasticity of beam segments

SEGMENT 1 (Cast 12/01/2005)		
Age (days)	**Compressive Strength (psi)**	**Modulus of Elasticity (ksi)**
77	9300	4862
124	9820	5000
350	10210	5362
SEGMENT 2 (Cast 01/19/2006)		
Age (days)	**Compressive Strength (psi)**	**Modulus of Elasticity (ksi)**
28	7090	3785
75	8360	4000
319	9690	5180
SEGMENT 3 (Cast 02/02/2006)		
Age (days)	**Compressive Strength (psi)**	**Modulus of Elasticity (ksi)**
28	7150	3836
62	7950	4000
361	10970	5443
SEGMENT 4 (Cast 12/12/2005)		
Age (days)	**Compressive Strength (psi)**	**Modulus of Elasticity (ksi)**
66	9110	4575
113	10030	5000
339	10250	5158

Table 10 – Coefficient of thermal expansion (CTE) of Segment 3 (age = 103 days)

	CTE (per ^{o}F)
Cylinder 1	7.92E-6
Cylinder 2	7.77E-6
Cylinder 3	7.83E-6
Average	7.84E-6

6.4 APPLICATION OF PRESTRESS

The goal of prestressing was to produce a net prestress with a selected vertical eccentricity and no net horizontal eccentricity. The magnitude and vertical eccentricity of prestress were chosen to impose a negative curvature (less compression in the extreme top fibers than in the bottom of the web) on the beam with stresses comparable to Service I stresses at a typical interior support of a four-span unit of the Santa Rosa Bay (SRB) bridge. The total prestress force was also required to provide sufficient compression in the extreme top fibers of the beam such that an appreciably high load at the cantilevered end of the beam, which could be accurately measured in the laboratory, would be required to open the joint at midspan. To achieve the stress state described above, a total prestress force of 376 kips (94 kips per bar) with a vertical eccentricity of 1.5 in. below the centroid of the beam was applied to the beam (see Figure 38).

Prior to post-tensioning, the segments were placed on wooden blocks at the same elevation with matching joint faces in contact. This reduced the possibility of excessive

movement as the joints closed during post-tensioning. The prestress anchorage systems were suspended from the ends of Segments 1 and 4 using a pair of threaded bars connected to two steel channels, which were bolted to the ends of the segments (Figure 39 and Figure 40). This arrangement allowed the vertical eccentricity of prestress to be varied as necessary. Four DYWIDAG post-tensioning bars were then installed. Tandem 60-ton Enerpac hollow core single-acting jacks, pressurized with a manifold system attached to a single pump, were used to stress two bars on either side of the web at a time. The set of four bars were stressed sequentially, 2 bars on either side of the beam at a time. Prestressing was applied incrementally as shown in Table 11 with the force monitored using 200 kip hollow core load cells mounted on each bar (Figure 40). Prestressing forces in opposing bars were slightly different (less than 8%) due to construction imperfections and variations in bar placement.

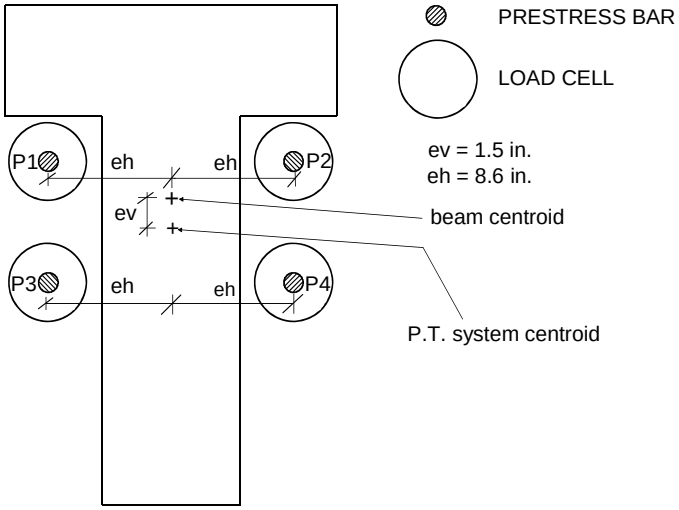

Figure 38 – Bar designations and design eccentricities (West)

Figure 39 – Prestress assembly (East)

Figure 40 – Elevation view of prestress assembly (North)

Table 11 – Selected post-tensioning force increments

Post-tensioning Step	Load Cell Readings(kips)			
	P1	P2	P3	P4
1	29.2	18	--	--
2	29.2	18	43.8	46.7
3	48.3	32.2	43.8	46.7
4	48.3	32.2	76.3	68.8
5	76.7	68.8	76.3	68.8
6	76.7	68.8	97.6	93.2
7	94.6	100.8	97.6	93.2
8	94.6	100.8	107.7	100.9
9	106.5	112.1	107.7	100.9
10	106.5	112.1	111.8	106.1
Final Loads	97.2	89.2	93.3	92.4

7 INSTRUMENTATION

Segments 2 and 3 of the laboratory segmental beam, designated “heated segments” because they were thermally controlled during testing, were internally instrumented with thermocouples prior to being cast, and externally instrumented with strain gauges, strain rings, and linear variable displacement transducers (LVDTs) prior to post-tensioning of the beam. Load cells were used to monitor reactions, applied mechanical loads, and prestress forces in the post-tensioning bars. This chapter presents a detailed description of the instrumentation used.

7.1 THERMOCOUPLES

Laboratory-fabricated thermocouples were embedded in the heated segments to monitor temperatures during thermal loading of the beam. The range of temperature that was to be measured was 50 ^{o}F to 130 ^{o}F. A Teflon-neoflon type T thermocouple wire, produced by OMEGA Engineering, Inc., was used for fabrication of the thermocouples due to its wide range of temperature sensitivity (-150 ^{o}F to 392 ^{o}F). Thermocouples were positioned in the segments with the aid of cages made of small-diameter steel, which were then placed in the forms at desired locations before concrete was cast (see Figure 41).

Thermocouples were vertically positioned to monitor temperature changes at heights corresponding to slope changes in the imposed thermal gradients. Additional thermocouples were placed at intermediate points between slope changes to facilitate control of the shape of the thermal gradient being imposed. The layout of thermocouples in relation to the shape of the AASHTO positive and negative thermal gradients is in shown in Figure 42. Three thermocouple cages were embedded in each of the two heated segments and total of thirty nine thermocouples were attached to each cage. Thermocouple cages were placed 3 in. away from the ends and at the middle of each segment (see Figure 43). This arrangement was used to ensure the thermal gradient being imposed was longitudinally uniform. Thermocouple labels at the sections in Figure 43 are shown in Figure 44.

Figure 41 – Thermocouple cage with attached thermocouples

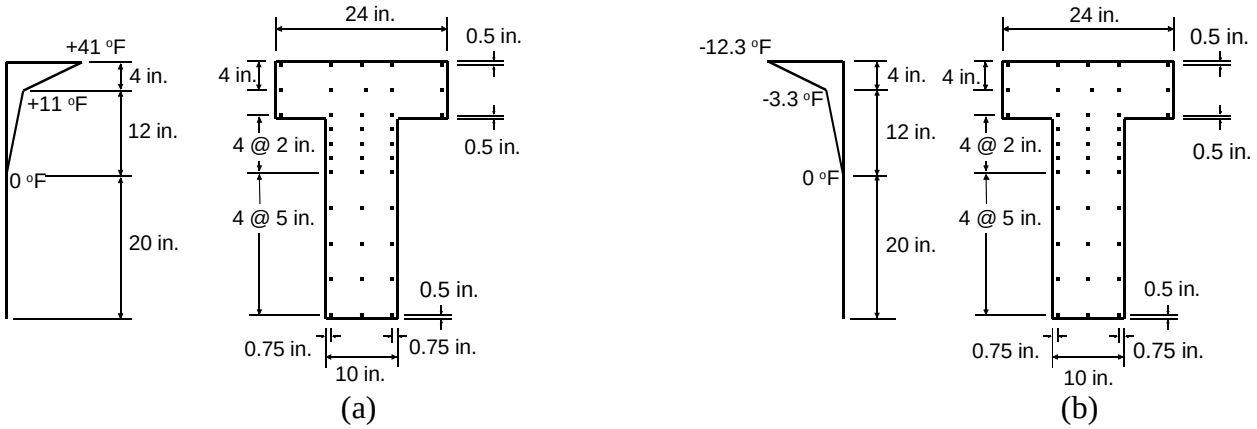

Figure 42 – Layout of thermocouples in relation to shape of (a) positive thermal gradient and (b) negative thermal gradient

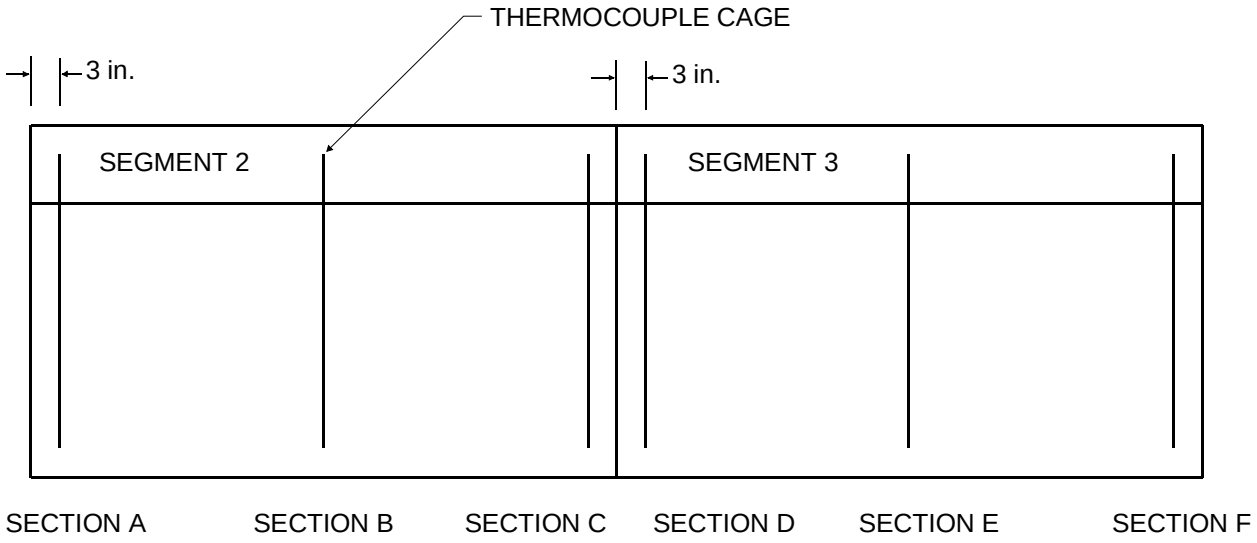

Figure 43 – Location of thermocouple cages in Segments 2 and 3

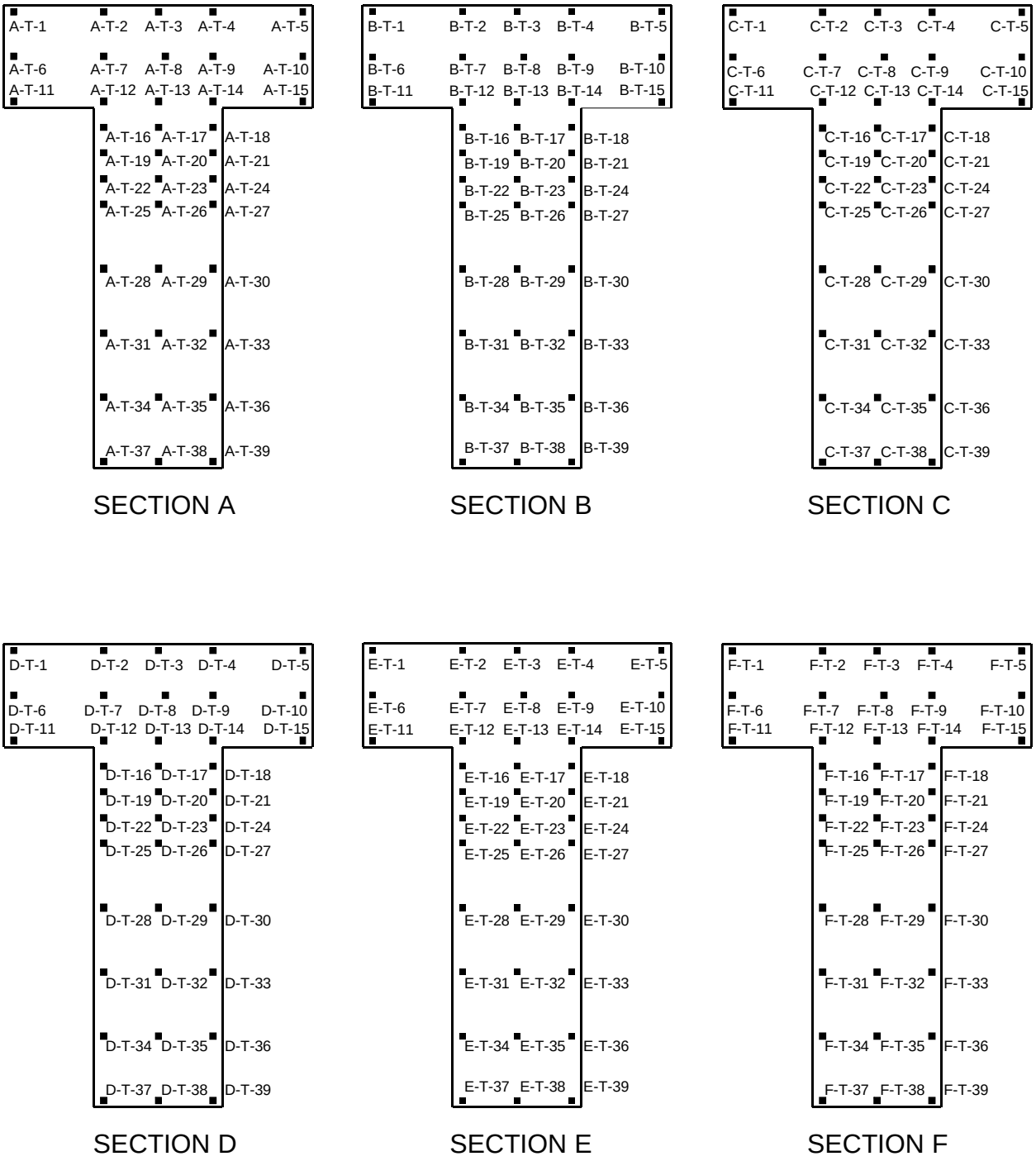

Figure 44 – Thermocouple labels in Segments 2 and 3

7.2 ELECTRICAL RESISTANCE CONCRETE STRAIN GAUGES AND STRAIN RINGS

Foil type electrical resistance strain gauges (Figure 45) were bonded to the surfaces of the heated segments of the beam for monitoring beam behavior under mechanical and thermal loading (Figure 46). The strain gauges were of type PL-60-11-5LT, manufactured by Tokyo Sokki Kenkyujo Co., Ltd. The gauges had a gauge length of 60 mm (2.4 in.), and a temperature compensation number of 11, which is adequate for eliminating strains due to unrestrained

thermal expansion/contraction of steel and concrete from measured strain values. To eliminate the influence of temperature variations (of the lead wires) on measured strains, three-wire type gauges were used.

In addition to strain gauges, four Strainstall Type-5745 sealed strain rings (Figure 47) were mounted at the centroid of the beam at midspan (Figure 46 (c) and (d)). Data from the strain rings were used to validate readings from strain gauges mounted at the same location. The detailed locations of strain gauges and strain rings through the depth of the beam on either side are shown in Figure 48, Figure 49, and Figure 50. The strain gauges located in the vicinity of the joint at midspan, (J2), were of particular importance in determining the load at which the joint opened. Strain gauges and strain rings located at the centroid of the beam at midspan were used to monitor movement of the neutral axis of the beam after the midspan joint began to open. With the exception of gauges located at the centroid of the beam, strain gauges located on the North and South of joint J2 were placed such that the center of each gauge was 2 in. away from the joint. Strain gauges located at the centroid at midspan were centered beneath strain rings, which had a greater gauge length (4.5 in.). Thus, the distance from the common center of these gauges to the joint at midspan was 3.6 in. Strain gauges on top of the flange were located 5.5 in. away from the joint. Because of the presence of copper tubes protruding from the concrete on the North side of the beam, two strain gauges were installed on the North side of the flange while three were installed on the South side. Therefore, a total of three strain gauges were located above the neutral axis of the section on the North side compared with four on the South side. The labeling convention used for strain gauges is explained in Figure 51. Strain rings were labeled in a similar manner by replacing the "S" for strain gauge with "R" for strain ring (see Figure 52).

Figure 45 – Strain (foil) gauge

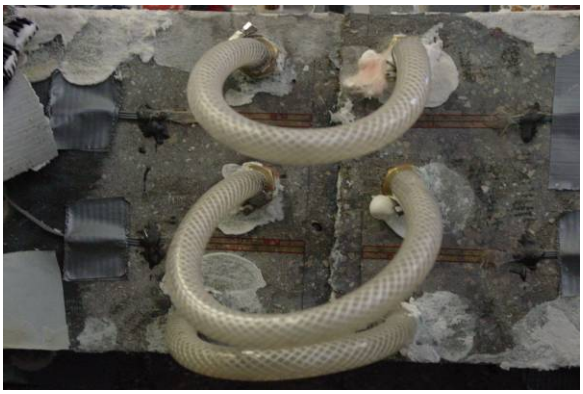

(a)

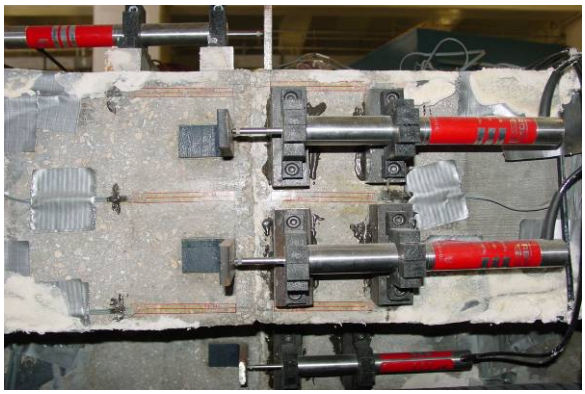

(b)

(c)

(d)

Figure 46 – Strain gauges close to joint at midspan; (a) North flange, (b) South flange, (c) North web, (d) South web

Figure 47 – Strain ring

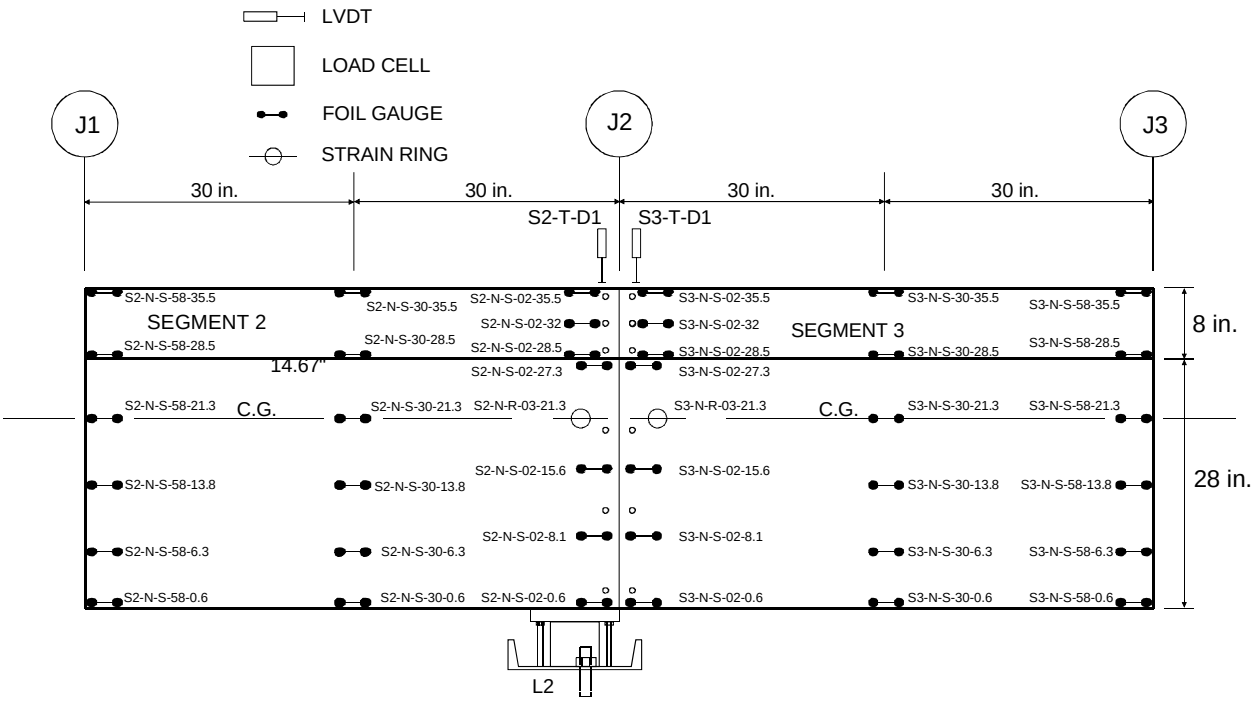

Figure 48 – Instrumentation details (North side)

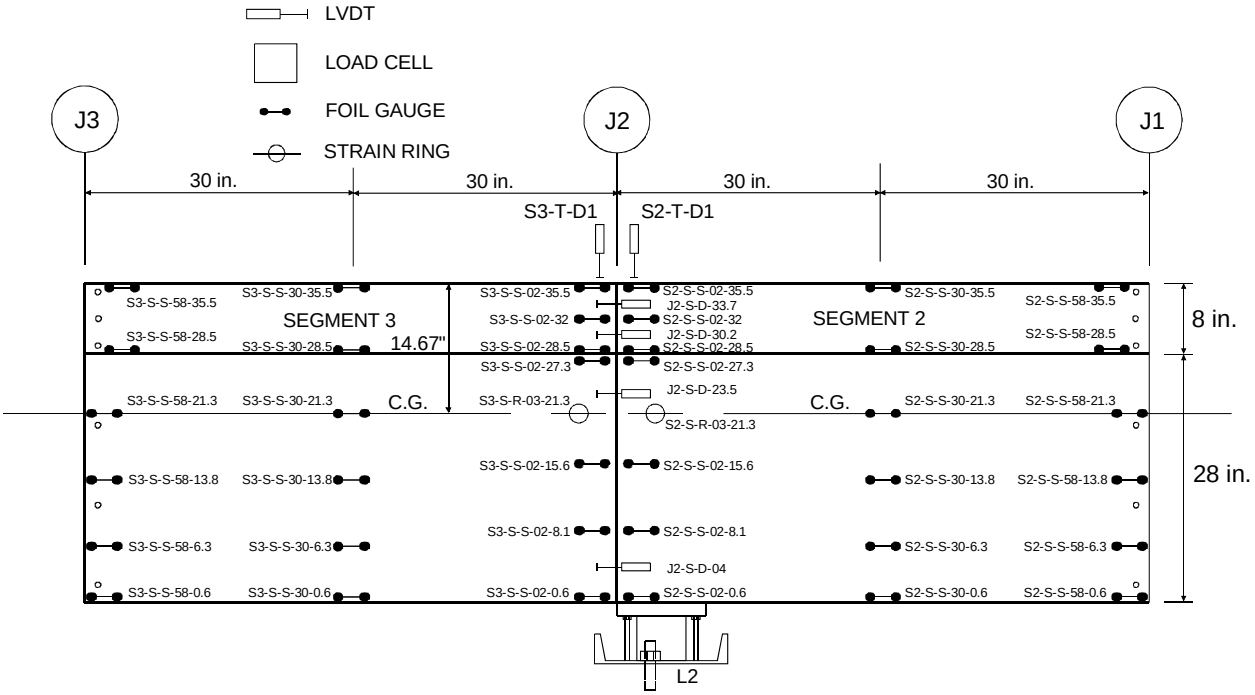

Figure 49 – Instrumentation details (South side)

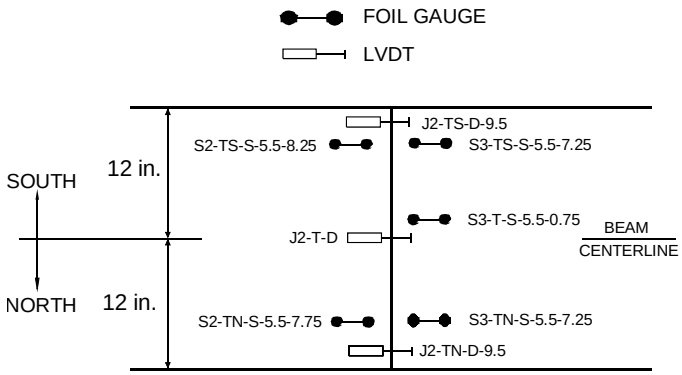

Figure 50 – Instrumentation at midspan (top flange)

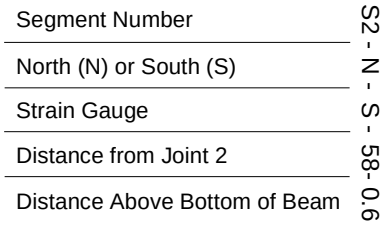

Figure 51 – Typical labeling convention for strain gauges

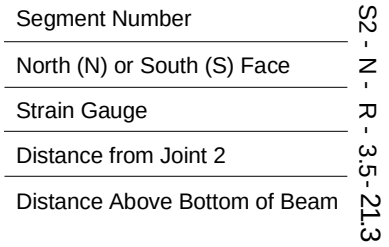

Figure 52 – Typical labeling convention for strain rings

7.3 LINEAR VARIABLE DISPLACEMENT TRANSDUCERS (LVDT)

DCTH Series LVDTs, produced by RDP Electrosense, were used in measuring deflections and opening of the joint at the midspan of the beam. The LVDTs had a stroke of 1 in. Four LVDTs were used to measure the vertical deflection at the cantilevered end of the beam (see Figure 53), relative sliding (if any) between Segments 2 and 3, deflections close to the mid-support, and deflections close to the end-support. To detect and track the depth of joint-opening at the midspan of the beam, six LVDTs were mounted on the South side and three were mounted on the top flange across the joint (see Figure 54). The labeling convention used for LVDTs is shown in Figure 55.

Figure 53 – LVDT for measuring deflection at cantilevered-end of beam

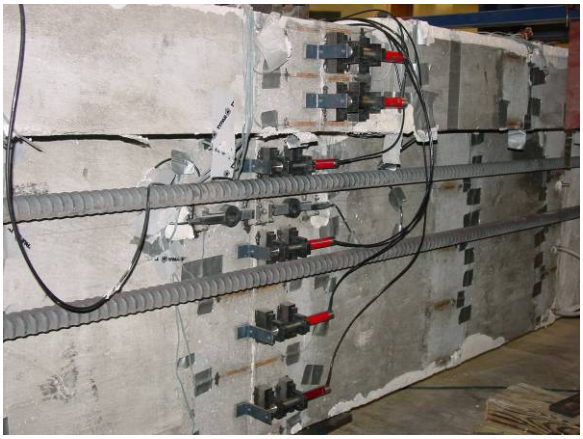

(a) South side

(b) Top flange

Figure 54 – LVDTs mounted across joint at midspan on (a) South side and (b) top flange

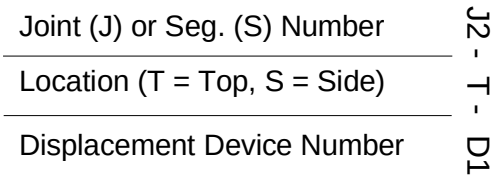

Figure 55 – LVDT labeling convention

7.4 LOAD CELLS

Load cells used to measure the magnitudes of applied loads and reactions were Model 3000 load cells, manufactured by Geokon, Inc. The layout of load cells on the post-tensioned beam is illustrated in Figure 56. The force in the hydraulic jack, which was used to load the beam at the cantilevered end, was measured using a 200-kip load cell (Figure 57 (a)). 200-kip load cells were mounted on each of the four DYWIDAG post-tensioning bars (Figure 57 (b)). These load cells were used to monitor prestress levels in the beam. 150-kip and 75-kip load cells were installed at the mid-support (Figure 57 (c)) and end-support (Figure 57 (d)) of the beam, respectively, for measuring reactions under the effect of applied loads.

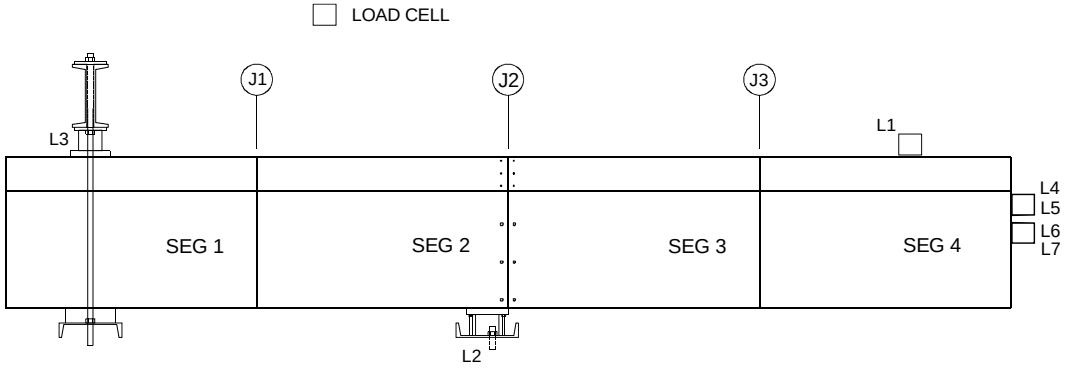

Figure 56 – Load cell layout

(a) (b)

(c) (d)

Figure 57 – Load cells for measuring; (a) applied load, (b) prestress, (c) mid-support reaction, (d) end-support reaction

7.5 DATA ACQUISITION

The instrumentation layout for the prestressed beam is shown in Figure 58 and Figure 59. Data from the variety of instruments shown in the figures were collected using the National

Instruments model SCXI-1000DC Data Acquisition (DAQ) System (see Figure 60). Data were collected from a total of 192 thermocouples (32 per section), 15 LVDTs, and 7 load cells. Forty-one data acquisition channels were reserved for collecting data from strain gauges, which were connected to the DAQ system based on the cross section of interest in the test being conducted. During the application of thermal loads, the DAQ system was set to acquire 3600 samples of data from each instrument in five minutes, which were then averaged and recorded at the end of each 5 minute interval. During the application of mechanical loads, the system was set to acquire 100 samples of data from each instrument, which were averaged and recorded every second. Compared with mechanical loading a lower data acquisition rate was used during thermal loading because of the longer time needed to heat or cool the concrete.

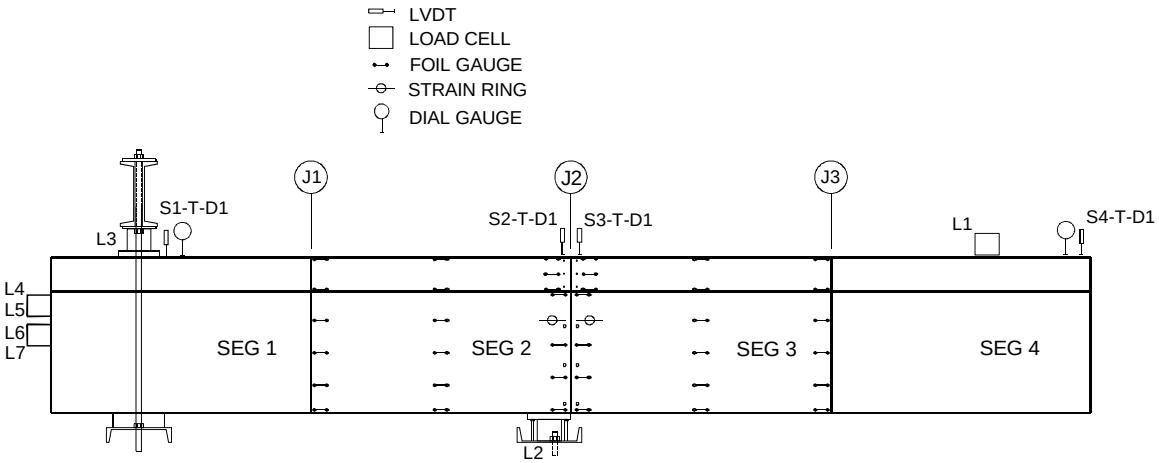

Figure 58 – Instrumentation layout (North)

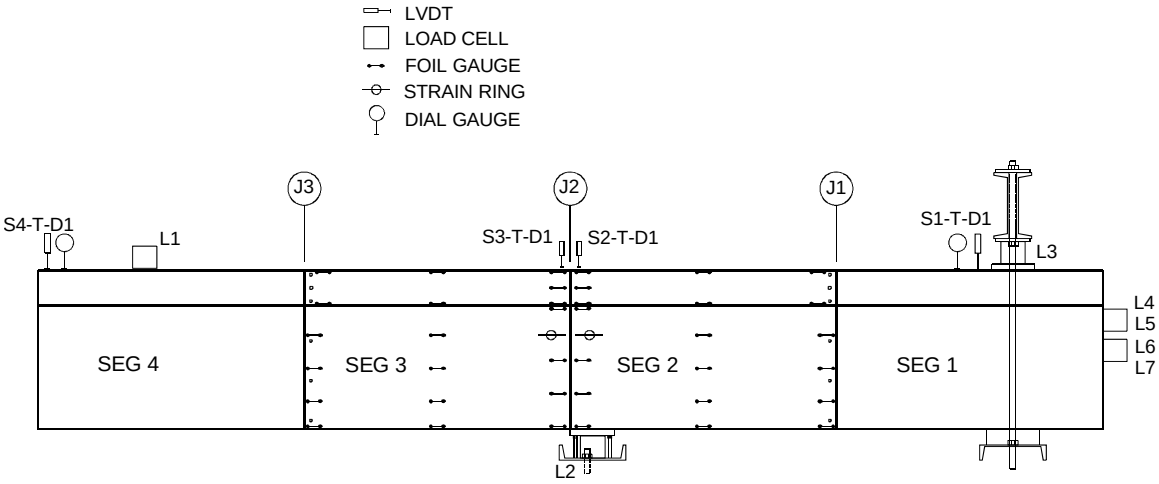

Figure 59 – Instrumentation layout (South)

(a) (b)

Figure 60 – (a) DAQ System; (b) Connection of instrumentation to DAQ System

8 SETUP AND PROCEDURES FOR MECHANICAL LOADING

The setup for conducting laboratory experiments is illustrated in Figure 61. A picture of the post-tensioned beam in the laboratory is shown in Figure 62. The beam was supported 1.7 ft from the end of Segment 1 (end-support) and 10.5 ft from the cantilevered-end of the beam (mid-support). It was mechanically loaded 2.7 ft from the cantilevered-end. Fabrication details of the support systems and loading frame can be found in Appendix B.

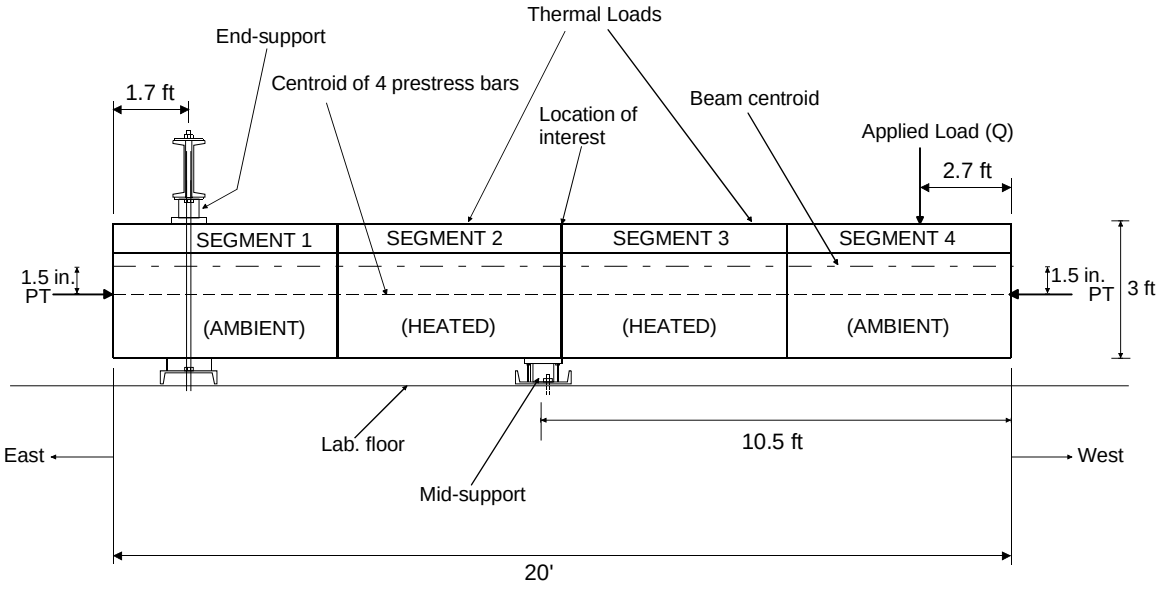

Figure 61 – Test setup

The end-support consisted of back-to-back channels supported by four all-thread bars bolted to the laboratory strong floor. A 75-kip load cell was placed between the back-to-back channels and a 3/8-in. thick, 12 in. by 12 in. steel plate. Between the steel plate and the surface of the beam a 5/8-in. thick, 12 in. by 12 in. neoprene pad was used to distribute the reaction to the concrete. The mid-support consisted of a 1.5 in.-thick, 10 in. by 10 in. steel plate supported by four all-thread rods. The rods were 0.5 in. shorter than the 150-kip load cell at mid-support, which was placed between the steel plate and a C15 x 33.9 channel bolted to the laboratory strong floor. The 0.5 in. clearance between the load cell and the steel rods allowed the load cell to fully carry loads due to the self-weight of the beam and the actuator without any contribution from the steel rods. A 5/8-in. thick, 12 in. by 12 in. neoprene pad was placed between the steel plate and the bottom web of the beam to distribute the mid-support reaction to the concrete. The loading frame, which was designed to carry loads up to 400 kips, consisted of two steel columns and two deep channel beams. For convenience, a temporary I-section was bolted to the load frame columns below the deep channel beams, to support a 60 ton manually pressurized jack, which was used to apply mechanical loads to the beam (see Figure 63). A 200-kip load cell was placed directly under the jack to measure applied loads. A 3/8-in. thick, 12 in. by 12 in. steel plate and 5/8-in. thick, 12 in. by 12 in. neoprene pad were used to distribute the applied load to the concrete.

Figure 62 – Segmental beam in laboratory

(a) (b)

Figure 63 – (a) Loading frame; (b) 60-ton jack

8.1 Opening of Joint Between Segments 2 and 3

The primary aim of applying mechanical loads to the beam was to open the joint between segments 2 and 3 (joint J2), creating zero stress conditions from which the effects of thermal loads could be quantified. This is illustrated in Figure 64 through Figure 66.

Stresses at joint J2 created by prestress and the self-weight of the beam were taken as the baseline or reference stresses. Stresses due to the AASHTO nonlinear thermal gradients, which were expected to be equal across the width of joint J2, were quantified relative to the baseline stresses at joint J2. Quantifying average stresses caused by the AASHTO nonlinear thermal gradients in the extreme top fibers of the beam at joint J2 required the determination of the load corresponding to the average reference stress, Q_{NT}, (see Figure 64). In addition, loads corresponding to average stresses in the extreme top fibers created by the superposition of the AASHTO nonlinear positive thermal gradient on the reference stresses , Q_{PG}, (see Figure 65) and the AASHTO nonlinear negative thermal gradient on the reference stresses, Q_{NG}, (see Figure 66) had to be determined. Average stresses due to the thermal gradients were quantified from the difference in loads initiating joint opening ($Q_{PG} - Q_{NT}$ for the positive gradient and $Q_{NG} - Q_{NT}$ for the negative gradient) through back calculation. Though the concept of quantifying thermal stresses by opening the joint between segments 2 and 3 is illustrated for the extreme top fibers in

Figure 64 through Figure 66, it is applicable at any depth at joint J2 where loads which cause the section fibers to loose contact at that depth can be determined.

It was determined from sectional analysis using conventional beam theory that a maximum load of about 40 kips was required to relieve the average longitudinal stress in the extreme top fibers of the beam at the joint (i.e. open the joint) created by the superposition of stresses due to the self-weight of the beam, prestress, and the AASHTO nonlinear positive or negative thermal gradient. To allow for the possibility that the experimental setup might deviate somewhat from beam theory, loads of up to 60 kips were applied during tests. The configuration of load and support points ensured that the maximum moment due to applied loads occurred in the vicinity of the joint at midspan (joint J2). This eliminated the development of high tensile stresses within the beam segments since tensile stresses could not be transmitted across the joint.

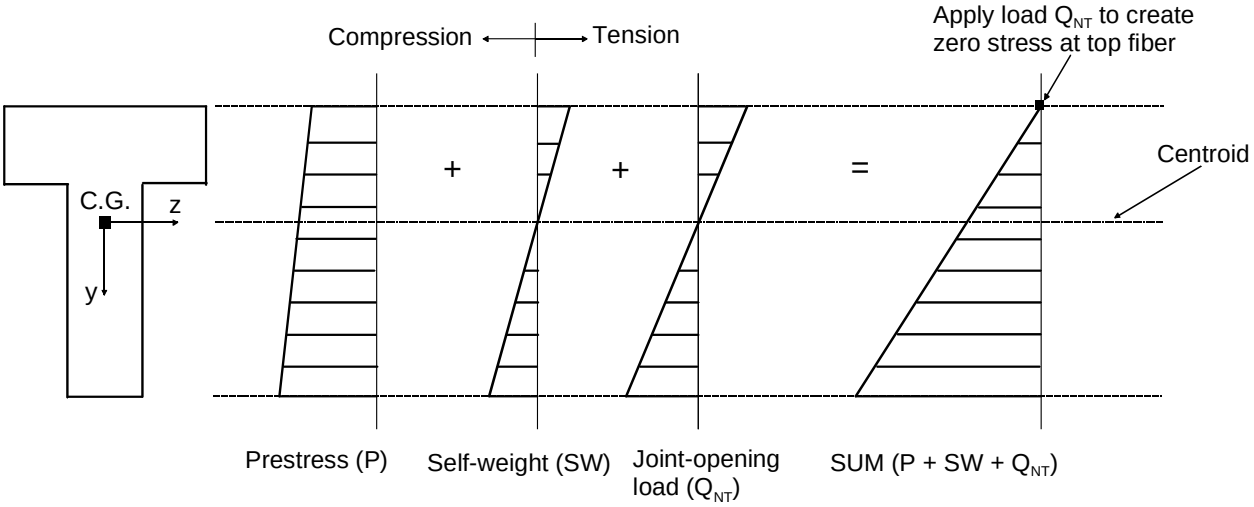

Figure 64 – Ideal stress diagrams without thermal loads

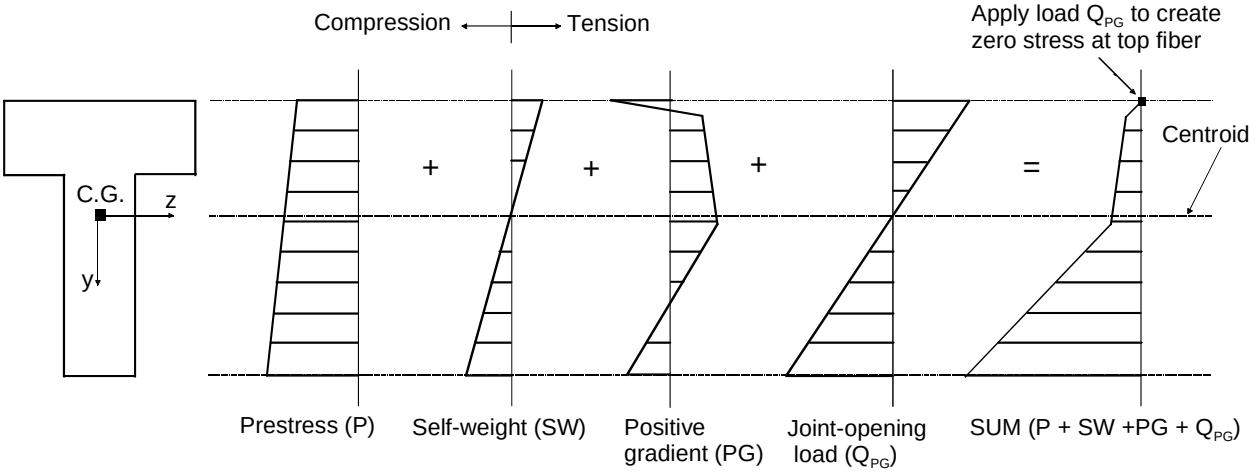

Figure 65 – Ideal stress diagrams with positive thermal gradient

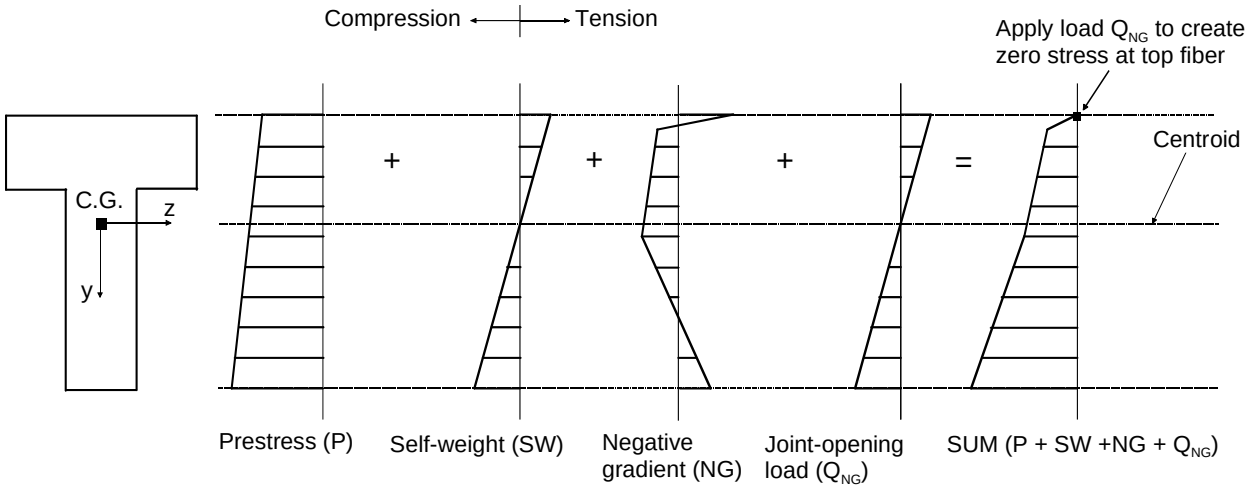

Figure 66 – Ideal stress diagrams with negative thermal gradient

9 SETUP AND PROCEDURES FOR THERMAL LOADING

Thermal profiles were imposed on the heated segments of the beam by passing heated water at laboratory controlled temperatures through strategically placed copper tubes embedded in the concrete. Four thermal profiles were imposed on the heated segments: uniform temperature distribution, linear thermal gradient, AASHTO nonlinear positive thermal gradient, and AASHTO nonlinear negative thermal gradient.

This chapter describes the methods and piping arrangements used to impose each thermal profile. Throughout this chapter, thermocouple locations, pipe layers, and heaters are referenced. Three water heaters were used to heat the water pumped through the beam. Heaters 1 and 2 (H1 and H2) were capable of supplying water at temperatures as high as 135 ^{o}F. These heaters were used to provide high temperatures typically ranging from 105 ^{o}F to 135 ^{o}F. Heater 3 (H3) was capable of supplying water at temperatures as high as 125 ^{o}F, and was utilized for temperatures ranging from 86 ^{o}F to 100 ^{o}F. Pipe layer designations, thermocouple section locations, and the layout of thermocouples at each section are shown in Figure 67 through Figure 69, respectively. The "x" markings in Figure 69 represent thermocouples that were not connected to the DAQ system because they were not needed to capture pertinent data. To minimize heat loss from the beam, 0.5-in. thick Styrofoam boards were used to insulate the surfaces of the beam (see Figure 70).

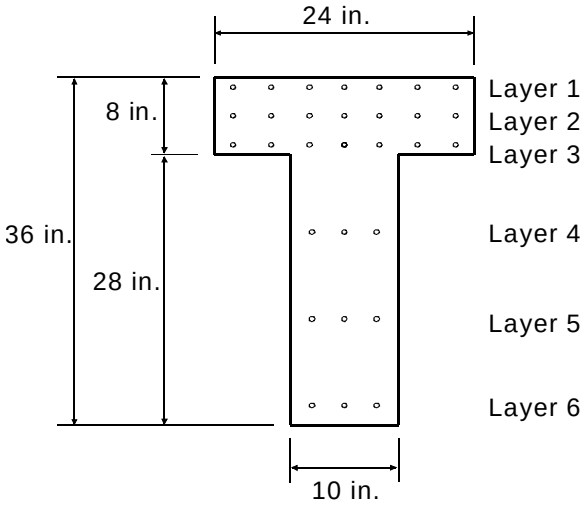

Figure 67 – Pipe layers

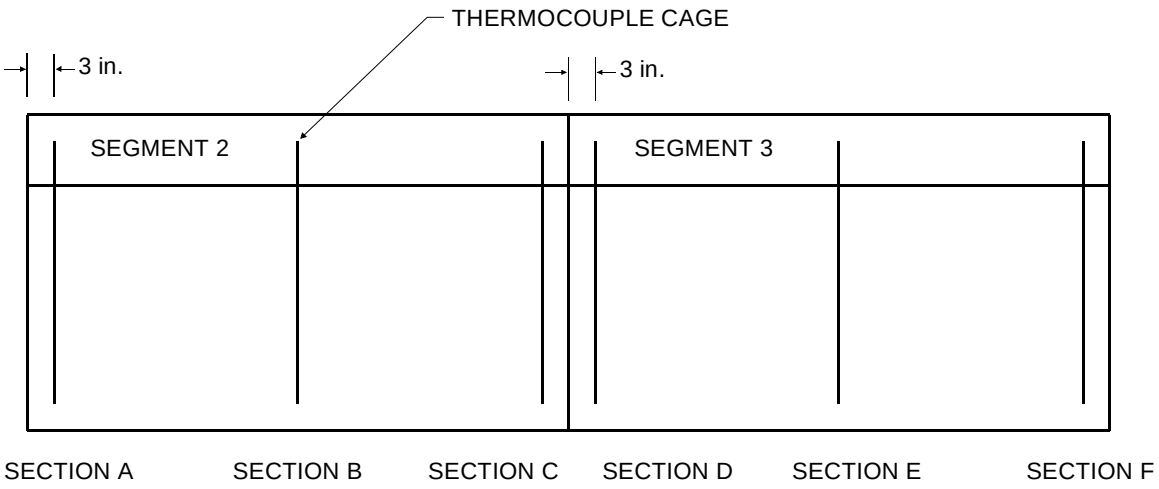

Figure 68 – Thermocouple locations in heated segments

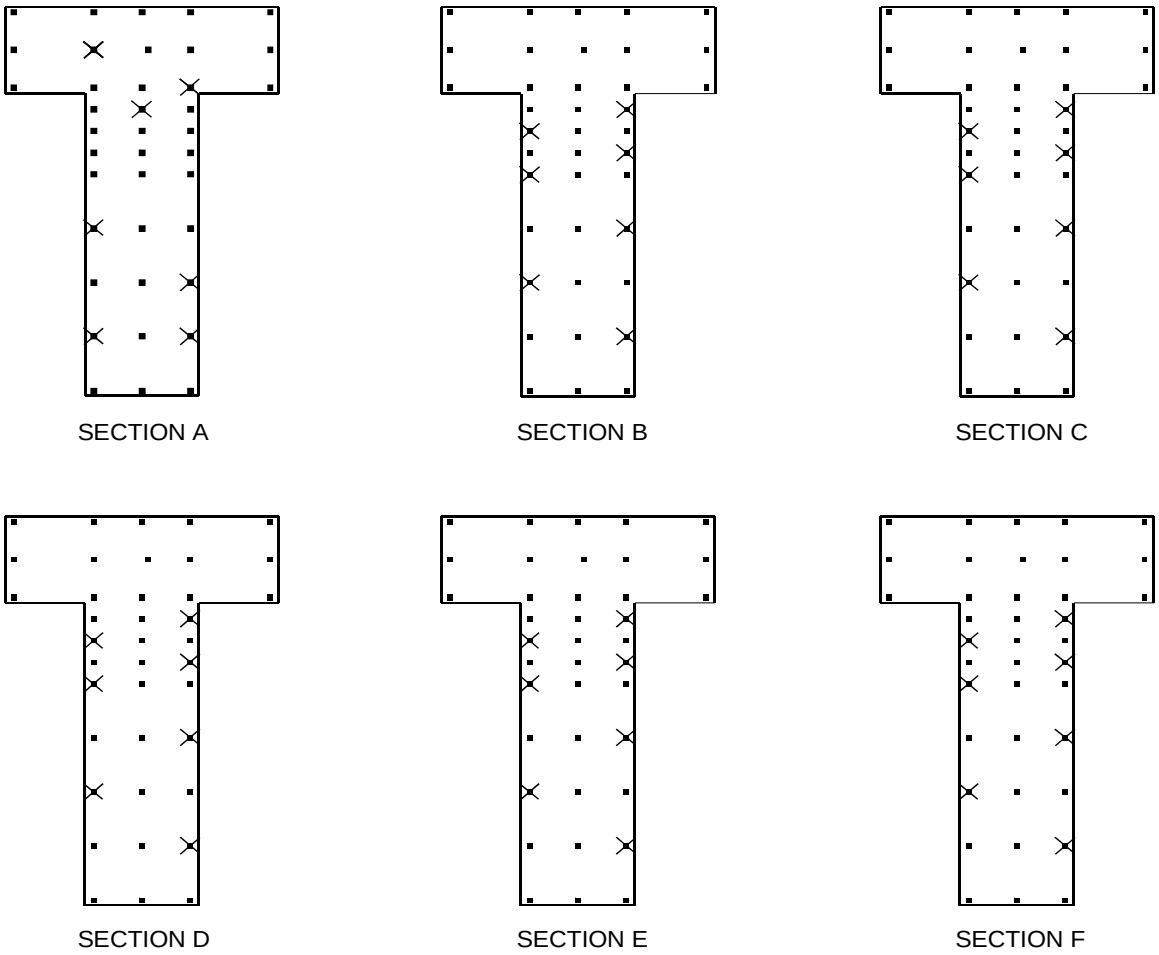

Figure 69 – Thermocouples used at each section (X indicates thermocouples that were not active during testing)

Figure 70 – Insulated heated segments

9.1 UNIFORM TEMPERATURE DISTRIBUTION

Before the beam was prestressed, initial thermal testing was conducted that involved heating the segments uniformly to determine the in-situ CTE. The uniform heating was also one part of the AASHTO negative thermal gradient.

Changing laboratory temperatures (i.e. from early morning through noon till evening) and the fact that the heated segments were insulated prevented the segments from being at a uniform temperature prior to the start of imposing prescribed thermal profiles. This was because the large mass and low thermal conductivity of the concrete segments prevented them from rapidly adjusting to changing laboratory temperatures. In particular, the bottom webs of the segments were generally cooler than the top flanges of the segments. Tap water, which ranged in temperature from 74 ^{o}F to 85 ^{o}F, depending on the month in which tests were conducted, was used to bring the entire segment to a uniform reference temperature by circulating the water through the segments overnight using the plumbing configuration shown in Figure 71. After the desired thermal condition had been imposed, this same approach was then used to cool the segments back to the reference temperature.

The piping configuration shown in Figure 72 was used to uniformly heat the segments. This created a temperature differential that was uniform over the height of the segment. With Heaters 1 and 2 set to the target temperature, water was continuously circulated through the segments. Heater 3 was not used in this setup primarily because of limitations on the heat energy that it could deliver at the high flow rates which were required to uniformly heat the segments longitudinally. Temperatures in the concrete were monitored from thermocouple readings. Thermal profiles at each section were also periodically plotted using an average of readings taken from each row of thermocouples throughout the depth of the beam. Heater settings were then updated to offset deviations from the target temperature. When the desired profile was achieved at each section, temperatures were held in steady state for about 30 to 45 minutes as readings were taken periodically. The segments were then cooled to the reference temperature. The average time it took to impose a uniform profile on a single heated segment was about 10 hours. In the case of two segments, the system was kept running for between 20 to 30 hours.

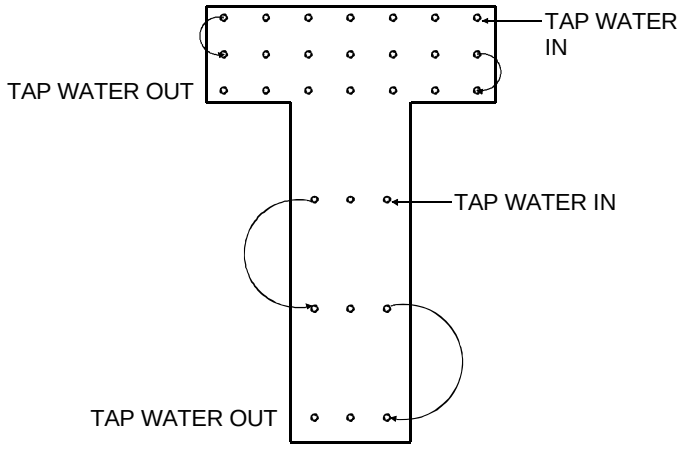

Figure 71 – Piping configuration used to impose initial condition

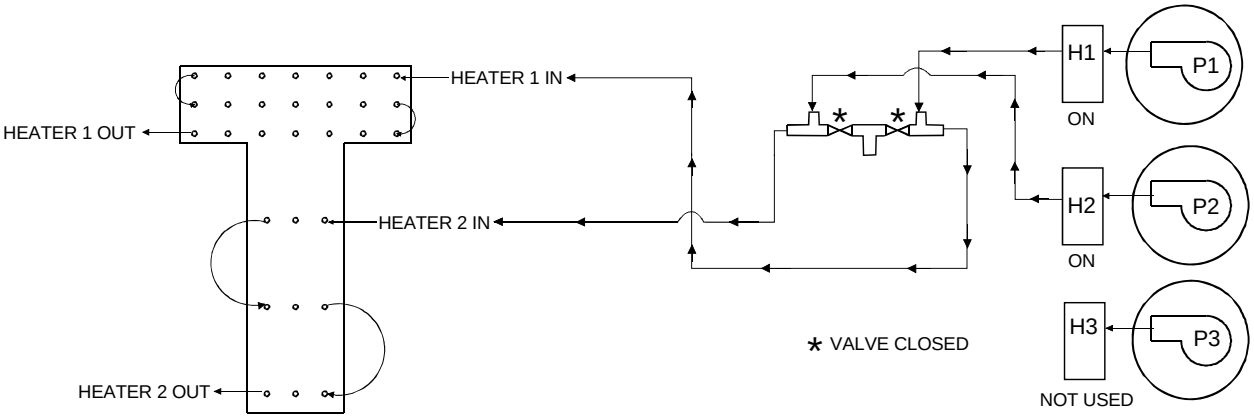

Figure 72 – Piping configuration used to impose uniform temperature differential

9.2 LINEAR THERMAL GRADIENT

A second set of thermal tests were conducted that involved imposing a linear thermal gradient from 0 ^{o}F at the bottom of the web to +41 ^{o}F at the top of the flange. This gradient, which leads to no stress development in a simply supported structure, was also used in determining the in-situ coefficients of thermal expansion of the heated segments.

The piping configuration shown in Figure 73 was used to impose the linear thermal gradient after circulating tap water through the segment to establish a uniform reference temperature. Heaters 1, 2, and 3 were set to temperatures 41 ^{o}F, 23 ^{o}F, and 12 ^{o}F above the reference temperature, respectively. Water from Heaters 1 and 2 was mixed and circulated through pipe layer 3. The temperature of mixed water was about 32 ^{o}F above the reference temperature. There was no flow in pipe layers 2 and 6. Thermocouple readings and thermal profiles at each section were monitored and changes to the heater settings made when necessary. When the target thermal gradient was achieved, temperatures were held in steady state for about 30 to 45 minutes as readings were taken periodically. The segment was then cooled back to the reference temperature. The average time it took to impose the linear profiles on a single heated segment was about 9 hours.

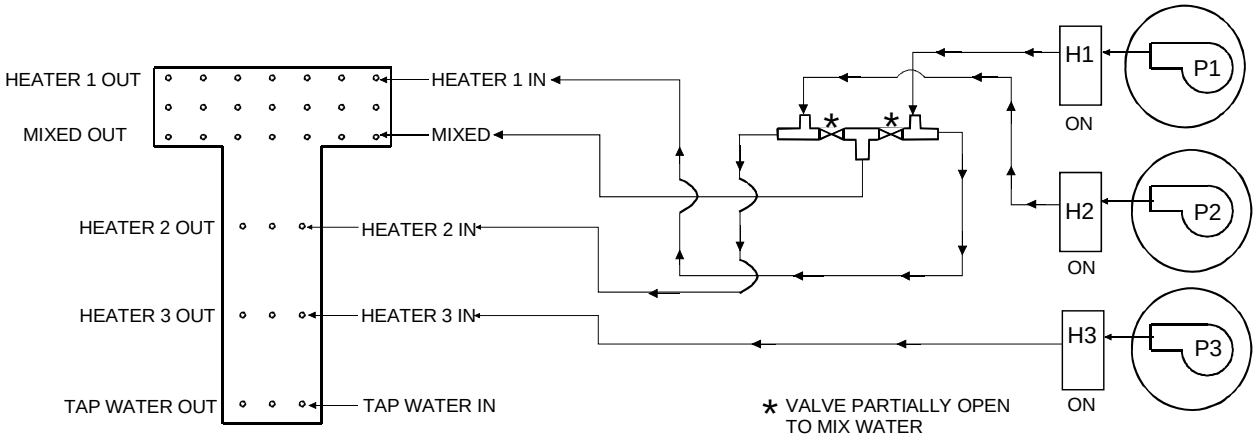

Figure 73 – Piping configuration used to impose linear thermal gradient

9.3 AASHTO POSITIVE THERMAL GRADIENT

The piping configuration shown in Figure 74 was used to impose the AASHTO nonlinear positive thermal gradient on the heated segments of the beam. Before circulating heated water through the segments, tap water was circulated overnight to establish the reference temperature. Heaters 1 and 3 were set to 41 ^{o}F and 11 ^{o}F above the reference temperature, respectively. Although tap water was pumped from a reservoir through Heater 2, the heater was turned off for the duration of the test. The water pumped through Heater 2 was mixed with water from Heater 1 and circulated through layer 3, which was required to be at a temperature about 7 ^{o}F above the reference temperature. The temperature of mixed water was regulated by controlling contributions to the mix from Heater 1 (turned on) and Heater 2 (turned off). The bottom 20-in. portion of the beam was maintained at the reference temperature by circulating tap water through layers 4, 5, and 6. This produced the 0 ^{o}F temperature change in the gradient (relative to the reference temperature). Thermocouple readings and the shape of the gradient at each section were monitored and changes to heater settings were made when necessary. When the AASHTO positive thermal gradient profile was achieved, temperatures were kept at steady state for about 30 to 45 minutes as readings were taken periodically. The beam was then cooled to the reference temperature. The average time it took to impose the AASHTO positive thermal gradient on the heated segments was about 7 hours.

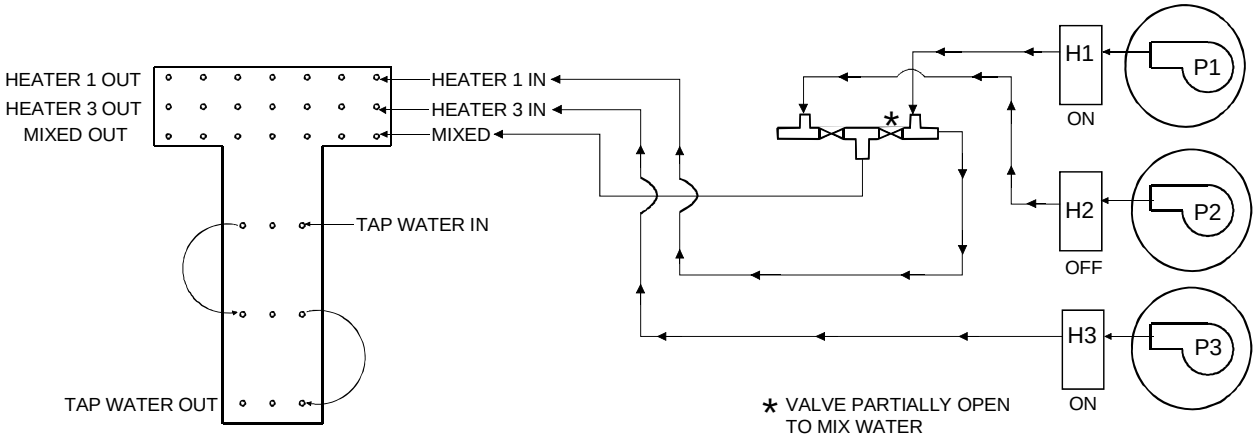

Figure 74 – Piping configuration used to impose AASHTO nonlinear positive thermal gradient

9.4 AASHTO NEGATIVE THERMAL GRADIENT

The AASHTO nonlinear negative thermal gradient was imposed on the heated segments using the setup shown in Figure 75. To impose this gradient, the segments had to be cooled from the reference temperature rather than heated. Since the setup for thermal control could only be used to heat the segments, two reference temperatures were involved in imposing the negative gradient. The first reference temperature (referred to as the low reference temperature) was imposed by circulating tap water through the segments using the piping configuration previously shown in Figure 71. The low reference temperature was imposed to maintain consistency with procedure for imposing the thermal profiles discussed previously. After establishing the low reference temperature, a uniform temperature increase of about 40 ^{o}F was imposed on the segments using the plumbing in Figure 72. The temperature of the segments after the 40 ^{o}F increase was referred to as the high reference temperature. Heater settings and layer temperatures required to impose the gradient were based on the high reference temperature. Heater 1 was set to a temperature 12.3 ^{o}F below the high reference temperature. This corresponded to the -12.3 ^{o}F temperature change in the AASHTO nonlinear thermal gradient. The bottom 20-in. portion of the beam was maintained at the high reference temperature by circulating water at that temperature through layers 4, 5, and 6, using Heater 2. This corresponded with the 0 ^{o}F temperature change in the gradient. Heater 3 was connected to layer 2 and was only used when needed to bring the temperature of layer 2 to 3.3 ^{o}F below the high reference temperature. Water from heaters 1 and 2 was mixed and circulated through layer 3. Thermocouple readings and the shape of the gradient were monitored throughout the test, and changes to heater settings were made as necessary. When the target gradient was achieved, temperatures were kept in steady state for about 30 to 45 minutes as readings were periodically taken. The beam was then cooled to the low reference temperature. The average time required to impose the AASHTO negative thermal gradient after imposing the high reference temperature was about 7 hours.

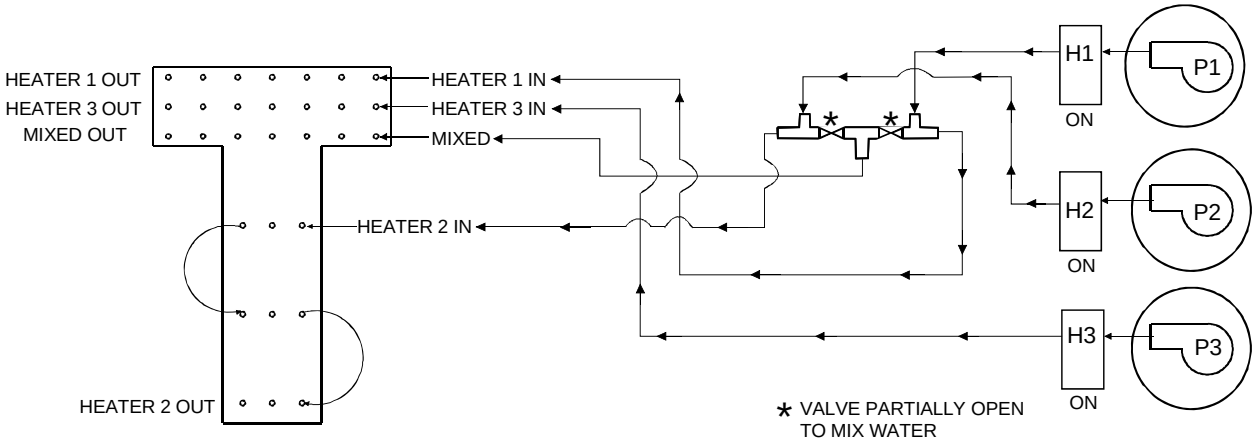

Figure 75 – Piping configuration used to impose AASHTO nonlinear negative thermal gradient

10 IN-SITU COEFFICIENT OF THERMAL EXPANSION

In-situ CTE tests were conducted to determine coefficients of thermal expansion that were representative of the composite behavior of the concrete segments, copper tubes, and thermocouple cages embedded in segments 2 and 3 of the laboratory test beam. The setup for the in-situ CTE tests is shown in Figure 76. The segment being tested was supported on two wooden blocks 6 in. away from the ends. LVDTs were placed vertically along the centerline of the cross section on both ends of the segment to record the elongation of the segment. Initially three LVDTs were used to record displacements at locations 0.5 in. below the top of the flange, at the centroid of the segment (21.3 in. from the bottom of the segment), and 0.5 in. above the bottom of the segment. Subsequently, with the acquisition of additional LVDTs, four and then five LVDTs were used in the testing. The three and four LVDT setups were used in tests conducted on Segment 2. The four LVDT setup was used in one test conducted on Segment 3. In the remaining tests conducted on Segment 3, the five LVDT setup was used.

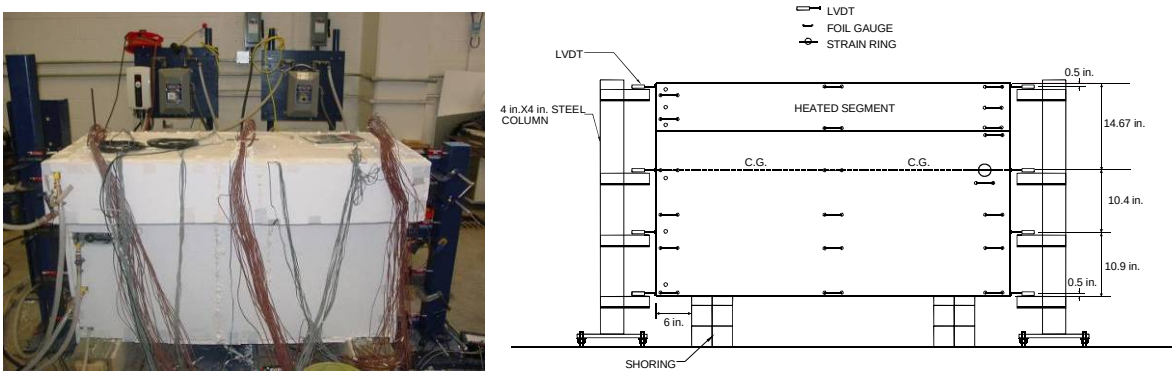

(a) (b)

Figure 76 – In-situ CTE test setup; (a) Photograph, (b) Details

Two non-stress inducing thermal profiles were imposed on the segment: a uniform temperature change of about 41 ^{o}F above the reference temperature of the segment, and a linear thermal gradient varying from 0 ^{o}F at the bottom of the web to +41 ^{o}F at the top of the flange. The uniform and linear thermal profiles were imposed using the piping setups in Figure 72 and Figure 73, respectively. The CTE of the segment was calculated using Equation 16 through Equation 19 below and the measured end displacements caused by the heating.

$$\Delta_{ave} = \frac{\int \delta_{total} \, dA_c}{A_c} \qquad \text{Equation 16}$$

$$\varepsilon_{ave} = \frac{\Delta_{ave}}{L} \qquad \text{Equation 17}$$

$$TG_{ave} = \frac{\int T_{grad}\, dA_c}{A_c}$$ Equation 18

$$\alpha = \frac{\varepsilon_{ave}}{TG_{ave}}$$ Equation 19

where:

Δ_{ave} = average axial elongation of segment
ε_{ave} = average engineering strain
TG_{ave} = average temperature differential
α = coefficient of thermal expansion
δ_{total} = total measured axial elongation at location of LVDT
L = length of segment
T_{grad} = temperature gradient/differential
A_c = cross sectional area of segment

It was expected that both uniform and linear temperature distributions would produce the same CTE values since neither involved nonlinearity of temperature profile, and since it was assumed that the segments had uniform distributions of moisture content.

A laboratory imposed uniform temperature change on Segment 2 and the corresponding measured end displacements are shown together with the target thermal profile and calculated longitudinal displacement in Figure 77 and Figure 78, respectively. A uniform temperature change imposed on Segment 3 and the corresponding measured end displacements are shown together with the target thermal profile and calculated longitudinal displacement in Figure 79 and Figure 80, respectively. Measured concrete temperatures in segments 2 and 3 after uniform profiles were imposed are shown in Figure 81 and Figure 82, respectively. Laboratory imposed thermal profiles were within 2% of the target profiles for both segments. In Figure 78 and Figure 80, calculated displacements were determined using CTEs determined from measured data and target temperature profiles. There was more variability in measured total displacements for Segment 3 (see Figure 80) about the calculated displacement than for Segment 2 (see Figure 78). This was partly because five LVDTs were used at each end of Segment 3 whereas only three LVDTs were used at each end of Segment 2. In addition, the coefficient of variation of the temperature profile imposed on Segment 3 with respect to the target (1.9%) was higher than the coefficient of variation of the temperature profile imposed on Segment 2 (1.4%). The variability in measured displacements was also partially attributed to nonlinearities in the laboratory imposed thermal profiles and varying moisture contents throughout the volume of the segments.

It should be noted that in the AASHTO standard test method for determining the coefficient of thermal expansion of concrete (AASHTO TP 60-00) the influence of moisture content on CTE is eliminated by fully saturating the concrete test cylinders (and thus ensuring a uniform distribution of moisture in the test specimen). Measured end displacements were higher at the ends where heated water entered the segments than at the ends where water exited the

segments. The orientations of Segment 2 and Segment 3 together with the inlet and outlet of heated water are shown in Figure 83 and Figure 84, respectively. In the in-situ CTE tests, measured end displacements were higher on the West end of Segment 2 than on the East end of the segment (see Figure 78). For Segment 3 measured end displacements were higher on the East end than on the West end of the segment (see Figure 80). This was because prior to achieving a constant temperature profile longitudinally, the inlet sections of each segment experienced higher temperatures than the outlet sections, which led to higher measured elongations at the inlet ends than at the outlet ends of the segments.

A laboratory imposed linear temperature profile on Segment 2 and the corresponding measured end displacements are shown together with the target thermal profile and calculated longitudinal displacement in Figure 85 and Figure 86, respectively. A linear temperature change imposed on Segment 3 and the corresponding measured end displacements are shown together with the target thermal profile and calculated longitudinal displacement in Figure 87 and Figure 88, respectively. Measured concrete temperatures in segments 2 and 3 after linear profiles were imposed are shown in Figure 89 and Figure 90, respectively. Laboratory imposed linear temperature gradients were within 2% of the target temperature profile for both segments. The coefficients of variation of the laboratory imposed thermal gradients with respect to the target gradients were 3.7% and 4% for Segment 2 and Segment 3, respectively. This is in agreement with the closer match between calculated and measured total displacements for Segment 2 (see Figure 86) than for Segment 3 (see Figure 88). In calculating the coefficient of variation of laboratory imposed linear gradients, the standard error about the target gradient was used in place of the standard deviation about the mean. This explains the higher coefficients of variation for laboratory imposed linear temperature gradients compared with laboratory imposed uniform temperature changes. In Figure 86, measured displacements at the West end of Segment 2 were lower than measured displacements at the East end in the lower half of the segment, which was expected since the inlet of heated water to the segment was at the East end. In the upper half of the segment, however, measured displacements were higher at the West end than at the East end of the segment. This was because the target temperature at the top of the flange was exceeded in imposing the linear thermal gradient. In an attempt to cool the top flange to the target temperature it was slightly overcooled, leading to lower temperatures and corresponding lower elongations at sections close to the inlet (East end) of water to the segment than at sections close to the outlet (West end) of water from the segment. For Segment 3, measured displacements were higher at the East end than at the West end of the segment. This was consistent with higher temperatures developing at the inlet of heated water to the segment (East end) than at the outlet of heated water from the segment (West end) prior to achieving a constant thermal profile longitudinally.

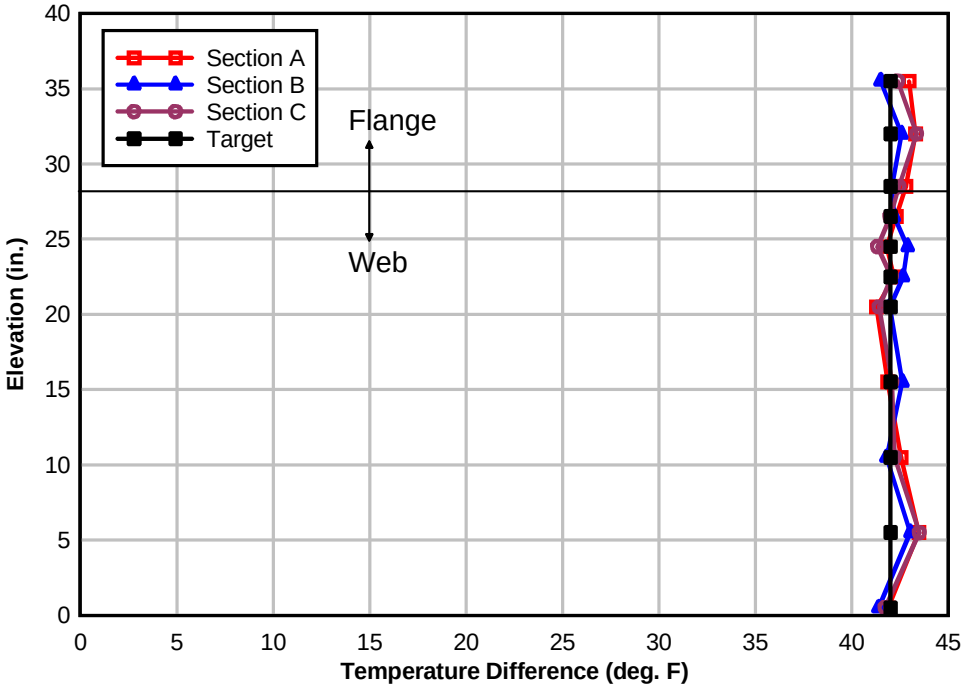

Figure 77 – Uniform temperature change imposed on Segment 2

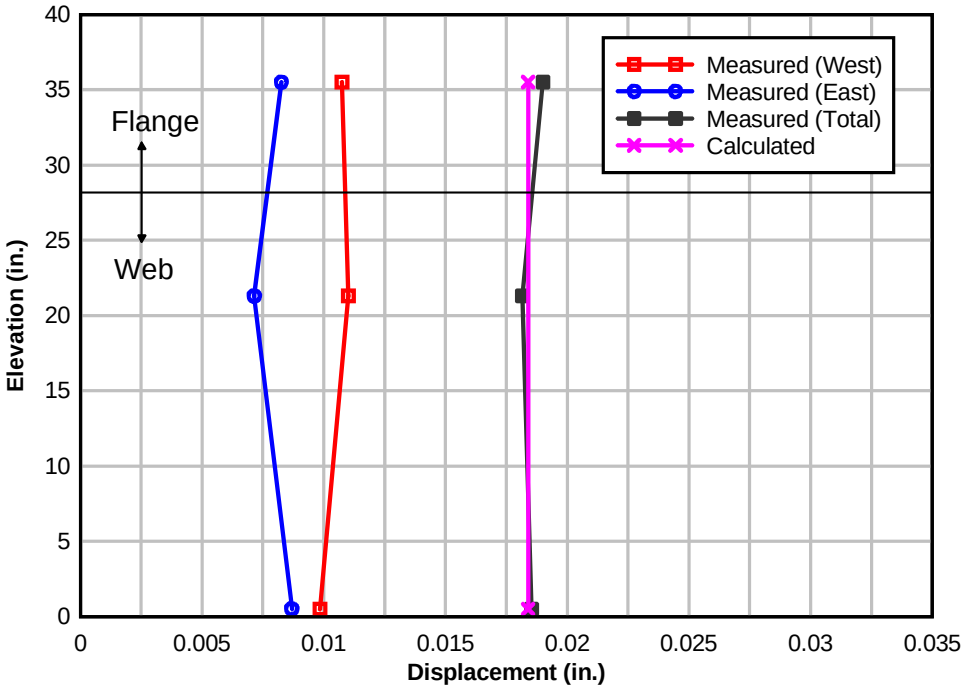

Figure 78 – Measured displacements due to uniform temperature change imposed on Segment 2

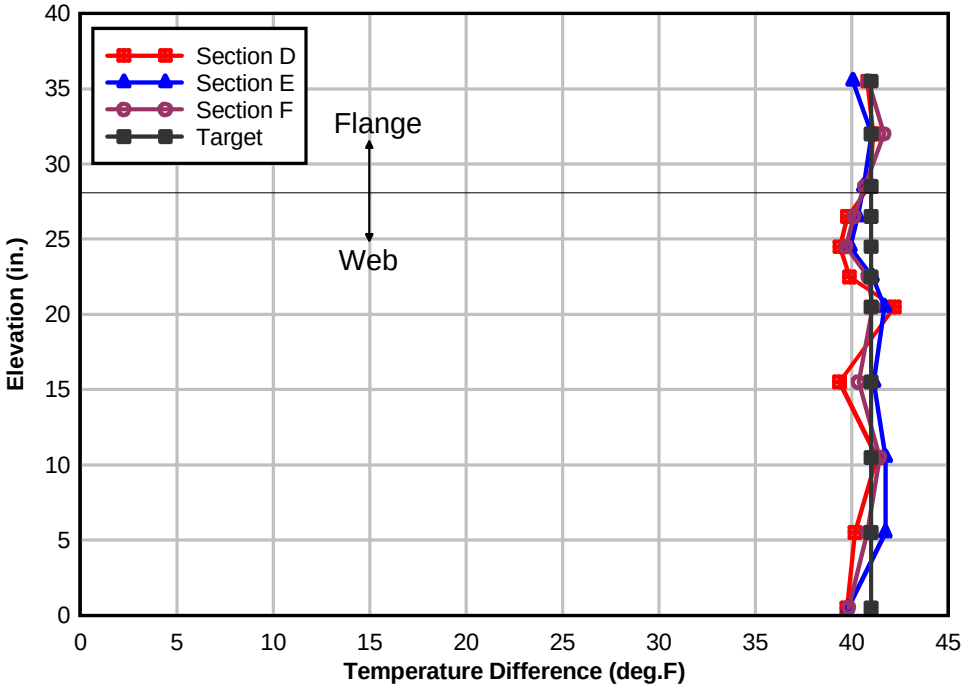

Figure 79 – Uniform temperature change imposed on Segment 3

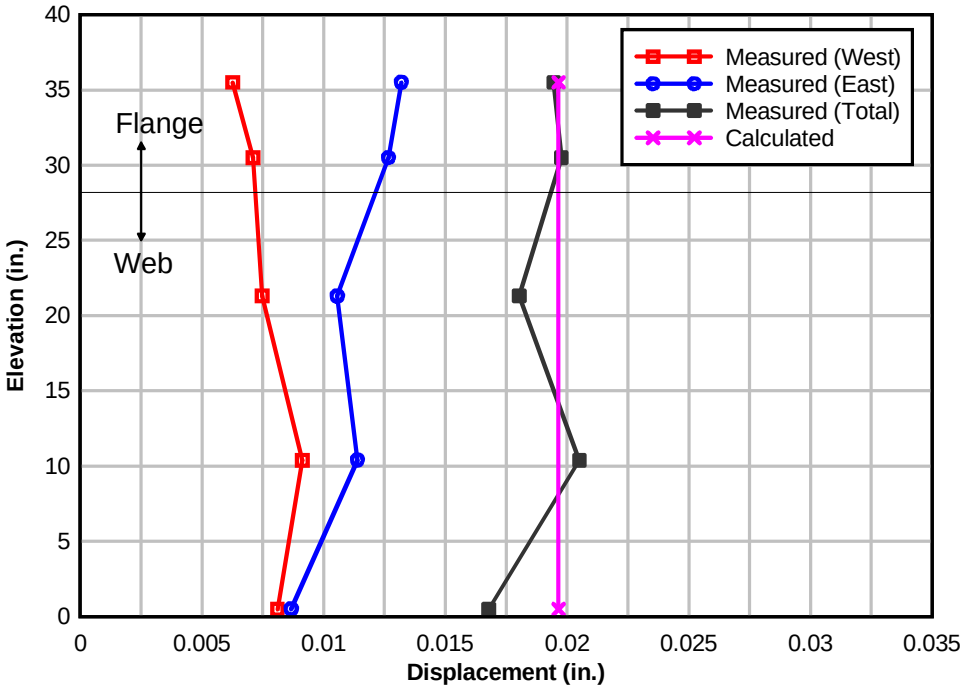

Figure 80 – Measured displacements due to uniform temperature change imposed on Segment 3

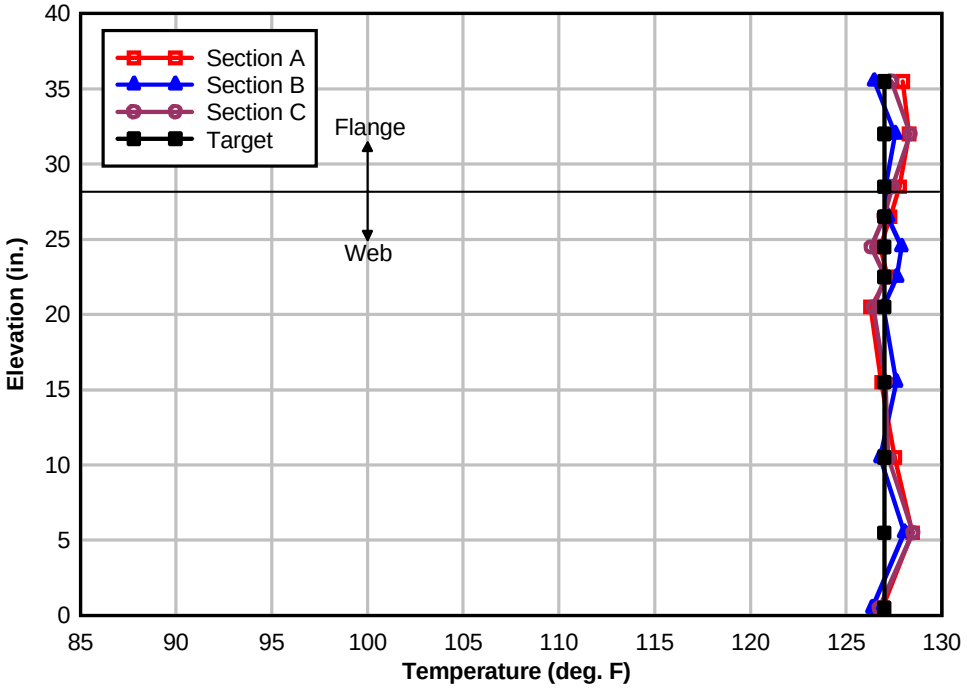

Figure 81 – Measured concrete temperatures in Segment 2 (uniform profile)

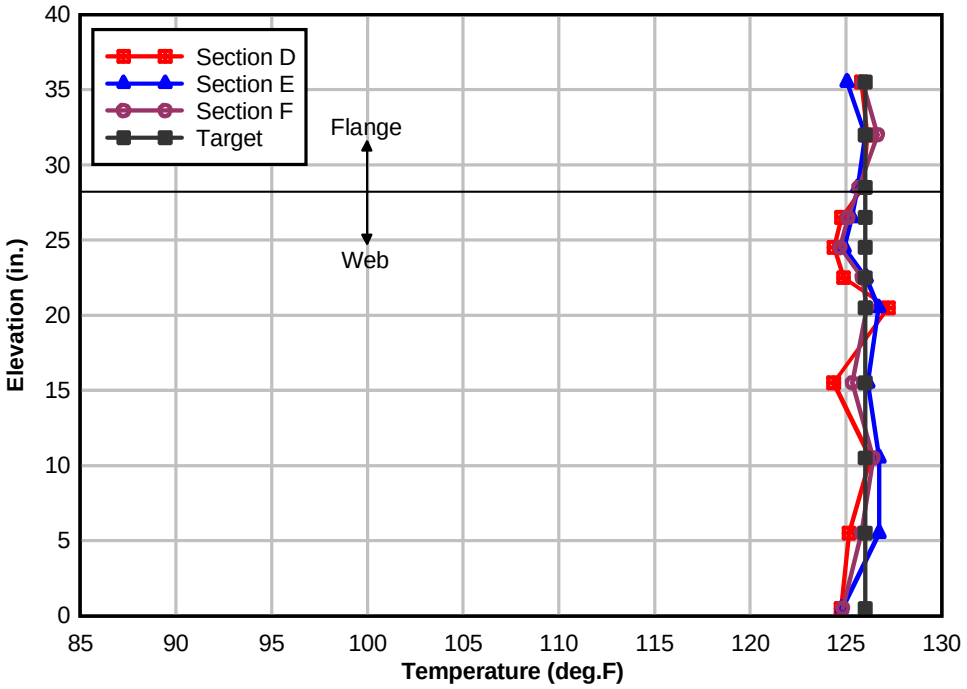

Figure 82 – Measured concrete temperatures in Segment 3 (uniform profile)

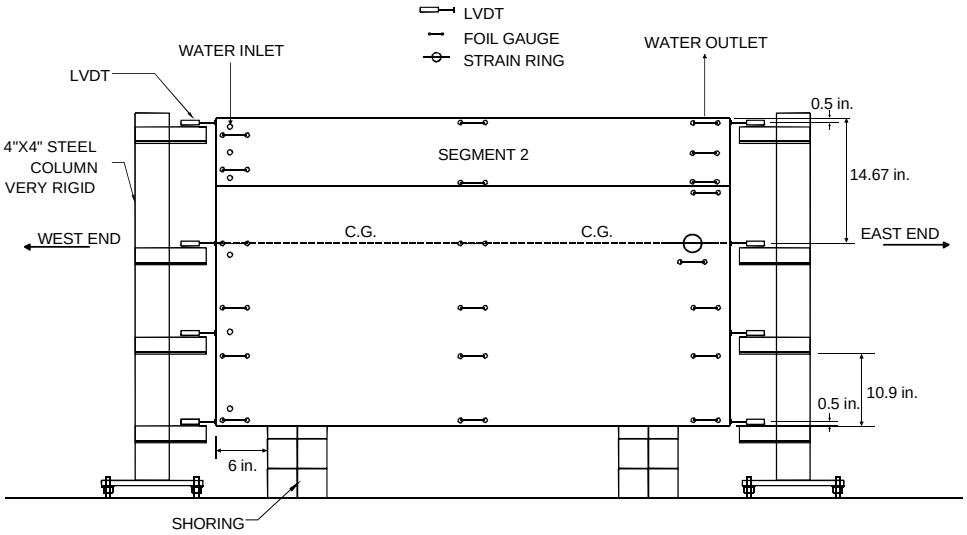

Figure 83 – Orientation of Segment 2 during testing

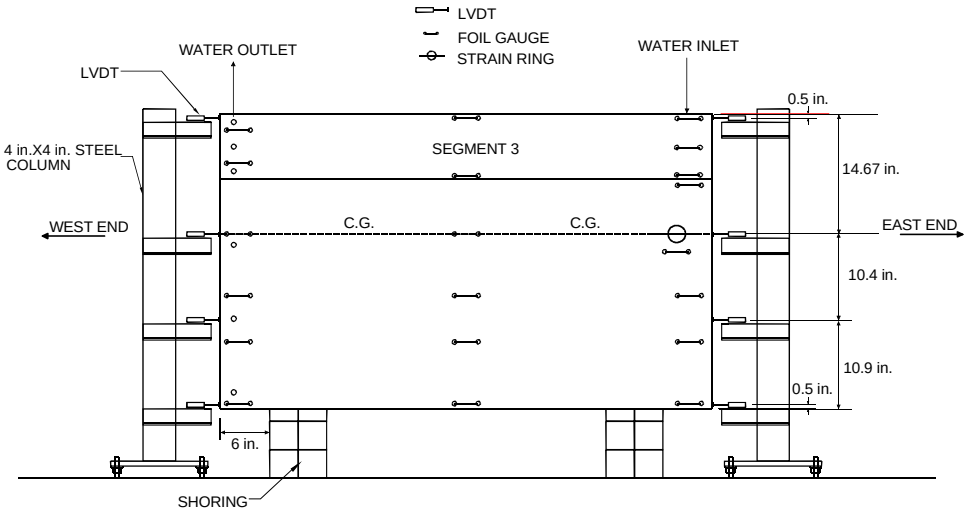

Figure 84 – Orientation of Segment 3 during testing

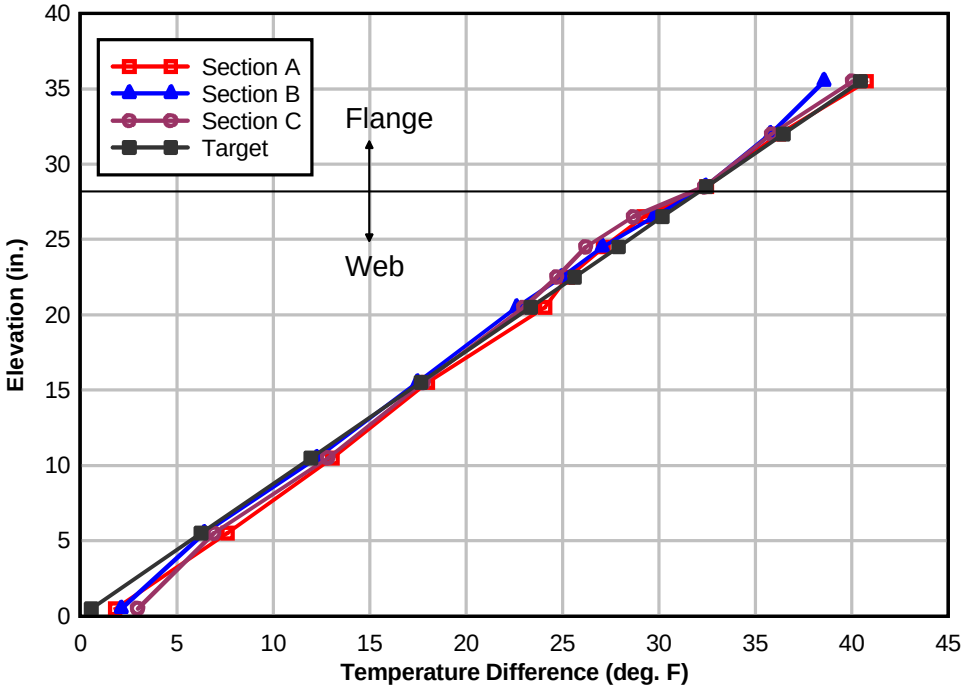

Figure 85 – Linear temperature gradient imposed on Segment 2

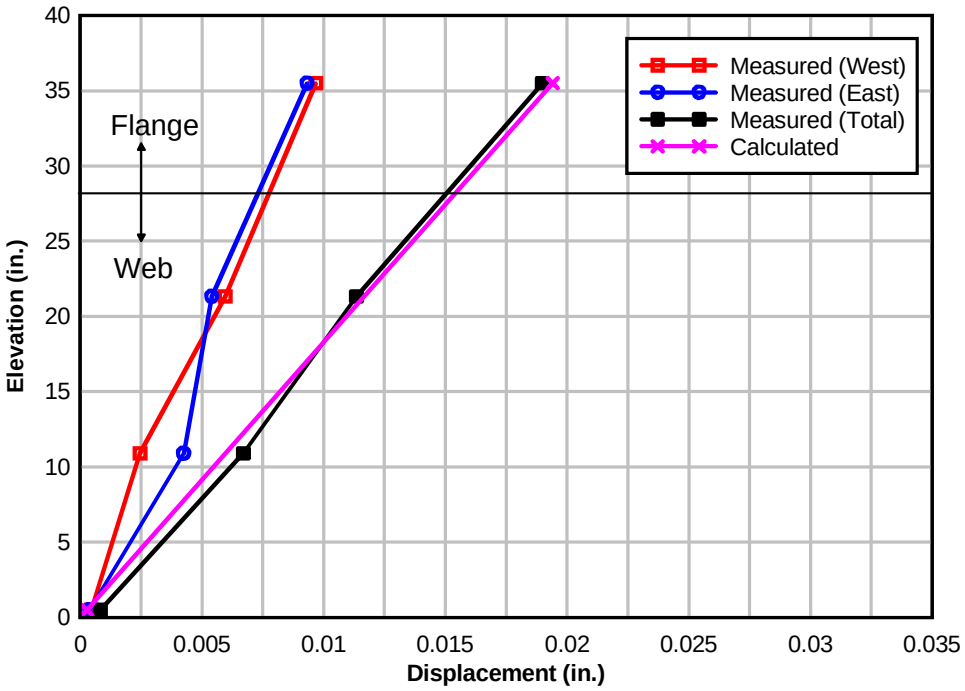

Figure 86 – Measured displacements due to linear thermal gradient imposed on Segment 2

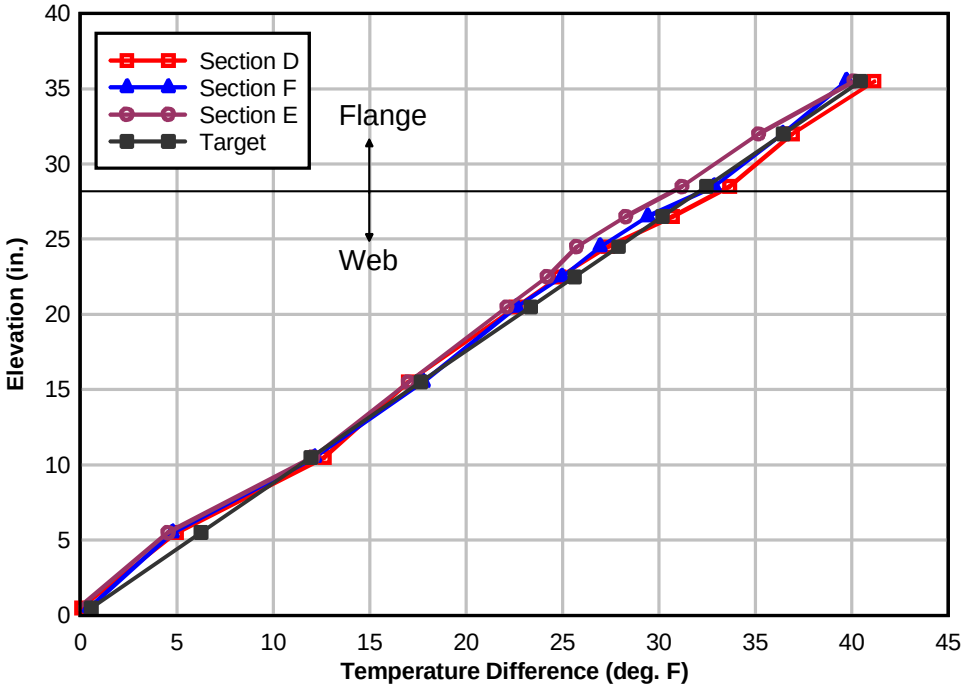

Figure 87 – Linear thermal gradient imposed on Segment 3

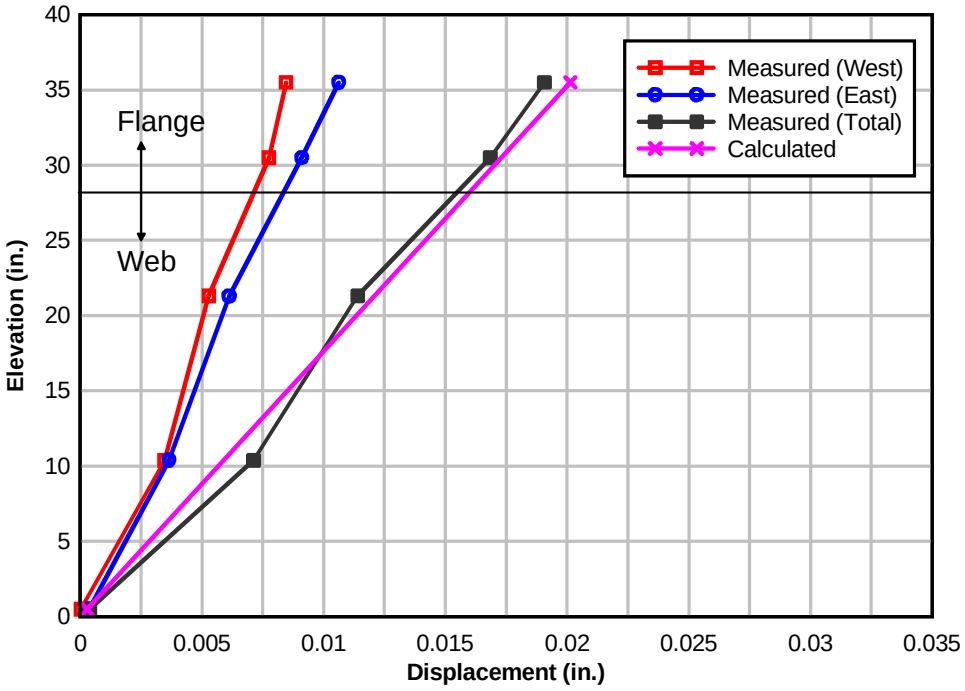

Figure 88 – Measured displacements due to linear thermal gradient on Segment 3

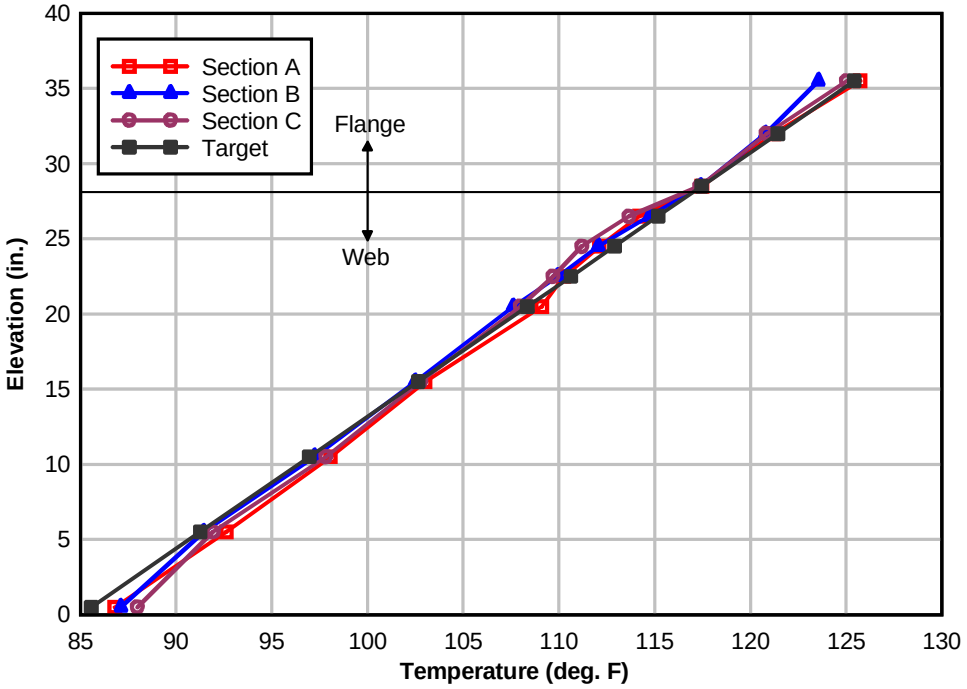

Figure 89 – Measured concrete temperatures in Segment 2 (linear profile)

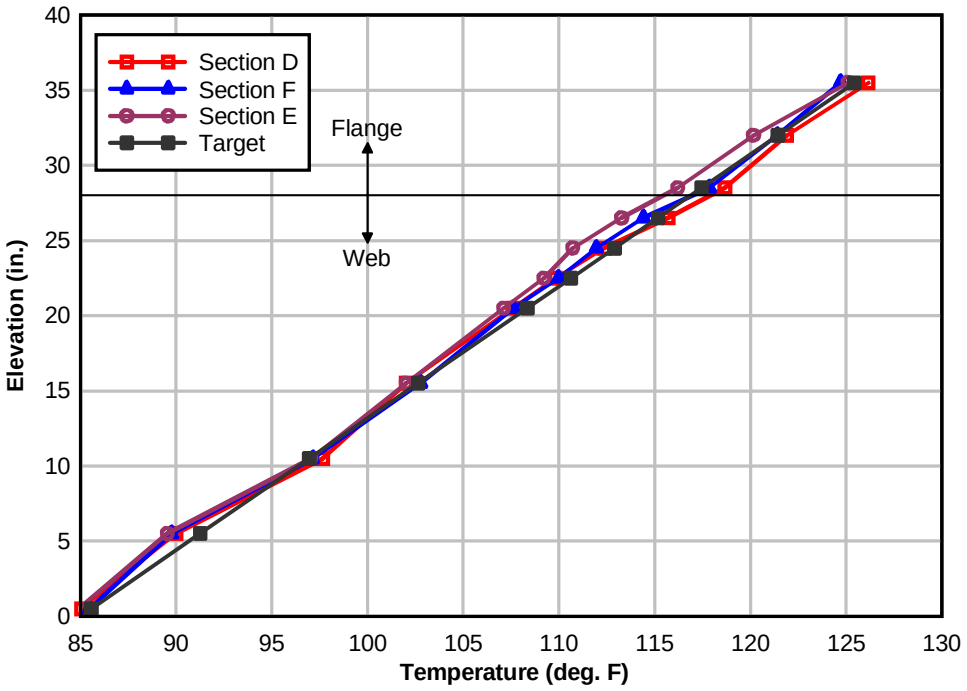

Figure 90 – Measured concrete temperatures in Segment 3 (linear profile)

The coefficients of thermal expansion determined from in-situ tests and the AASHTO TP 60-00 procedure, which was discussed in Section 6.3, are summarized in Table 12. In-situ CTEs determined with linear thermal gradients were generally higher than in-situ CTEs determined with uniform temperature distributions. The slight increase in CTE (an average of

about 8%) associated with linear thermal gradients was attributed to the influence of copper tubes on the longitudinal expansion of the concrete segments and non-uniform moisture contents of the segments. The influence of thermocouple positioning steel cages on the longitudinal expansion of the segments was deemed insignificant since they were placed transversely in the segments.

The CTE for Segment 3, determined using the uniform temperature profile, was equal to the CTE of the segment determined using the AASHTO standard method (AASHTO TP 60-00). It is, however, likely that a repeat of the in-situ test would have yielded a slightly different CTE for the segment. In the AASHTO procedure, the tolerance within which two CTEs determined from the same cycle can be averaged is 0.5E-6/^{o}F. The differences between CTEs determined with the linear profile and CTEs determined with the uniform temperature distribution were 0.7E-6/^{o}F and 0.5E-6/^{o}F for segments 2 and 3, respectively. Since the in-situ CTEs were determined from different tests using different temperature distributions, these differences were deemed acceptable. The arithmetic average of the CTEs of each segment determined using the procedures discussed above was used in predicting thermal stresses and strains later in this study.

Table 12 – Experimentally determined coefficients of thermal expansion

	Uniform Temp. Distribution (In-situ)	**Linear Thermal Gradient (In-situ)**	**AASHTO TP 60-00 Method**
Segment 2	7.3E-6/^{o}F	8.0E-6/^{o}F	N/A
Segment 3	7.8E-6/^{o}F	8.3E-6/^{o}F	7.8E-6/^{o}F

11 RESULTS – PRESTRESSING

In this chapter strains recorded during prestressing of the laboratory segmental beam are presented and discussed. The four segments of the beam were supported on wooden blocks as shown in Figure 91 during prestressing. This support system was changed to that shown in Figure 92 prior to the beginning of mechanical and thermal load tests on the laboratory beam. Labels assigned to the DYWIDAG post-tensioning bars and the design eccentricities of the bars from the centroid of the beam were presented in Section 6.4. They are duplicated in Figure 93 for convenience. Final forces in the prestress bars and measured horizontal eccentricities immediately after release are given in Table 13. The vertical eccentricity of the four-bar group was 1.5 in. below the centroid of the beam.

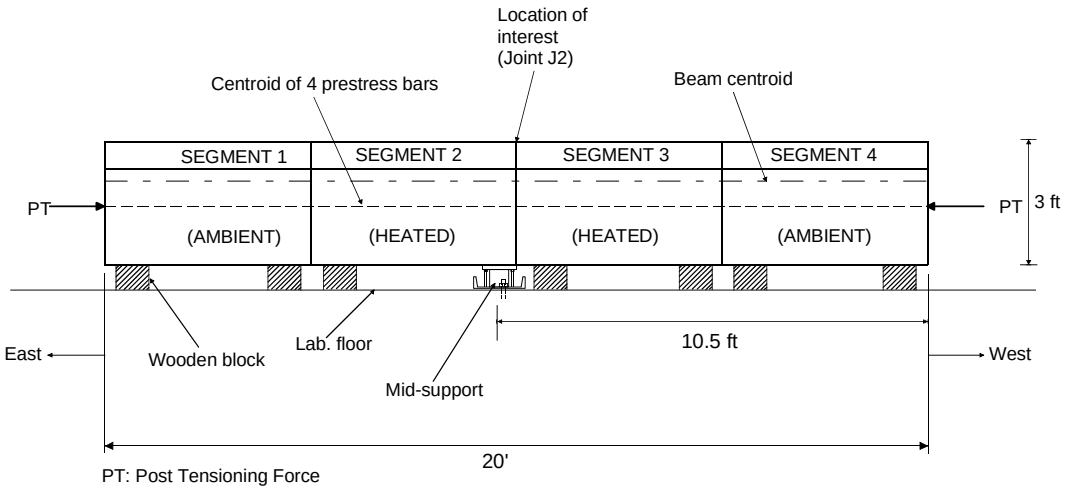

Figure 91 – Segment support during prestressing

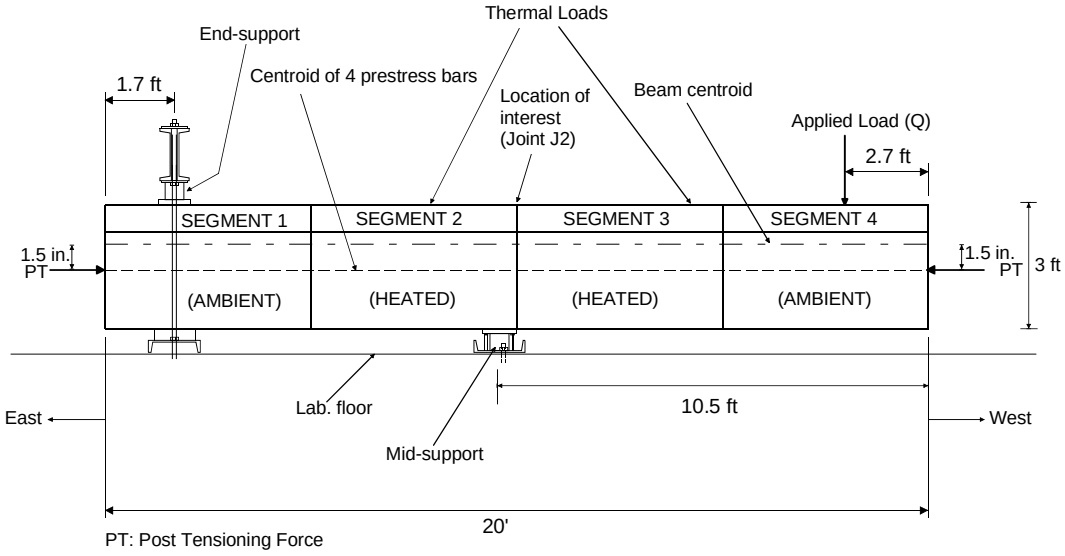

Figure 92 – Beam support for mechanical and thermal load tests

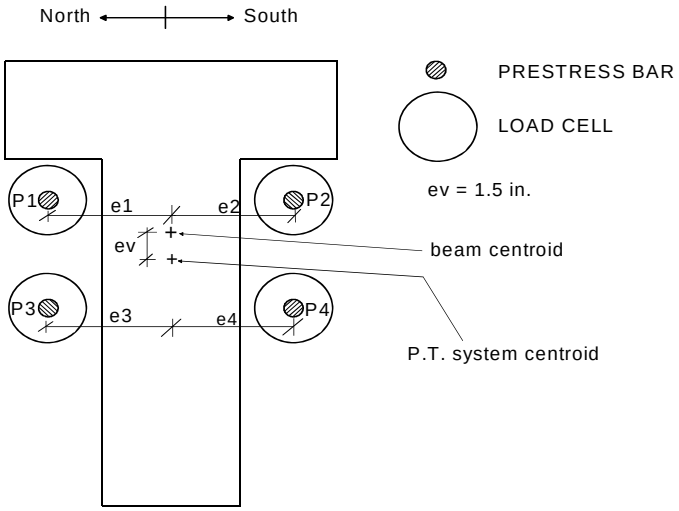

Figure 93 – Post-tensioning bar designations and eccentricities

Table 13 – Prestress magnitudes and horizontal eccentricities

Bar Designation	Force (kips)		Horizontal Eccentricity Designation	Horizontal Eccentricity (in.)
P1	97.2		**e1**	8.6
P2	89.2		**e2**	8.1
P3	93.2		**e3**	8.6
P4	92.4		**e4**	8.1

Concrete strains near (joint J2) were continuously recorded as the beam was prestressed. The strain data collected during prestressing provided important information regarding the distribution of strains at the joint. This information was vital in interpreting data collected during later mechanical load tests in which the joint was slowly opened to relieve stresses due to the initial pre-compression and self-weight of the beam. The locations of strain gauges on the beam can be found in Chapter 7.

Figure 94 and Figure 95 show the increase in strain at joint J2 on the North side of the beam. Figure 96 and Figure 97 show the strains at the same joint on the South side and Figure 98 shows the strains on top of the top flange. Also included in Figure 94 through Figure 98 are calculated strains at the top flange at joint J2. Strains were calculated using laboratory determined concrete material properties (e.g. elastic modulus) and measured prestress forces. Gaps, if any, at joint J2 prior to prestressing were neglected in the calculations. In these figures negative strains indicate compression. The top two bars, which were located above the centroid of the beam, were tensioned first (up to a total prestress of about 50 kips). As shown in Figure 98 the top flange strain gauges detected very little strain until the prestress force was between 50 kips and 125 kips. One explanation for this behavior is differential shrinkage of concrete at the edges of the beam segments. As Figure 99 shows, the top surfaces of the segments were exposed to the laboratory environment after segment casting. It is likely that shrinkage was greater in the exposed portion of the top flange than at other surfaces which remained covered during curing. It is believed that this differential shrinkage led to a narrow gap between the top flanges of

segments 2 and 3. Consequently, no strain was detected until sufficient prestress force had been applied to close the gap.

Differential shrinkage is also believed to be the reason for the systematically lower strains measured at the top flange compared with calculated strains (see Figure 98). This may have been due to the assumption in the calculations, that contact surfaces at joint J2 were smooth and in full contact (with no gaps). Calculated strains at the top flange close to joint J2 were higher than measured strains at the top flange for all prestress levels. The same was not the case for measured strains close to the top flange on the sides of the joint (see Figure 94 through Figure 97). Comparison of data from gauges on the sides of the joint with calculated top flange strains was more representative of expected behavior. This was because the 1.5 in. vertical eccentricity in prestressing was expected to lead to the development of lower compressive strains on top of the flange than at lower elevations.

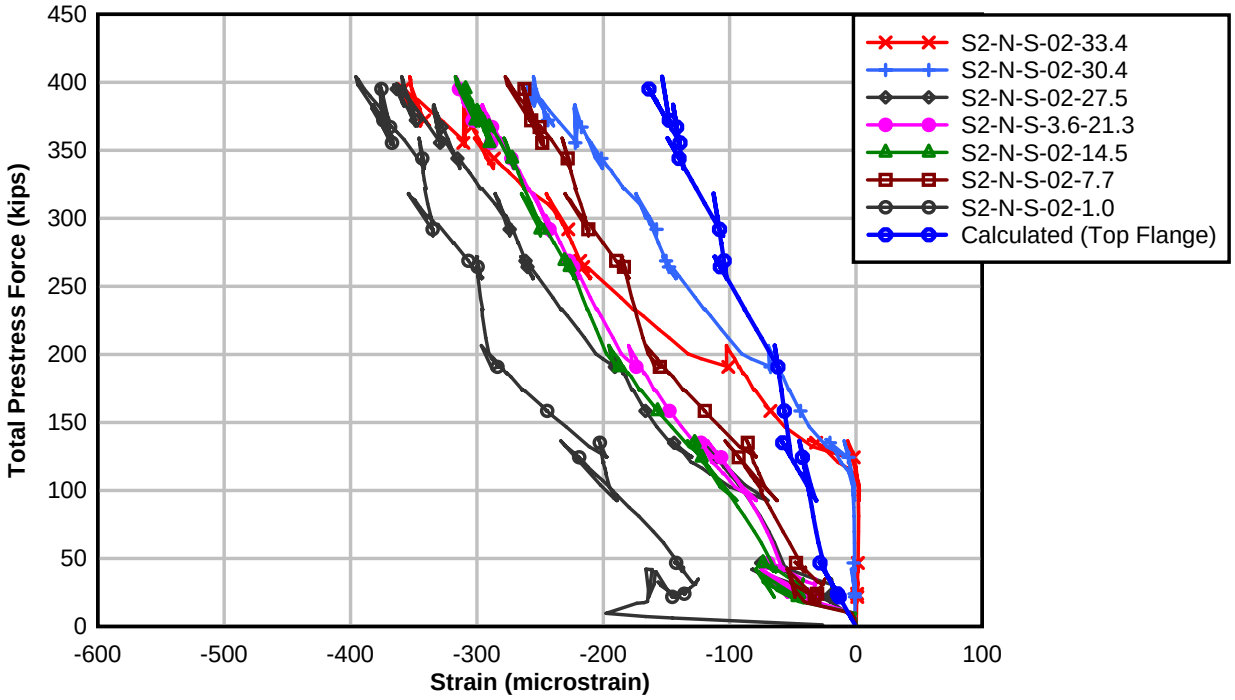

Figure 94 – Measured concrete strains close to joint J2 due to prestress (Segment 2, North)

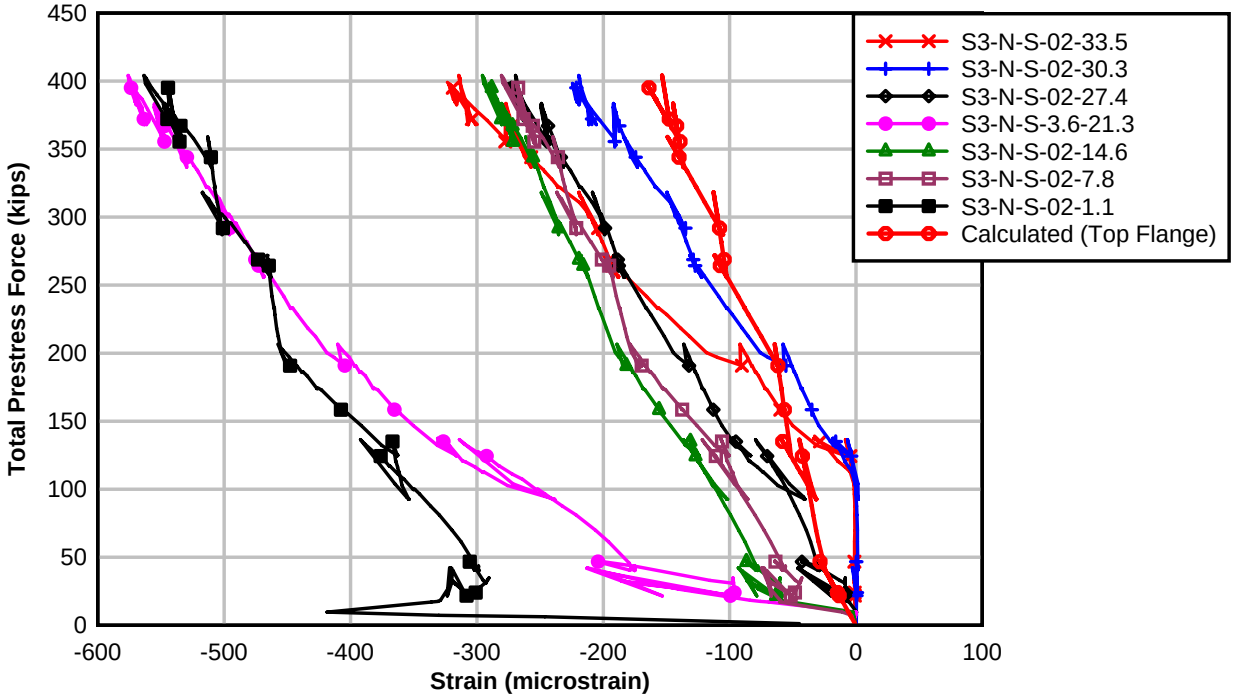

Figure 95 – Measured concrete strains close to joint J2 due to prestress (Segment 3, North)

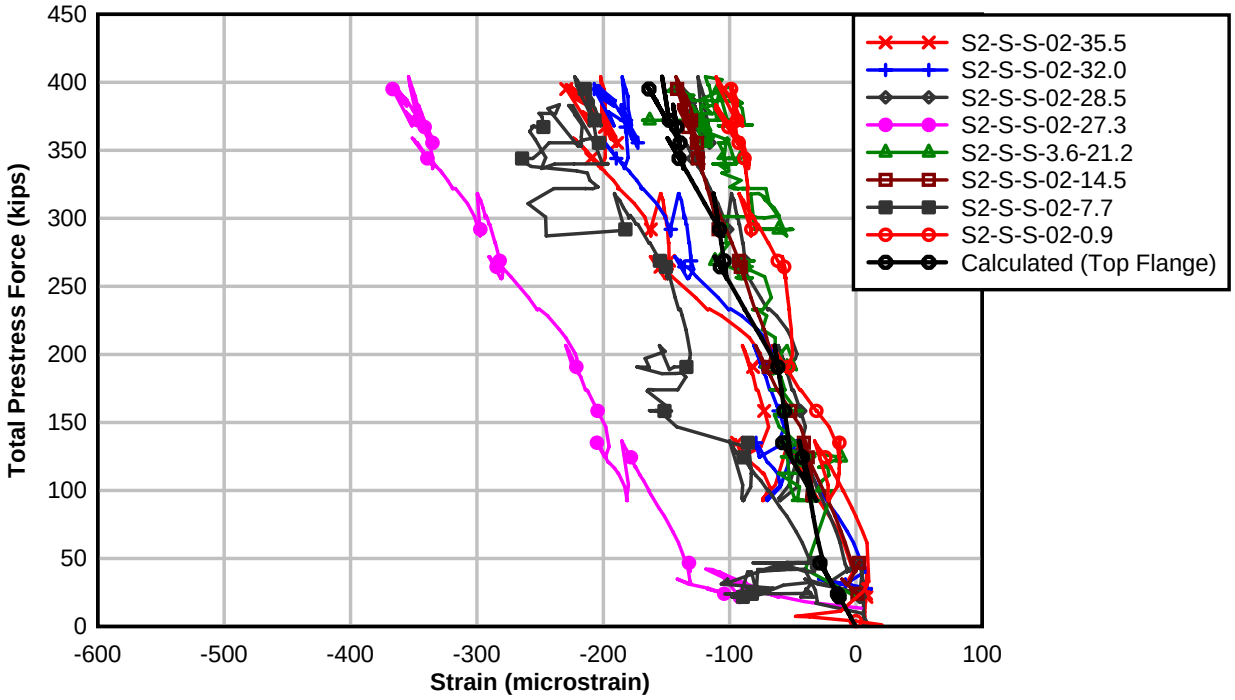

Figure 96 – Measured concrete strains close to joint J2 due to prestress (Segment 2, South)

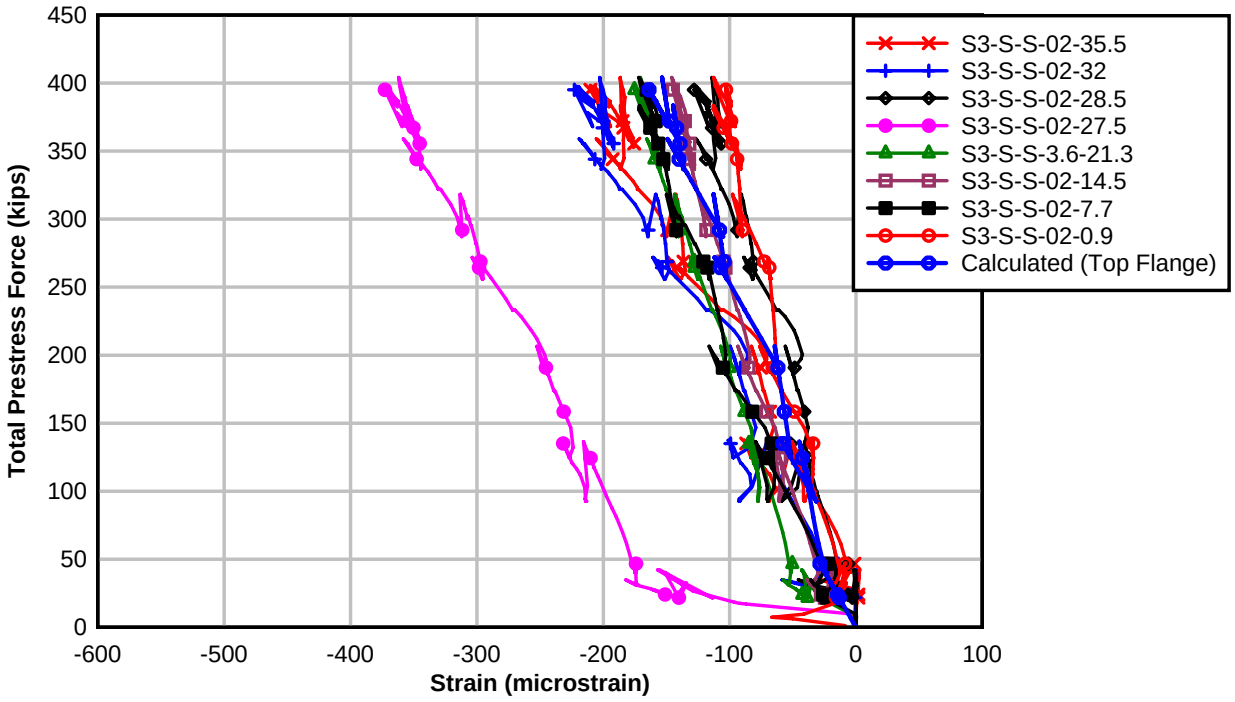

Figure 97 – Measured concrete strains close to joint J2 due to prestress (Segment 3, South)

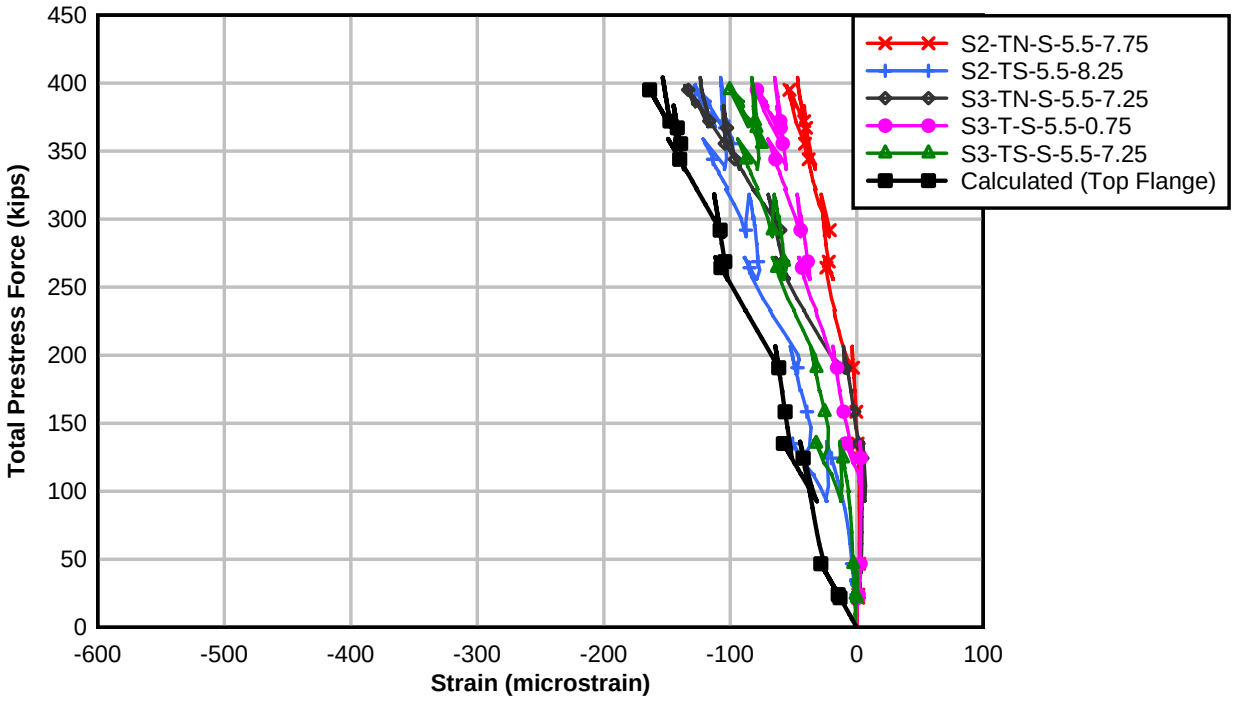

Figure 98 – Measured concrete strains close to joint J2 due to prestress (Top flange)

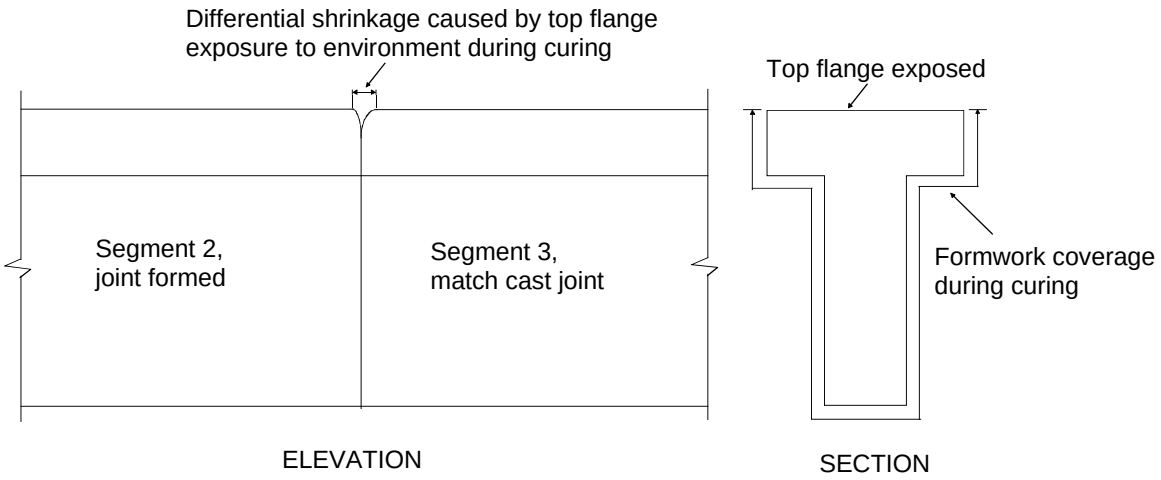

Figure 99 – Effect of differential shrinkage on top flange strains

Measured concrete strains through the depth of the beam segments near joint J2 are shown in Figure 100. These readings were taken immediately after prestressing was completed. Also shown in the plot are calculated strain profiles determined with the measured prestress forces and eccentricities (horizontal as well as vertical) shown in Table 13. Two observations can be made when comparing the measured and calculated strains. The first is that strains vary considerably with depth. The other is that the average measured strains on the North side are greater in magnitude than those on the South side with calculated strains along the vertical line of symmetry of the beam between the two.

Differences in the average measured strains on the North and South sides of the segments can be attributed to the unequal total prestress forces on the North (190.4 kips) and South (181.6 kips) sides of the beam, and the 0.5 in. net horizontal eccentricity in prestressing (see Figure 93 and Table 13). As Figure 100 shows, calculated strains on the North and South sides of joint J2 determined with measured prestress forces and measured horizontal and vertical eccentricities were higher on the North side than on the South side of the joint. It was explained in Chapter 6 that the goal of applying an equal prestress force to each bar was not achieved because the prestress anchorage system prevented independent post-tensioning of the DYWIDAG bars. The 0.5 in. net horizontal eccentricity was most likely the result of movement of the suspended post-tensioning anchorage system as the beam was prestressed. The moment due to the unintended horizontal eccentricity caused the development of compressive strains on the North side and tensile strains on the South side of the vertical axis of the beam. This moment, together with the moment developed as a result of the inequality in the total prestress on the North and South sides of the beam, led to the development of lower magnitude strains on the South side of the beam compared to the North side.

A likely explanation for the variation in measured strains through the depth of the segments is an imperfect fit (segment-to-segment contact) at joint J2. This could have occurred during the match-casting process or during positioning of the segments for prestressing. An imperfect fit would lead to data from the strain gauges being influenced by stress concentrations in the surface fibers of the beam segments. The unusually high strains measured on the North side of Segment 3 from strain gauges located 1.1 in. and 21.3 in. from the bottom of the segment (see Figure 100) might have been due to localized effects at those points on the segment. The exact causes of the high measured strains at these locations are unknown, however, at about 7%

of the total prestress force the strain gauges designated S3-N-S-02-1.1 and S3-N-S-3.6-21.3 (see Figure 95) had registered about 36% and 55% of the respective total measured strains at their locations. Except for the two high strain points in the profile of Segment 3 on the North side, strain profiles on identical sides of segments 2 and 3 compared quite well.

Strains measured transversely across the width of the flanges of segments 2 and 3 near joint J2 are shown in Figure 101. Also shown in the figure are calculated strains that take into account the vertical eccentricity in prestressing only (shown as *average calculated* strains in the legend) and calculated strains that take into account both vertical and net horizontal eccentricities in prestressing (shown as *calculated* strains in the legend). Data in Figure 101 were collected from three strain gauges on Segment 3 and two strain gauges on Segment 2. The presence of LVDT mounts on Segment 2 prevented the placement of a strain gauge close to the center of the flange of that segment. In an ideal situation, strains measured across the width of the flanges near joint J2 should be uniform (see the *average calculated* strains in Figure 101). Because of the measured net horizontal eccentricity in prestressing, the distribution of measured strains across the width of the flange was expected to look like the *calculated* strains in the figure. A possible reason for the nonlinear distribution of measured strains across the width of the flange is a lack of a full contact fit at the joint.

The nonlinearities in the measured strains were not expected to affect the quantification of thermal stresses caused by the AASHTO nonlinear thermal gradients. As discussed in Chapter 8, stresses due to prestress, self-weight, and any additional forces that may have been induced at joint J2 when the support system of the beam was changed (see Figure 91 and Figure 92), were taken as reference stresses. These stresses were then relieved when joint J2 was opened, and therefore did not directly enter into calculations of thermally induced stresses.

Partial losses in prestressing force were initially measured over a period of approximately three weeks and are plotted for each bar in Figure 102. The percentage change in total prestress with time is shown in Figure 103. Fluctuations about the general downward trend in Figure 102 and Figure 103 were the result of daily temperature variations. Prestress levels were also checked before and after each mechanical and thermal load test conducted after the initial monitoring period. The maximum percentage reduction in total prestress over the course of the 4-month period during which tests were conducted on the laboratory segmental beam was about 3.5% of the initial total prestress.

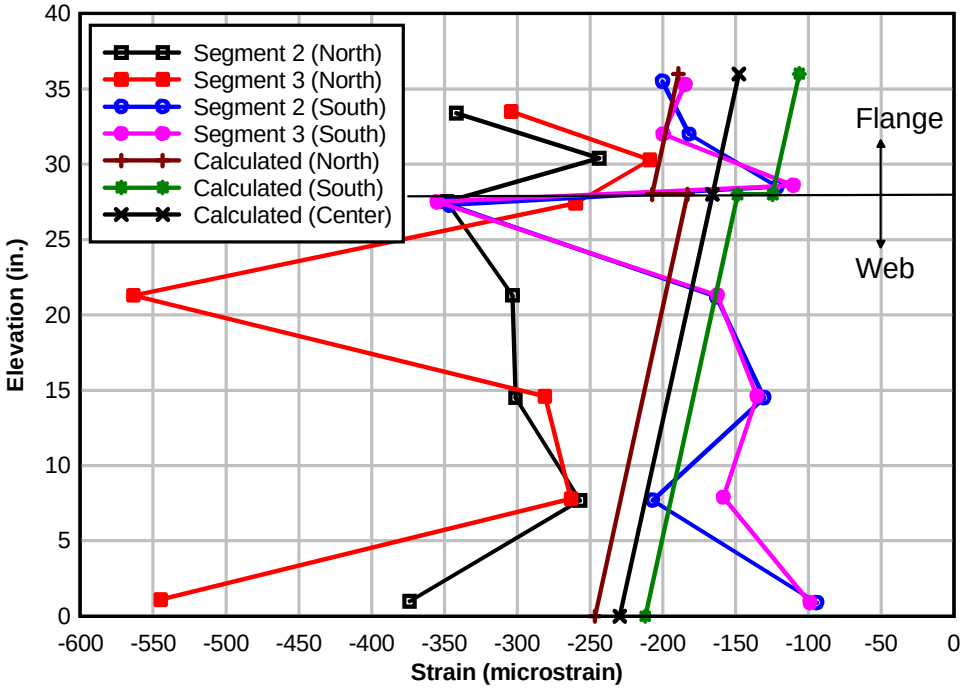

Figure 100 – Measured concrete strains due to prestress through depth of segments near joint J2

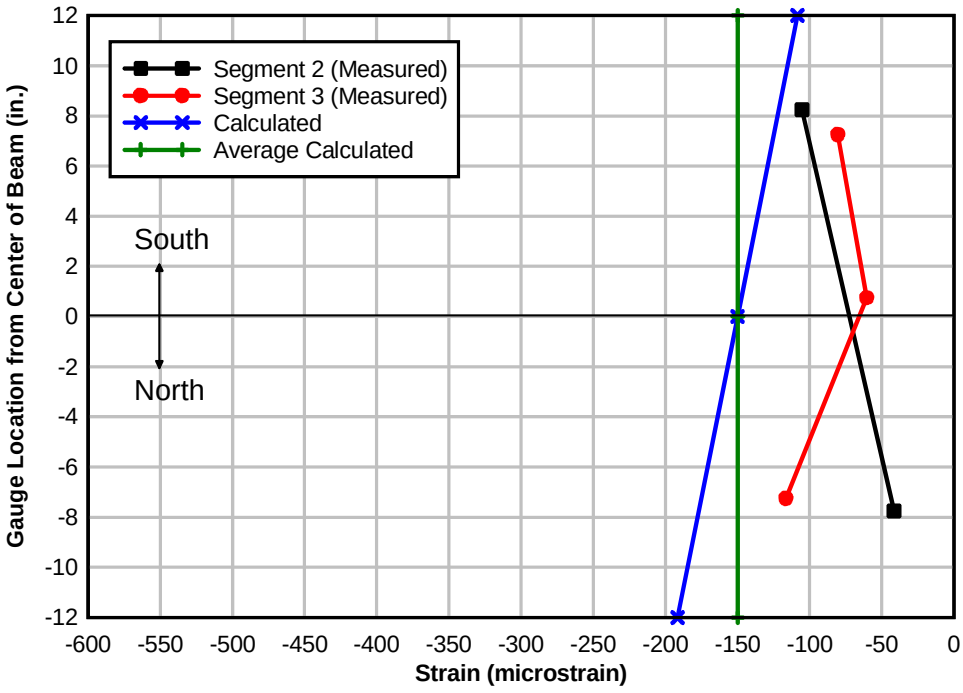

Figure 101 – Measured concrete strains due to prestress across width of segment flanges near joint J2 (Top flange)

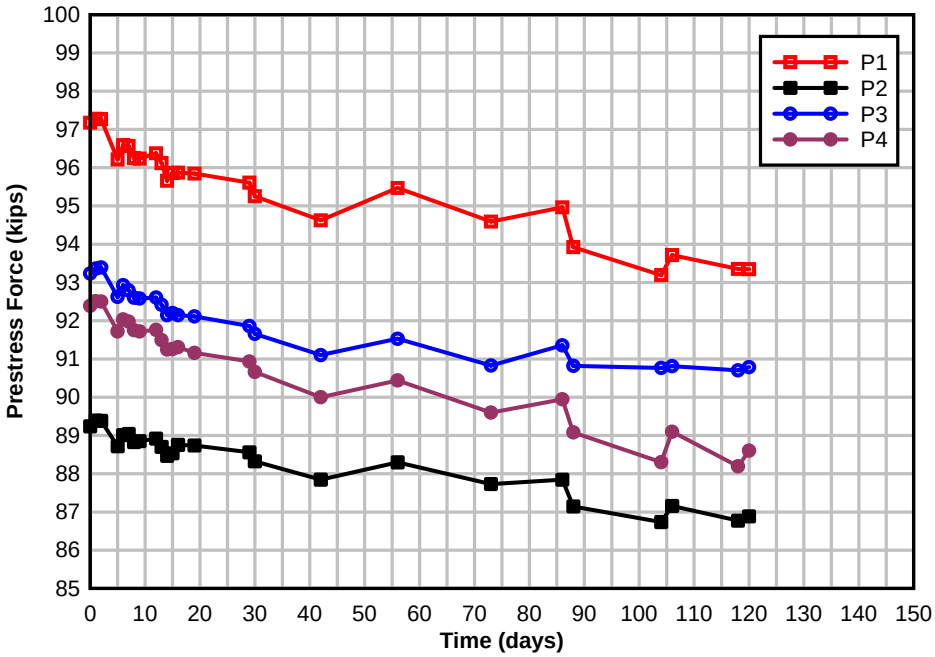

Figure 102 – Variation of prestress forces with time

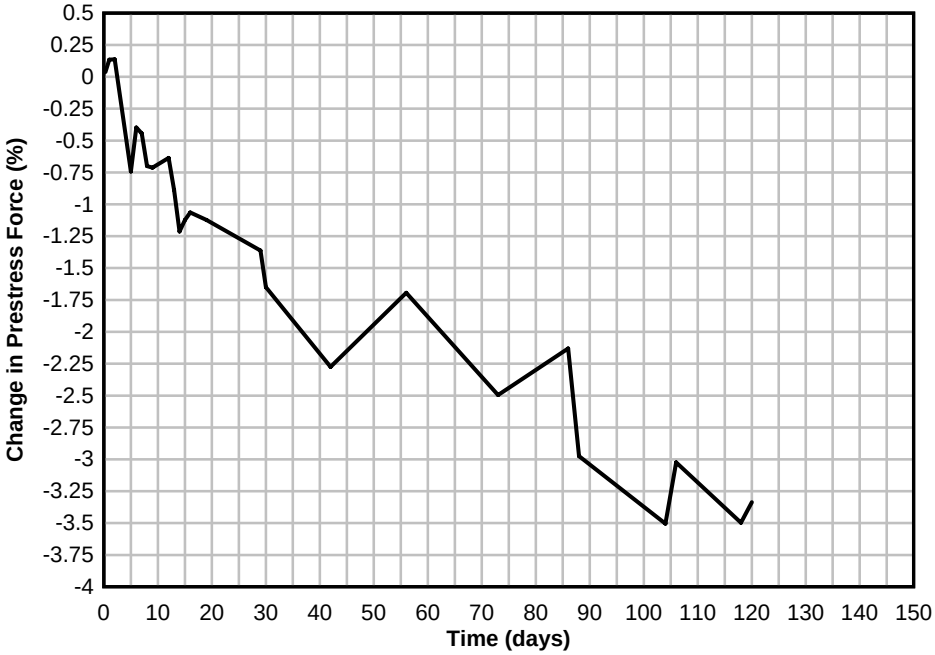

Figure 103 – Change in total prestress force with time

12 RESULTS – MECHANICAL LOADING

The behavior of the laboratory segmental beam under the action of mechanical loads applied at the cantilevered end of the beam is discussed in this chapter. The objective of the mechanical load tests was to determine the load at which the joint at midspan (joint J2) opened and the effect that this opening had on the overall behavior of the beam. As discussed in Section 8.1, opening of joint J2 was used to create zero reference stress conditions from which stresses due to the AASHTO nonlinear thermal gradients could later be quantified.

Two methods of detecting joint opening were used. One involved the use of strain gauges mounted close to joint J2. The other involved the use of LVDTs mounted across joint J2 at specified depths. Data collected from the LVDTs and strain gauges are presented and compared in the following sections. In addition, data collected from strain gauges located at the middle of segments 2 and 3 (30 in. away from joint J2 on both sides) and vertical deflection data will be presented and discussed.

In the plots presented in the following sections, loads refer to mechanical loads applied by the hydraulic jack. Beam response is also due to loads applied by the hydraulic jack. The total vertical mechanical load carried by the beam during tests was the sum of the self-weight of the beam (measured at about 11 kips) and the load applied by the hydraulic jack. Tensile strains, which represent relief of initial compressive strains prior to the application of mechanical loads, are positive and, compressive strains, which represent an addition to the initial compressive strains, negative. It should be noted that symbols in load vs. response curves were used to distinguish between plots and are not representative of actual data values. The curves represent actual data values connected with straight lines.

12.1 Detection of Joint Opening – Strain Gauges Close to Joint at Midspan

The detection of joint opening with strain gauges is illustrated in Figure 104 and Figure 105. Prior to opening of the joint, the change in strain is linear with respect to applied load. After the joint opens, concrete fibers initially in contact are unable to carry any significant additional strain. Strain gauges located at the level of joint opening therefore show no change in strain with increasing load, and the load vs. strain curve becomes almost vertical. The load at which strains initially stop increasing is the load that causes the joint to open at the location of the strain gauge. Strain at this load is equal in magnitude, but opposite in sign, to the initial strain at the same location that was caused by prestress and self-weight.

For strain gauges located on the side of the beam (see Figure 104), the initial slope of the load vs. strain curve is inversely proportional to the distance of the gauge from the neutral axis of the gross section. Strain gauges located farther away from the centroid of the contact area of the gross section indicate lower joint-opening loads than strain gauges located closer in distance to the centroid. In Figure 104, Q1 is less than Q2 because SG1 and SG2 are closer in distance to the centroid of the contact area than SG3 and SG4. This is because the joint starts opening at the top and slowly progresses downward as indicated by the direction of the moment in Figure 104. The point at which the load vs. strain curve changes slope (becomes vertical) is dependent on the compressive strain at the location of the strain gauge. In Figure 104 it is assumed that the initial strain, ε_1, at the location of SG1 and SG2 is less than the initial strain, ε_2, at the location of SG3 and SG4 (due to the location of the line of action of the post-tensioning force, i.e. below the centroid of the contact area of the gross cross section).

Strain gauges located on top of the flange have identical load vs. strain curves (see Figure 105). This is because strain is uniformly distributed across the width of the flange. The strain at which the load vs. strain curve becomes vertical, ε_i, is the initial uniform strain in the top fibers of the flange before the application of mechanical loads.

Though the post-joint-opening curves are shown as vertical in Figure 104 and Figure 105, this is not always the case. In prestressed beams, the sudden increase in prestress associated with opening a joint may lead to a slight compression in fibers that are no longer in contact. The post-joint-opening curve then has a slight curvature, which diminishes as the depth of joint-opening moves farther away from the location of the fibers (with increasing load).

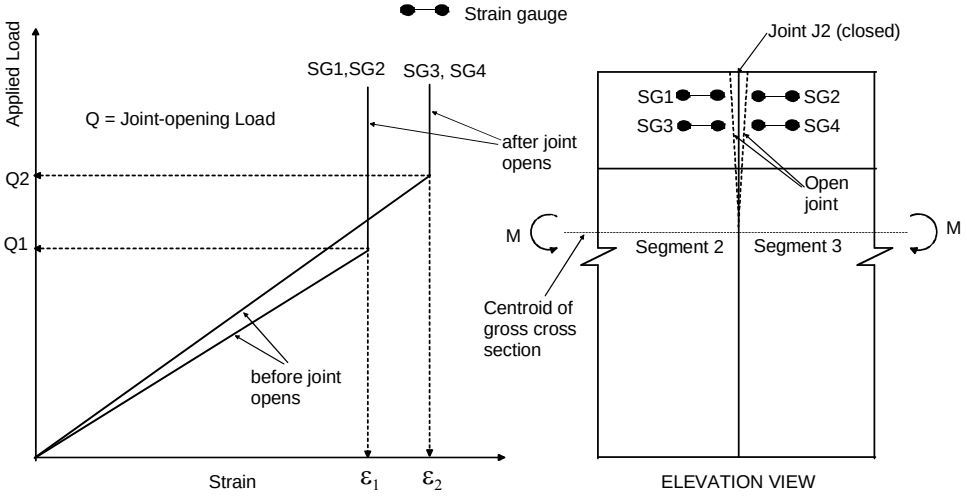

Figure 104 – Expected behavior of strain gauges close to joint on side of beam

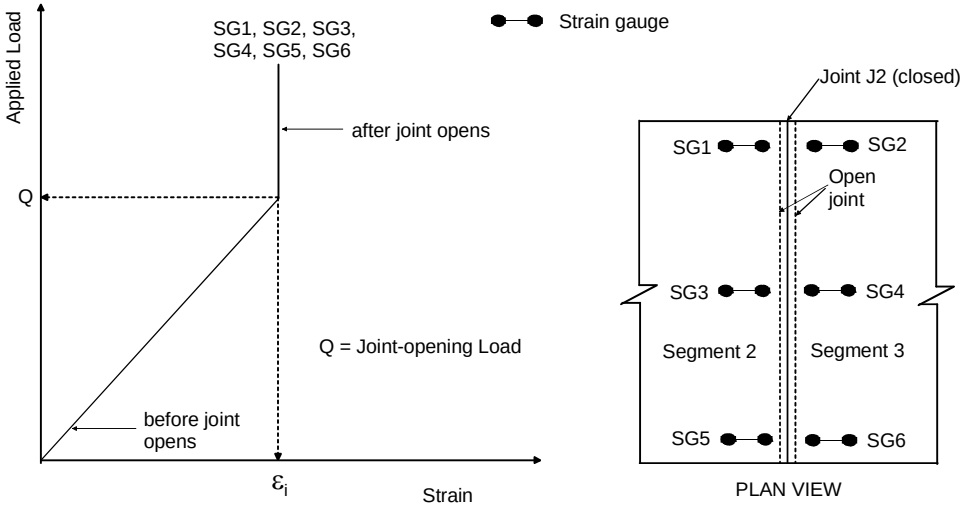

Figure 105 – Expected behavior of strain gauges close to joint on top of flange

Typical load vs. strain curves on the North and South sides of joint J2, plotted with laboratory measured loads and concrete strains, are shown in Figure 106 and Figure 107, respectively. Opening of the joint at the location of each strain gauge was indicated by the point at which the curves initially became vertical. Generally, strain gauges located above the centroid

of the contact area of the cross section prior to the joint opening (referred to simply as the centroid of the gross cross section in the figures) indicated opening of the joint. Strain gauges located below the centroid of the gross cross section registered compressive strains. This was expected since the moment at joint J2 due to the applied loads led to relief of existing compressive strains above, and the addition of compressive strains below the centroid of the contact area at the joint. The high decompression shown by the strain gauge located at the centroid of the gross cross section in Figure 106 (S3-N-S-3.6-21.3) as the depth of joint opening approached the centroid was consistent with the high compressive strain recorded by the same gauge during prestressing (see Figure 95 and the measured strain profile on the North side of Segment 3 at elevation 21.3 in. in Figure 100).

Figure 108 shows the variation of concrete strain with load on top of the flanges of segments 2 and 3 close to joint J2. Strain gauges located on the top flange generally detected very low strains with applied load compared with strain gauges on the sides of the segments. This was expected since low strains were recorded in the extreme top fibers of the segment flanges during prestressing (see Figure 98 and Figure 101). Of the five strain gauges on the top flange, it was possible to detect joint-opening from two: one on the South of Segment 2 and the other on the North of Segment 3 (see Figure 108). The load vs. strain curves of the other three strain gauges were almost vertical throughout the entire loading process. Normally, the behavior of the three gauges with almost vertical load vs. strain curves would indicate that the joint opened at the top flange almost immediately after the beam was loaded. This, however, was not the case. As shown in Figure 109, some concrete at the top flange at joint J2 had broken off during transportation and handling of the segments. Gauges at the locations where a significant amount of concrete had broken off showed almost no change in strain with load even though the joint was not open. This was because concrete fibers on opposite sides of the joint at the locations were not in contact prior to loading the beam. Strain gauges at other locations where this condition was less severe registered some strain as the beam was loaded.

The nonlinear behavior of measured strain with load in Figure 106 through Figure 108 was the result of the condition of joint J2 at the top flange as shown in Figure 109, and changes in the stiffness of the contact area at the joint as it was slowly opened.

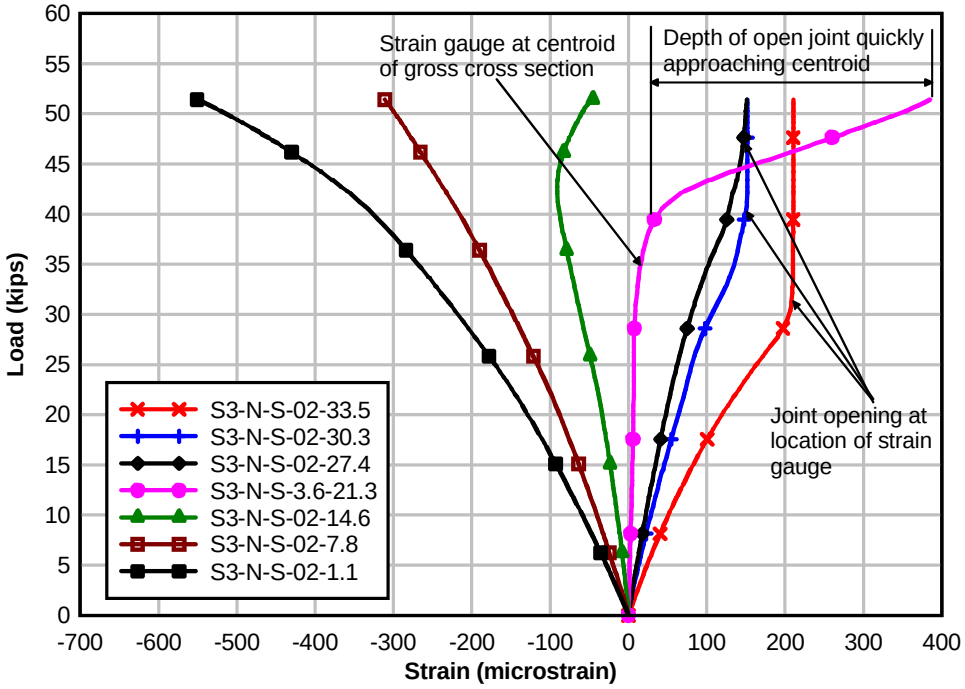

Figure 106 – Load vs. Strain close to joint at midspan (North side)

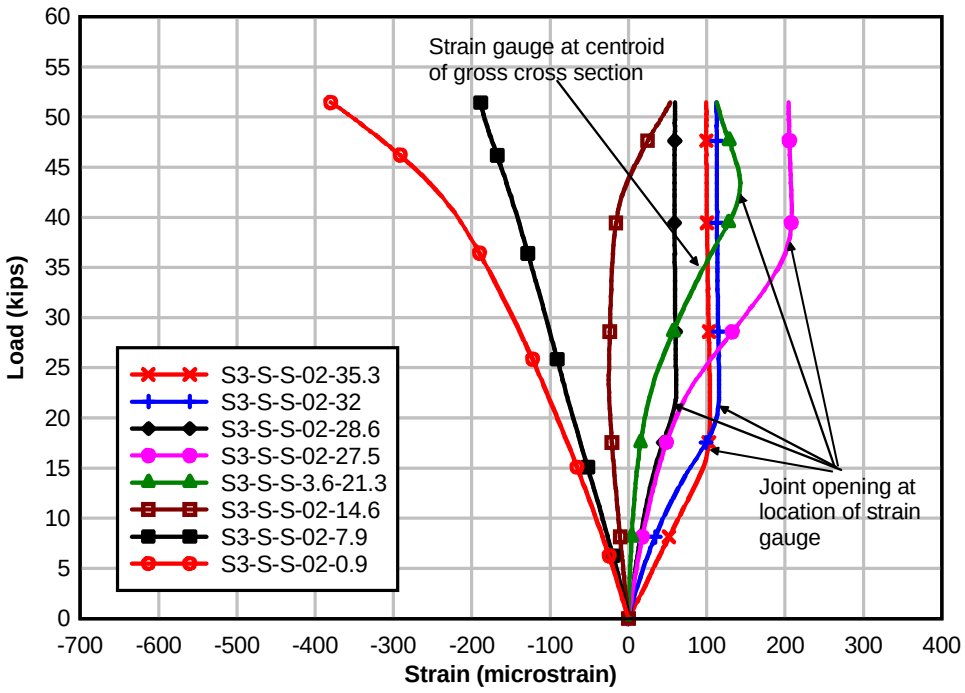

Figure 107 – Load vs. Strain close to joint at midspan (South side)

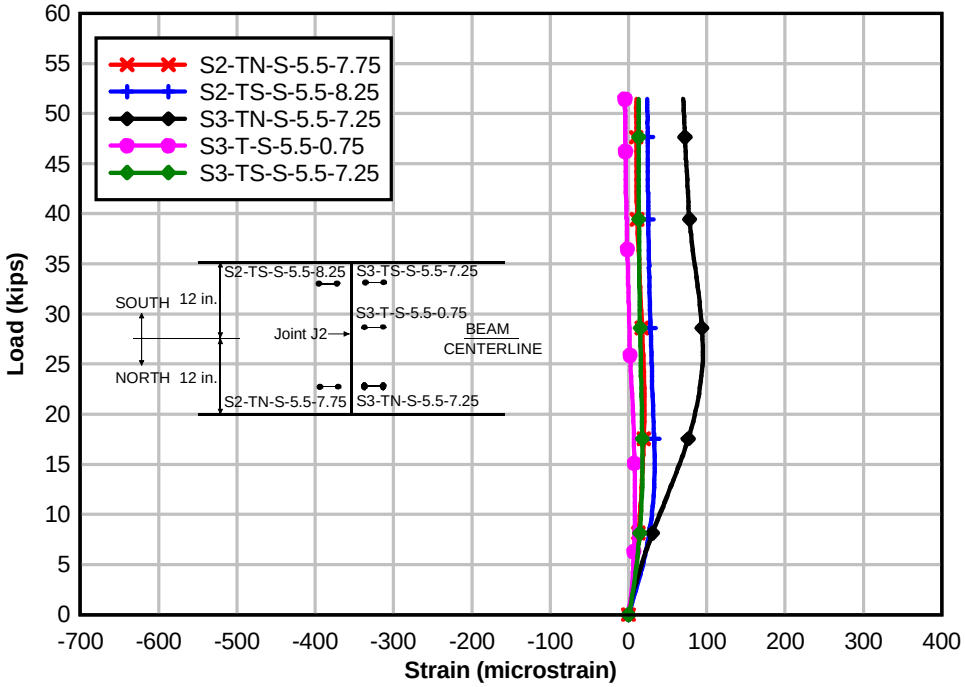

Figure 108 – Load vs. Strain close to joint at midspan (Top flange)

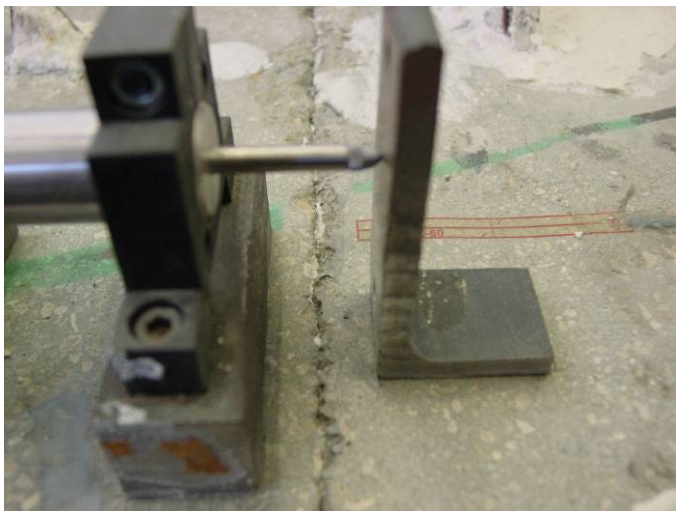

Figure 109 – Condition of joint J2 on top of flange

As discussed in the beginning paragraphs of this section, the strain at which the joint opened at the location of a gauge was expected to be equal to the initial compressive strain at that location. Before beginning of mechanical load tests on the beam, the supports were changed from the system shown in Figure 91 to that shown in Figure 92. The changes in strain that took place during this transition were not recorded. Hence the exact distribution of strain at joint J2 was therefore not known prior to the application of mechanical loads. In spite of the unknown changes in strain that took place while changing the support conditions of the beam, the measured strains at which the joint opened, though not equal in magnitude, were still consistent with the distribution of strains due to prestress. As shown in Table 14, strain gauges near joint J2

on the sides of the flange, which showed higher strains due to prestress, indicated opening of joint J2 at higher strains than gauges located in areas of lesser prestrain.

Strain gauges above the centroid of the contact area of the section and at identical locations on either side of the joint were expected to detect joint-opening at the same load. Furthermore, it was expected that gauges at higher elevations would indicate opening of the joint at lower loads than gauges at lower elevations (see Figure 104). However, strain gauges located above the centroid of the contact area showed the joint opening at higher loads on the North side (Figure 106) than on the South side (Figure 107). This was partly due to differences in the elevations of the gauges. The strain gauge designated S3-N-S-02-27.4 on the North side of the joint showed the joint opening at a load of about 48 kips (see Figure 106), while the strain gauge at the same location on the South (S3-S-S-02-27.5) showed the joint opening at a load of about 38 kips (see Figure 107). Furthermore, the strain gauge located at elevation 28.6 in. on the South side of the joint (see Figure 107) showed the joint opening at a lower load (21 kips) than two strain gauges located above it on the North side of the joint as shown in Figure 106 (31 kips for the gauge at elevation 33.5 in. and 41 kips for the gauge at elevation 30.3 in.). This was indicative of the joint opening earlier on the South side than on the North side, and was consistent with the distribution of measured strains through the depth of the beam due to prestress (see Figure 100).

Because of the distinct change in strain that occurred when the joint opened, strain gauges were the instrument of choice in determining joint-opening loads.

Table 14 – Comparison of measured strains due to prestress and measured strains when joint opens

Gauge Location	Gauge Designation	Strains due to Prestress (με)	Strains measured at joint opening condition (με)
North Flange	S3-N-S-02-33.5	-304	210
	S3-N-S-02-30.3	-209	151
South Flange	S3-N-S-02-35.3	-185	103
	S3-N-S-02-32.0	-200	115
	S3-N-S-02-28.6	-110	60

Measured concrete strains through the depth of the beam near joint J2 on the North and South sides are shown in Figure 110 and Figure 111, respectively. Strain data shown in Figure 106 through Figure 108 were used in plotting the strain profiles in Figure 110 and Figure 111. In Figure 110 and Figure 111, joint-opening at each elevation within joint J2 is indicated when no further strain change with load occurs at that depth. As explained previously, the fact that top flange strains were nearly constant with respect to load in Figure 111 was not indicative of opening of joint J2, but was probably the result of the condition at the joint shown in Figure 109.

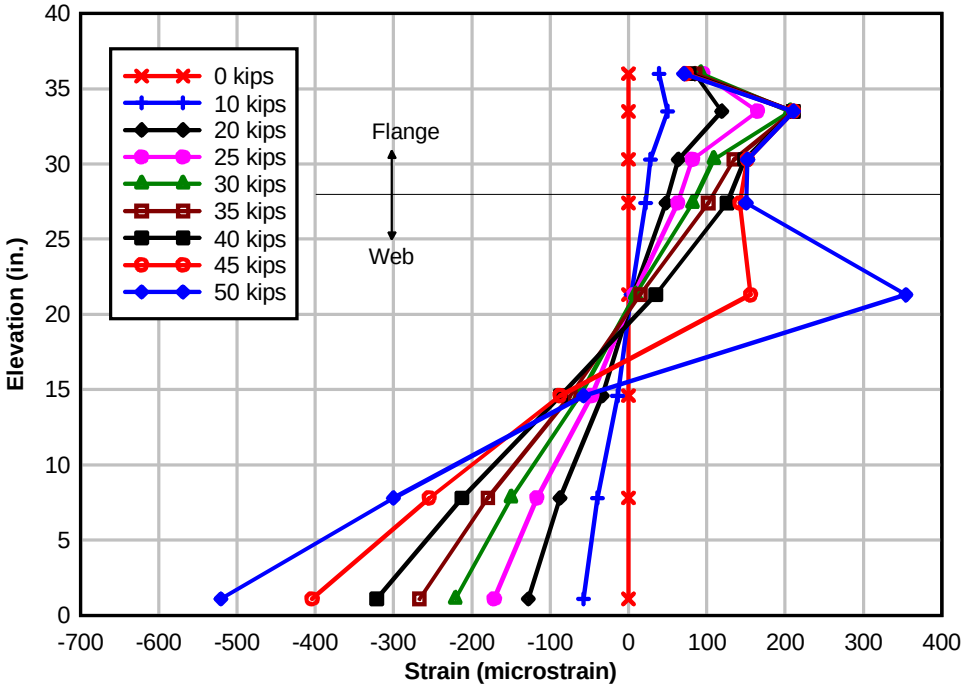

Figure 110 – Measured strain distributions close to joint at midspan (North side)

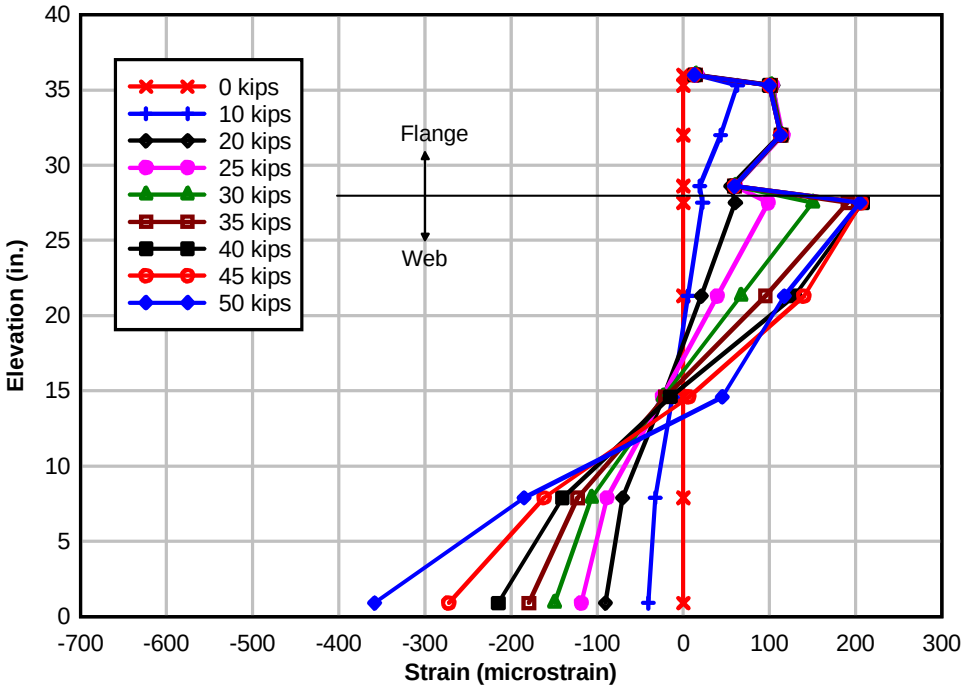

Figure 111 – Measured strain distributions close to joint at midspan (South side)

As shown in Figure 110 and Figure 111, the neutral axis of the contact area at joint J2 (point of intersection of strain profile with zero strain axis) gradually moved downward with increasing load. Furthermore, the movement of the neutral axis was smaller on the North side of the joint (see Figure 110) than on the South side (see Figure 111), indicating a rotation of the

neutral axis about the centroid of the contact area. As illustrated in Figure 112, the downward movement of the centroid of the contact area at joint J2, as the beam was incrementally loaded, was due to opening of the joint. Rotation of the neutral axis about the centroid of the contact area was attributed to the net out-of-plane horizontal eccentricity in prestressing. Movement of the neutral axis with load is illustrated in Figure 113.

The change in prestress as the beam was incrementally loaded is shown in Figure 114. Bars 1 and 2 were expected to undergo the same change in force with load since they were at the same elevation. Similarly, bars 3 and 4 were expected to undergo the same change in force. However, because the opening of joint J2 was greater on the South side than on the North side of the beam the change in force in the bars on the South side (P2 and P4) was greater than the change in force in the bars on the North side (P1 and P3, respectively) after the joint opened. The forces in bars 1 and 2 increased with load while forces in bars 3 and 4 generally decreased with load. This was because bars 1 and 2 were located above the centroid of the gross section and bars 3 and 4 were located below the centroid of the gross section (see the position of prestress bars in Figure 114). At a load of about 40 kips (see Figure 112) the depth of joint opening caused the centroid of the contact area at joint J2 to move below the location of bars 3 and 4, leading to an increase in force with load in these bars.

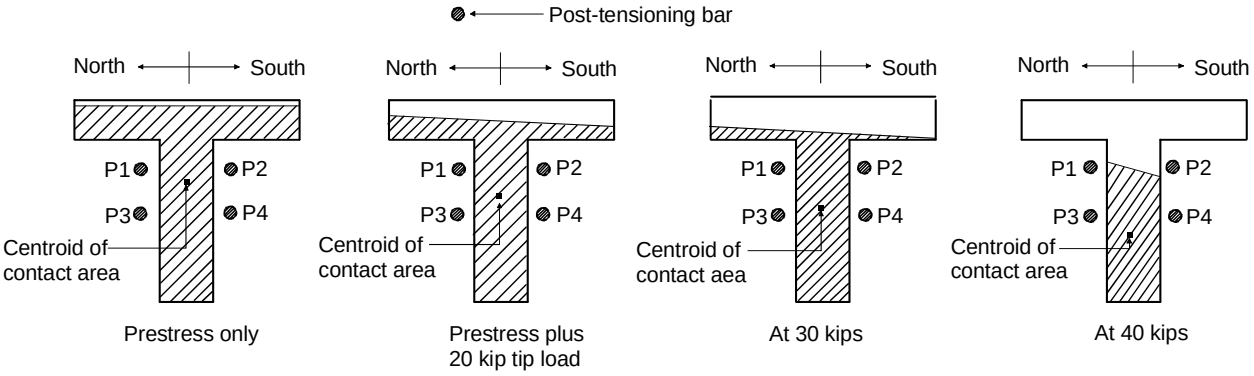

Figure 112 – Estimated progression of joint-opening with load (based on strain gauge data)

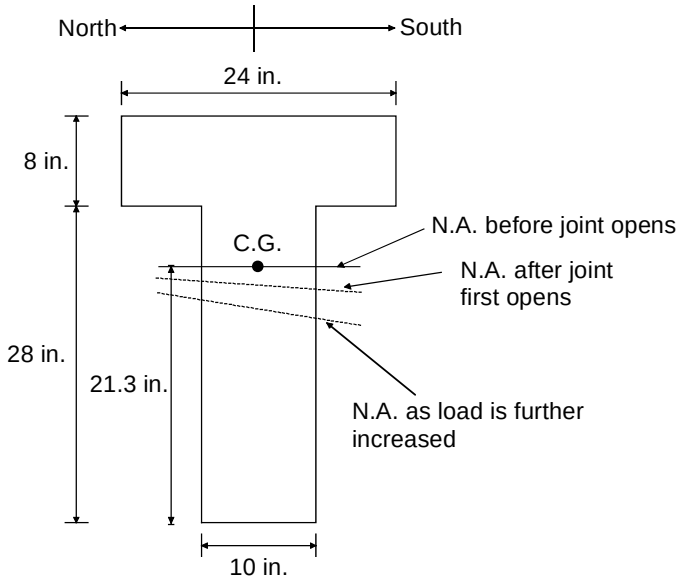

Figure 113 – Movement of neutral axis (N.A.) with load

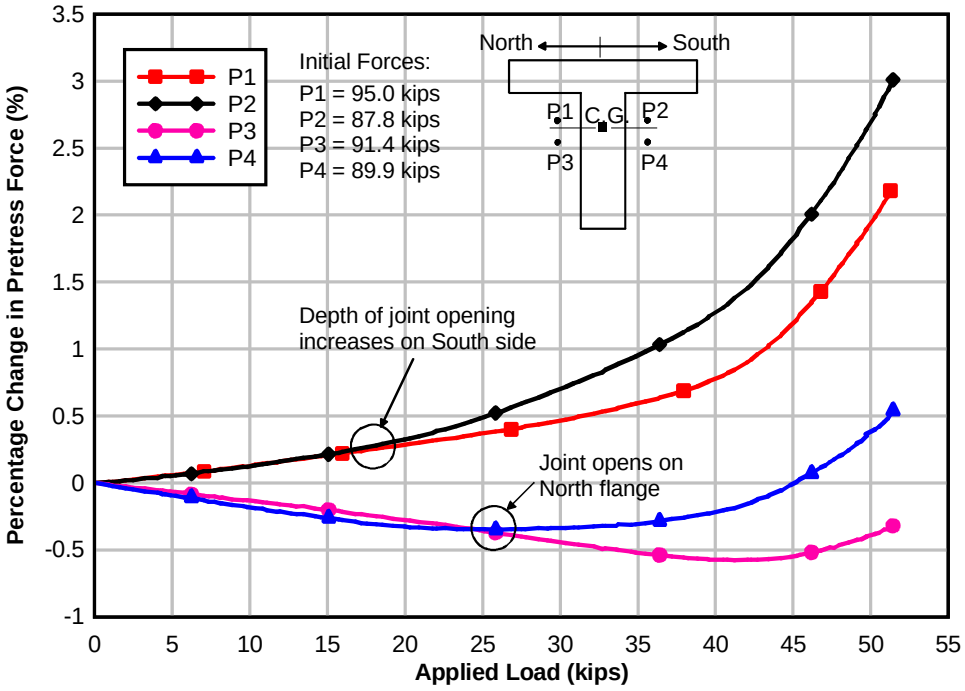

Figure 114 – Changes in prestress force with load

12.2 Detection of Joint Opening – LVDTs Across Joint at Midspan

Determination of joint-opening using LVDTs mounted across the joint is illustrated in Figure 115 and Figure 116. LVDTs mounted across a joint indicate opening of the joint at the location of the LVDT when the initial slope of the load vs. displacement curve changes as a result of the reduction in stiffness of the section. Because the slope change was relatively sharp, the opening load was determined by visual inspection of the load displacement curves.

Prior to the joint opening, LVDTs measure the displacement between the mounts (supports) of the LVDT as a result of strain in concrete. The initial slope of the load vs. displacement curve is inversely proportional to the distance between the mounts of the LVDT and the distance of the LVDT from the centroid of the contact area at the joint prior to the application of mechanical loads (see Figure 115). The bending moment in Figure 115 causes the joint to start opening at the top flange and gradually progress downward. Therefore, LVDTs that are farther above the centroid of the contact area prior to the joint opening indicate lower joint-opening loads than LVDTs that are closer to the centroid of the contact area. LVDTs at identical distances from the centroid of the contact area of the gross section have the same load vs. displacement curves if the joint opens uniformly across the width of the section (see Figure 116). After the joint opens, fibers that were initially in contact separate and are unable to carry any significant additional strain. LVDTs then measure the distance between the separated fibers or the width of joint opening.

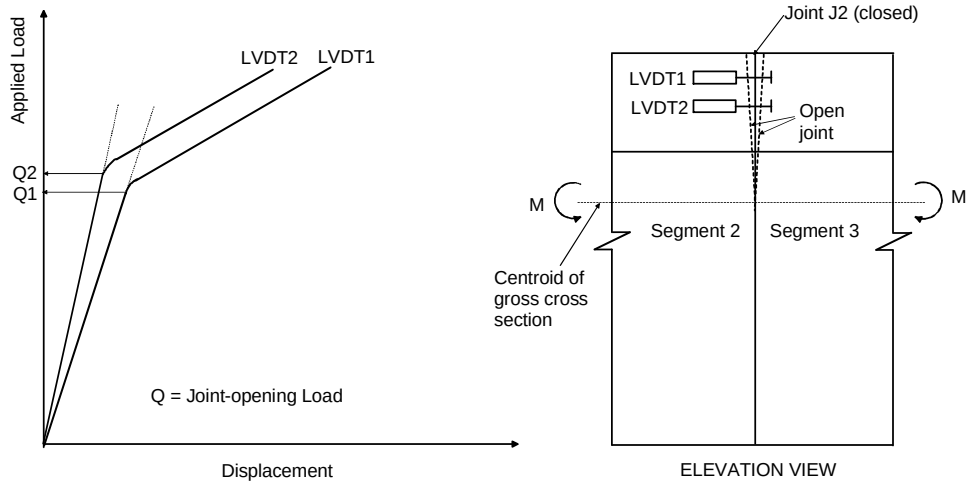

Figure 115 – Expected behavior of LVDTs across joint on side of beam

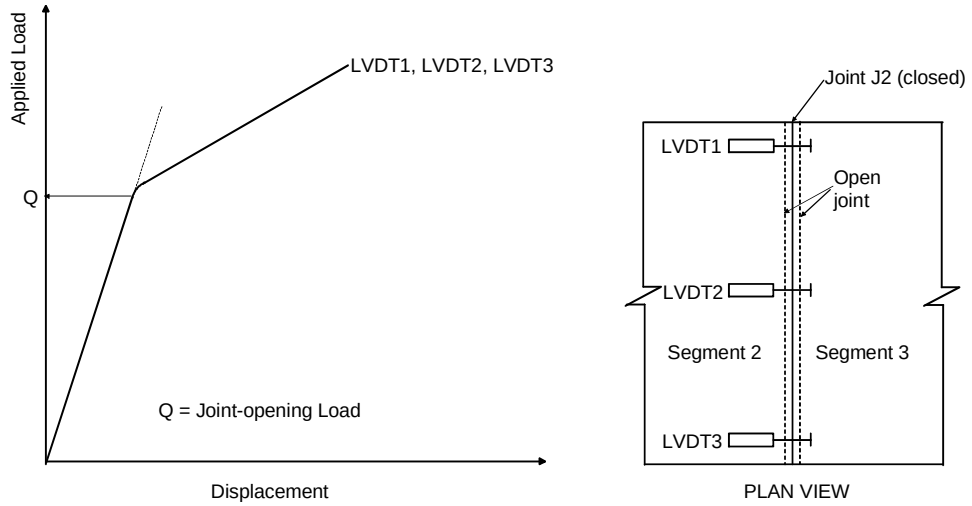

Figure 116 – Expected behavior of LVDTs across joint on top of flange

Figure 117 shows data from LVDTs distributed throughout the depth of joint J2 on the South side of the beam. In this figure, the last number in each LVDT label indicates the distance of the LVDT from the bottom of the beam. The centroid of the contact area of the gross section at joint J2 was 21.3 in. from the bottom of the segments. As expected, LVDTs located at elevations above the centroid of the contact area of the gross section indicated lower joint-opening loads than LVDTs at lower elevations. Furthermore, LVDTs located close to the bottom of the joint indicated little or no joint-opening, and in the case of the LVDT at the lowest elevation (J2-S-D-4.275) some compression. This was because the moment at joint J2 due to applied mechanical loads caused the relief of compressive strains above the centroid of the contact area but increased the existing compressive strains below the centroid. At the level of each LVDT the initial compressive strains had to be relieved by strains due to the applied moment in order for the joint to open. It was therefore expected that only LVDTs located above the centroid of the contact area would indicate joint-opening. This was evident in data from the top three LVDTs, designated J2-S-D-33.75, J2-S-D-30.25, and J2-S-D-25.0 in Figure 117, which were located above the centroid of the contact area at joint J2 prior to opening of the joint.

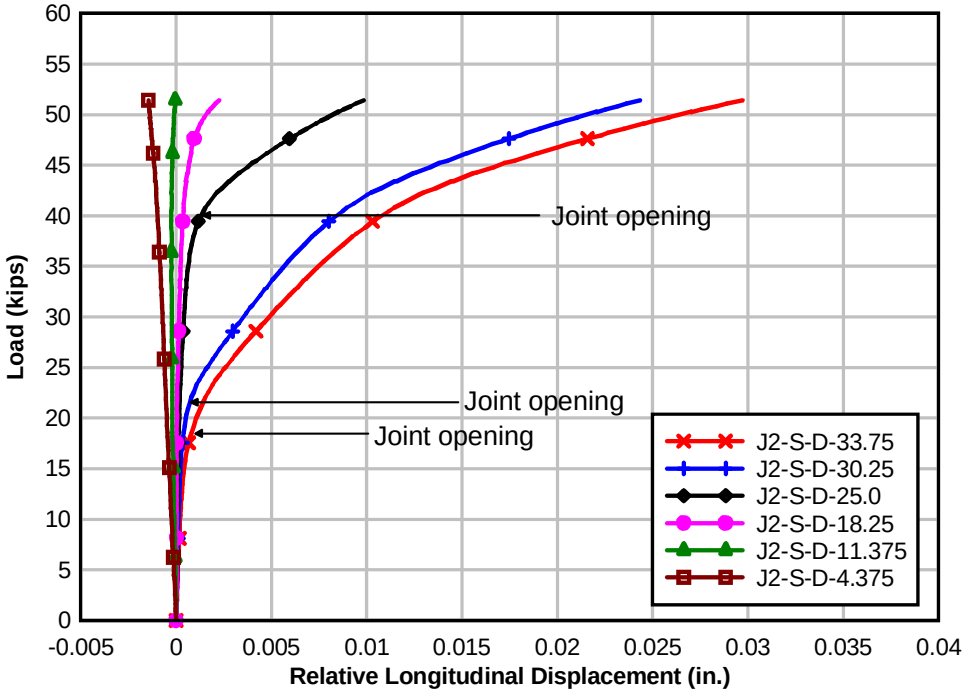

Figure 117 – Load vs. Joint opening (Side LVDTs)

Figure 118 shows data from LVDTs mounted across joint J2 on top of the flanges of segments 2 and 3. Unlike the ideal curve in Figure 116, the load vs. displacement curves in Figure 118 were essentially nonlinear from the beginning of load application. This was most likely caused by lack of contact between top flange concrete fibers at joint J2 (see Figure 109). Similar to the measured strain gauge data, the nonlinear form of the LVDT curves at higher loads was due to changes in stiffness of the contact area at joint J2 as it was opened. Opening of joint J2 at the flange top fibers was estimated from the curves in Figure 118 by locating the points at which the various curves initially deviated from one another.

Ideally, if the joint opened uniformly across the width of the flange, all three LVDTs would have indicated opening of the joint at the same load and would have had identical load vs. displacement curves. As discussed in the previous chapter, however, joint J2 initially opened on the South side before opening on the North side. This caused displacements recorded by the LVDT on the South flange, designated J2-TS-D-9.5, to be larger than displacements recorded by the LVDT at the center of the flange (J2-T-D), and the LVDT at the North flange (J2-TN-D-9.5).

LVDTs mounted across joint J2 on top of the flanges of segments 2 and 3, and the LVDTs designated J2-S-D-33.75 and J2-S-D-30.25 in Figure 117 showed two distinct linear regions after the joint initially opened. In the first linear region of the curves, which occurred after the joint initially opened at the location of each LVDT, the centroid of the concrete contact area was between the top and bottom post-tensioning bars. Thus, tensile stresses due to the applied moment were resisted by the post-tensioning bars and existing compressive stresses at the joint. In the second linear region, which began at a load of about 40 kips, the centroid of the concrete contact area was below the bottom post-tensioning bars (see Figure 112). Tensile stresses due to the applied moment were therefore effectively resisted by the post-tensioning bars with little contribution from existing concrete compressive stresses, leading to a significant change in slope (from the first linear region).

Due to nonlinearities in the load vs. displacement curves for LVDTs mounted across joint J2, there was less confidence in determining joint-opening loads with these instruments compared to strain gauges located close to the joint. LVDT data were, however, useful in checking joint-opening loads determined from strain gauge data.

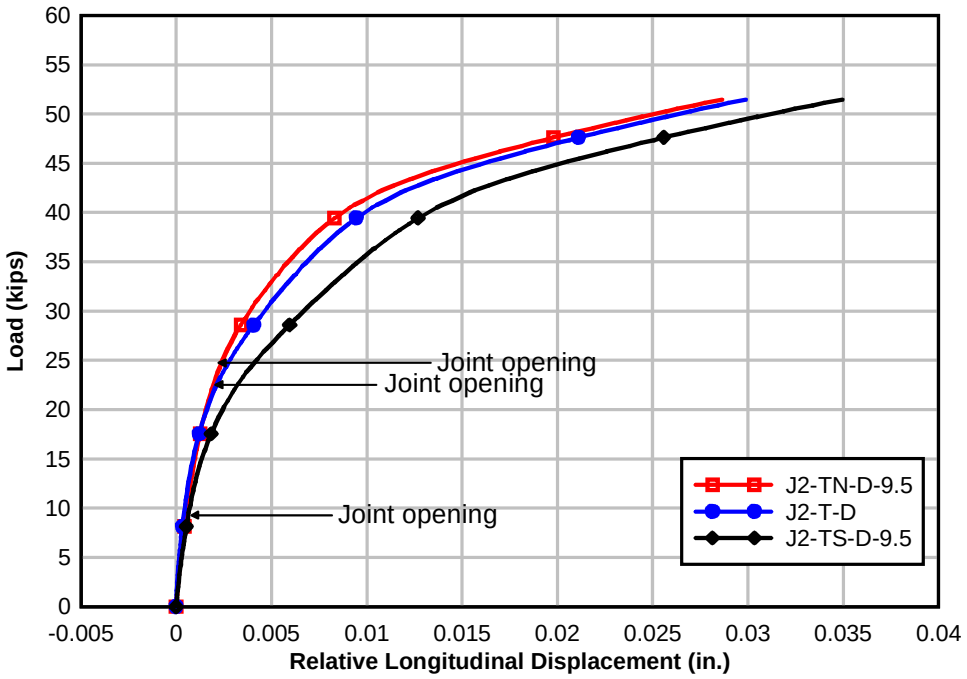

Figure 118 – Load vs. Joint opening (Top flange LVDTs)

12.3 STRAINS AT MID-SEGMENT

During tests in which data were collected from strain gauges at the middle of segments 2 and 3, loads applied to the beam did not exceed 40 kips. This was because strain data from the middle of the segments were not needed for joint-opening analysis.

Strain distributions at the middle of Segment 3 on the North and South sides of the beam are shown in Figure 119 and Figure 120, respectively. Data obtained from gauges at the middle of Segment 2 (see Appendix D) were nearly identical to the Segment 3 data and are therefore not shown here.

Opening of the joint at the beam midspan (at joint J2) did not affect the location of the neutral axis at the middle of the segments, which remained at elevation 21.3 in. However, the non-uniform opening of joint J2 across the width of the section at the joint affected the distribution of strains at mid-segment. Lesser magnitude strains were detected in the North flange than the South flange, and higher strains were detected in the North web than the South web. This was indicative of biaxial bending as illustrated in Figure 121. The horizontal component of the moment at mid-segment equilibrated the moment due to the applied load at the cantilevered end of the beam. The vertical component of the moment at mid-segment, which was the result of the net out-of-plane horizontal eccentricity in prestressing and the changes in prestress shown in Figure 114, formed a self-equilibrating system with the concrete.

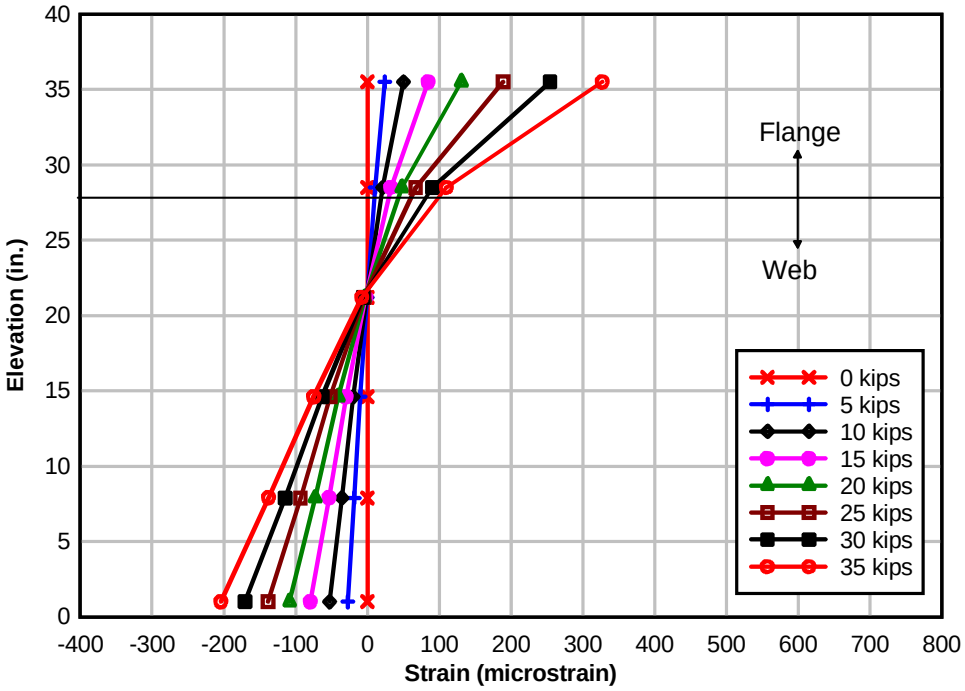

Figure 119 – Measured strain distributions at middle of Segment 3 (30 in. from joint J2) on North side of beam

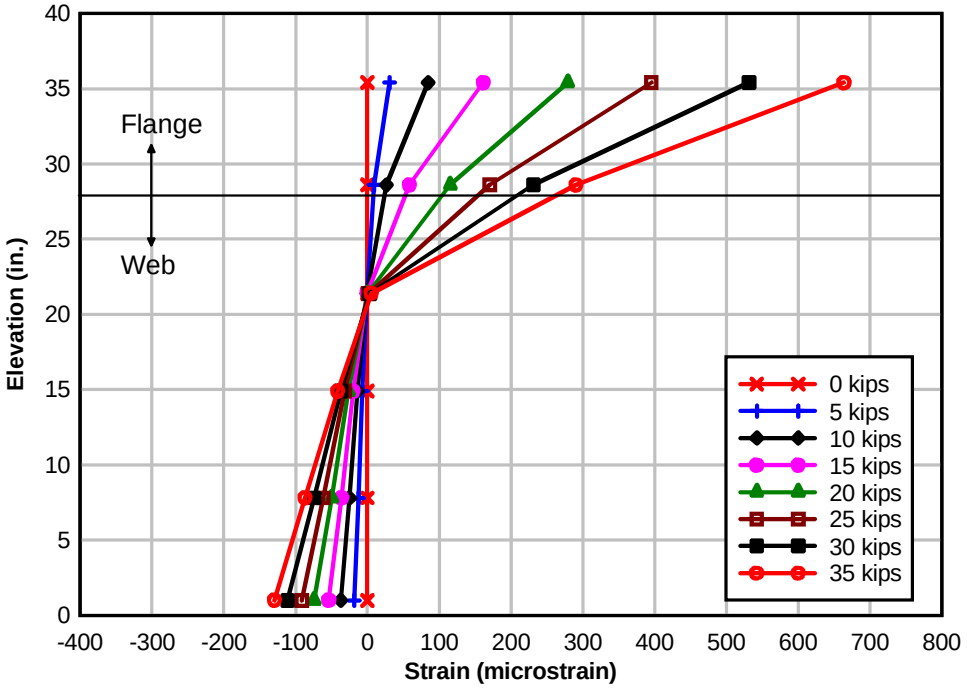

Figure 120 – Measured strain distributions at middle of Segment 3 (30 in. from joint J2) on South side of beam

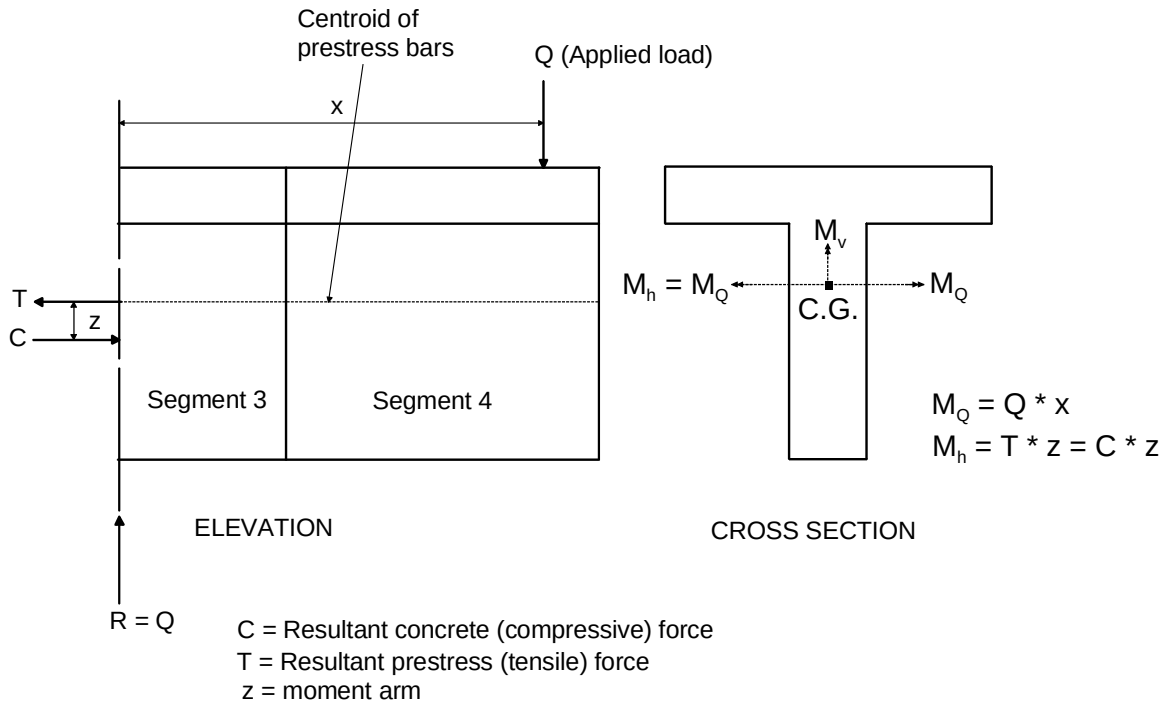

Figure 121 – Forces and moments acting at mid-segment

12.4 DEFLECTION

Vertical deflection of the beam during application of load (Figure 61), measured at a location 7.25 in. from the cantilevered end, is shown in Figure 122. The initial nonlinear part of the deflection curve was attributed to a slight deflection at the end-support of the beam as it was initially loaded. Movement of the neutral axis at the midspan of the beam, as the joint opened, was expected to affect the vertical deflection of the beam. This is indicated by the deviation of the straight line drawn through the deflection curve from the nonlinear parts of the curve. The initial deviation of the straight line from the deflection curve occurred at a load of about 9 kips, the load at which the centroid of the contact area at joint J2 initially began to move downward. After this point the deflection curve was almost linear with load until the depth of joint opening was sufficient enough to cause the centroid of the contact area to move below the bottom prestress bars (bars 3 and 4 in Figure 114) at a load of about 41 kips. Though the section stiffness at joint J2 continuously changed in the linear part of the deflection curve, the change in stiffness was local to the joint and did not affect the overall stiffness of the beam, and therefore the cantilever tip deflection.

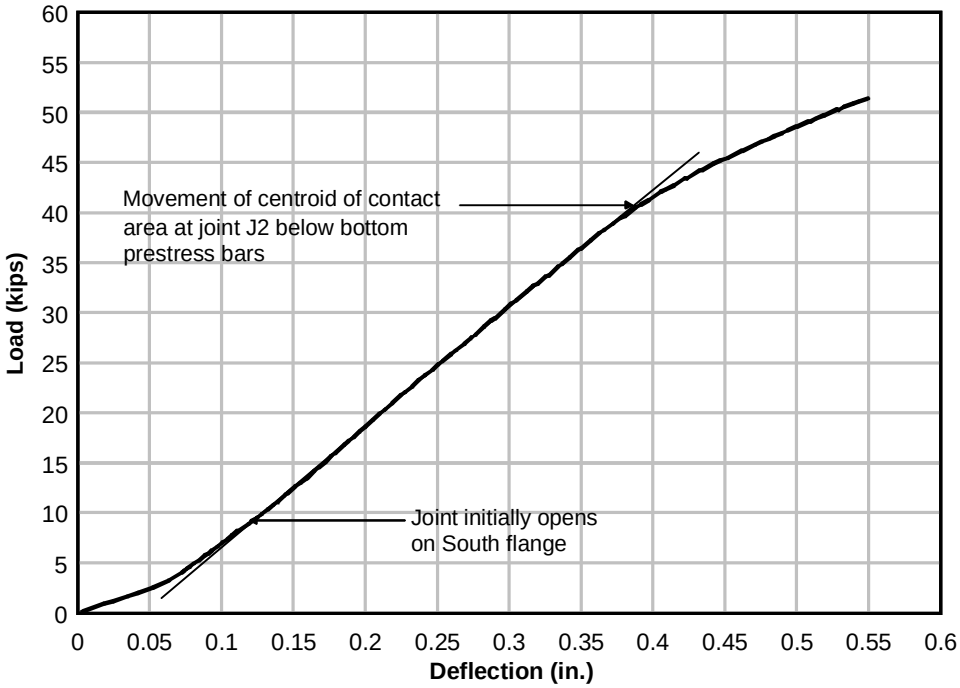

Figure 122 – Measured vertical deflection close to cantilevered end of beam

12.5 SUMMARY

Results from mechanical load tests on the laboratory beam indicated elastic behavior of the beam. The tests were also repeatable (i.e. neglecting small changes of prestress that occurred with time, the response of the beam under the action of mechanical loads was repeatable across tests). The distinct change in strain with load at incipient opening of the joint at midspan (joint J2) resulted in the use of strain gauges near the joint as instruments for detecting joint-opening loads. The contact area at joint J2 could also be estimated using joint-opening loads and elevations of strain gauges near the joint. The relative magnitude of joint-opening loads at identical elevations on the North side and South side of joint J2 together with the shape of

contact areas at the joint showed that the beam underwent biaxial bending when mechanically loaded. Measured strain distributions through the height of contact areas at joint J2 showed that strain was a linear function of curvature.

These experimental observations made it possible for normal stresses at incipient opening of joint J2 to be determined without explicitly using material properties (e.g. elastic modulus and coefficient of thermal expansion) of segments 2 and 3.

13 RESULTS – UNIFORM TEMPERATURE CHANGE

A uniform temperature change was imposed on segments 2 and 3 of the laboratory beam (Figure 123) to investigate thermal behavior in the absence of self-equilibrating thermally induced stresses. The goal was to determine the maximum change in prestress that would result from application of thermal loads on the concrete segments while the DYWIDAG post-tensioning bars remained essentially at laboratory temperature. Though the beam was statically determinate with respect to the supports, expansion of the concrete segments relative to the post-tensioning bars was expected to lead to an increase in prestress and the development of net compressive stresses in the concrete. Conversely, contraction (due to cooling) of the concrete segments relative to the post-tensioning bars was expected to lead to a reduction in prestress and the development of net tensile stresses (i.e. a reduction in compressive stresses) in the concrete. Understanding how such changes in prestress affected concrete stresses was important in estimating the effects, if any, of thermally induced changes in prestress on self-equilibrating thermal stresses when the AASHTO nonlinear thermal gradients were later imposed on the beam.

The test sequence started with the circulation of tap water through segments 2 and 3 for about 24 hours to establish a uniform reference temperature of about 84 ^{o}F (low reference temperature). Segments 2 and 3 were then heated to an average temperature of about +41 ^{o}F above the low reference temperature using the piping configuration shown in Figure 72. Forces in the post-tensioning bars and concrete strains at joint J2 were continuously recorded during this period, which will subsequently be referred to as the "heating phase". Following the heating phase, the temperature of the concrete segments was taken as the new reference temperature (high reference). With the data acquisition system still running, the segments were cooled from the high reference temperature back to the initial (low) reference temperature using the piping configuration shown in Figure 71. This phase of the test will subsequently be referred to as the "cooling phase". Laboratory imposed temperature changes in the heating and cooling phases of the test are shown together with target temperature changes for Segment 2 and Segment 3 in Figure 124 and Figure 125, respectively. Measured concrete temperatures in Segment 2 and Segment 3 are shown in Figure 126 and Figure 127, respectively. Temperature changes in Figure 124 and Figure 125 are with respect to the low reference temperature (about 84 ^{o}F) for the heating phase and the high reference temperature (about 125 ^{o}F) for the cooling phase. The average (uniform) temperature increase during the heating phase of the test was about 40 ^{o}F and the average decrease in the cooling phase was about 38 ^{o}F. The difference between the average temperature changes in the heating and cooling phases was due to a slight increase in tap water temperature during the three day period over which the test was conducted. This slight increase caused segments 2 and 3 to be cooled to a temperature that was higher than the initial temperature from which they were heated.

Significant deviation from the target profile occurred at Section A (see Figure 124) and Section F (see Figure 125). These deviations were due to the fact that sections A and F were adjacent to the ambient segments (segments 1 and 4). These segments (1 and 4) acted as heat sinks because they remained essentially at laboratory temperature during application of the thermal profiles on the heated segments (Segments 2 and 3). Additionally, the bottom surfaces of segments 2 and 3 could not be adequately heated at sections C and D because these locations were close to the mid-support point and could not be adequately insulated with Styrofoam. This issue was resolved in later tests by using flexible fiberglass to insulate the mid-support area of

the beam. Temperature profiles were non uniform not only through the height of the segments but also across the width. The distribution of temperature change through the height and across the width of the beam at Section C and Section D during the heating phase are shown in Figure 128 and Figure 129, respectively. The color bar in each figure represents change in temperature (in ^{o}F) relative to the low reference temperature. These figures show that temperatures along the perimeter of each section were generally slightly lower than temperatures in the interior. This was more pronounced in the web, where the ratio of concrete area to copper tubes was only about a third of that in the flange. There were two main reasons for this. First, the segment heating system was designed to efficiently impose the AASHTO nonlinear gradients while keeping the number of copper tubes embedded in concrete to a minimum. Thus, there was a higher concentration of copper tubes in the flange (where the maximum temperature changes in the gradients occur) than in the web (where there was almost no change in temperature). Second, heating the two concrete segments uniformly, by approximately 40 ^{o}F, was the most thermally demanding situation imposed on the heating system, due to the total volume of concrete and temperature increase involved.

Average measured temperature changes in the heated segments were used together with the average measured coefficients of thermal expansion (CTE) in Table 15, elastic moduli (MOE) in Table 16, and DYWIDAG bar properties to predict anticipated changes in prestress. Concrete elastic moduli in Table 16 were obtained by linearly interpolating between MOEs which were derived from cylinder test data between test ages of 28 and 360 days. Moments caused by the vertical and horizontal eccentricities of the prestress bars and slight curvatures caused by non-uniformity of the imposed temperature profiles were neglected in the prediction of prestress change. It was also assumed that for the duration of the test, the prestress bars and ambient concrete segments did not undergo any changes in temperature. Predicted and measured changes in prestress during the heating and cooling phases of the test are compared in Table 17 and Table 18, respectively. Measured total changes in prestress were within 11% of corresponding calculated values. Calculated changes were of higher magnitude than measured changes mainly because the ambient segments and prestress bars were subjected to a slight temperature increase due to an increase in laboratory temperature during the course of the test. It was expected that the steel prestress bars would respond to such non-stress-inducing temperature changes more rapidly than the ambient segments because of the relatively high thermal conductivity of steel and the small volume of steel compared with concrete (about 1%). Measured total changes in prestress even under this worst case thermal loading condition were less than 6% of the initial total prestress.

Table 15 – Average measured coefficients of thermal expansion (CTE) of concrete segments

Segment	Average CTE
1	N/A
2	7.7E-6/^{o}F
3	8.0E-6/^{o}F
4	N/A

Table 16 – Calculated modulus of elasticity (MOE) of concrete segments

Segment	Age (days)	MOE (ksi)
1	268	5231
2	219	4696
3	206	4695
4	257	5101

Table 17 – Changes in prestress due to heating of Segments 2 and 3

Bar Designation	Measured Initial Prestress (kips)	Increase in Measured Prestress (kips)	Percentage Increase in Measured Prestress (%)	Calculated Increase in Prestress (kips)	Difference b/n Measured and Calculated Increase in Prestress (%)
P1	94.6	5.6	5.9	5.9	-5.1
P2	87.7	5.2	5.9	5.9	-11.9
P3	90.8	4.5	5.0	5.9	-23.7
P4	89.6	5.8	6.5	5.9	-1.7
Total	362.7	21.1	5.8	23.6	-10.6

Table 18 – Changes in prestress due to cooling of Segments 2 and 3

Bar Designation	Measured Initial Prestress (kips)	Decrease in Measured Prestress (kips)	Percentage Decrease in Measured Prestress (%)	Calculated Decrease in Prestress (kips)	Difference b/n Measured and Calculated Increase in Prestress (%)
P1	100.2	-5.5	-5.5	-5.6	-1.8
P2	93.0	-5.2	-5.6	-5.6	-7.1
P3	95.3	-4.1	-4.3	-5.6	-26.8
P4	95.4	-5.3	-5.6	-5.6	-5.4
Total	384.0	-20.0	-5.2	-22.4	-10.7

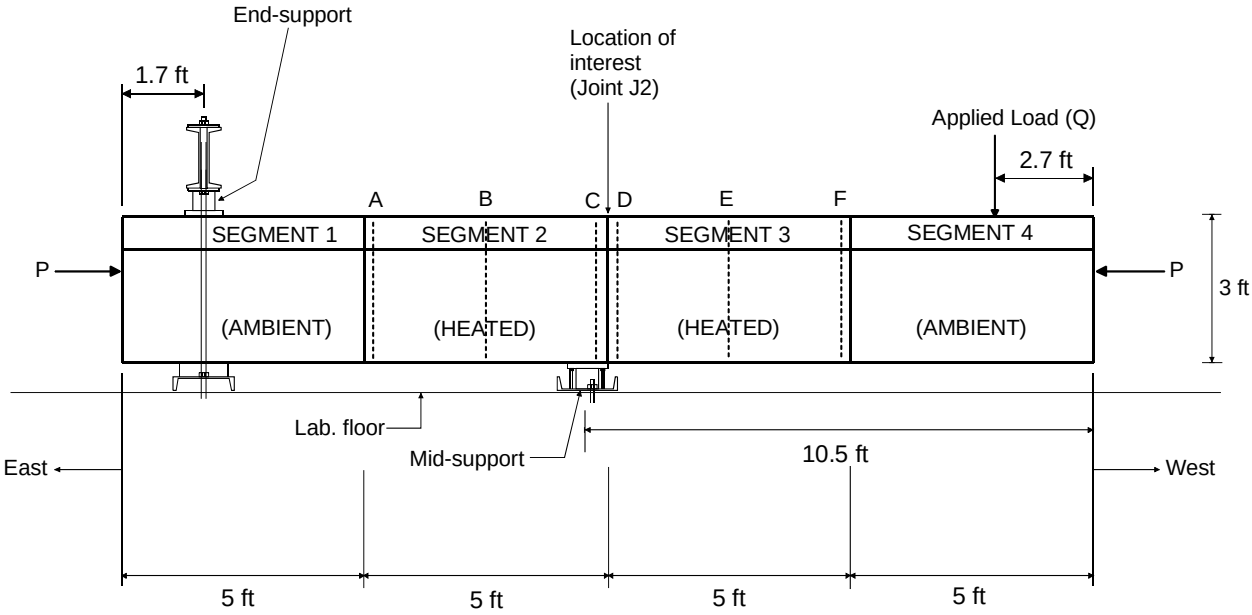

Figure 123 – Laboratory beam

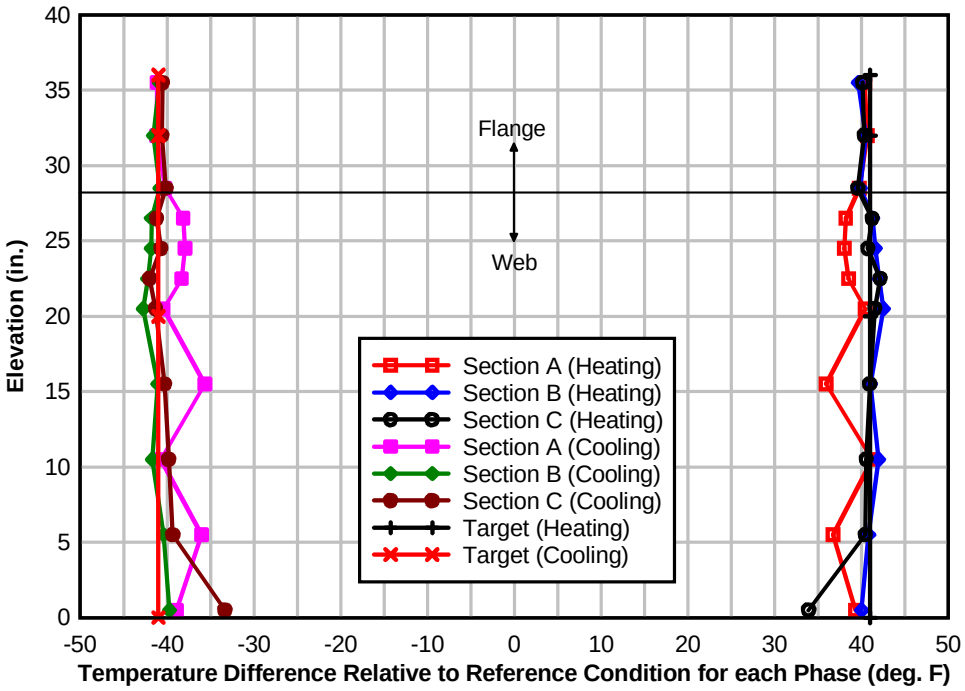

Figure 124 – Laboratory imposed temperature changes on Segment 2

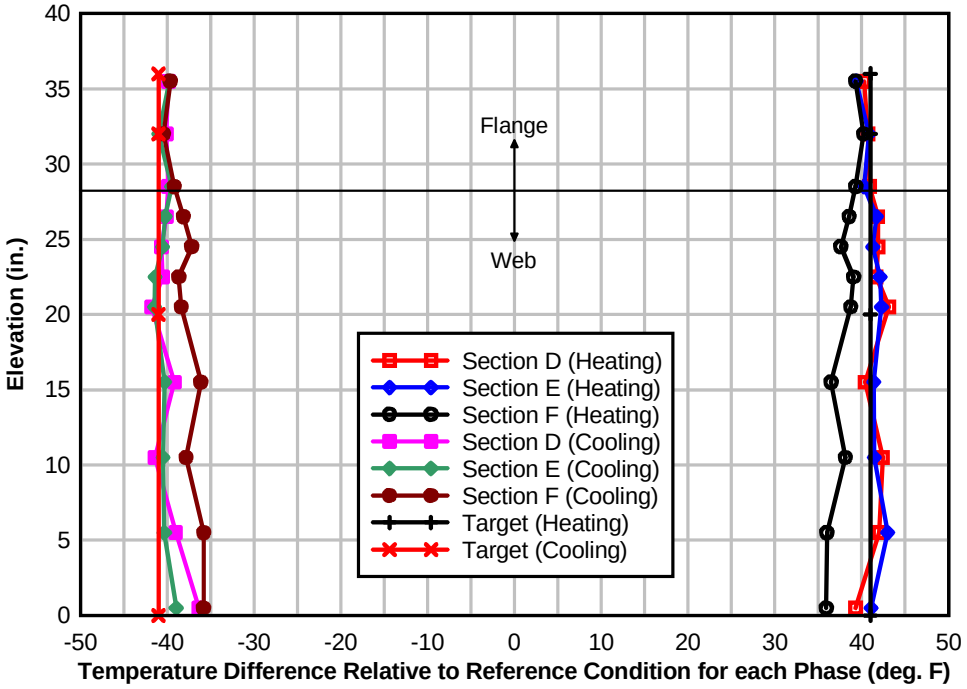

Figure 125 – Laboratory imposed temperature changes on Segment 3

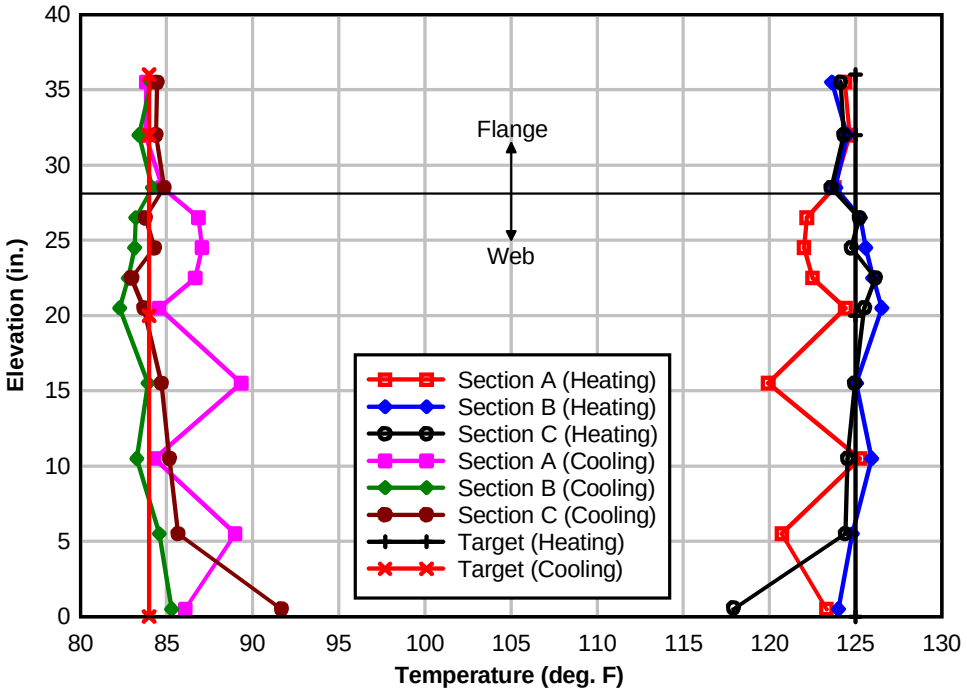

Figure 126 – Measured concrete temperatures in Segment 2

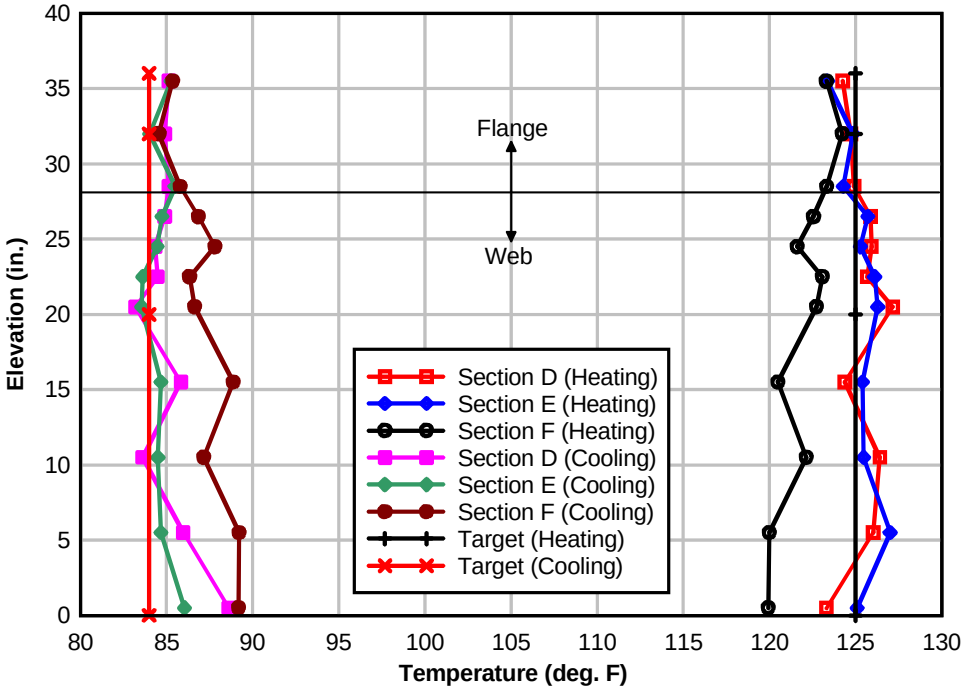

Figure 127 – Measured concrete temperatures in Segment 3

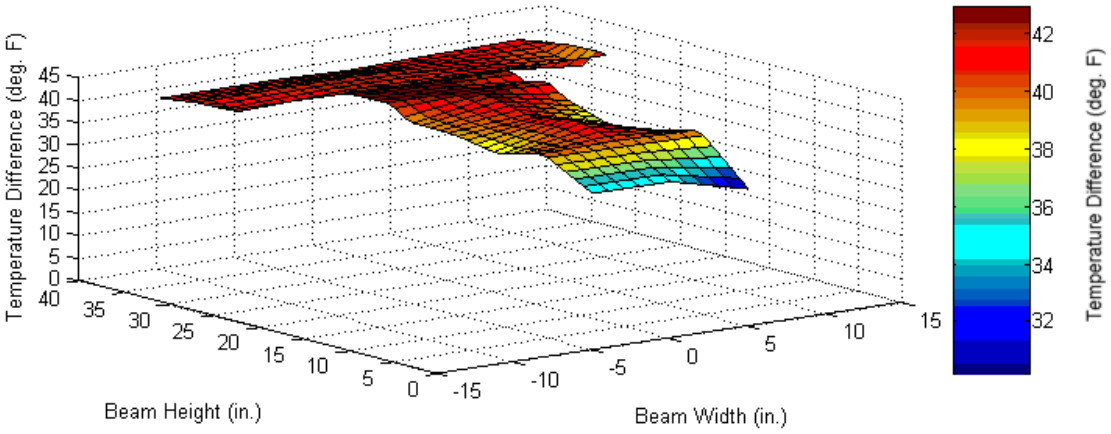

Figure 128 – Measured temperature changes at Section C (Heating phase)

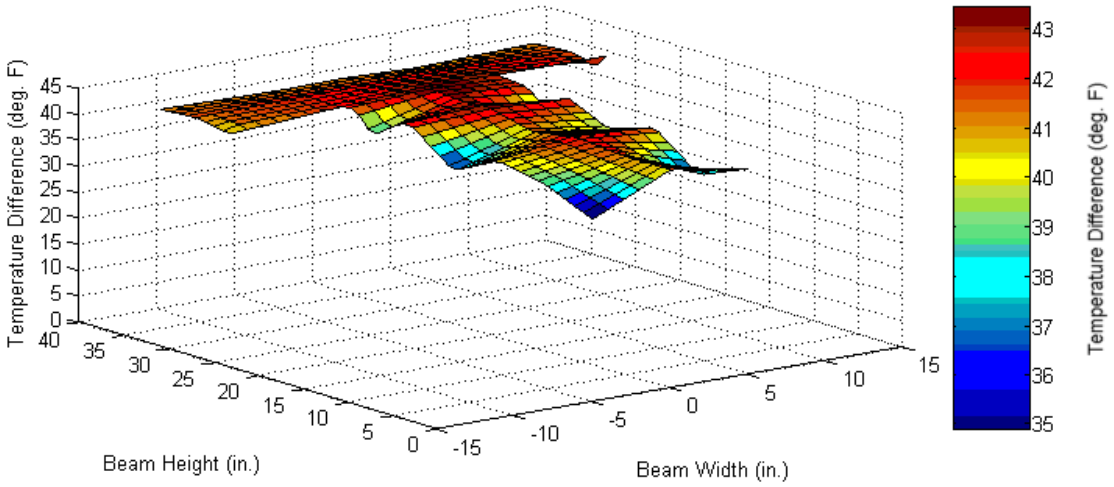

Figure 129 – Measured temperature changes at Section D (Heating phase)

Measured concrete strains near joint J2 from strain gauges located on segments 2 and 3 during the heating and cooling phases of the test are shown in Figure 130 and Figure 131, respectively. Expected (calculated) strain distributions are also shown in the figures for comparison. Calculated strains were determined using measured prestress forces and eccentricities, concrete section properties, and the elastic moduli shown in Table 16. Concrete strains measured during the heating phase were essentially a mirror image of concrete strains measured during the cooling phase. This showed that strains induced in the heated segments when the beam was heated were relieved when the beam was cooled; evidence that the beam remained elastic under the action of the thermal loads. Because the strain gauges installed on the concrete segments were self-temperature-compensating (STC) gauges, it was expected that the measured strains (assuming uniformity of temperature distributions) would arise solely from changes in prestress, and therefore would be compressive during heating and tensile during cooling. It is, however, evident from Figure 130 and Figure 131 that the opposite was the case. Measured concrete strains during the heating phase were instead tensile. A similar reversal was observed during the cooling phase. Furthermore, the measured strains were non-uniform through the height of the segments. The observed reversals were attributed to the fact that the temperature profiles imposed on the segments were somewhat non-uniform over the cross sectional area of the segments (recall Figure 128 and Figure 129). Thus, while the total change in prestress was a result of the average (uniform) temperature change imposed on the heated segments, strains measured on the surfaces of the sections were affected by non-uniform temperature changes. Concrete strains measured during the heating phase are compared with calculated strains which take into account both changes in prestress and the non-uniformity in temperature distributions in Figure 132 and Figure 133. The calculated strains in were determined by superimposing strains caused by the increase in prestress and stress-inducing strains caused by the non-uniform temperature distributions shown in Figure 128 and Figure 129, respectively. Stress-inducing strains caused by the two-dimensional thermal gradients in the figures were calculated using Equation 8 through Equation 12 (see Section 3.2). Though the calculated strain magnitudes shown in Figure 132 and Figure 133 do not exactly match the measured strains they are consistent in sign (i.e. positive, tensile). A possible explanation for the difference in magnitude of measured and calculated strains is that precise measurements of

temperature at the surface of the concrete sections, where the strains were measured, were not available. Instead surface temperatures were obtained by extrapolating data from thermocouples nearest to, but not exactly at, the surface of the concrete. Hence the extrapolated surface temperatures may have been less than the actual surface temperatures.

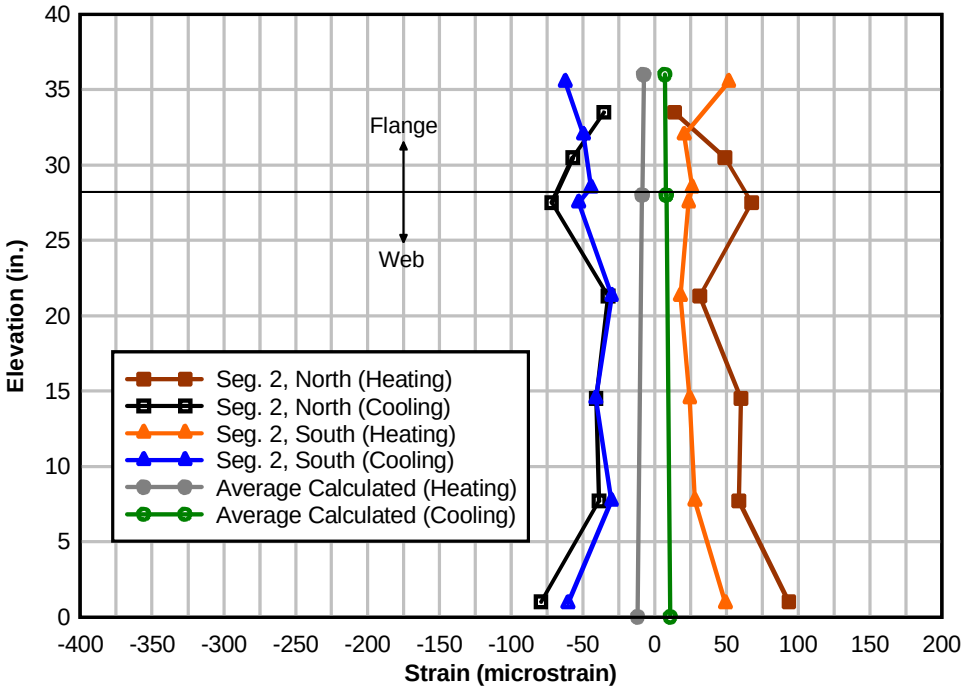

Figure 130 – Measured strain distribution on Segment 2 (Section C) due to temperature changes

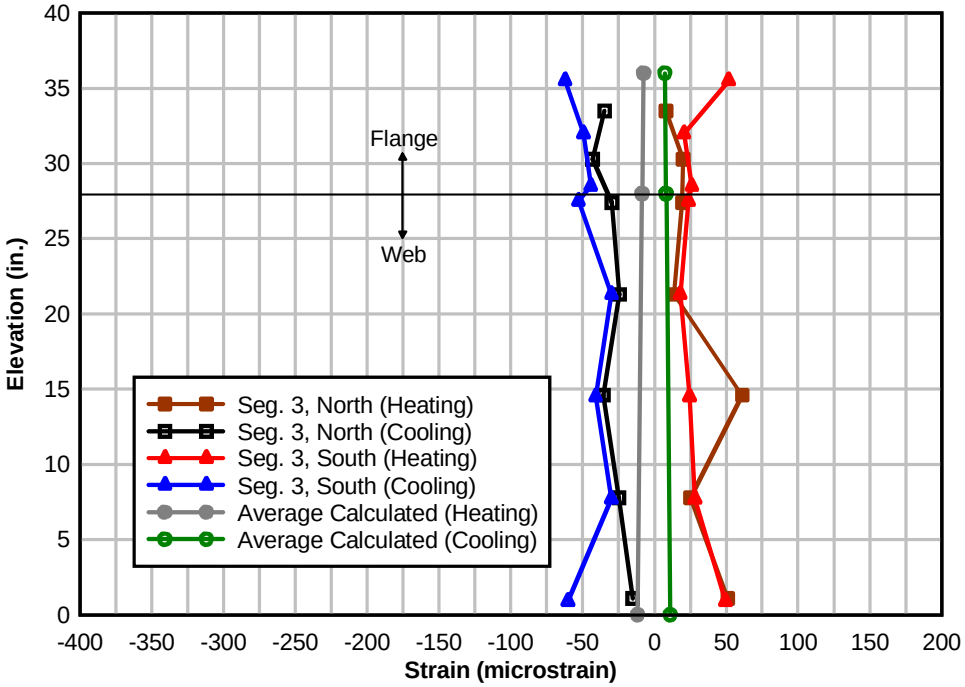

Figure 131 – Measured strain distribution on Segment 3 (Section D) due to temperature changes

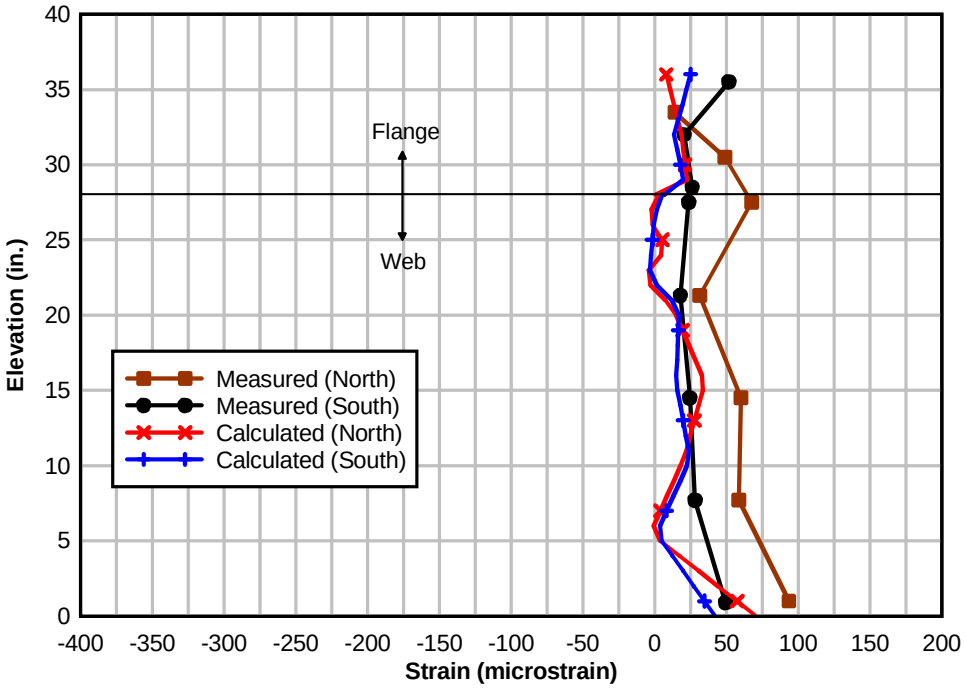

Figure 132 – Comparison of measured and calculated strains at Section C due to moderately nonuniform temperature distribution (Segment 2, Heating)

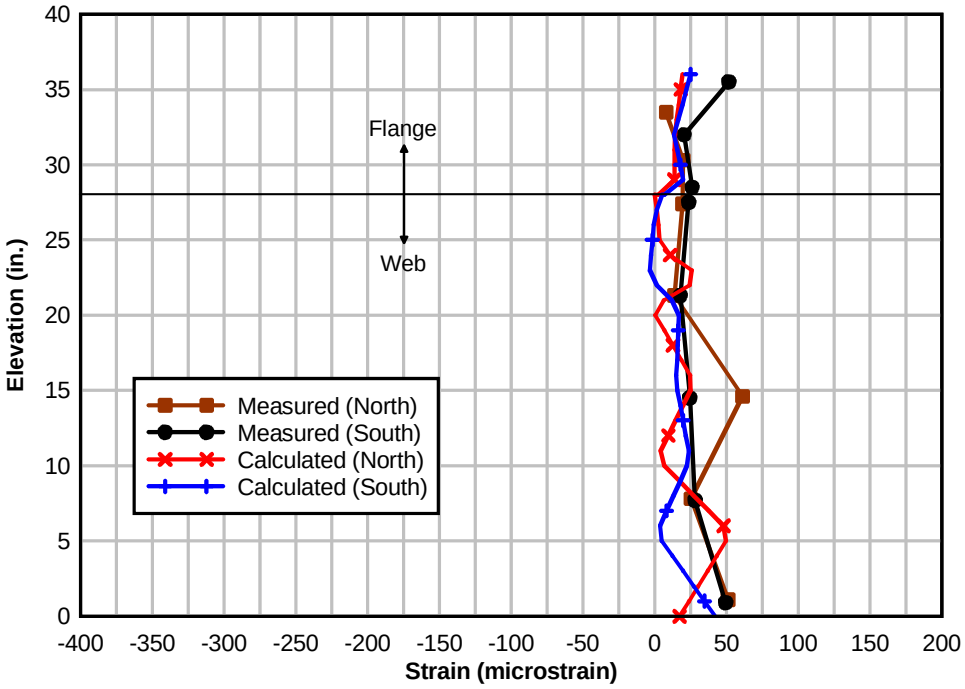

Figure 133 – Comparison of measured and calculated strains at Section D due to moderately nonuniform temperature distribution (Segment 3, Heating)

14 RESULTS – AASHTO POSITIVE THERMAL GRADIENT

Results from the application of mechanical loading in combination with the AASHTO positive thermal gradient are presented and discussed in this chapter. The objective of the mechanical-thermal load tests was to experimentally quantify the self-equilibrating thermal stresses caused by the AASHTO nonlinear positive thermal gradient in the top 4 in. of the combined flanges of segments 2 and 3. Two independent methods were used to quantify stresses. The first was to convert measured strains using the elastic modulus, which was determined from tests on cylinders made from the same concrete that was used to construct the beam. Stresses determined using this method will be referred to as elastic modulus derived stresses (E stresses). This is the method most often used to determine stresses, but may be subject to variation from local strain contributions in the concrete surrounding the strain gauge, size effect between cylinder and specimen, or creep and shrinkage. The second method was a more direct measure of stress using the known stress state at incipient joint opening. Stresses determined in this manner will be referred to as joint opening derived stresses (J stresses). In both methods concrete behavior was assumed to be linear elastic.

Figure 134 illustrates the test sequence that was used. Before mechanical or thermal loads were applied, the forces acting on the beam consisted of prestress and self-weight. The test sequence started with partial opening and closing of the joint at midspan (joint J2) with the beam at a constant reference temperature (about 80 ^{o}F). As indicated in the figure, strain data from this step were used to establish a reference stress state at joint J2. The AASHTO positive thermal gradient was then imposed on segments 2 and 3. After achieving and maintaining the steady state thermal gradient on the heated segments for 30 to 45 minutes, joint J2 was again partially opened and closed. Strains at this stage were used to determine the thermal stress state. The heated segments were then cooled to the original reference temperature at the start of the test, after which joint J2 was again partially opened and closed, completing the load cycle.

Joint-opening loads and contact areas at joint J2, as the joint was gradually opened, which were determined from data collected from steps 1 and 3 of the load sequence, were used to calculate self-equilibrating stresses caused by the nonlinear gradient (J stresses). Note that neither the elastic moduli nor the coefficients of thermal expansion of segments 2 and 3 were used in the calculation of the J stresses.

Elastic modulus derived thermal stresses calculated from measured thermal strains close to joint J2 (E stresses) and joint opening derived thermal stresses (J stresses) are presented and discussed in the following sections.

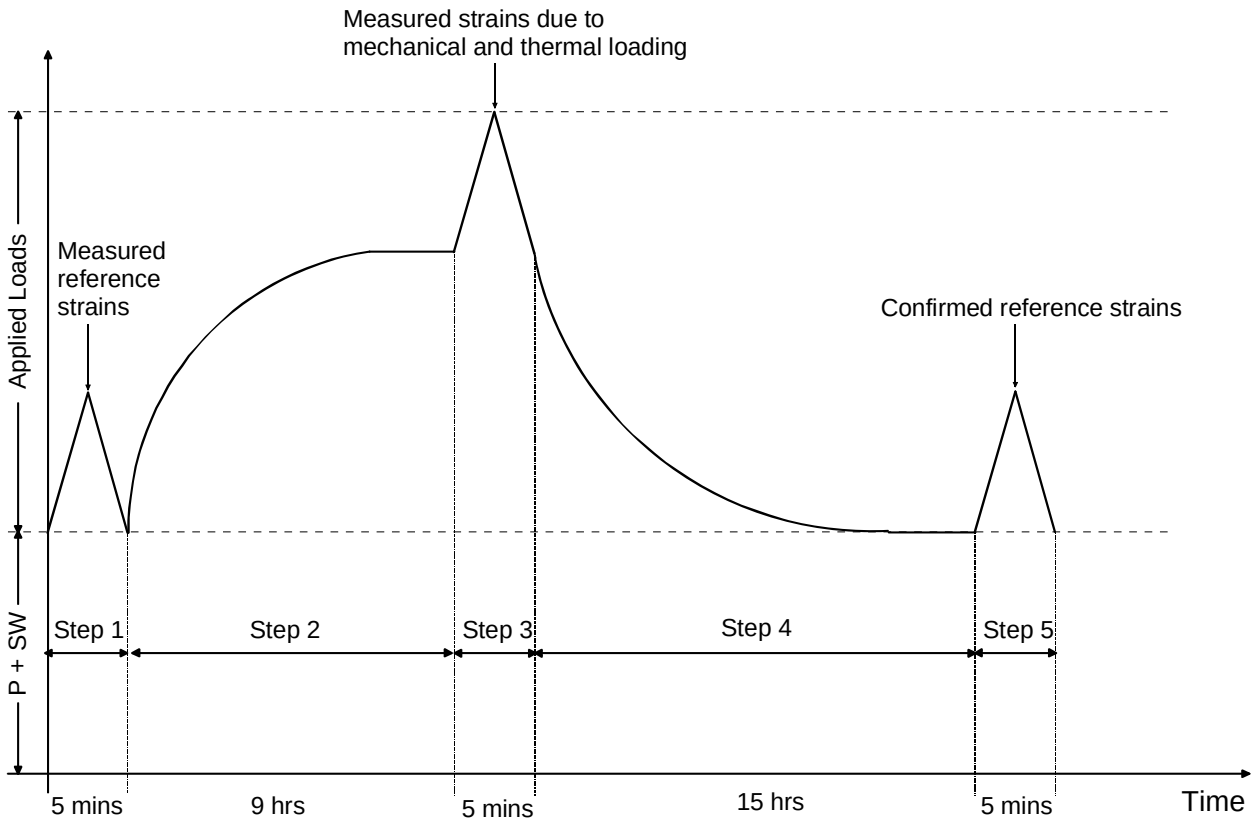

P + SW: Pretress + Self-weight

Applied Loads:

Step 1: Opening and closing of joint J2 (application and removal of mechanical loads)
Step 2: Positive thermal gradient (application of thermal load)
Step 3: Opening and closing of joint J2 (application and removal mechanical loads)
Step 4: Cooling to reference temperature at start of test (removal of thermal loads)
Step 5: Opening and closing of joint J2 (application and removal of mechanical loads)

Figure 134 – Sequence of load application (positive gradient test)

14.1 Elastic Modulus Derived Stresses (E Stresses)

The nonlinear positive thermal gradient imposed on the heated segments of the laboratory beam (see Figure 135) in Step 2 of the load sequence is shown in Figure 136. For comparison Figure 136 also shows the AASHTO design positive gradient. Though it did not exactly match the AASHTO gradient, the shape of the laboratory gradient was more representative of typical field measured gradients (see Figure 137). Measured temperatures in the heated segments after the positive thermal gradient was imposed are shown in Figure 138.

Temperature data for the laboratory-imposed thermal gradient profile was available up to an elevation of 35.5 in. (0.5 in. below the top surface of the flange): the elevation of the topmost thermocouples embedded in the heated segments. Thus the concrete temperature at the top surface of the flanges (at an elevation of 36 in.) was not measured. Because the segments were heated from the inside, rather than externally from solar radiation, it is likely that the top flange surface temperature was equal to or even slightly less than the measured temperature at 35.5 in.

For the purpose of calculating theoretical stresses and strains caused by the laboratory gradient, the magnitude of the thermal gradient at the top surface of the flange was obtained by extrapolating from measured thermal gradient magnitudes at elevations 32 in. and 35.5 in.

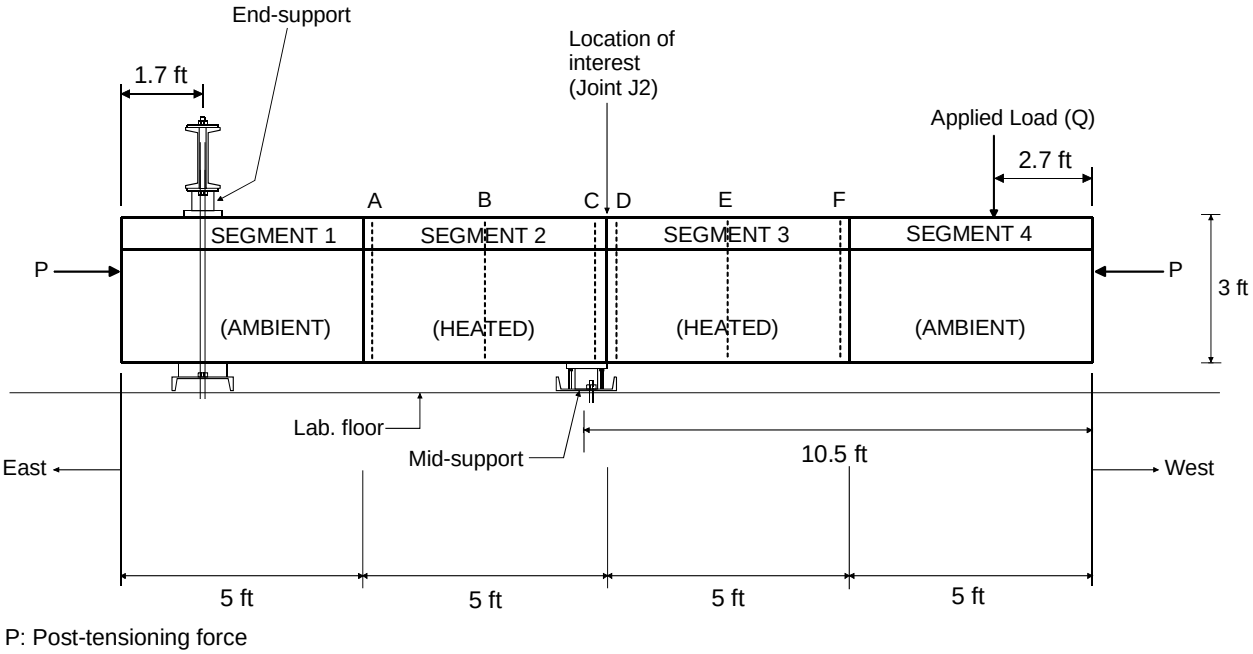

Figure 135 – Laboratory beam

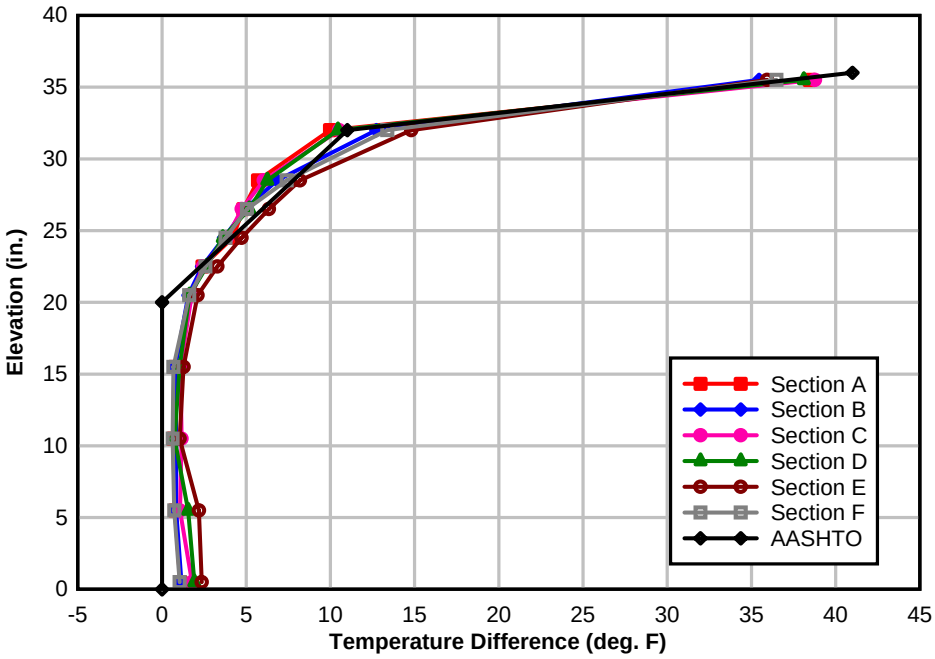

Figure 136 – Laboratory imposed positive thermal gradient

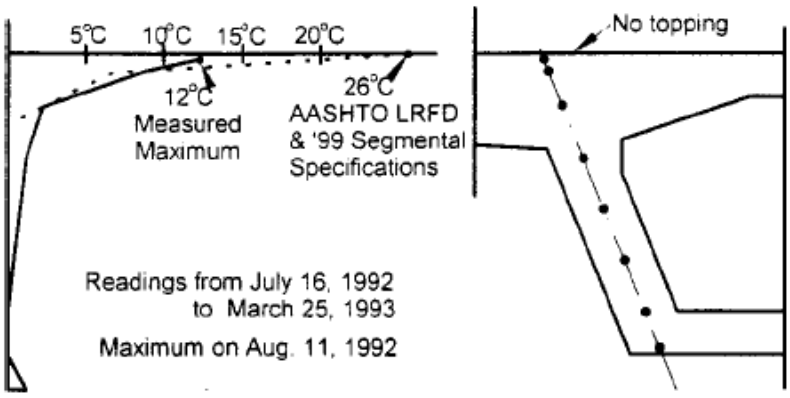

Figure 137 – Typical field measured positive thermal gradient (Roberts, C. L.; Breen J. E.; Cawrse, J. (2002))

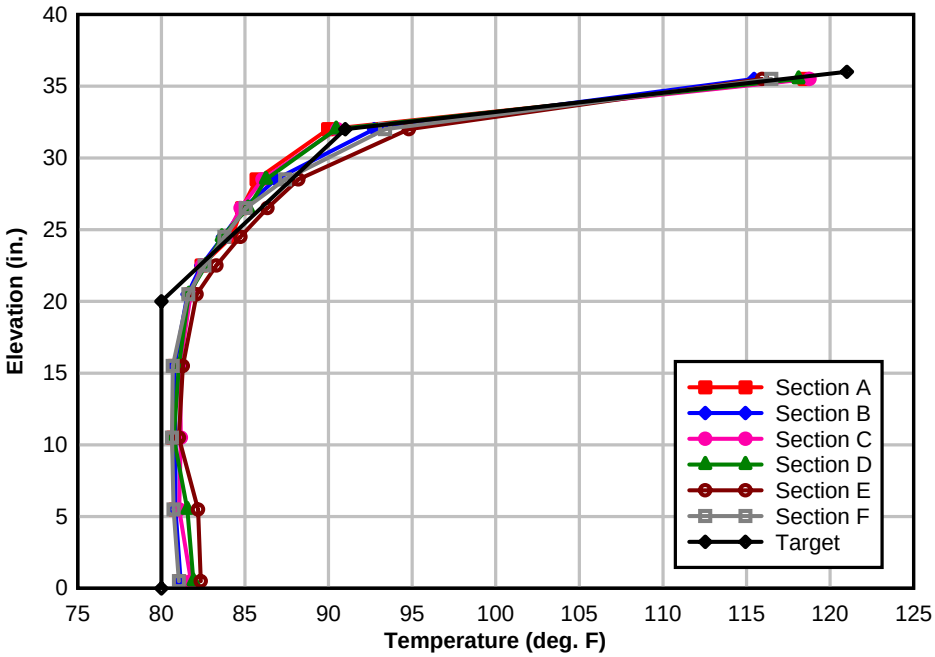

Figure 138 – Measured temperatures in heated segments (positive thermal gradient)

Figure 139 shows an ideal representation of the components of strains induced in the laboratory beam by the AASHTO design gradient. These strains were calculated according to the procedure outlined in the AASHTO (1989a) guide specifications and the coefficients of thermal expansion given in Table 15 (see Chapter 13) using the equation:

$$\varepsilon_T = \alpha \cdot \delta T(z) + \varepsilon_{SE} \qquad \text{Equation 20}$$

where the unrestrained thermal strain profile ($\alpha * \delta T(z)$) represents the strains that the section would undergo if the section were layered and the layers were free to deform

independently. The total strains (ε_T) are generated when compatibility between the layers is enforced. Assuming that plane sections remain plane under the action of flexural deformations, this strain distribution is linear. The total strain (ε_T) includes components caused by axial and flexural restraint, which were not present in the laboratory set-up. The self-equilibrating strains (ε_{SE}), which are the only strains measurable with temperature compensating strain gauges (see Section 3.2 for a complete discussion), make up the final component of the total strains.

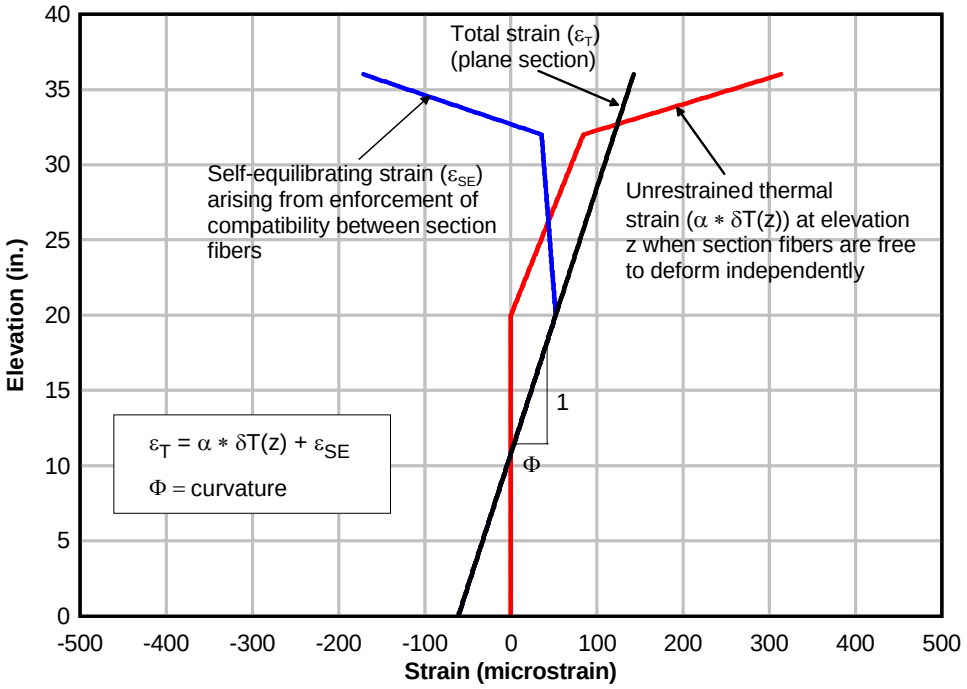

Figure 139 – Calculated strain components of the AASHTO positive thermal gradient

The change in strain between the beginning and end of Step 2 at joint J2 are plotted in Figure 140 through Figure 142. Figure 140 and Figure 141 show the strain differences along the height of segments 2 and 3, respectively. Figure 142 shows a plan view of the strain differences on the top flange near the same joint. Also shown in the figures are two sets of strain changes predicted using the AASHTO design procedure: one using the AASHTO design thermal gradient, and the other using the laboratory-imposed thermal gradient. Because the strain gauges were self-temperature compensating (STC) gauges, and because there was no axial or flexural restraint on the beam, the measured strains consisted only of the self-equilibrating component of the total strains. The average laboratory-imposed thermal gradient profile (average of profiles at Section A through Section F (see Figure 136)) was used in calculating the 'laboratory gradient' strains in Figure 140 through Figure 142.

No marked difference is apparent between measured and predicted strains below approximately 20 in. elevation. Compressive strains were present in the bottom of the section up to about 10 in. elevation. Tensile strains arose in the section mid-height from about 10 in. to 32 in. elevation. A maximum predicted tensile strain (due to the laboratory gradient) of about 52 με was predicted at elevation 28 in., whereas a maximum measured tensile strain of about 65 με occurred at elevation of 27.5 in. The maximum predicted tensile strain due to the AASHTO design gradient, of magnitude about 53 με, occurred at an elevation of 20 in.

The difference between locations of maximum predicted tensile strains due to the imposed laboratory gradient and the AASHTO design gradient was due to the difference in the shape of the laboratory and the AASHTO design thermal gradients. In each case maximum tensile strain occurred at the location where the change in slope (in units of ^{o}F/in.) of the thermal gradient profile was algebraically at a maximum. This occurred between elevations of 27.5 in. and 28.5 in. for the laboratory gradient and at an elevation of 20 in. for the AASHTO design gradient. Compressive strains also occurred above the mid-thickness of the flange with a gradient steeper than that of the remainder of the profile.

Some additional differences between the measured and predicted strains are also notable. Measured compressive strains were significantly smaller in magnitude than predicted at the top of the section in both segments (see Figure 142). This was also the case during prestressing (see Chapter 11) and mechanical load tests (see Chapter 12). One explanation for the lower measured compressive strains at the top of the section is the shape of the thermal gradient in the top 4 in. of the flange. The placement of copper tubes in the flange allowed for a linear gradient between elevations of 32 in. and 35.5 in. The shape and magnitude of the thermal gradient in the top 0.5 in. of the flange was, however, not known. To predict top fiber strains, the magnitude of the thermal gradient in the top 0.5 in. of the flange was obtained by extrapolating from the linear thermal gradient between elevations 32 in. and 35.5 in.

Another possibility is that differential shrinkage on top of the flange at joint J2 contributed to the lower measured strains. Between elevations of 32 in. and 35.5 in., the measured compressive strains more or less followed a linear distribution as did the predicted strains. The measured strains were, however, generally larger than predicted strains between elevations 32 in. and 34 in. and smaller than predicted strains above 34 in. This was attributed to variations between the measured thermal gradient profiles at sections A through F, and the average of these thermal gradient profiles Figure 143, which was used to predict strains per the AASHTO design procedure.

The uniform and linear sub-components of the overall nonlinear thermal gradient were expected to lead to additional stresses in the concrete as segments 2 and 3 were heated during Step 2. Expansion of the segments relative to the prestressing caused a net increase in prestressing force. However, the measured peak increase was only 0.4% of the initial prestress and was therefore considered negligible.

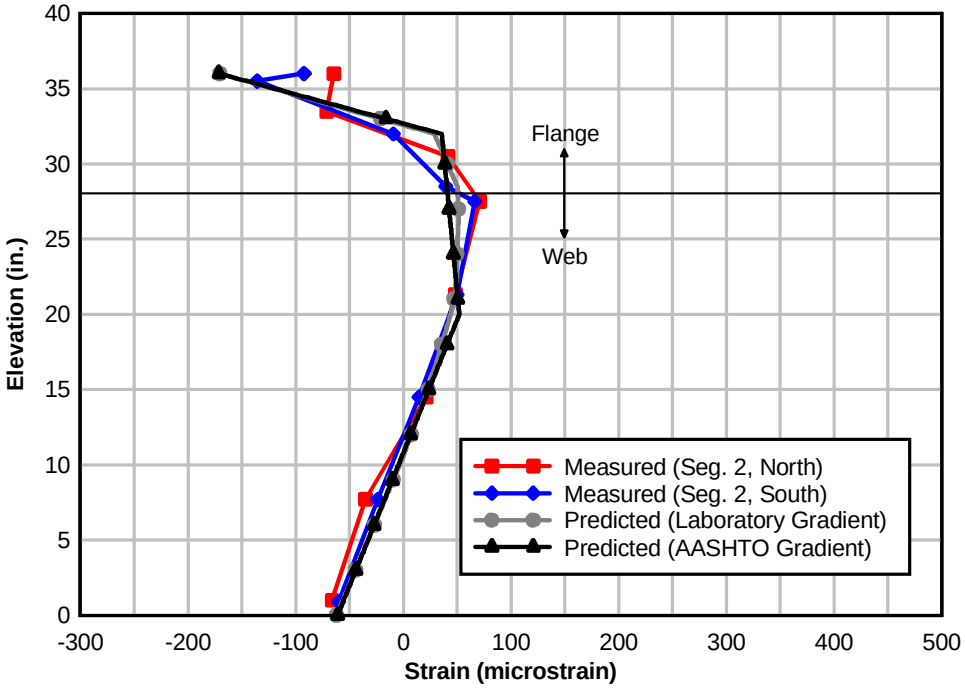

Figure 140 – Measured and predicted strains near joint J2 (Segment 2)

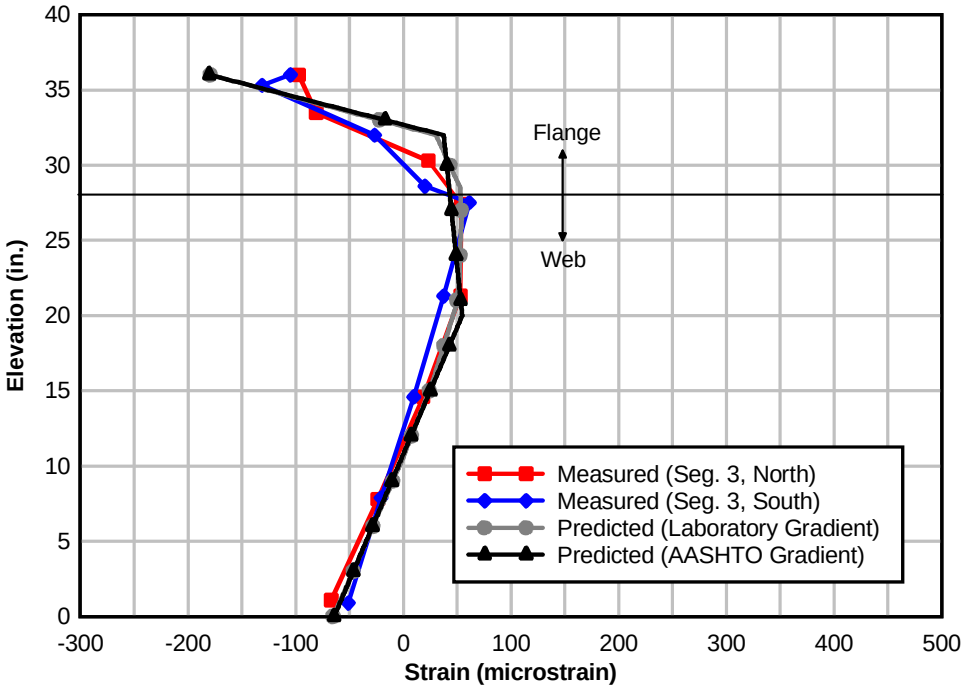

Figure 141 – Measured and predicted strains near joint J2 (Segment 3)

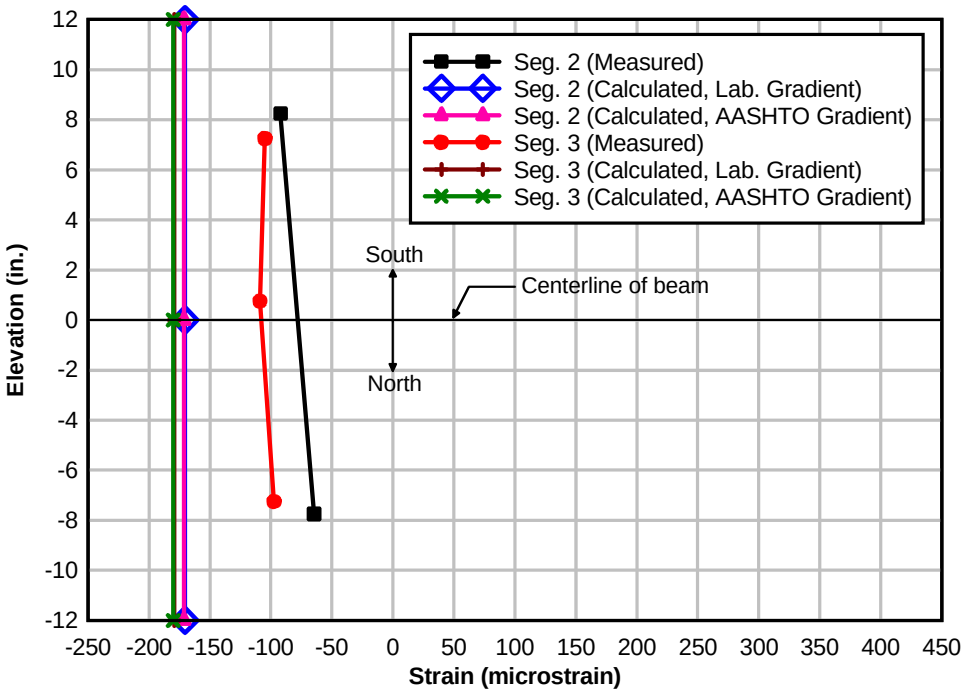

Figure 142 – Plan view of measured and predicted strains near joint J2 (Top Flange)

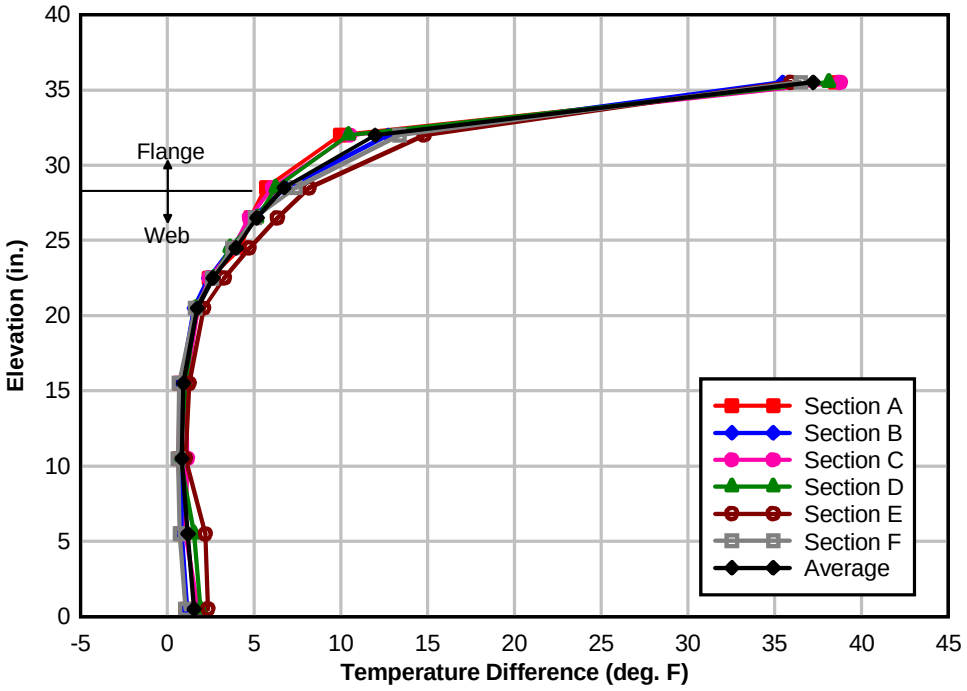

Figure 143 – Comparison of measured thermal gradient profiles with average profile

Elastic modulus derived stresses (E stresses) were the self-equilibrating thermal stresses caused by the positive thermal gradient, and were determined by multiplying the measured strains in Figure 140 and Figure 141 by the elastic moduli of Segment 2 (4760 ksi) and Segment 3 (4760 ksi), respectively. The elastic moduli were calculated by linearly interpolating

cylinder modulus of elasticity data between test ages of 28 and 360 days. At the time of the test, the ages of segments 2 and 3 were 232 and 219 days, respectively.

Figure 144 and Figure 145 show E stress distributions near joint J2 on Segment 2 and Segment 3, respectively. For comparison, self-equilibrating thermal stresses were also calculated using the AASHTO recommended procedure discussed in Section 3.2, the laboratory thermal gradient, and the AASHTO design gradient were calculated.

Table 19 compares E stresses computed at the top of the flanges of segments 2 and 3 with similar stresses obtained by extrapolating from the linear E stress distributions between elevations 32 in. and 35.5 in. (see Figure 144 and Figure 145) on the sides of the segment flanges. E stresses in the extreme top flange fibers were significantly lower than stresses extrapolated to the same location. This condition follows from the relatively smaller stress-inducing thermal strains that were measured at the top surfaces of the flanges (see Figure 142). As discussed previously, the smaller strains were attributed to differential shrinkage at joint J2 and to a lower thermal gradient magnitude than was targeted for the top of the flanges of the segments. At an elevation of 32 in., E stresses in segments 2 and 3 (see Figure 144 and Figure 145) were compressive whereas predicted stresses were tensile. This was attributed to the difference in magnitude of the laboratory thermal gradients at sections A through F (from the average thermal gradient used in predicting stresses) at that elevation; the location of the maximum slope change in the thermal gradients (see Figure 146).

E stresses and predicted stresses caused by the laboratory-imposed thermal gradient in the top 4 in. of the flanges of segments 2 and 3 are compared in Table 20. Predicted stresses in the extreme top flange fibers (where the maximum compressive stresses were expected to occur had the gradient been linear in the top 4 in. of the flanges) are not shown in the table because the shape and magnitude of the thermal gradient at that location were not measured. E stresses 0.5 in. below the top flange (maximum E stresses) were approximately 3% and 8% less than corresponding predicted stresses in Segment 2 and Segment 3, respectively. Taking into consideration the possible effects of differential shrinkage at joint J2, these differences were considered to be within the limits of experimental error.

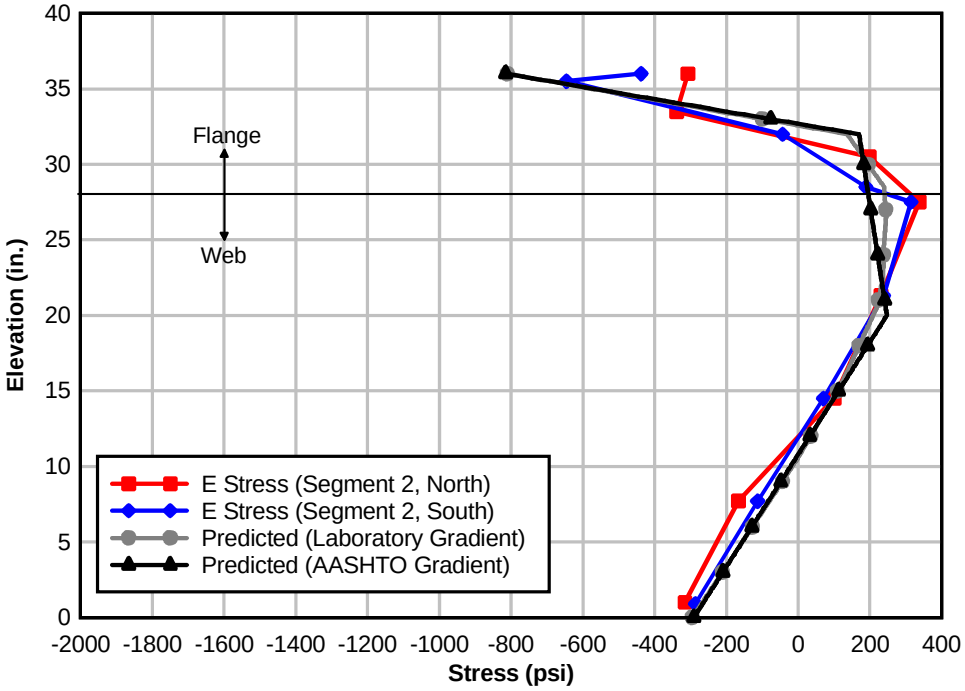

Figure 144 – E stresses near joint J2 (Segment 2)

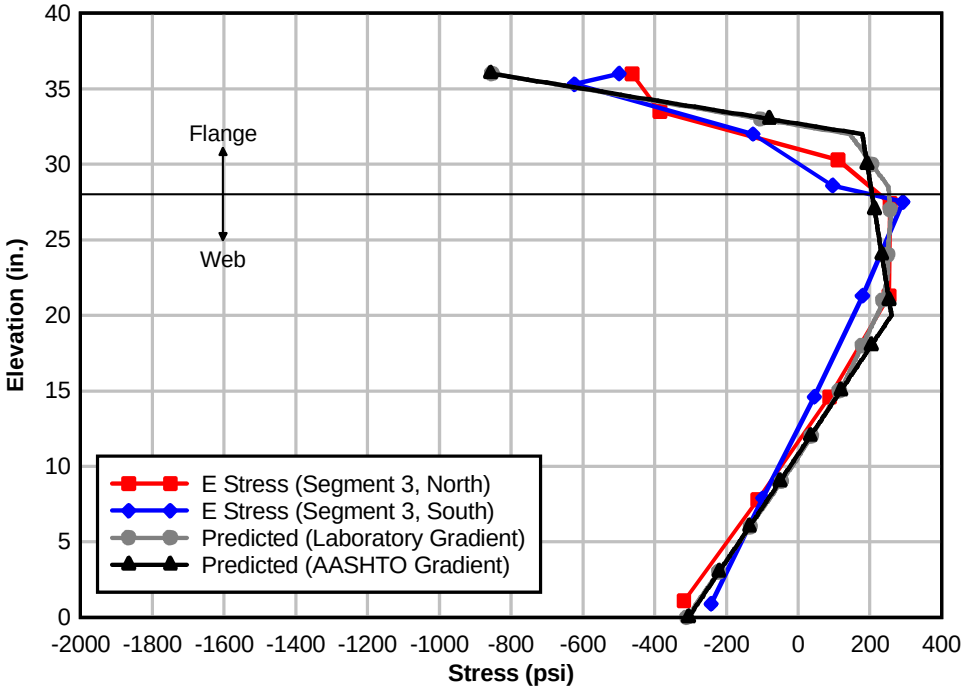

Figure 145 – E stresses near joint J2 (Segment 3)

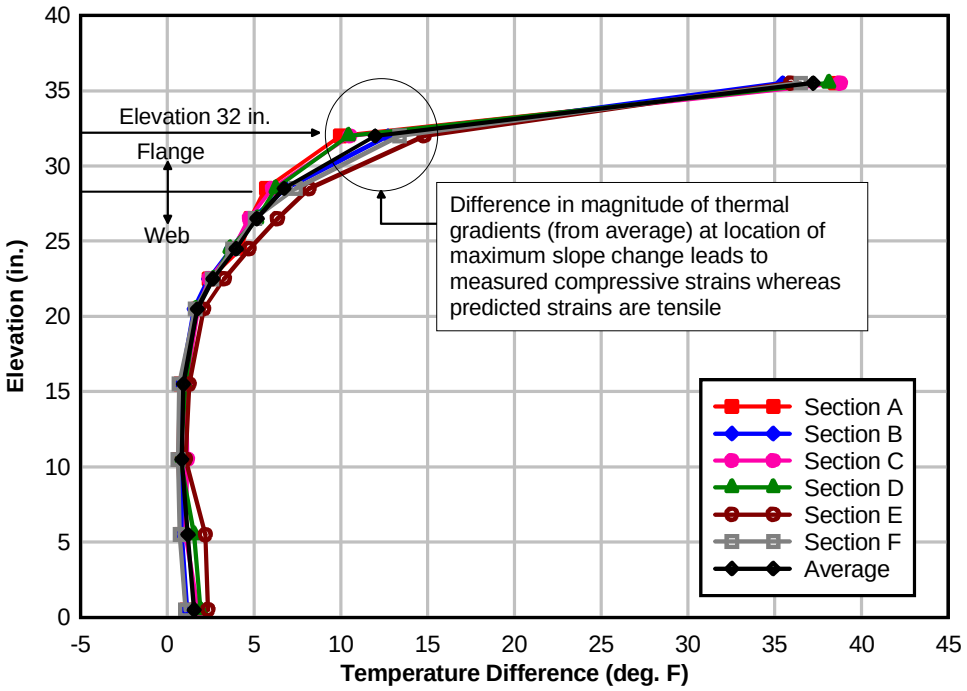

Figure 146 – Difference in magnitude of imposed thermal gradients at location of maximum slope change (elevation 32 in.)

Table 19 – Comparison of E stresses and extrapolated stresses on top of segment flanges near joint J2 (laboratory positive thermal gradient)

	Measured (psi)	Extrapolated (psi)	Measured/Extrapolated
Segment 2, North	-307	-786	0.391
Segment 2, South	-438	-732	0.598
Segment 3, North	-463	-772	0.600
Segment 3, Middle	-518	-751	0.690
Segment 3, South	-499	-729	0.684

Table 20 – Comparison of E stresses and predicted self-equilibrating thermal stresses caused by laboratory positive thermal gradient near joint J2

	Elevation (in.)	Average E Stress (psi)	Average Predicted (psi)	E Stress/Predicted
Segment 2	36	-373	N/A	N/A
	35.5	-671	-693	0.968
	33.5	-320	-219	1.461
	32	-57	137	-0.416
Segment 3	Elevation (in.)	Average E Stress (psi)	Average Predicted (psi)	E Stress/Predicted
	36	-493	N/A	N/A
	35.5	-674	-729	0.925
	33.5	-369	-230	1.604
	32	-140	144	-0.972

14.2 JOINT-OPENING DERIVED STRESSES (J STRESSES)

The known stress state at incipient joint opening was used to determine stresses caused by the laboratory positive thermal gradient without converting measured strains to stresses using the elastic moduli of the concrete segments. The magnitude of stresses caused by the thermal gradient in the top 4 in. of segments 2 and 3 at joint J2 were quantified using data collected from steps 1 and 3 of the load sequence shown in Figure 134. This was accomplished by loading the specimen until joint J2 began to open. At the condition of joint opening, it is known that the normal concrete stress near the joint face is zero (due to lack of contact). Assuming linear elastic behavior for subsequent short-term loads (thermal or mechanical), it was possible to extrapolate concrete stresses from the known (zero) stress state. Section properties of the contact area at joint J2, after joint opening, were used to calculate these stresses (J stresses).

Figure 147 illustrates the J stress calculation procedure using component stress blocks. Stresses at joint J2 prior to Step 1 of the load sequence consisted of stresses caused by prestress (P) and the self-weight (SW) of the beam. In Step 1, joint J2 was opened and closed at the reference temperature of the beam. The state of stress in the contact area at the joint caused by the joint-opening load, Q_R, will be referred to as the reference stress state. In Step 2 the positive thermal gradient was applied. Stresses at joint J2 consisted of stresses caused by prestress (P), self-weight (SW), and the nonlinear positive thermal gradient (PG). In Step 3 of the load sequence, joint J2 was again opened and closed. The state of stress in the contact area at the joint caused by the joint-opening load, Q_T, will be referred to as the thermal stress state. At incipient joint opening, flexural stresses caused by Q_R and Q_T in the extreme top flange fibers were equal, but opposite, to the existing normal stresses caused by ($P + SW$) and ($P + SW + PG$), respectively, at the same location. This condition was used to quantify self-equilibrating thermal stresses caused by the nonlinear positive thermal gradient. Though the concept of creating a zero stress condition at joint J2 is illustrated for the extreme top flange fibers, it is generally applicable to any shape of contact area. A general discussion of joint-opening and its uses in quantifying self-equilibrating thermal stresses follows.

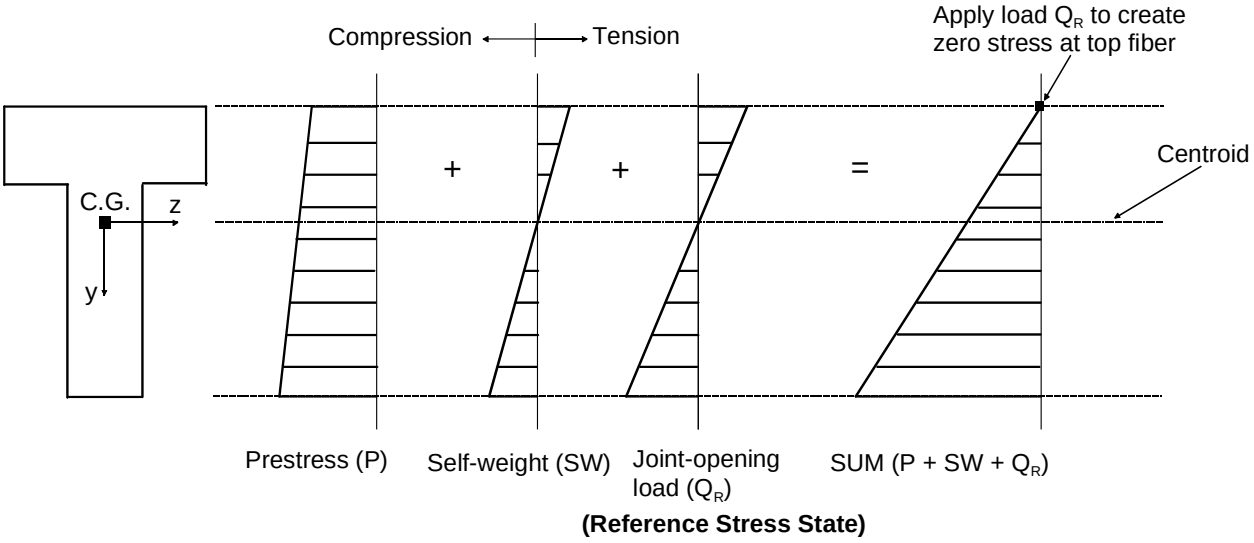

(a) Mechanical

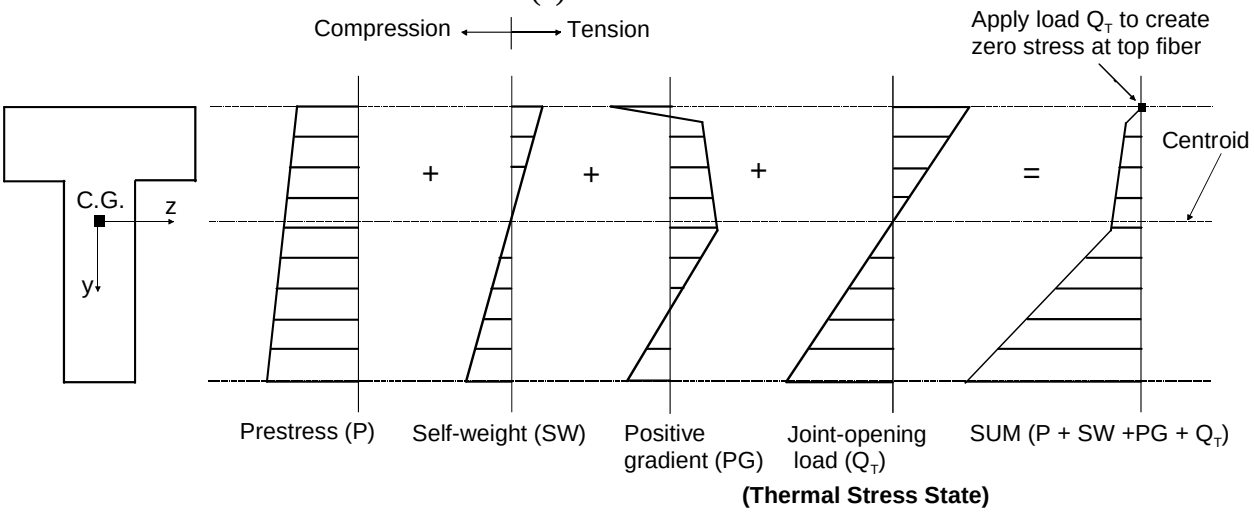

(b) Mechanical and thermal

Figure 147 – Superposition of component stress blocks

Figure 148 shows uniform opening of joint J2 to a known depth 'h' below the extreme top flange fibers. Because the joint opens uniformly across the width of the section, the boundary (referred to as the contact boundary in the figure) between open and closed parts of the joint is perpendicular to the sides of the segments. The joint opens in this manner when the line of action of the joint-opening load passes through the axis of symmetry of the contact area, and normal stresses existing prior to opening the joint are a function of depth only (i.e. uniformly distributed across the width of the section at all depths). If these conditions hold true for load cases without the thermal gradient (*P + SW*) and with the thermal gradient (*P + SW + PG*), then the contact area at the reference and thermal stress states is the same (Figure 148 (b)). If the distribution of existing normal stresses at the joint caused by (*P + SW*) and/or (*P + SW + PG*) varies across the depth and width, the depth of joint opening would not be uniform across the width of the segments, as was found to be the case for the laboratory beam. As shown in Figure

149, the contact areas at the reference and thermal stress states are in general not the same under these conditions.

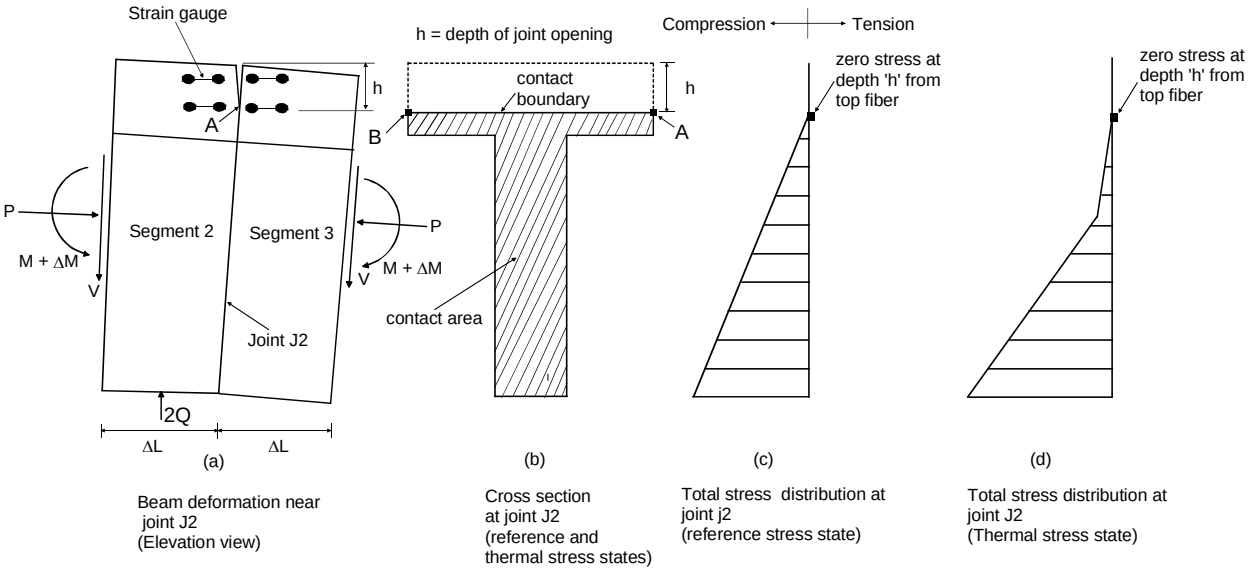

Figure 148 – Uniform opening of joint across section width

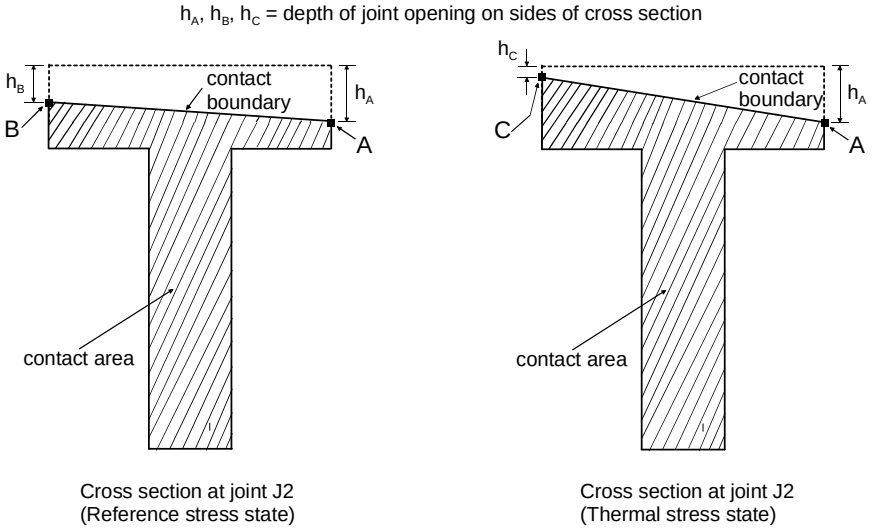

Figure 149 – Non-uniform opening of joint across section width

The zero stress condition created by superimposing stresses caused by the joint-opening loads Q_R and Q_T (see Figure 147) on existing normal stresses along corresponding contact boundaries is shown mathematically in the following equations:

$$f_P(y,z) + f_{SW}(y,z) + f_R(y,z) = 0, \{(y,z) \in R\} \quad \text{Equation 21}$$

$$f_P(y,z) + f_{SW}(y,z) + f_J(y,z) + f_T(y,z) = 0, \{(y,z) \in T\} \quad \text{Equation 22}$$

$$f_J(y,z) = f_R(y,z) - f_T(y,z), \{(y,z) \in R \cap T\}$$ Equation 23

where:

f_P = concrete stress in contact area due to prestressing force
f_{SW} = stress due to self-weight
f_J = J stresses (self-equilibrating concrete stress caused by nonlinear positive thermal gradient)
f_R = reference stress state
f_T = thermal stress state
R = contact boundary at reference stress state
T = contact boundary at thermal stress state
y, z = vertical and horizontal coordinates of points on contact boundaries

These equations are valid only along the contact boundary corresponding to each stress state. For example, Equation 21 and Equation 22 are applicable along line AB in Figure 148. In Figure 149, however, Equation 21 is applicable along line AB while Equation 22 is applicable along line AC. Equation 23, which is obtained by taking the difference between the reference stress state and thermal stress state, is valid only at point A in Figure 149, where the contact boundary at the reference stress state is at the same elevation as the contact boundary at the thermal stress state. Equation 23 shows that self-equilibrating thermal stresses caused by the nonlinear positive thermal gradient at the points of intersection of the contact boundaries can be determined if stresses caused by Q_R and Q_T are known.

The load that caused joint J2 to open at a known depth 'h' at the reference and final stress states was determined from load vs. strain curves of strain gauges adjacent to the joint. Because the laboratory beam was statically determinate, the bending moment at joint J2 was determined from the joint-opening load without taking the change in stiffness of the beam, caused by opening the joint, into account. Assuming that plane sections remained plane under the actions of the forces and moments acting at the joint, stresses caused by joint-opening loads at the reference and final stress states along corresponding contact boundaries were determined with the aid of stress-strain diagrams of the concrete segments and equations of statics. Assuming further that the behavior of the beam was linear elastic under the action of the applied loads, it became possible to determine stresses without measuring strain.

For stresses due to joint-opening loads to be determined without explicitly using the elastic/tangent modulus of concrete (i.e. without the stress-strain curve), the material behavior of concrete within the load ranges considered had to be linear elastic. Furthermore, the distribution of strain through the depth of the contact area at joint J2 (after opening the joint) had to be a linear function of curvature (i.e. plane sections remain plane). It was assumed that concrete was homogeneous and isotropic. Linear elastic material behavior of the beam segments within the range of mechanical loads applied during testing was supported by data from cylinder tests, which showed that the beam segments were linear elastic up to stresses of about 6000 psi (uniaxial compression). Distributions of measured concrete strain through the depth of evolving contact areas near joint J2 were approximately linear as the joint was opened (Figure 119 and Figure 120). This was evidence of plane sections remaining plane, within the contact area, under flexure. Data collected from in-situ CTE tests conducted on the heated segments showed that,

within the temperature ranges to which the segments were subjected during testing, plane sections remained plane and thermal strains were a linear function of temperature difference. Based on these observations flexural stresses due to joint-opening loads were determined using classical flexural stress formulas.

Figure 150 and Figure 151 show variations of concrete strain with applied load near joint J2 on the North side of Segment 3 at the reference stress state (reference temperature) and thermal stress state (with positive thermal gradient), respectively. Similar plots near the same joint on the South side of Segment 3 are shown in Figure 152 and Figure 153, respectively. The variation of concrete strain with applied load on top of the flanges of segments 2 and 3 near joint J2 at the reference and thermal stress states are shown in Figure 154 and Figure 155, respectively. Data collected from strain gauges near joint J2 on Segment 2 (which were similar to those from Segment 3), LVDTs mounted across joint J2 on top of the flanges of segments 2 and 3, and LVDTs mounted across the same joint on the South side can be found in Appendix E. The variation of measured strains and measured displacements with load near joint J2 on the South side, North side, and on top of the flanges of segments 2 and 3 was discussed in detail in Chapter 12.

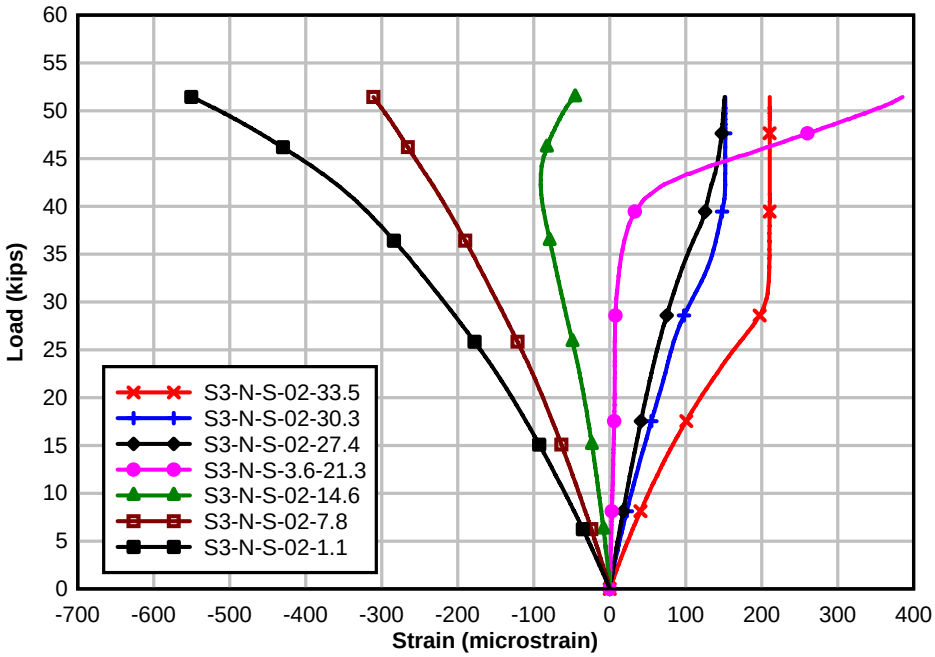

Figure 150 – Load vs. strain at reference temperature (Segment 3, North)

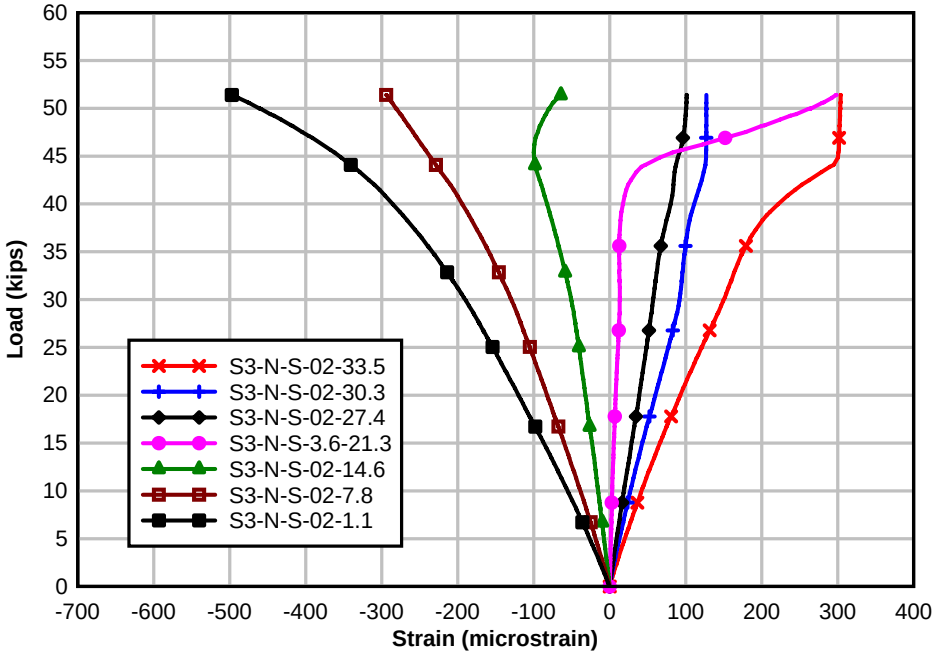

Figure 151 – Load vs. strain with positive thermal gradient (Segment 3, North)

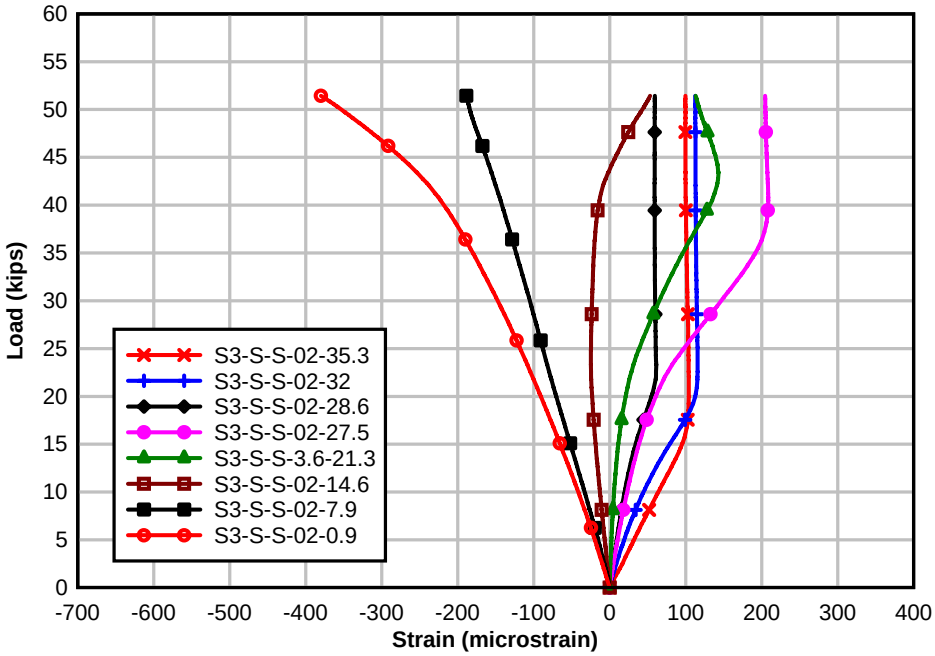

Figure 152 – Load vs. strain at reference temperature (Segment 3, South)

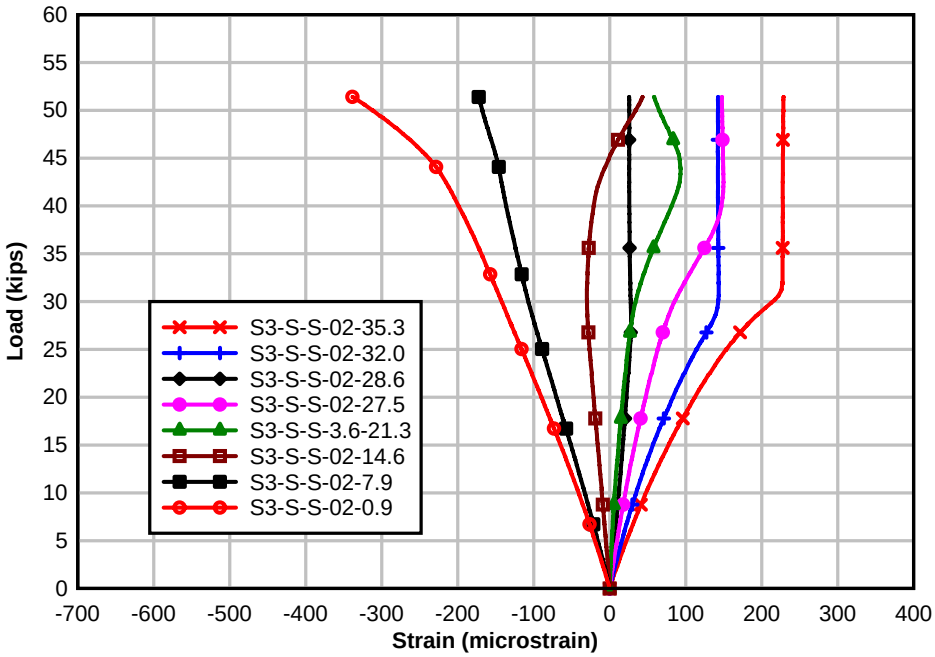

Figure 153 – Load vs. strain with positive thermal gradient (Segment 3, South)

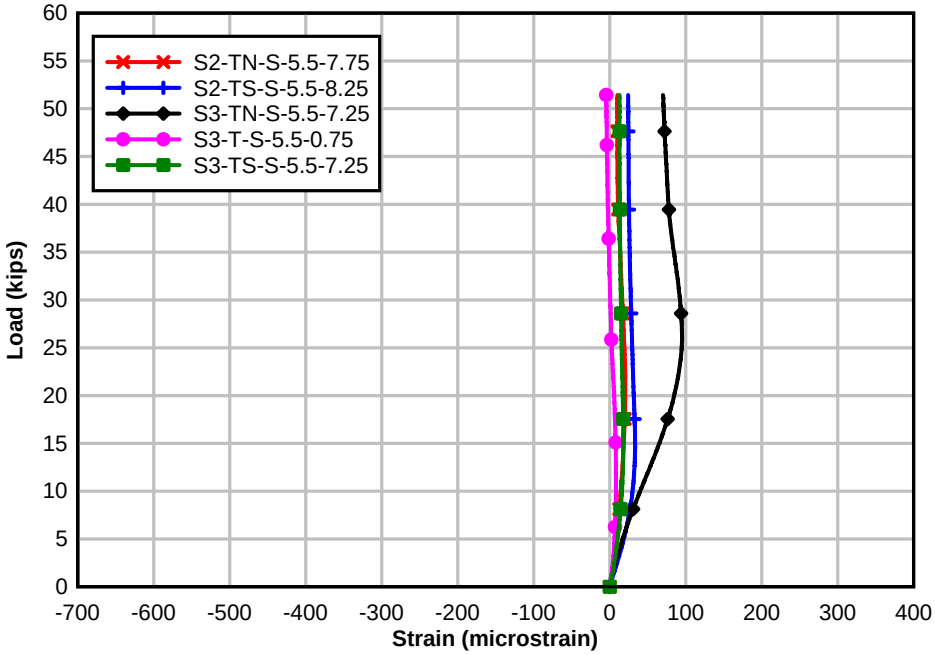

Figure 154 – Load vs. strain at reference temperature (Top flange)

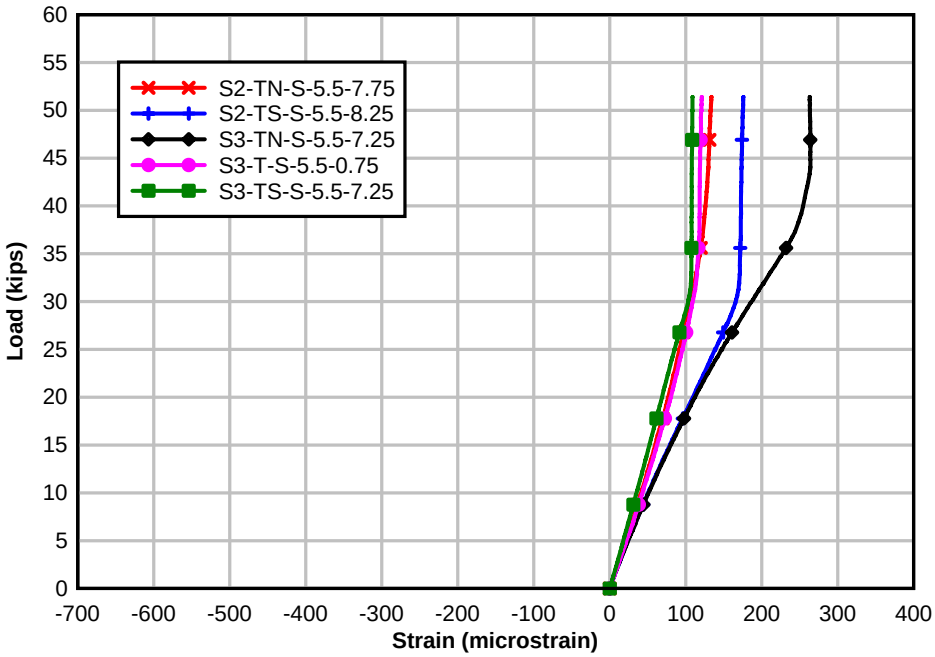

Figure 155 – Load vs. strain with positive thermal gradient (Top flange)

Two general observations can be made when measured concrete strains at the same side of joint J2 and LVDT readings at the reference and thermal stress states are compared. These observations are illustrated in Figure 156 with data from the strain gauges at elevations 33.5 in. and 35.3 in. on the North and South sides of joint J2, respectively. The first is that at the same elevation in the top 4 in. of the flange, the joint opened at higher loads at the thermal stress state than it did at the reference stress state (i.e. $Q_{TN} > Q_{RN}$ and $Q_{TS} > Q_{RS}$). This is also evident in the top flange strains shown in Figure 154 and Figure 155, and LVDT data (see Figure 265 through Figure 268 in Appendix E). Opening of joint J2 at higher loads at the thermal stress state was consistent with the development of compressive strains in the top concrete fibers caused by the positive thermal gradient.

The second observation is that although smaller strains were recorded on the South side of the joint than on the North side (i.e. $\varepsilon_{RS} < \varepsilon_{RN}$ and $\varepsilon_{TS} < \varepsilon_{TN}$ in Figure 156), the strain difference between vertical portions of strain diagrams at the reference and thermal stress states ($\Delta\varepsilon_S$ and $\Delta\varepsilon_N$) was independent of the side of the joint on which the gauge was located. The strain difference was, however, dependent on the distribution of stress-inducing concrete strains caused by the positive thermal gradient at joint J2 (and therefore the elevation of gauges). In Figure 156 the strain difference on the North side at elevation 33.5 in. ($\Delta\varepsilon_N$) was less than the strain difference on the South side of the joint at elevation 35.3 in. ($\Delta\varepsilon_S$). This was because the gauge on the South side was at a higher elevation than the gauge on the North side.

Since the strain difference between vertical portions of strain curves at the reference and thermal stress states represented strains caused by the positive thermal gradient at joint J2, it was evident that within the top 4 in. of the flange, these strains (and corresponding stresses) decreased in compression, with the maximum strains and stresses occurring in the top fibers of the section. This was consistent with the expected distribution of self-equilibrating thermal stresses within the top 4 in. of the flange (see predicted strains and stresses in Section 14.1)

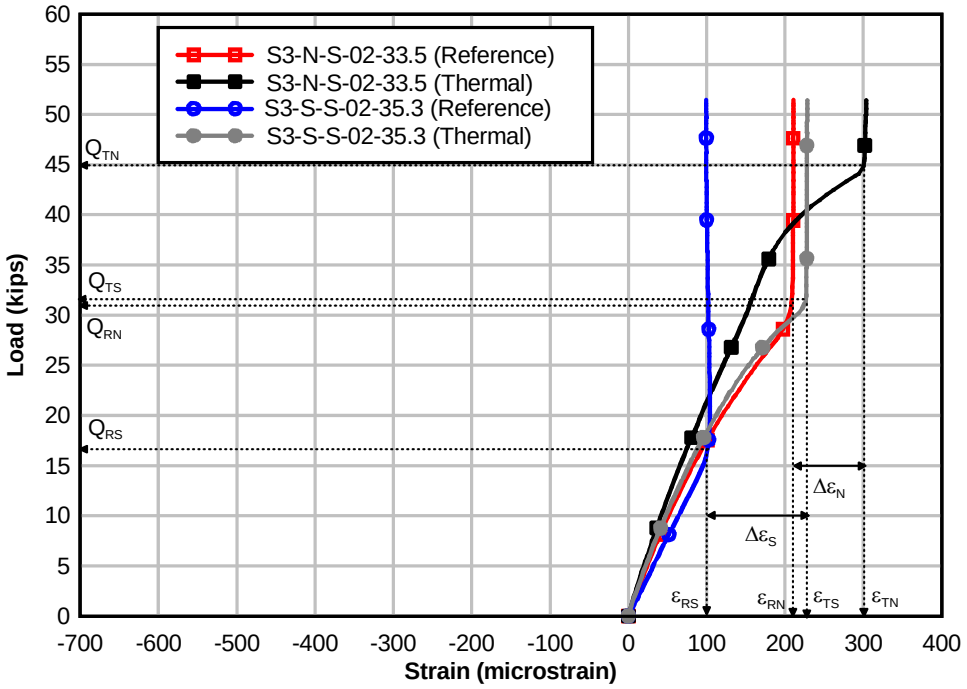

Figure 156 – Comparison of strain differences on North and South sides of joint J2 (Positive thermal gradient)

Loads that caused joint J2 to open at the reference and thermal stress states were detected using load vs. strain data (detection of joint-opening loads using strain gauges was discussed in Section 12.1). LVDT data were mainly used to check joint-opening loads determined with strain gauges, especially on top of the flange, where very low strains were recorded at the reference stress state. Applied loads at the cantilevered-end of the test beam, that caused joint J2 to open at various depths, are shown in Figure 157. Each point in the figure shows the average load (determined from gauges on segments 2 and 3 on the same side (North or South) of the joint) at which the change in strain at that location became zero. These points were used to define the boundary of the contact area at varying loads. The sign convention for moments and curvatures is shown in Figure 158. Tensile stresses caused by joint-opening loads are positive and compressive stresses are negative. Recall that tensile stresses are actually reductions of the initial compressive stresses caused by prestressing.

Figure 159 through Figure 161 show estimated contact areas at joint J2 at the reference and thermal stress states just as opening of the joint was detected from strain gauges at elevations of 35.5 in. (South), 33.5 in. (North), and 32.0 in. (South), respectively. Contact boundaries are indicated by dashed lines. Contact areas were estimated by interpolating between joint-opening loads and the positions of the strain gauges from which the loads were determined (see Figure 157). Total stresses caused by moments at joint J2 due to joint-opening loads and changes in prestress were determined using the contact area cross sections and Equation 24 through Equation 30. Though data from strain gauges and LVDTs on top of the flanges of segments 2 and 3 were useful in estimating contact areas, top flange stresses could not be determined with these equations. This was because of the condition of the joint at the top of the flanges (see Figure 109).

$$f(z, y, M_z, M_y, I_z, I_y, I_{zy}, \Delta p, A) = \frac{(M_y \cdot I_z + M_z \cdot I_{zy}) \cdot z - (M_z \cdot I_y + M_y \cdot I_{zy}) \cdot y}{I_y \cdot I_z - I_{zy}^2} - f_N(\Delta p, A)$$ Equation 24

$$M_y = -\Delta M_{P\_v}$$ Equation 25

$$M_z = M_Q - \Delta M_{P\_h}$$ Equation 26

$$f_N(p, A) = \frac{-\left(\sum_{i=1}^{4} p_i\right)}{A}$$ Equation 27

$$\Delta M_{P\_h}(\Delta p, e_y) = \sum_{i=1}^{4} (\Delta p_i \cdot ei_y)$$ Equation 28

$$\Delta M_{P\_v}(\Delta p, e_z) = \sum_{i=1}^{4} (\Delta p_i \cdot ei_z)$$ Equation 29

$$M_Q = x_{J2} \cdot Q$$ Equation 30

where:

f	=	total stress caused by joint-opening load (Q) at joint J2
f_N	=	stress due to change in prestress at load Q
M_Q	=	moment of joint-opening load (Q) at joint J2
Δ_p	=	change in prestress at load Q
ei_y	=	vertical eccentricity of prestress bar ‘i’
ei_z	=	horizontal eccentricity of prestress bar ‘i’
ΔM_{P_v}	=	moment about vertical axis due to change in prestress
ΔM_{P_h}	=	moment about horizontal axis due to change in prestress
I_z	=	moment of inertia of section about horizontal axis
I_y	=	moment of inertia of section about vertical axis
I_{zy}	=	product of inertia of section
z	=	horizontal coordinate of point at which stress is calculated
y	=	vertical coordinate of point at which stress is calculated
x_{J2}	=	moment arm of joint-opening load from joint J2

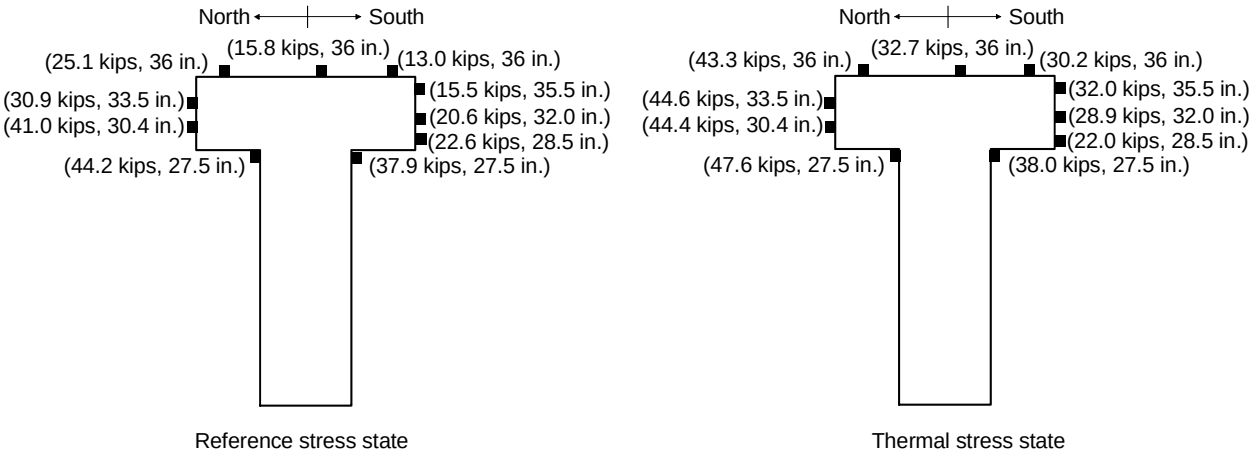

Figure 157- Joint opening loads detected from strain gauges close to joint J2

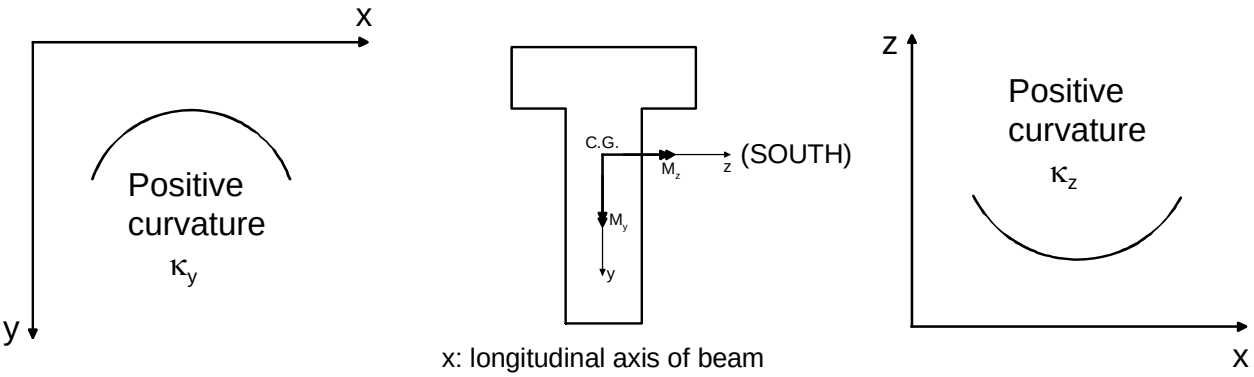

Figure 158 – Sign convention for moments and curvature

S-S-S-02-35.5

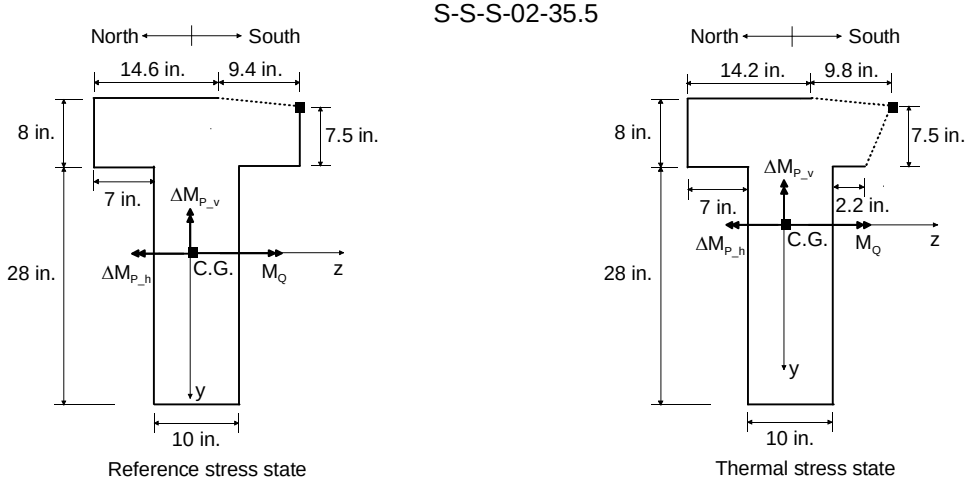

Figure 159 – Contact areas at joint J2 at incipient joint opening on South side at elevation 35.5 in.

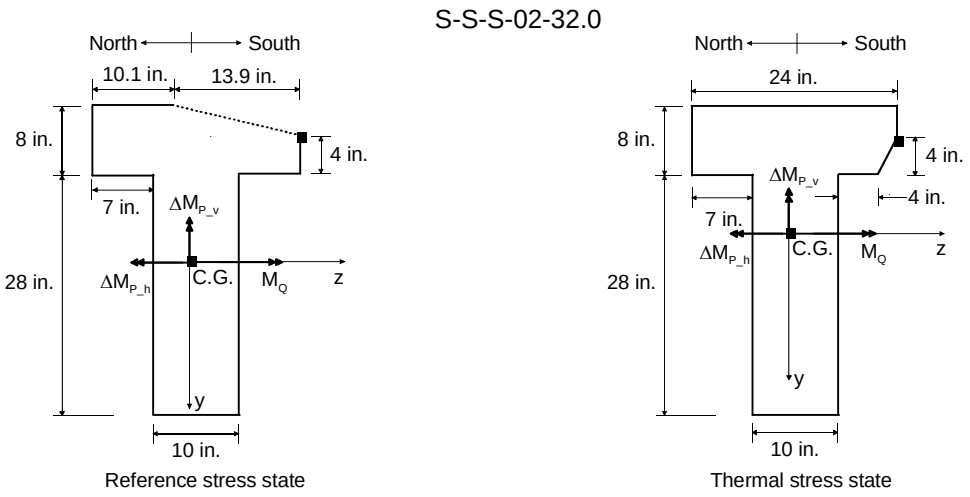

Figure 160 – Contact areas at joint J2 at incipient joint opening on North side at elevation of 33.5 in.

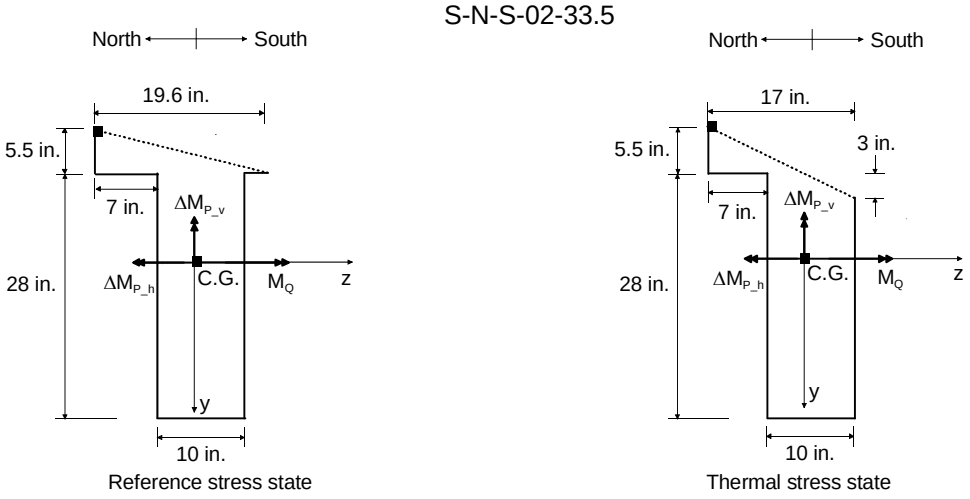

Figure 161 – Contact areas at joint J2 at incipient joint opening on South side at elevation 32.0 in.

Table 21 shows calculated J stresses at the locations of strain gauges on the sides of the beam within the top 4 in. of the flange. Though the total stresses (stresses determined from Equation 24) are positive, indicating tension, they actually represent relief of prestressing-induced compressive stresses at J2 that were present prior to the application of joint-opening loads. The J stresses were then determined by taking the difference between total stresses at the reference stress state and total stresses at the final stress state.

In Equation 24, the total stress is made of two components; the stress component due to the joint opening load and the stress component due to changes in prestress. Changes in prestress (determined from measured prestress forces and section properties) accounted for less than 0.5% of total stresses. The calculated total stresses were therefore essentially dependent on the magnitude of joint opening loads. J stresses, however, were dependent only on the difference between the joint-opening loads at the reference and thermal stress states. For example, the

loads initiating opening of joint J2 on the North side at an elevation of 33.5 in. were greater than on the South side at an elevation of 35.5 in. as can be seen from the magnitudes of the moments in Table 21. However, calculated J stresses at an elevation of 33.5 in. were lower than J stresses at an elevation of 35.5 in. This was expected since the distribution of self-equilibrating thermal stresses within the top 4 in. of the flanges of segments 2 and 3 was expected to increase linearly (in compression) from a minimum magnitude at an elevation of 32 in. to a maximum magnitude at the top flange (elevation 36 in.).

J stresses and predicted stresses in the top 4 in. of the flange are compared in Table 22. J stresses 0.5 in. below the top of the flange (maximum J stresses) were approximately 10% and 15% less than corresponding predicted stresses in Segment 2 and Segment 3, respectively. At elevation 32 in., J stresses were about 82% less than predicted stresses. Both predicted and J stresses were, however, tensile. As was the case for E stresses, this was attributed mainly to the difference in magnitude between the measured thermal gradients and the average thermal gradient (with which stresses were predicted).

J stresses and E stresses in the top 4 in. of the flange are compared in Table 23. Both sets of stresses compared well except at elevation 32 in. A possible reason for this was noted above. Maximum J stresses (at elevation 35.5 in.) were about 7% and 8% less than maximum E stresses on Segment 2 and Segment 3, respectively.

Table 21 – J stresses in top 4 in. of flange

Gauge Elevation	Moments due to Joint-opening Loads (kip-in.)		Total Stresses (psi)		J Stress (psi)
	Reference	Thermal	Reference	Thermal	
35.5 in. S	1399	2889	366	989	-623
33.5 in. N	2790	4063	801	1124	-323
32.0 in. S	1833	2645	558	533	25

Table 22 – Comparison of J stresses and predicted stresses in top 4 in. of flange

Segment 2			
Gauge Elevation	J Stress (psi)	Predicted Stress (psi)	J Stress/Predicted Stress
35.5 in. S	-623	-693	0.899
33.5 in. N	-323	-219	1.475
32.0 in. S	25	137	0.182
Segment 3			
Gauge Elevation	J Stress (psi)	Predicted Stress (psi)	J Stress/Predicted Stress
35.5 in. S	-623	-729	0.855
33.5 in. N	-323	-230	1.404
32.0 in. S	25	144	0.174

Table 23 – Comparison of J stresses and E stresses in top 4 in. of flange

Segment 2			
Gauge Elevation	J Stress (psi)	E Stress (psi)	J Stress/E Stress
35.5 in. S	-623	-671	0.928
33.5 in. N	-323	-320	1.009
32.0 in. S	25	-57	-0.439
Segment 3			
Gauge Elevation	J Stress (psi)	E Stress (psi)	J Stress/E Stress
35.5 in. S	-623	-674	0.924
33.5 in. N	-323	-369	0.875
32.0 in. S	25	-140	-0.179

15 RESULTS – AASHTO NEGATIVE THERMAL GRADIENT

Results from the application of mechanical loading in combination with the AASHTO negative thermal gradient are presented and discussed in this chapter. The objective of the mechanical-thermal load tests was to experimentally quantify the self-equilibrating thermal stresses caused by the AASHTO nonlinear negative thermal gradient in the top 4 in. of the flanges of segments 2 and 3. As with the positive gradient, two independent methods were used to quantify stresses. Elastic modulus derived stresses (E stresses) were determined by converting measured strains into stresses using the elastic modulus of concrete. Independently, joint opening derived stresses (J stresses) were determined using the known stress state at incipient joint opening. In both methods concrete behavior was assumed to be linear elastic.

The test sequence, illustrated in Figure 162, shows that before mechanical or thermal loads were applied, the only forces acting on the beam were prestress and self-weight. The test sequence started with partial opening and closing of the joint at midspan (joint J2) with the beam at the ambient temperature of the laboratory (about 80 ^{o}F). This was followed by application of a uniform temperature increase of about 45 ^{o}F on segments 2 and 3 of the beam, after which the top portion of the segments could be cooled to impose the negative thermal gradient (see Section 9.4). Joint J2 was partially opened and closed after achieving and maintaining the steady state uniform temperature increase on the heated segments for 30 to 45 minutes. Data from this step of the load sequence were used to establish a zero reference stress state at joint J2. The top of the segments were then cooled to impose the AASHTO negative thermal gradient. After achieving and maintaining the steady state negative thermal gradient on the heated segments for 30 to 45 minutes, joint J2 was partially opened and closed to determine the thermal stress state. The heated segments were then cooled to the reference temperature (tap water temperature) at the start of the test, after which joint J2 was again opened and closed, completing the load cycle.

Data collected from steps 3 and 5 of the load sequence were used to quantify self-equilibrating thermal stresses caused by the laboratory-imposed negative thermal gradient. Joint-opening loads and contact areas at joint J2, as the joint was gradually opened, were used to calculate self-equilibrating stresses caused by the nonlinear gradient (J stresses). Neither elastic moduli, nor coefficients of thermal expansion of segments 2 and 3 were used in the calculation of J stresses.

Elastic modulus derived thermal stresses calculated from measured thermal strains close to joint J2 (E stresses) and joint opening derived thermal stresses (J stresses) are presented and discussed in the following sections.

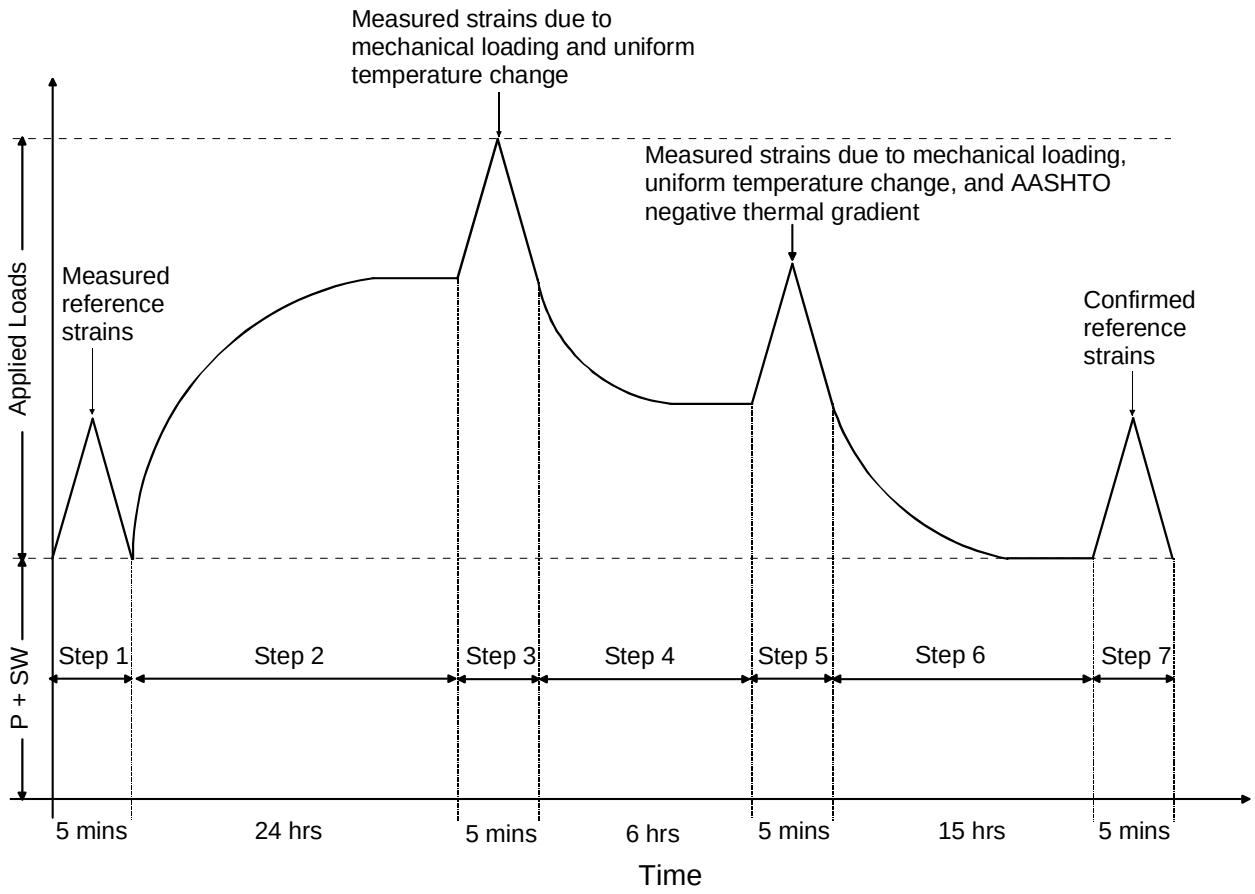

P + SW: Pretress + Self-weight

Applied Loads:

Step 1: Opening and closing of joint J2 (application and removal of mechanical loads)
Step 2: Uniform temperature change (application of thermal load)
Step 3: Opening and closing of joint J2 (application and removal mechanical loads)
Step 4: Negative thermal gradient (application of thermal load)
Step 5: Opening and closing of joint J2 (application and removal of mechanical loads):
Step 6: Cooling to reference temperature at start of test (removal of thermal loads)
Step 7: Opening and closing of joint J2 (application and removal of mechanical loads)

Figure 162 – Sequence of load application (negative gradient test)

15.1 ELASTIC MODULUS DERIVED STRESSES (E STRESSES)

The nonlinear negative thermal gradient imposed on the heated segments of the laboratory beam (see Figure 163) in Step 4 of the load sequence is shown in Figure 164. For comparison, Figure 164 also shows the AASHTO design negative gradient. Measured temperatures in the heated segments after imposing the negative thermal gradient are shown in Figure 165.

As was done for the positive gradient (described in Chapter 14) temperature on top of the flange was obtained by extrapolating the measured temperature data from elevations 32 in. and 35.5 in. The idealized strain components induced by the AASHTO design negative thermal gradient are shown in Figure 166 (A detailed description of the strain components is given in Section 3.2 and Chapter 14).

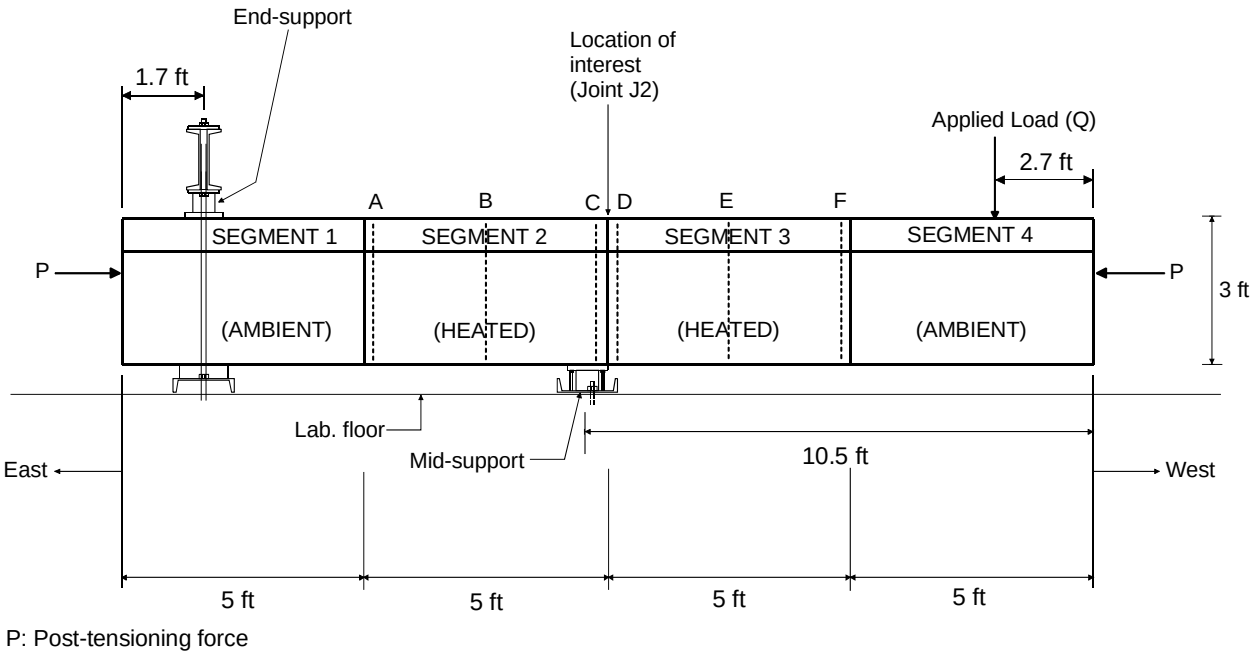

Figure 163 – Laboratory beam

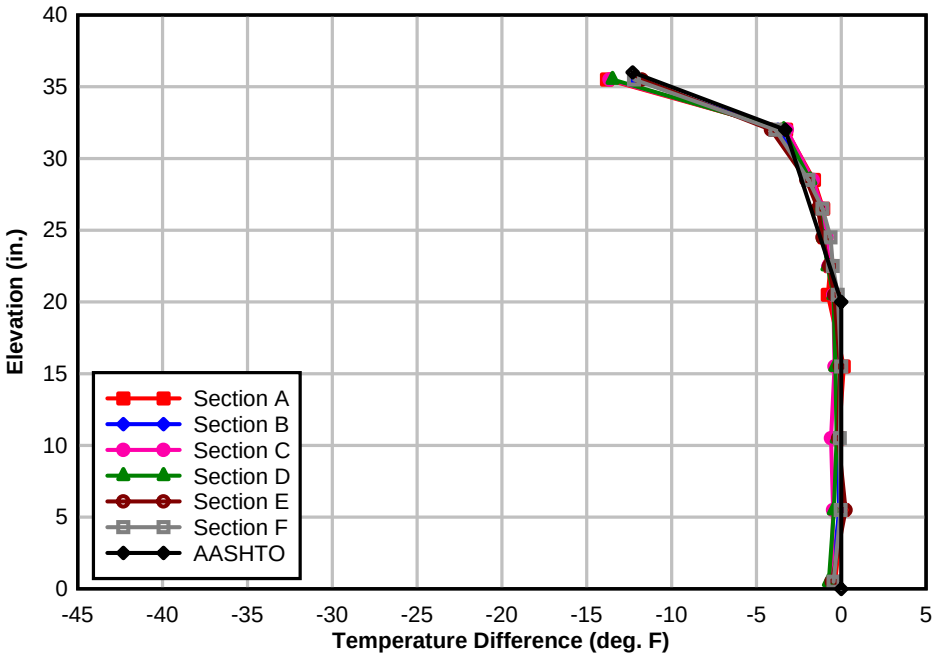

Figure 164 – Laboratory imposed negative thermal gradient

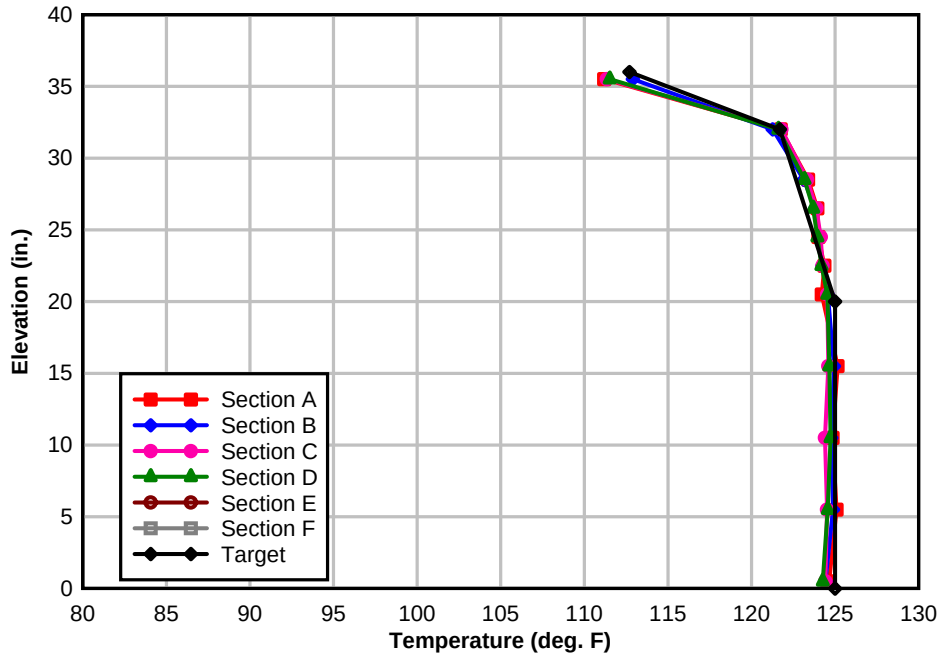

Figure 165 – Measured temperatures in heated segments (negative thermal gradient)

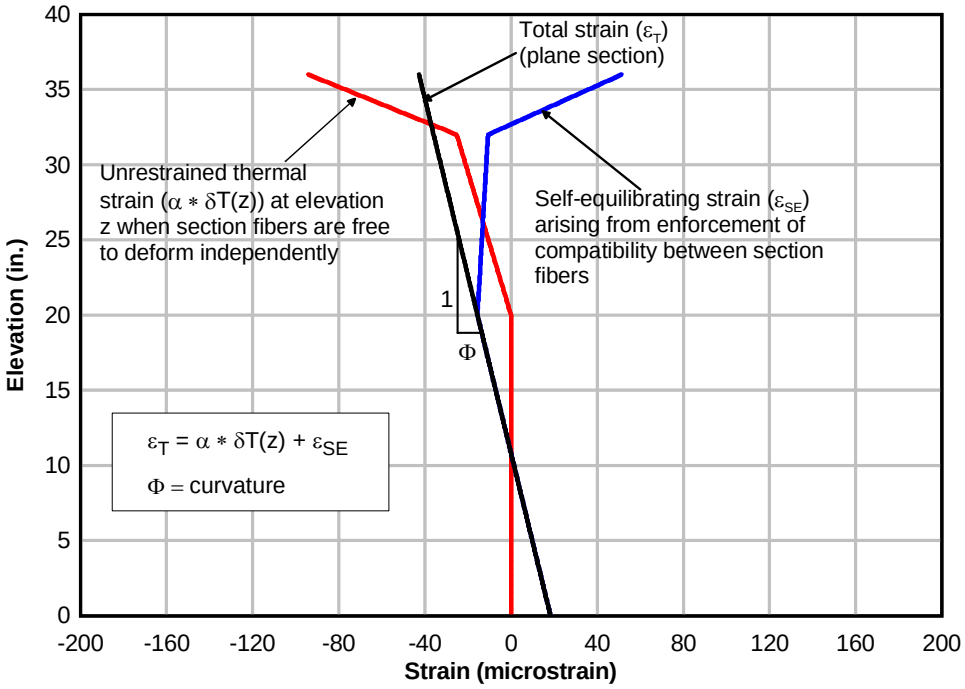

Figure 166 – Calculated strain components of the AASHTO negative thermal gradient

The change in measured strain between Step 3 and 5 at joint J2 are plotted in Figure 167 through Figure 169. Figure 167 and Figure 168 show the strain difference along the height of segments 2 and 3, respectively. Figure 169 shows a plan view of the strain differences on the top

flange near the same joint. Also shown in the figures are the two sets of strain changes predicted using the AASHTO design procedure: one using the AASHTO design thermal gradient, and the other using the laboratory-imposed thermal gradient. Because the strain gauges installed on the beam were self-temperature compensating (STC) gauges, and because there was no axial or flexural restraint on the beam, the measured strains consisted only of the self-equilibrating strain component of the total strains. The average laboratory-imposed thermal gradient profile (average of profiles at Section A through Section F (Figure 164)) was used in calculating the 'laboratory gradient' strains in Figure 167 through Figure 169.

No marked difference is apparent between measured and predicted strains due to the laboratory gradient below approximately 28 in. elevation. Tensile strains were present in the bottom of the section up to an elevation of about 10 in. Compressive strains arose in the section mid-height from about 10 in. to 32 in. elevation. A maximum compressive strain (due to the laboratory gradient) of about 21 με was predicted at elevation 27.5 in. whereas a maximum measured compressive strain of about 26 με occurred at the same elevation. The maximum predicted tensile strain due to the AASHTO design gradient, of magnitude about 15 με, occurred at an elevation of 20 in.

The difference between locations of maximum predicted compressive strains due to the imposed laboratory gradient and the AASHTO design gradient was due to the difference in the shape of the laboratory and AASHTO design thermal gradients. In each case, the maximum compressive strain occurred at the location where the change in slope (in units of ^{o}F/in.) of the thermal gradient profile was algebraically at a maximum. This occurred at an elevation of 27.5 in. for the laboratory gradient and at an elevation of 20 in. for the AASHTO design gradient. Tensile strains also occurred above the mid-thickness of the flange with a steeper gradient than that of the remainder of the profile.

Some additional differences between the measured and predicted strains are also notable. Measured tensile strains were significantly smaller than predicted at the top of the section in both segments except for the North top flange of Segment 3 (see Figure 169). As with the positive thermal gradient, the smaller measured tensile strains on top of the section were thought to be caused by a likely discontinuity in the shape of the thermal gradient in the top 0.5 in. of the flange. Although not measured, it is probable that the temperature at the top surface of the flange was less than that of the temperature of the topmost thermocouples (located at an elevation of 35.5 in.). In determining predicted strains, however, the magnitude of the thermal gradient in the top flange was obtained by extrapolating the linear thermal gradient between elevations of 32 in. and 35.5 in. The approximately 53% difference between strains measured on the North and South top flange of Segment 3 was attributed to the condition at the top surface of the flange at joint J2 shown in Figure 109 (see Chapter 12).

Measured concrete strains on the North side at midspan (joint J2) and at mid-segment of segments 2 and 3 are compared in Figure 170 and Figure 171, respectively. The distributions of measured strain on the side of the flange at mid-segment did not match the predicted strain profile as well as the measured strains at midspan because only two strain gauges were located on the side of the flange at mid-segment. Additionally, measured tensile strains on top of the flange at mid-segment were significantly less than predicted strains at the same locations. Measured strains on top of the flange at mid-segment were, however, generally greater than corresponding measured tensile strains at joint J2. This observation reinforces the possibility that differential shrinkage at joint J2 led to a greater discrepancy between measured and predicted strains at the joint. Between elevations 32 in. and 35.5 in., measured tensile strains

followed a linear distribution as did the predicted strains. The measured strains were, however, generally larger than predicted strains between elevations 32 in. and 33 in. and smaller than predicted strains above 33 in. As was the case for the positive thermal gradient, a possible reason for the difference between measured and predicted strains in this region of the flange was a variation between measured thermal gradients at sections A through F, and the average of these gradients (see Figure 172), which was used to predict strains per the AASHTO design procedure.

The uniform and linear sub-components of the overall negative thermal gradient were expected to lead to additional stresses in the concrete as the top portions of segments 2 and 3 were cooled during Step 4. Contraction of the segments relative to the prestressing caused a net reduction in prestressing force, however the measured peak reduction was only 0.2% of the initial prestress and was therefore considered negligible.

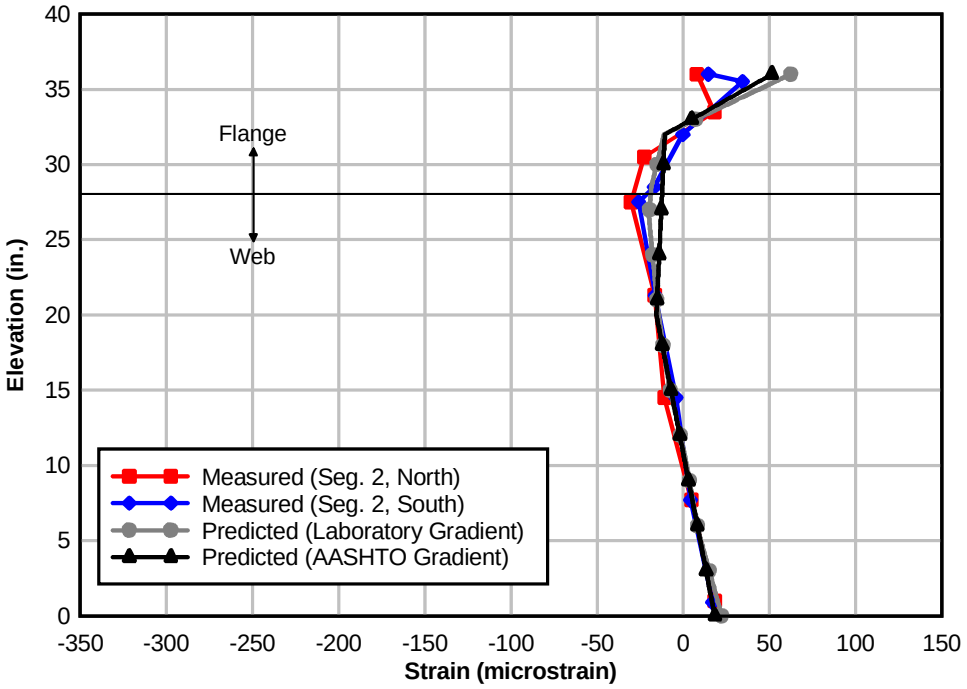

Figure 167 – Measured and predicted strains near joint J2 (Segment 2)

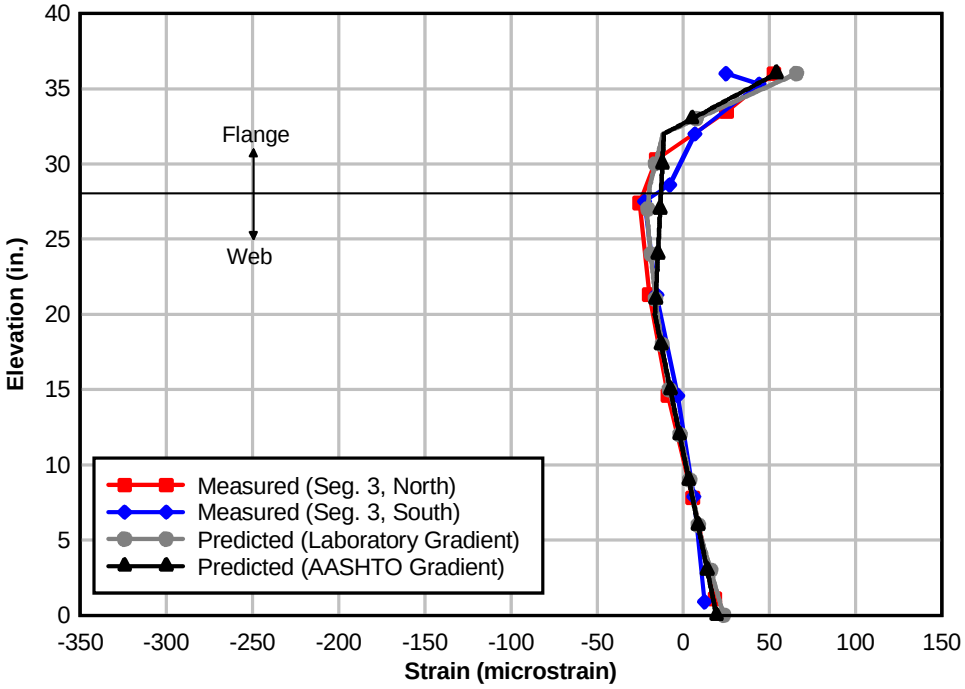

Figure 168 – Measured and predicted strains near joint J2 (Segment 3)

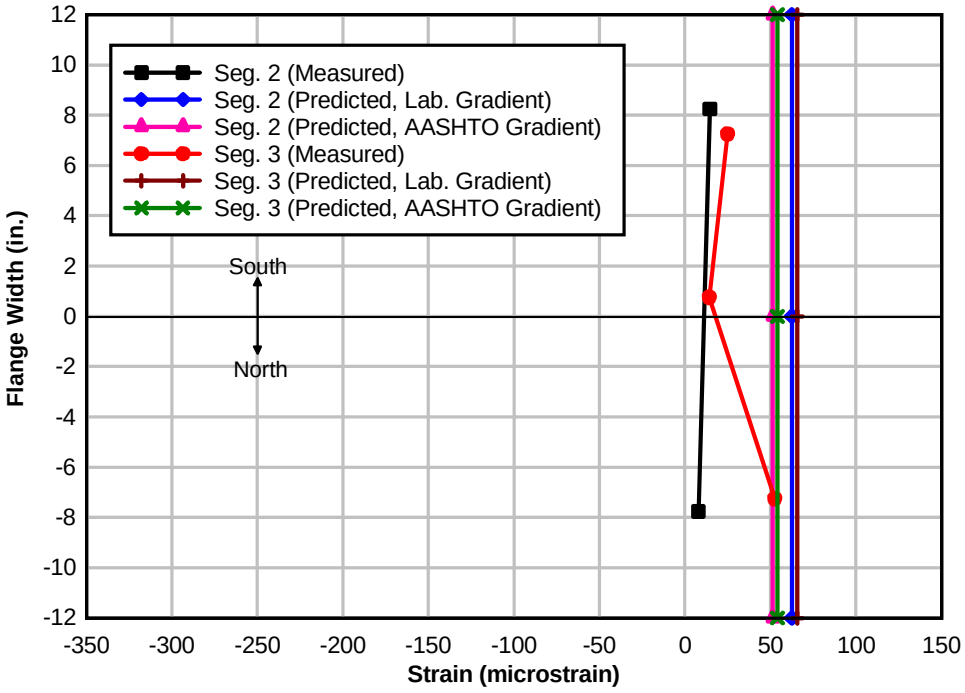

Figure 169 – Plan view of measured and predicted strains near joint J2 (Top Flange)

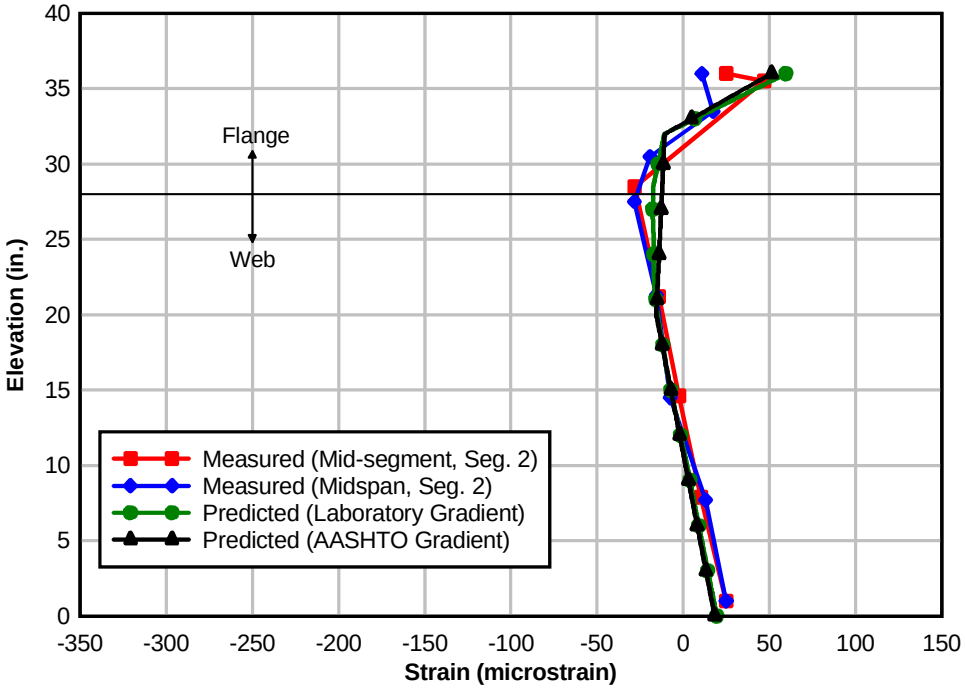

Figure 170 – Measured and predicted strains at midspan and mid-segment (Segment 2, North)

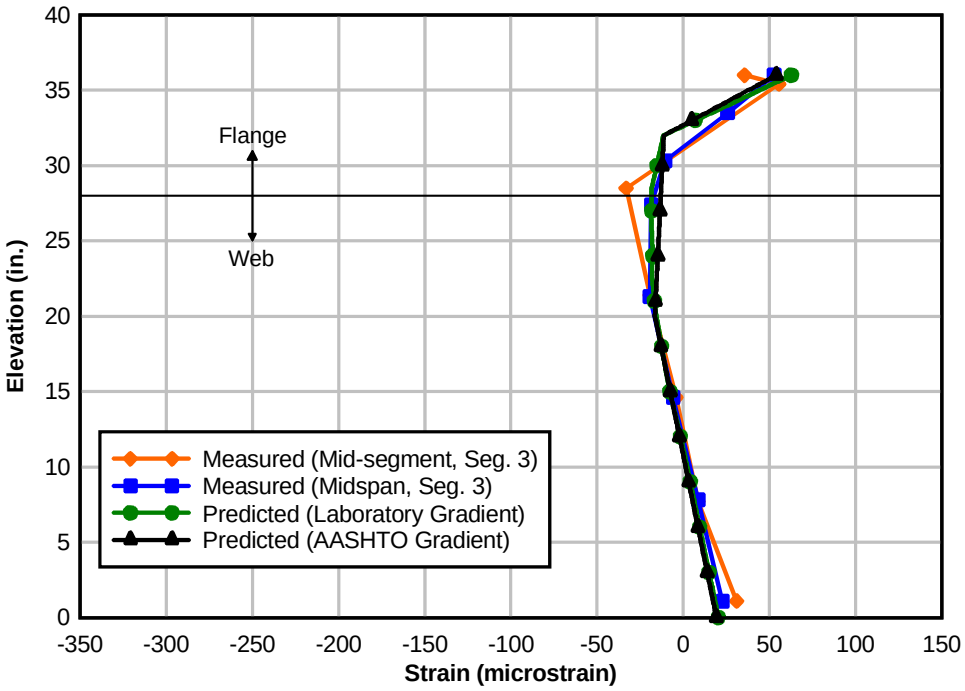

Figure 171 – Measured and predicted strains at midspan and mid-segment (Segment 3, North)

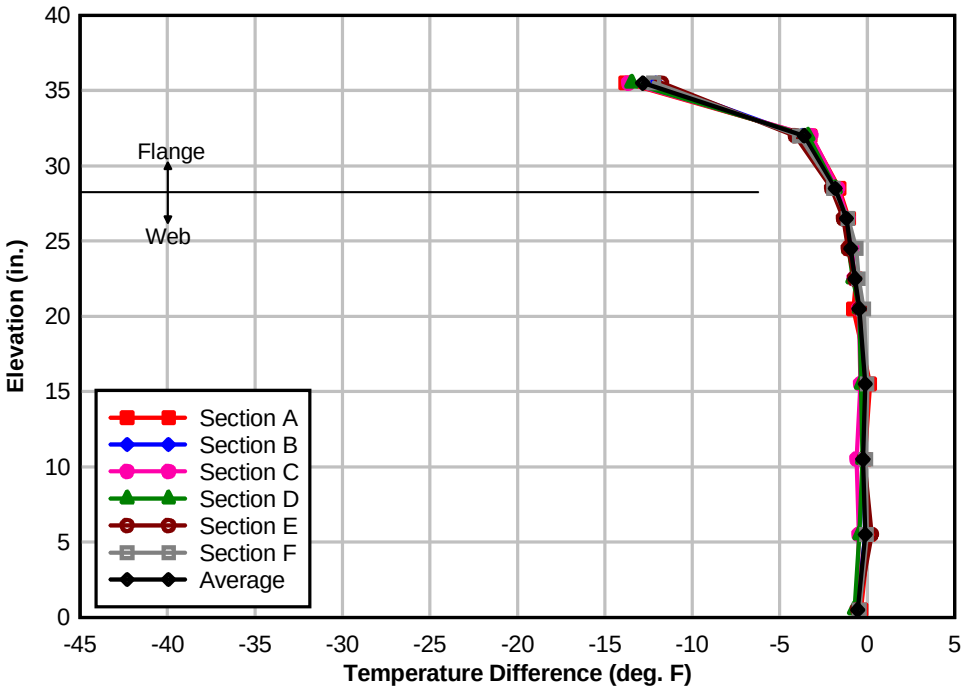

Figure 172 – Comparison of measured thermal gradient profiles with average profile

Elastic modulus derived stresses (E stresses) were the self-equilibrating thermal stresses caused by the negative thermal gradient, and were determined by multiplying the measured strains in Figure 167 and Figure 168 by the elastic moduli of Segment 2 (4850 ksi) and Segment 3 (4850 ksi), respectively. The elastic moduli were calculated by linearly interpolating between cylinder modulus of elasticity data between test ages of 28 and 360 days. At the time of the test, the ages of segments 2 and 3 were 251 and 238 days, respectively.

Figure 173 and Figure 174 show E stress distributions near joint J2 on Segment 2 and Segment 3, respectively. E stresses at midspan and mid-segment on the North side of segments 2 and 3 are compared in Figure 175 and Figure 176, respectively. Also for comparison, self-equilibrating thermal stresses due to the laboratory thermal gradient and the AASHTO design gradient were calculated using the AASHTO recommended procedure discussed in Section 3.2, and are shown in the figures. CTEs from Table 15 and the segment MOEs noted above were used in these calculations.

Table 24 compares E stresses computed at the top of the flanges of segments 2 and 3 with similar stresses obtained by extrapolating from the linear E stress distributions between elevations 32 in. and 35.5 in. (see Figure 173 and Figure 174) on the sides of the segment flanges. E stresses in the extreme top flange fibers were significantly lower than stresses extrapolated to the same location. This condition follows from the relatively smaller stress-inducing thermal strains that were measured at the top surfaces of the flanges (see Figure 169). As discussed previously, the smaller strains were attributed to differential shrinkage at joint J2 and to a lower thermal gradient magnitude than was targeted (as prescribed by the AASHTO gradient) for the top of the flanges of the segments. At an elevation of 32 in., the E stress on Segment 2 was about 88% less than the predicted stress. Both stresses were compressive. The E stress on Segment 3 at the same elevation, however, was tensile whereas the predicted stress was compressive. As was the case for the positive thermal gradient, this was

attributed to the difference in magnitude of the laboratory thermal gradients at sections A through F (from the average thermal gradient used in predicting stresses) at that elevation; the location of the maximum slope change in the thermal gradients (see Figure 177).

E stresses and predicted stresses caused by the laboratory-imposed nonlinear negative thermal gradient in the top 4 in. of the flanges of segments 2 and 3 are compared in Table 25. Predicted stresses in the extreme top flange fibers (where the maximum tensile stresses were expected to occur, had the gradient been linear in the top 4 in. of the flanges) are not shown in the table because the shape and magnitude of the thermal gradient in this region were not measured. E stresses 0.5 in. below the top of the flange (maximum E stresses) were approximately 25% and 14% less than corresponding predicted stresses in Segment 2 and Segment 3, respectively. E stresses caused by the positive thermal gradient (see Section 14.1) at the same location were 3% and 8% less than corresponding stresses predicted in Segment 2 and Segment 3, respectively. Beam response was more sensitive to small errors in thermocouple readings in the negative thermal gradient case than in the positive thermal gradient case because of the relatively lesser magnitude (temperature change) of the negative thermal gradient. This was thought to be the reason for the greater discrepancy between maximum E stresses and corresponding predicted stresses due to the negative gradient. Taking into consideration the effects of differential shrinkage at joint J2, small errors in measuring gauge elevations, and differences between thermal gradient profiles (at sections A through F) and the average thermal gradient profile within the top 4 in. of the segment flanges, these differences were considered to be within the limits of experimental error.

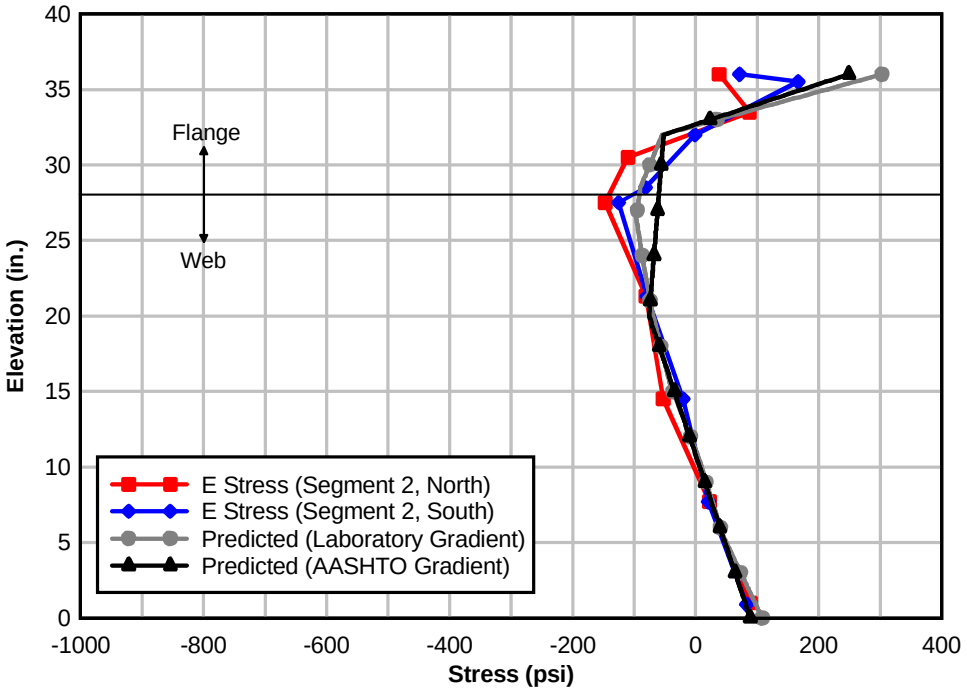

Figure 173 – E stresses near joint J2 (Segment 2)

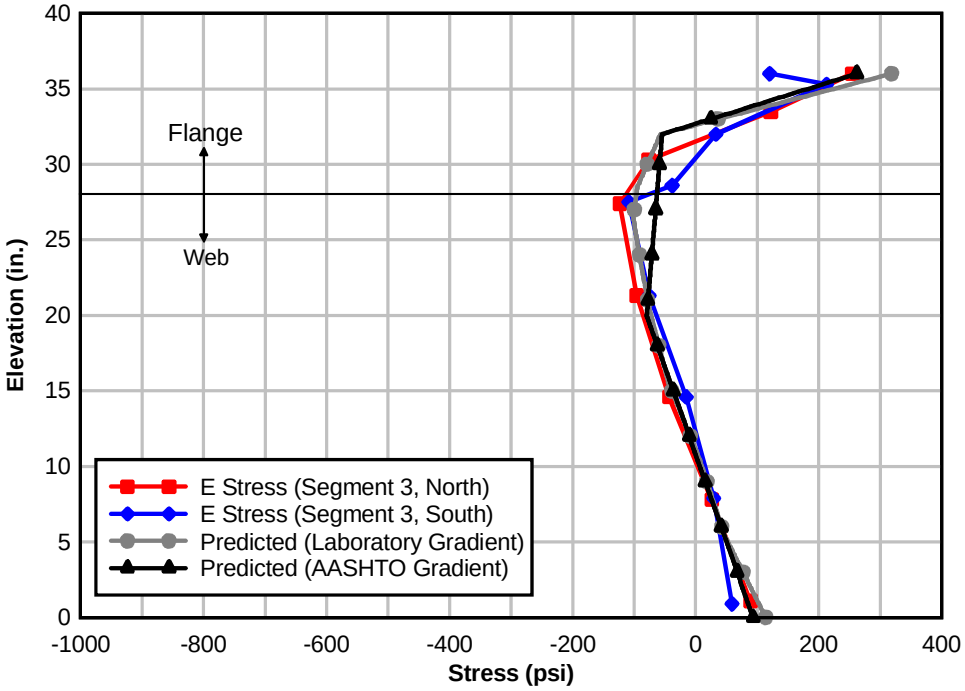

Figure 174 – E stresses near joint J2 (Segment 3)

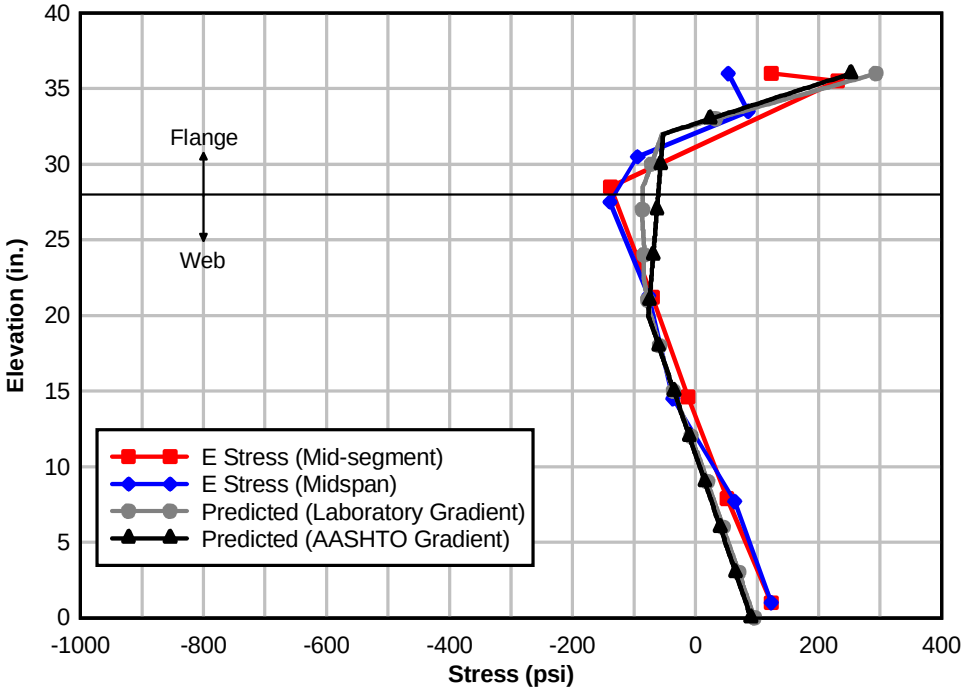

Figure 175 – E stresses at mid-segment and midspan (Segment 2, North)

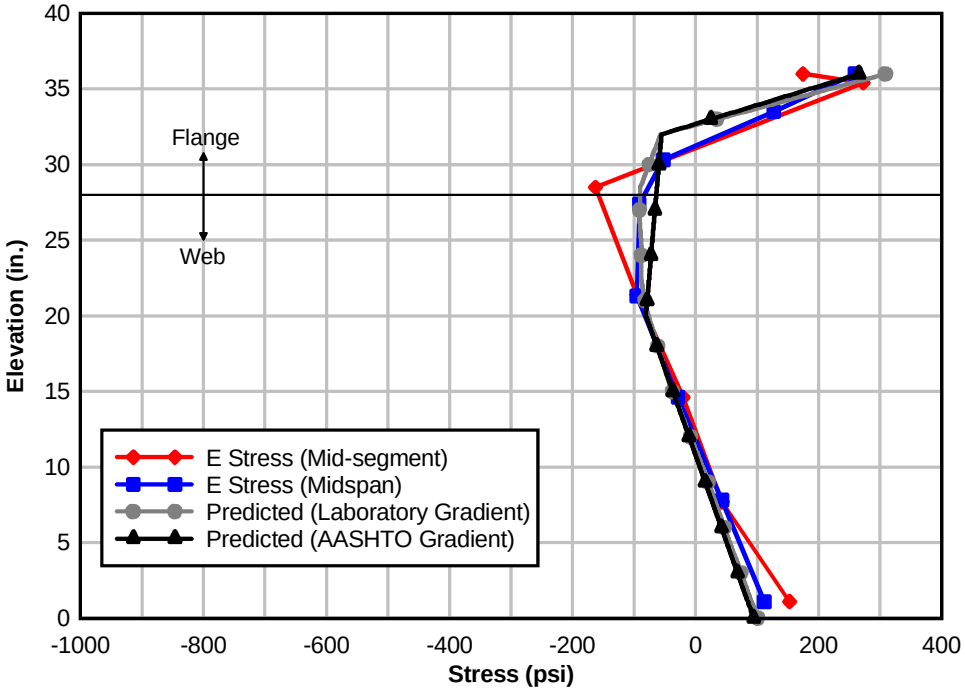

Figure 176 – E stresses at mid-segment and midspan (Segment 3, North)

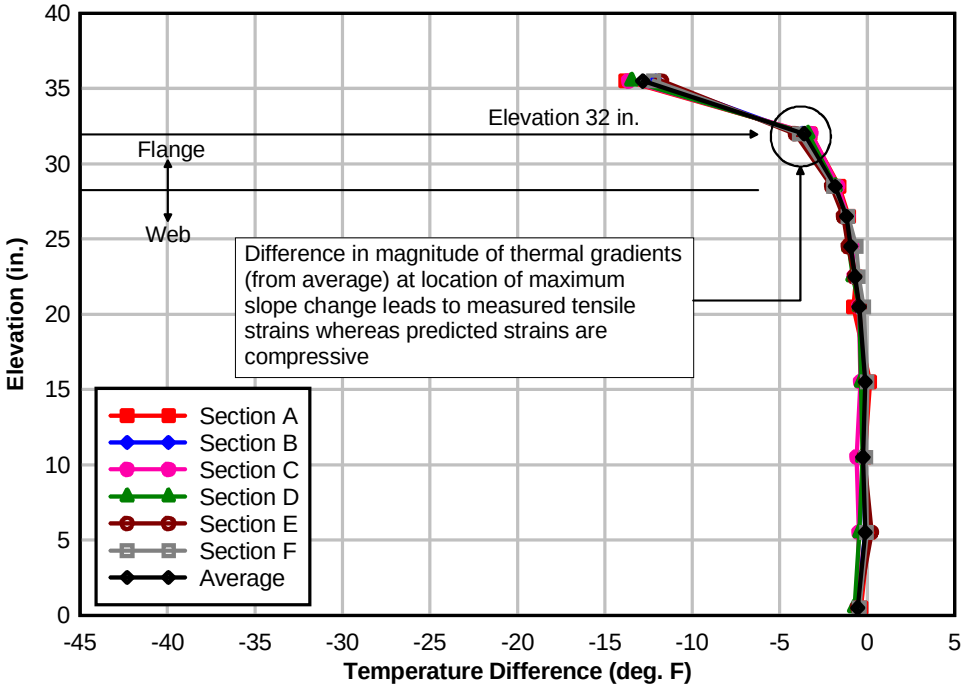

Figure 177 – Difference in magnitude of imposed thermal gradients at location of maximum slope change (elevation 32 in.)

Table 24 – Comparison of E stresses and extrapolated stresses on top of segment flanges near joint J2 (laboratory negative thermal gradient)

	E Stress (psi)	Extrapolated (psi)	Measured/Extrapolated
Segment 2, North	38	252	0.151
Segment 2, South	71	191	0.372
Segment 3, North	255	277	0.921
Segment 3, Middle	69	265	0.260
Segment 3, South	120	252	0.476

Table 25 – Comparison of E stresses and predicted self-equilibrating thermal stresses caused by laboratory negative thermal gradient near joint J2

	Elevation (in.)	Average E Stress (psi)	Average Predicted (psi)	E Stress/Predicted
Segment 2	36	55	N/A	N/A
	35.5	193	258	0.748
	33.5	79	80	0.994
	32	-6	-54	0.116
Segment 3	Elevation (in.)	Average E Stress (psi)	Average Predicted (psi)	E Stress/Predicted
	36	148	N/A	N/A
	35.5	235	272	0.865
	33.5	118	84	1.413
	32	31	-57	-0.539

15.2 JOINT-OPENING DERIVED STRESSES (J STRESSES)

Joint-opening derived stresses (J stresses) were determined using the procedure outlined in Section 14.2 and data collected from steps 3 and 5 of the load sequence shown in Figure 162. For the thermal loading sequence used in the negative gradient tests, Equation 21 and Equation 22 were modified as follows:

$$f_P(y,z) + f_{SW}(y,z) + f_{UT}(y,z) + f_R(y,z) = 0, \{(y,z) \in R\} \quad \text{Equation 31}$$

$$f_P(y,z) + f_{SW}(y,z) + f_{UT}(y,z) + f_J(y,z) + f_T(y,z) = 0, \{(y,z) \in T\} \quad \text{Equation 32}$$

where, f_{UT} represents stresses caused by the expansion of the concrete segments (against the restraint of the prestress bars) due to a uniform temperature increase (see Figure 178) and all other quantities are as described in Section 14.2. The f_{UT} term was added to account for the fact that the negative gradient was imposed by first heating the entire section and then cooling the top portion.

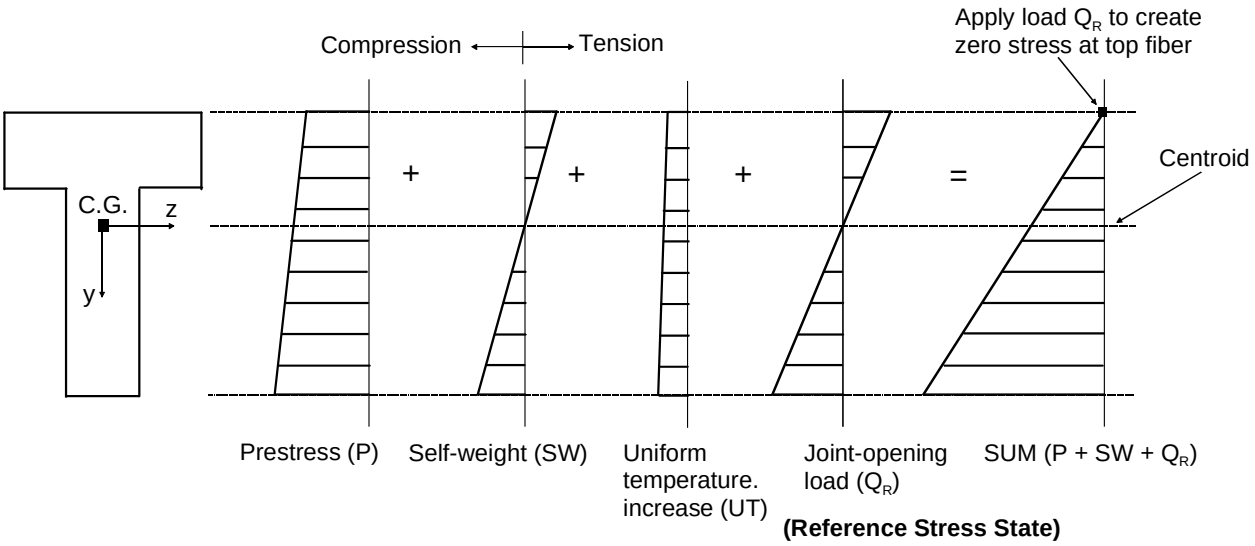

(a) Mechanical and uniform temperature change

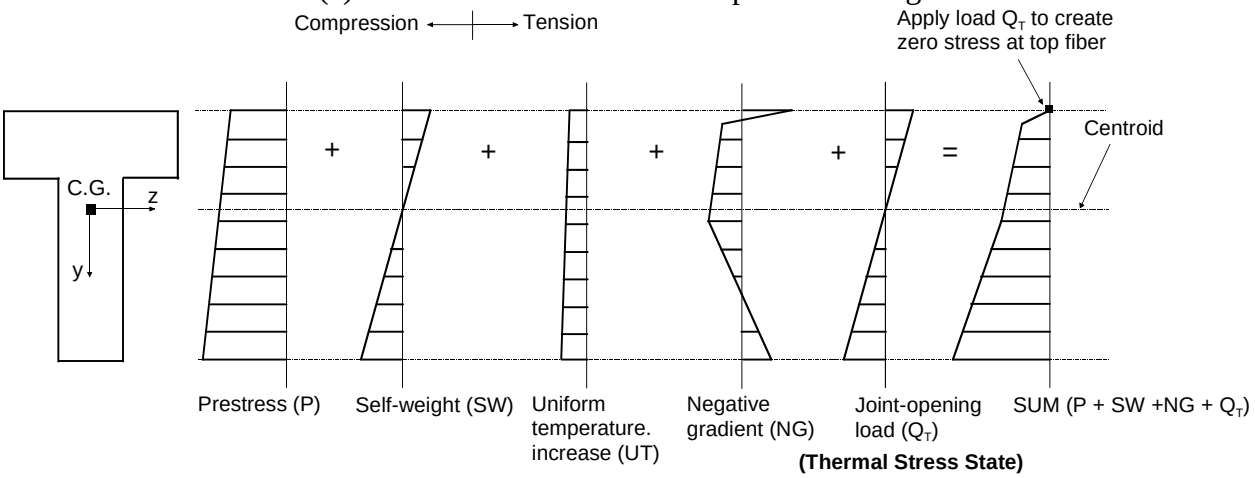

(b) Mechanical, uniform temperature change, and negative thermal gradient

Figure 178 – Superposition of component stress blocks

Figure 179 and Figure 180 show variations of concrete strain with applied load near joint J2 on the North side of Segment 3 at the reference stress state (reference temperature) and thermal stress state (with negative thermal gradient), respectively. Similar plots near the same joint on the South side are shown in Figure 181 and Figure 182, respectively. The variation of concrete strain with applied load on top of the flanges of segments 2 and 3 near joint J2 at the reference and thermal stress states are shown in Figure 183 and Figure 184, respectively. Data collected from strain gauges near joint J2 on Segment 2, LVDTs mounted across joint J2 on top of the flanges of segments 2 and 3, and LVDTs mounted across the same joint on the South side can be found in Appendix F.

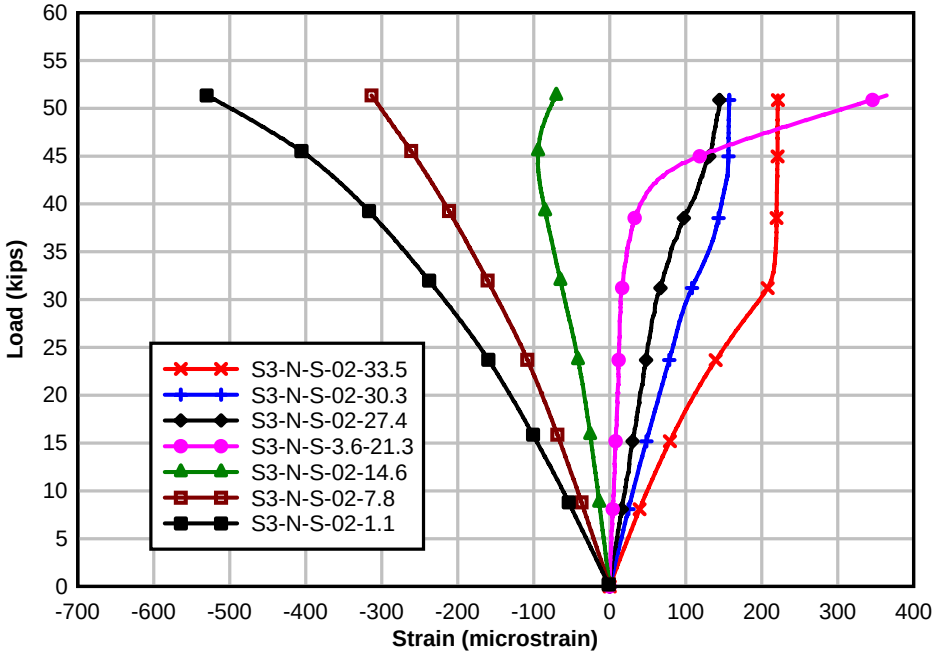

Figure 179 – Load vs. strain at reference temperature (Segment 3, North)

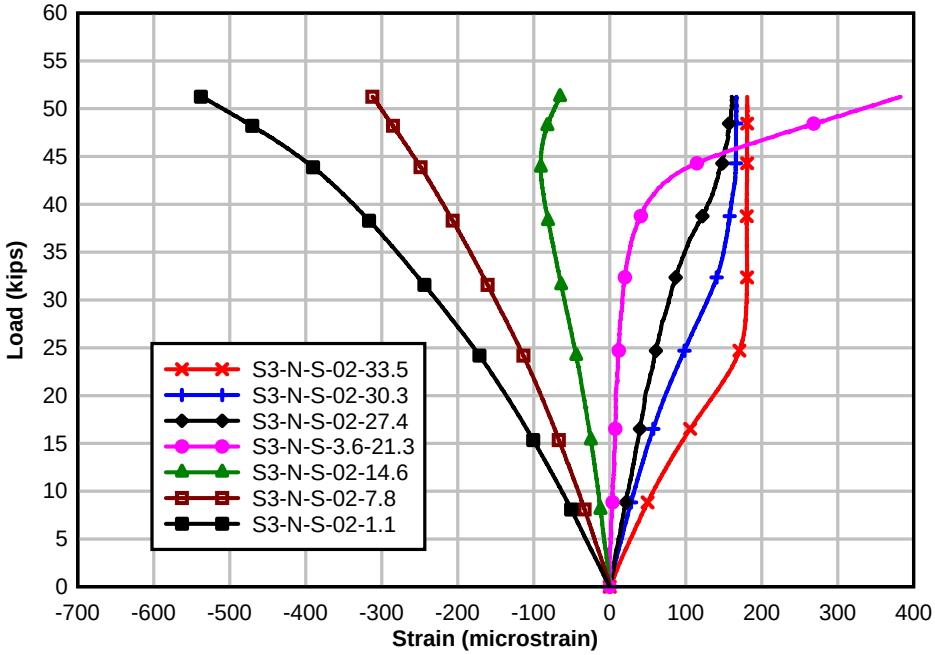

Figure 180 – Load vs. strain with negative thermal gradient (Segment 3, North)

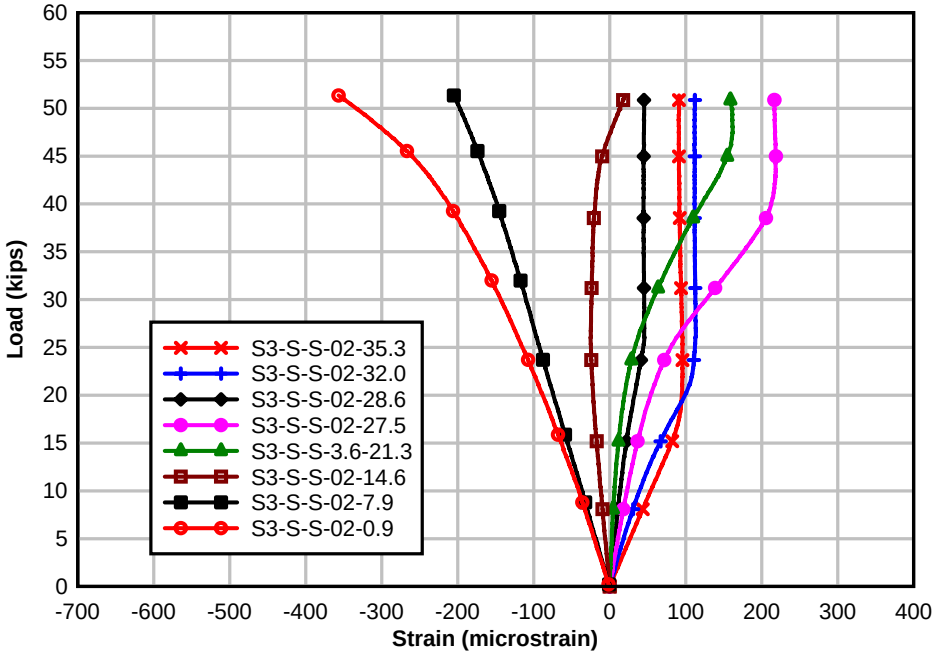

Figure 181 – Load vs. strain at reference temperature (Segment 3, South)

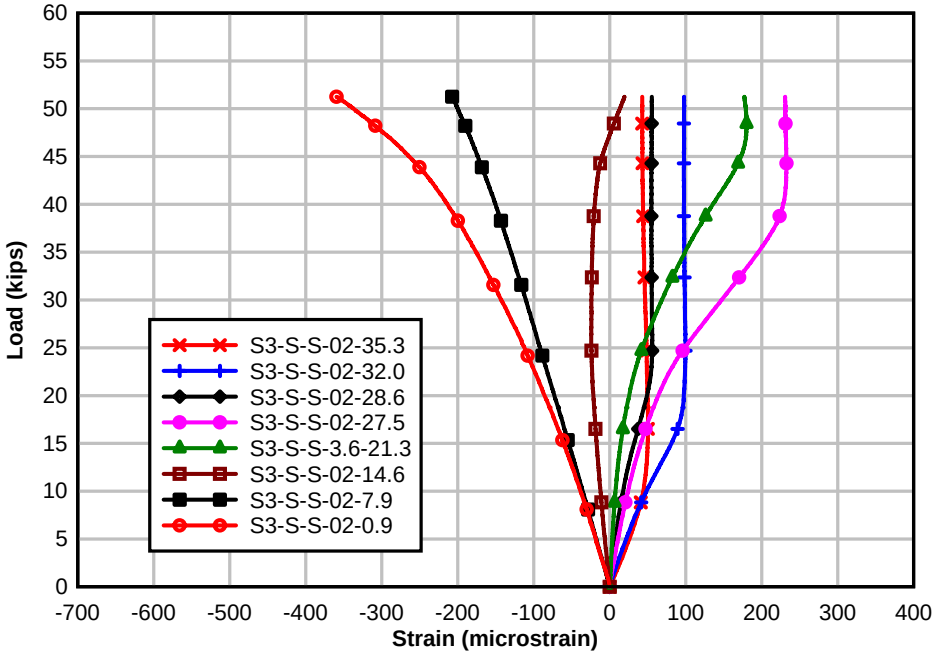

Figure 182 – Load vs. strain with negative thermal gradient (Segment 3, South)

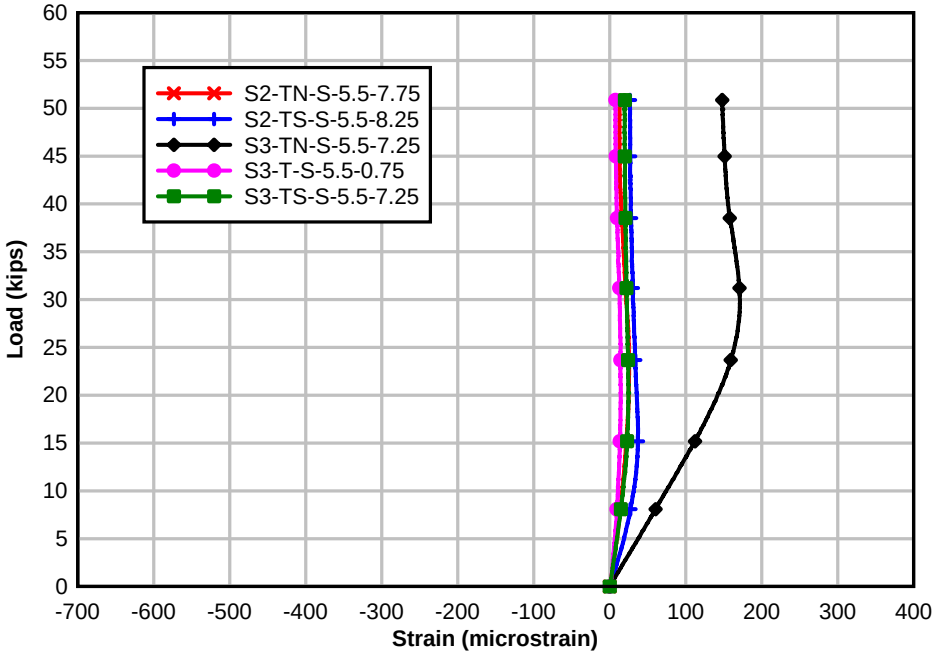

Figure 183 – Load vs. strain at reference temperature (Top flange)

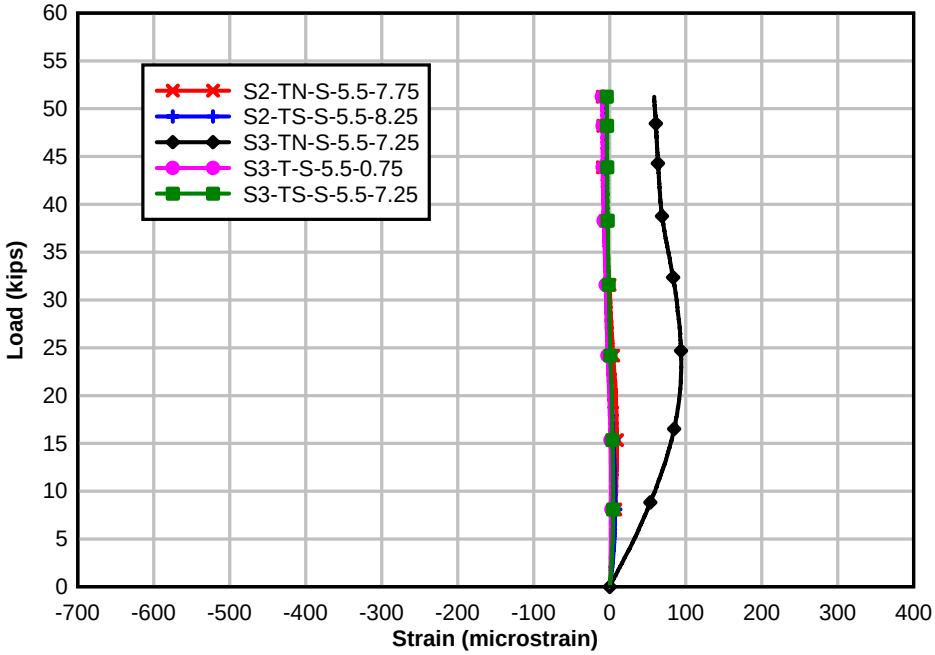

Figure 184 – Load vs. strain with negative thermal gradient (Top flange)

A comparison of concrete strains at same side of joint J2 at the reference and thermal stress states shows that at identical elevations in the top 4 in. of the flange, the joint opened at lower loads at the thermal stress state than it did at the reference stress state. This is illustrated in Figure 185 with data taken from the strain gauges at elevations 33.5 in. on the North and 35.3 in.

on the South side of the joint. The same is true of the top flange strains shown in Figure 183 and Figure 184. LVDTs on the sides and top of the flange (see Appendix F) also show the joint opening at lower loads at the thermal stress state than at the reference stress state. This was indicative of the development of tensile stresses in the top concrete fibers at joint J2 due to the negative thermal gradient. It is also evident in Figure 185 that, similar to the positive thermal gradient, the strain difference between vertical portions of strain diagrams, at the reference and thermal stress states, was dependent only on the elevation of the gauge and not on the side (North/South) of the joint on which the gauge was located.

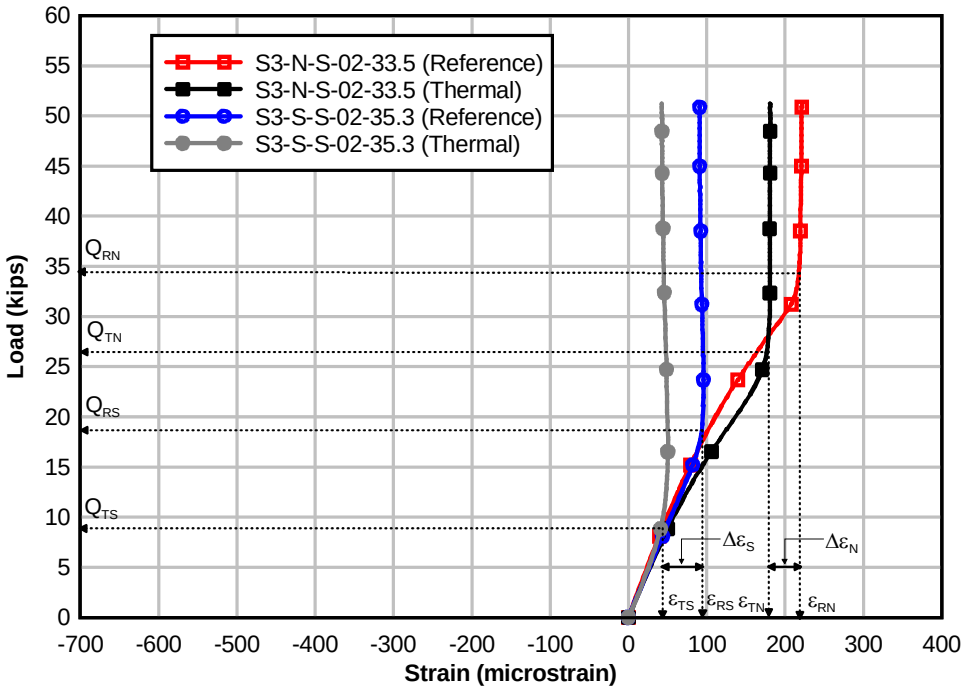

Figure 185 – Comparison of strain differences on North and South sides of joint J2 (Negative thermal gradient)

Loads that caused joint J2 to open at the reference and thermal stress states were detected using the strain data shown in Figure 179 through Figure 184 above, and Figure 269 through Figure 276 in Appendix F. Applied loads at the cantilevered-end of the test beam, which caused joint J2 to open at various depths, are shown in Figure 186. The sign convention for moments and curvatures which is the same as that used in Chapter 14, is shown (for convenience) in Figure 187.

Figure 188 through Figure 190 show estimated contact areas at joint J2 at the reference and thermal stress states just as opening of the joint was detected from strain gauges at elevations of 35.5 in. (South), 33.5 in. (North), and 32.0 in. (South), respectively. These plots were developed using the same approach detailed in Chapter 14.

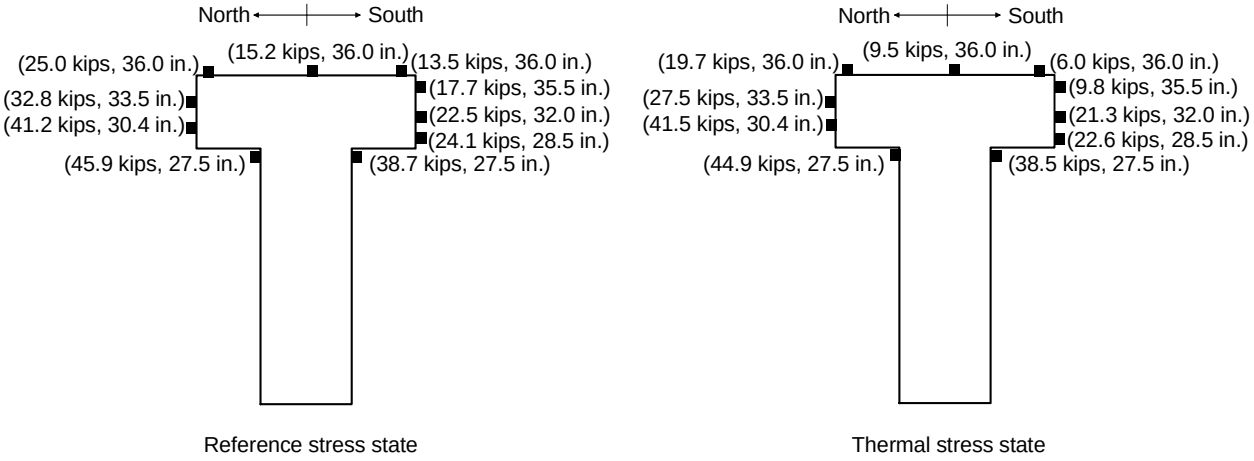

Figure 186 – Joint opening loads detected from strain gauges close to joint J2

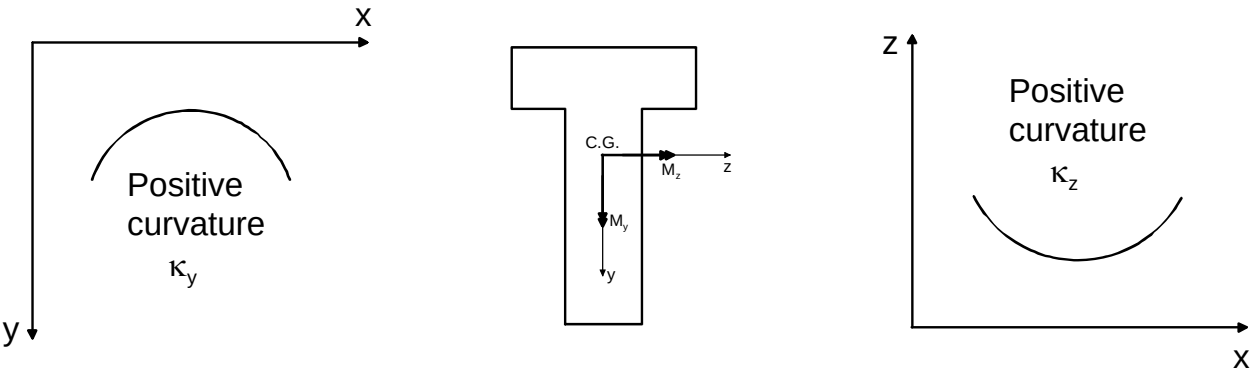

Figure 187 – Sign convention for moments and curvature

S-S-S-02-35.5

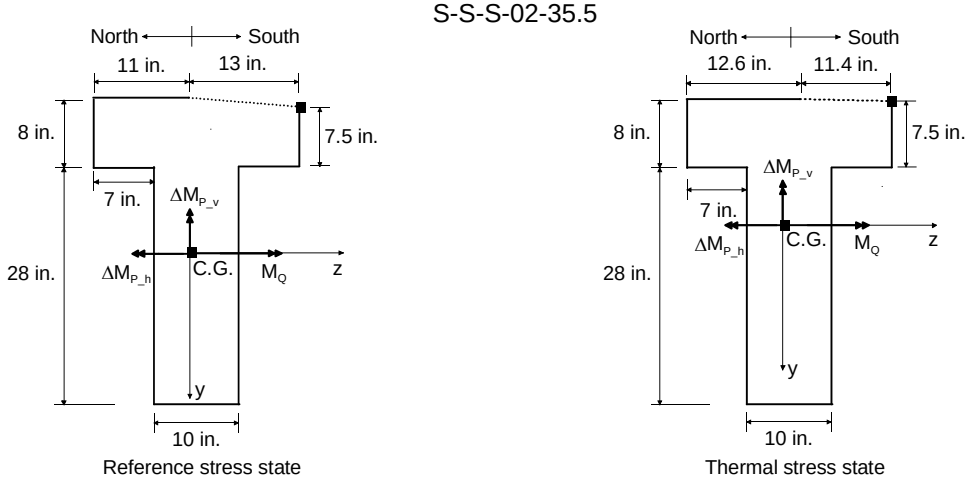

Figure 188 – Contact area at joint J2 at incipient joint opening on South side at elevation 35.5 in.

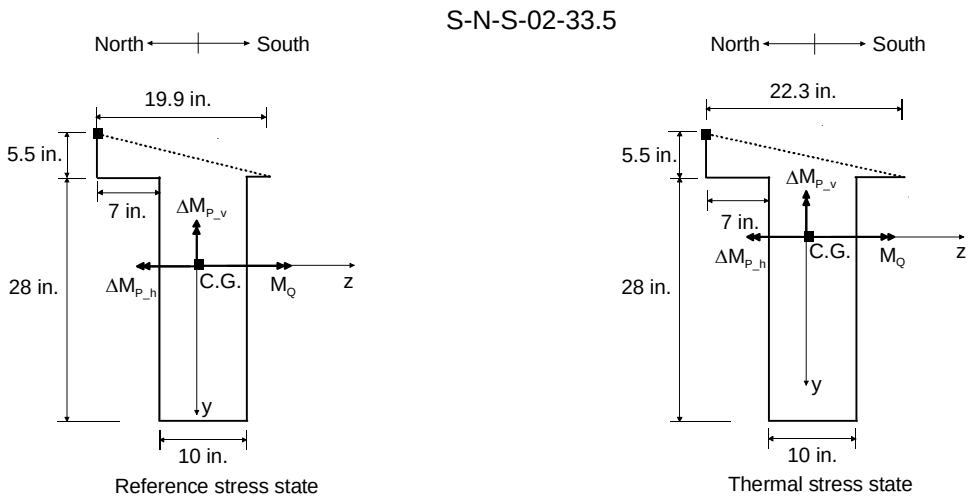

Figure 189 – Contact areas at joint J2 at incipient joint opening on North side at elevation 33.5 in.

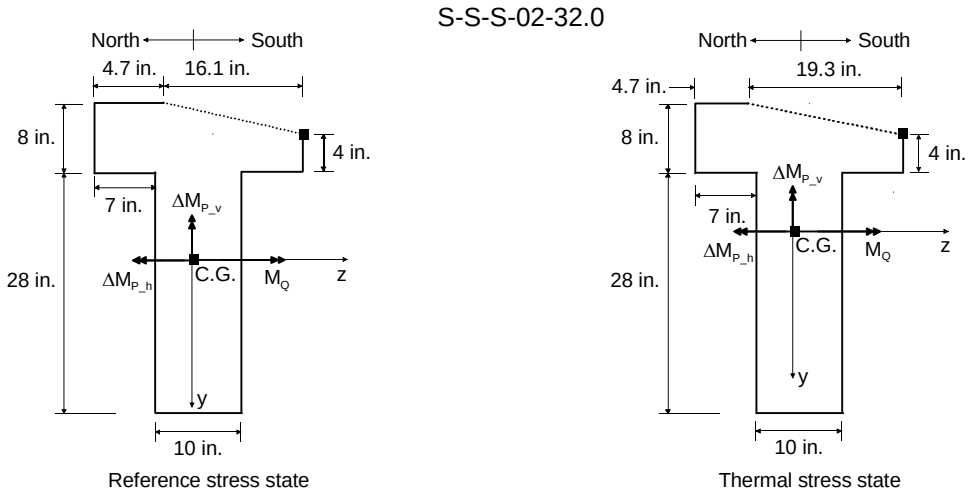

Figure 190 – Contact areas at joint J2 at incipient joint opening on South side at elevation 32.0 in.

In Table 26 shows calculated J stresses are presented for the locations of strain gauges on the sides of the beam within the top 4 in. of the flange. As for the positive thermal gradient, the total stresses (stresses determined from Equation 24) though positive, indicating tension, actually represent relief of existing compressive stresses at J2 prior to the application of joint-opening loads. J stresses were determined by taking the difference between total stresses at the reference stress state and total stresses at the final stress state.

Changes in prestress (as the beam was mechanically loaded and joint J2 opened) accounted for less than 1% of total stresses. Calculated total stresses were, therefore, essentially dependent on the magnitude of joint-opening loads. J stresses, however, were dependent on the difference between the joint-opening loads at the reference and final stress states. For example, the loads initiating opening of joint J2 on the North side at an elevation of 33.5 in. were greater than they were on the South side at an elevation of 35.5 in. as can be seen from the magnitudes

of the moments in Table 26. However, calculated J stresses at an elevation of 33.5 in. were lower than J stresses at an elevation of 35.5 in. because the difference in joint-opening moments at elevation 33.5 in. was lower than the difference in moments required to open the joint at elevation 35.5 in.

J stresses and stresses predicted with the AASHTO procedure using the laboratory thermal gradient, in the top 4 in. of the flange, are compared in Table 27. J stresses 0.5 in. below the top of the flange (maximum J stresses) were approximately 17% and 23% less than corresponding predicted stresses in Segment 2 and Segment 3, respectively. At elevation 32 in., J stresses were about 82% less than predicted stresses. Both predicted and J stresses were compressive.

J stresses and E stresses in the top 4 in. of the flange are compared in Table 28. Maximum J stresses were within 11% of maximum E stresses. J stresses were, in general, higher than E stresses on Segment 2 and lower than E stresses on Segment 3. This could possibly be due to small errors in estimating contact areas and determining joint-opening loads. Another possibility is that J stresses represented the average stress between segments 2 and 3 at joint J2 whereas E stresses represented stresses on each segment about 2 in. away from joint J2.

Table 26 – J stresses in top 4 in. of flange

Gauge Elevation	Moments due to Joint-opening Loads (kip-in.)		Total Stresses (psi)		J Stress (psi)
	Reference	Thermal	Reference	Thermal	
35.5 in. S	1679	885	443	229	214
33.5 in. N	2961	2510	861	740	121
32.0 in. S	1986	1896	625	635	-10

Table 27 – Comparison of J stresses and predicted stresses in top 4 in. of flange

Segment 2			
Gauge Elevation	J Stress (psi)	Predicted Stress (psi)	J Stress/Predicted Stress
35.5 in. S	214	258	0.829
33.5 in. N	121	80	1.500
32.0 in. S	-10	-54	0.185
Segment 3			
Gauge Elevation	J Stress (psi)	Predicted Stress (psi)	J Stress/Predicted Stress
35.5 in. S	214	272	0.787
33.5 in. N	121	84	1.440
32.0 in. S	-10	-57	0.175

Table 28 – Comparison of J stresses and E stresses in top 4 in. of flange

Segment 2			
Gauge Elevation	J Stress (psi)	E Stress (psi)	J Stress/E Stress
35.5 in. S	214	193	1.109
33.5 in. N	121	79	1.532
32.0 in. S	-10	-6	1.667
Segment 3			
Gauge Elevation	J Stress (psi)	E Stress (psi)	J Stress/E Stress
35.5 in. S	214	235	0.911
33.5 in. N	121	118	0.975
32.0 in. S	-10	31	-0.323

16 SUMMARY AND CONCLUSIONS – PART ONE

Results from a series of tests conducted on a 20 ft-long 3 ft-deep segmental concrete T-beam, aimed at quantifying self-equilibrating thermal stresses caused by AASHTO design nonlinear thermal gradients, have been presented and discussed. The beam consisted of four 5 ft long segments that were post-tensioned together. Layers of copper tubes, which would later carry water, were embedded in the middle two segments of the beam (Segments 2 and 3), designated "heated" segments. Thermocouples were also cast into the heated segments to monitor the distribution of temperature. The two end segments of the beam (Segments 1 and 4), which were designated "ambient" segments, were strengthened using steel reinforcing bars to carry loads at the prestress anchorage zones. The beam was vertically supported at midspan and at the end of one ambient segment. Mechanical loads were applied at the cantilevered end and thermal profiles were imposed on the heated segments by passing water at specific temperatures through each layer of copper tubes. The region of interest in the experimental program was the dry joint between the two heated segments of the beam (designated joint J2), which was heavily instrumented with surface strain gauges and LVDTs. Detection of opening of the joint was of primary importance in quantifying stresses caused by the application of AASHTO nonlinear thermal gradients.

The experimental program consisted of determining the in-situ coefficient of thermal expansion (CTE) of the heated segments; investigating the behavior of the beam under the action of mechanical loads; applying a uniform temperature change on the heated segments to investigate the free expansion behavior of the beam; and imposing the AASHTO design nonlinear thermal gradients in combination with mechanical loads for the purpose of quantifying self-equilibrating thermal stresses due to the thermal gradients.

In-situ CTEs of Segments 2 and 3 were determined by imposing uniform and linear temperature distributions on each segment. The CTE of Segment 3 was also determined using a procedure specified by AASHTO. Good agreement was found between the in-situ CTEs determined using uniform and linear thermal profiles for both segments. Good agreement was also found between the CTE determined using the AASHTO method and the average in-situ CTE of Segment 3. AASHTO CTE testing was not conducted for Segment 2 because the cylinders required for the test were not cast for this Segment.

Mechanical load tests indicated that strain gauges mounted on the side surfaces of the beam close to the joint at midspan (joint J2) were the most reliable instruments in detecting opening of the joint. However, strain gauges mounted on the top surfaces of the segment flanges near the joint showed little change in strain with increasing applied load. This was attributed to an imperfect fit (despite match-casting of the segments) at the joint, and differential shrinkage in the top flange fibers which were unsealed and exposed to the laboratory environment during curing of the segments. Strain distributions through the height of the contact area at the joint (before and after the joint opened) were generally found to be linearly dependent on applied load, which allowed for the use of classical flexural stress formulas in quantifying stresses due to the AASHTO nonlinear thermal gradients. Observations and conclusions that were drawn from the directly measured experimental data are as follows:

- A uniform temperature increase of 41 ^{o}F increased the prestress force by about 6% of the initial prestress due to differential movement and heating between the bars and concrete segments. The measured change in prestress compared well with predicted

values determined using in-situ CTEs and laboratory determined concrete elastic moduli.

- Measured concrete strains caused by the uniform temperature increase were generally tensile, whereas predicted strains (determined using the AASHTO recommended procedure) were compressive. The difference was attributed primarily to slight variations in temperature between the inner core and the outer perimeter of the heated segments.
- Measured stress-induced concrete strains caused by the laboratory-imposed nonlinear thermal gradients on top of the flanges of the heated segments near joint J2 were significantly less than predicted for both positive and negative thermal gradients. For the positive thermal gradient, average measured strains on top of the flanges of segments 2 and 3 were about 56% and 39% less than predicted strains, respectively. For the negative thermal gradient, average measured strains at the same locations on segments 2 and 3 were about 81% and 53% less than predicted. The differences were attributed to differential shrinkage in the top flange fibers and a possible discontinuity in the thermal gradients (positive and negative) within the top 0.5 in. of the flanges of the heated segments.
- At elevations below 0.5 in. from the top surface of the segment flanges near joint J2, measured stress-induced concrete strains caused by the laboratory-imposed nonlinear thermal gradients agreed well with strains predicted using the AASHTO recommended method for the analysis of nonlinear thermal gradients. Maximum measured stress-induced concrete strains (which occurred at elevation 35.5 in.) under the action of the positive thermal gradient were about 3% and 7% less than predicted strains on segments 2 and 3, respectively. For the negative thermal gradient, maximum measured stress-induced concrete strains (at the same location as for the positive thermal gradient) were about 25% and 14% less than predicted strains on segments 2 and 3, respectively.

Two independent methods were also used to quantify concrete stresses caused by the laboratory-imposed nonlinear thermal gradients at the joint between the heated segments. The first method involved multiplying measured thermal stress-induced concrete strains by elastic moduli (E stresses) and the second method involved determining of stresses at the joint using the known stress state at incipient joint opening (J stresses). J stresses were determined within the top 4 in. of the flanges of the heated segments near joint J2 while the E stresses were determined at the strain gage locations. Conclusions drawn from quantifying the E stresses and J stresses are as follows:

- Maximum E stresses caused by the positive thermal gradient, which occurred at elevation 35.5 in. (i.e. 0.5 in. below the top surface of the segment flanges), were about 3% and 8% less than corresponding predicted self-equilibrating thermal stresses in Segment 2 and Segment 3, respectively. Maximum J stresses caused by the positive thermal gradient (also at elevation 35.5 in.) were about 10% and 15% less than the predicted self-equilibrating thermal stresses in segments 2 and 3, respectively.
- In the case of the negative thermal gradient, maximum E stresses (which also occurred at elevation 35.5 in.) were about 25% and 14% less than corresponding

predicted self-equilibrating thermal stresses in segments 2 and 3, respectively. Maximum J stresses (at the same elevation) were about 17% and 23% less than predicted stresses in segments 2 and 3, respectively. Recall that the peak temperature difference in the negative thermal gradient is 30% of positive thermal gradient peak. The larger differences for the negative thermal gradient were likely due to the sensitivity of the average temperature to local deviations across the width of the flange.

E stresses and J stresses in the top few inches of the flanges of segments 2 and 3 were in general lower than stresses predicted using the AASHTO recommended procedure. In particular, the maximum quantified stresses due to the negative thermal gradient were on the average about 20% less than corresponding predicted stresses (at the same location). These differences between quantified and AASHTO predicted stresses could, however, not be attributed to any flaw in the AASHTO procedure. They were considered to be likely the result of effects of differential shrinkage of the top portion of the segment. This shrinkage resulted in a joint that did not match perfectly. Consequently, contact stresses due to prestress were lower at the top. Differential shrinkage of full-size segments will exacerbate this issue on bridges with dry joints. It is possible that bridges with epoxy joints will have a more uniform prestress at the joints under stresses applied after the epoxy sets.

This study focused mainly on quantifying stresses caused by the AASHTO nonlinear thermal gradients. Some suggestions on future research are proposed:

- The current AASHTO nonlinear thermal gradients are computationally inconvenient and do not work well with most structural analysis software. Furthermore, the stresses of interest in design are the stresses in the top 4 in. of box-girder flanges. A study on simplifying the nonlinear thermal gradients in a combination of linear gradients, such that stresses of equal magnitude (especially the maximum stresses) caused by the nonlinear thermal gradients in the top 4 in. are generated by the combination of linear gradients, would greatly simplify the computational effort that currently goes into calculating self-equilibrating stresses in complex box-girder sections.
- The effect on concrete durability of tensile stresses generated by the AASHTO negative thermal gradient in the top few inches of the flanges of segmental bridges needs investigation. Though tensile stresses have been known to cause damage to concrete, this damage has been difficult to quantify. A study into the effect of the relatively steep self-equilibrating stress gradient in the top few inches of concrete (compared with typical bending stresses) on the potential for cracking would lead to a better understanding of the level of damage that gradient-induced tensile stresses may cause. Part Two of this report covers tests to determine the effect of the gradient on cracking behavior.

PART TWO – EFFECT OF SELF-EQUILIBRATING THERMAL STRESSES ON CRACKING

17 OVERVIEW – PART TWO

This portion of the research report covers component testing of prestressed concrete specimens and a final test to cracking on the beam used for the research reported in Part One. The component testing consisted of prestressed concrete specimens constructed to replicate the top 8 in. of a segmental concrete bridge deck where the self-equilibrating stresses from the negative thermal gradient causes net tension. A series of six test sets were performed during which the specimens were initially prestressed and then loaded in tension until a crack formed. The objective was to determine the effect of an applied nonlinear thermal gradient on the cracking stress and behavior of the concrete specimen relative to a specimen that had no thermal gradient applied. A negative nonlinear thermal gradient was applied to one specimen from each test set using an open-channel flow of chilled water. The specimens were each loaded to failure and the results of each test set compared.

The beam reported on in Part One of this report was loaded to cracking with the AASHTO negative thermal gradient imposed. The intent of this final test was to further investigate the effect of the AASHTO negative thermal gradient and resulting self-equilibrating stresses on cracking behavior in prestressed concrete. The segmental beam joints were sealed with epoxy and prestressed to ensure that net tensile stresses would form during loading. The test setup and application of the AASHTO negative thermal gradient was similar to that of Part One tests. The beam was loaded three times. The first and third loading were in conjunction with the negative thermal gradient. The second loading was with the girder at ambient conditions.

18 TEST DESIGN

This section describes the overall test setup, test specimen design, load frame design, setup for thermal application, and concrete mixture design used in the test program. The purpose of the test setup and design of multiple components was to allow for the prestressing and direct tensile loading of the concrete specimens.

18.1 APPROACH

As in Phase I, the Santa Rosa Bay (SRB) Bridge located near Milton, FL was used as a prototype for developing a component specimen that could be used to evaluate the effect of a nonlinear thermal gradient on cracking behavior in concrete. The section immediately adjacent to the pier segment of the SRB Bridge, shown in Figure 191, was used to establish the stress states and geometry of the test specimen. The maximum negative moment under combined loads will occur at this location resulting in maximum tensile stresses. The addition of the negative thermal gradient imposes a sharp increase of predicted tensile stress in the top of the SRB Bridge section. This predicted tensile stress resulting from the thermal gradient leads to additional post-tensioning requirements in design.

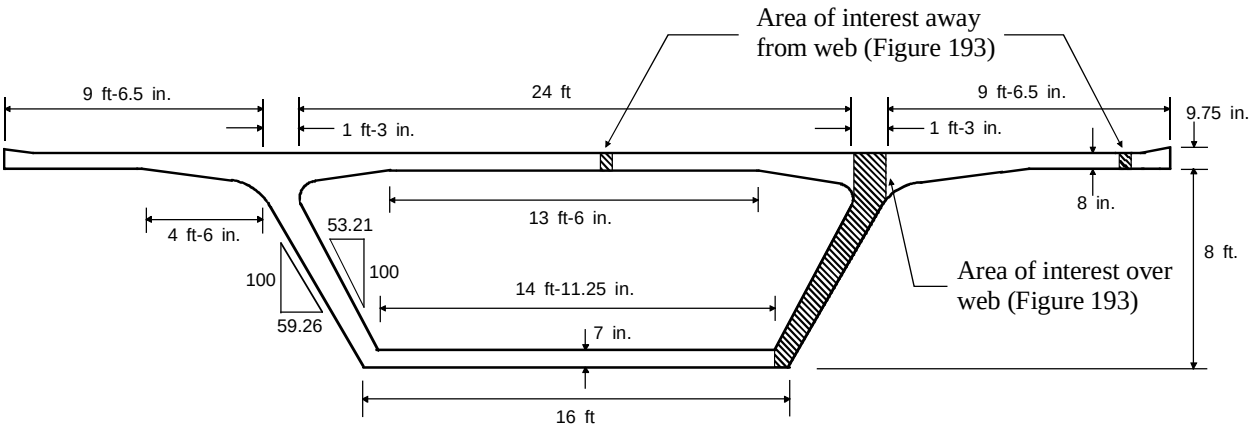

Figure 191: Typical cross section of Santa Rosa Bay Bridge

Initially, the design loads and thermal gradients of the SRB Bridge were investigated over the full height of the box section as shown in the figure. Stress profile components of a simplified load combination for the SRB Bridge are shown in Figure 192 for the section immediately adjacent to the pier segment. The stress profiles show the components of prestress, combined dead loads, superimposed service loads, and predicted self-equilibrating stress due to the nonlinear AASHTO negative thermal gradient. The total stress gradient is shown with and without the predicted self-equilibrating stress. The self-equilibrating stresses create a severe tensile stress gradient in the upper four to six inches of the deck. Although not addressed in the AASHTO *Guide Specifications for Design and Construction of Segmental Concrete Bridges* (1999) it is likely that this stress state is different in the deck away from the web due to shear lag. The deck slab at the tip of the cantilever or midway between the webs does not have the restraint offered by the web for the deck sections over the web. To satisfy the design requirements for

serviceability, however, this severe self-equilibrating tensile stress gradient must be offset by prestressing ostensibly over the full width of the slab.

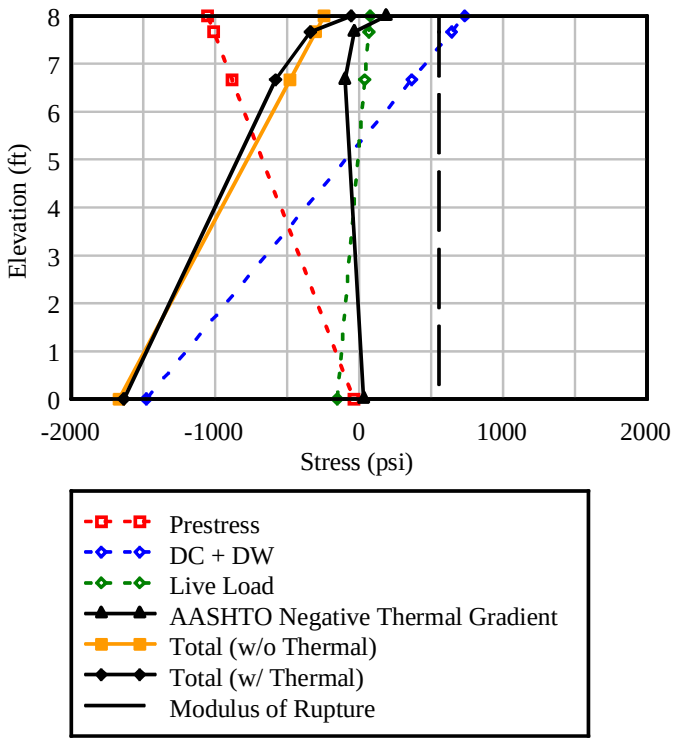

Figure 192: SRB Bridge stress profiles

Figure 193a shows the stress state in the deck over the web of the SRB Bridge prototype. Each stress block is plotted to scale relative to the zero stress datum and the modulus of rupture ($f_{r.}$). The self-equilibrating stresses were calculated with the negative design gradient applied over the full depth of the box section. The service stresses include both the precompression and stresses from applied loads such that the sum of these stresses and the self-equilibrating stresses equal the modulus of rupture.

Figure 193b shows the stress state of the deck if it were completely unrestrained by the web under the negative design gradient. It has been assumed that the negative thermal gradient developed in the deck away from the web would be that specified by AASHTO *Guide Specifications for Design and Construction of Segmental Concrete Bridges* (1999), shown in Figure 5 with the depth "A" taken as 4 in. Although the Guide indicates that these provisions are intended for members over 24-in. deep, the self-equilibrating stresses for the thermal gradient are calculated for comparison to those determined for the full depth of the structure. Depending on the distance between webs, it is postulated that the deck sections away from the restraint of the webs will have self-equilibrating stress profiles that are more similar to Figure 193b rather than Figure 193a due to shear lag.

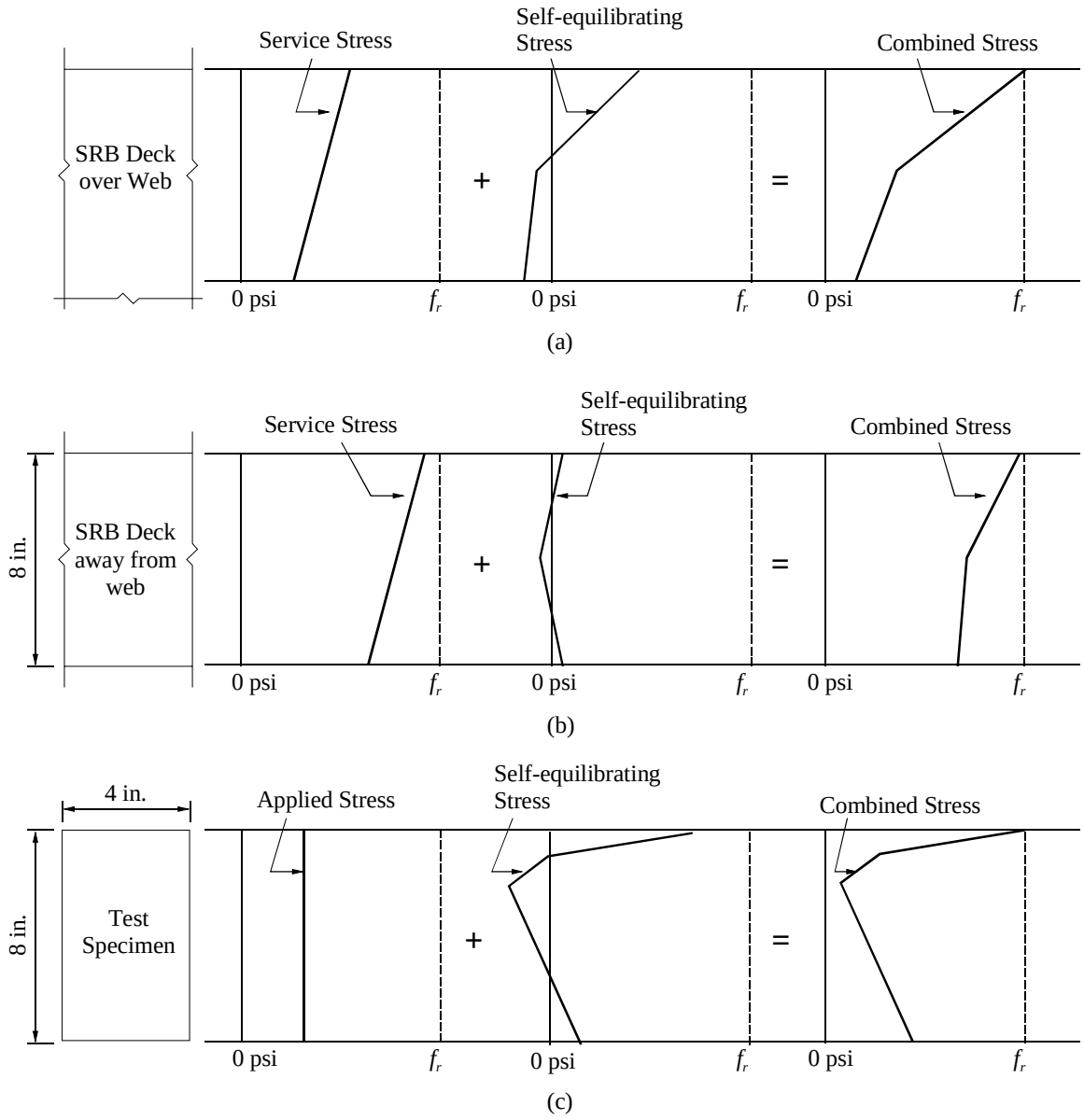

Figure 193: Stress profiles of (a) SRB Bridge over the web, (b) SRB Bridge away from the web, and (c) test specimen.

Ideally, multiple full scale models of the SRB Bridge would be constructed and tested with and without nonlinear thermal gradients under an applied mechanical load. This would capture the behavior illustrated in both Figure 193a and Figure 193b. Laboratory and budget constraints, however, restricted the size of the specimen. Consequently, a portion of the top flange of the box girder (Figure 191), where the self-equilibrating stress has a severe gradient relative to that of the imposed stresses, was isolated for use in component testing. Mechanically, the test specimen represents the unrestrained condition of the deck distant from the web. But in order to achieve the maximum tension stresses that occur in the prototype near the web (restrained), a more severe thermal gradient was used with the test specimen, which resulted in the self-equilibrating stresses shown in Figure 193c.

These isolated segments were constructed and tested as shown in Figure 194 with and without an applied thermal gradient to determine the effect that the gradient has on the cracking behavior of the concrete specimen. Prestressing, tensile loading, application of a nonlinear thermal gradient, constructability, and replication were all considerations in the design and development of the test specimen and procedures. A test specimen section with a depth of 8 in., the thickness of the SRB Bridge deck, was selected. Within this depth in the SRB Bridge deck the stress gradient due to the negative thermal gradient is the most severe and is likely where cracking would occur in the prototype. The stress gradient proposed for the test specimen (Figure 193c) was more severe than those likely to result in the prototype either near the web or away from the web. Further, limiting the cross-sectional area allowed a sufficient number of specimens to be economically constructed and tested.

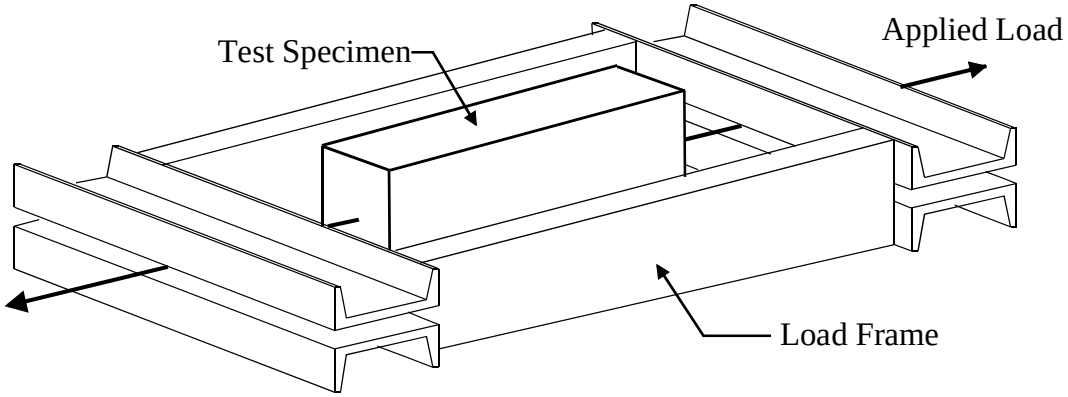

Figure 194: Load frame used to test concrete specimens

In general, direct or indirect tensile tests of concrete produce lower tensile strengths than the modulus of rupture test that uses flexural tension (Neville 1995). Consequently, more severe tensile strain gradients will tend to cause cracking at higher extreme fiber tensile stresses in specimens with the same concrete. Although the thermal stress gradient of the SRB Bridge is shallower than that of the specimen, the difference is not considered significant enough to affect the results. Ultimately, the results of tests on identical specimens with and without thermal gradients will be compared to determine if the cracking behavior is affected by the thermal gradients. If the addition of the self-equilibrating stress profile to the uniform direct tensile stress profile causes no significant difference in observed cracking behavior of the concrete specimens, then cracking of the SRB Bridge deck under the addition of the self-equilibrating stress profile would not be expected.

The thermal gradient imposed on the specimen was intended to replicate the natural development (due to environmental conditions) of a thermal gradient and resulting self-equilibrating strain. The target for developing a nonlinear negative thermal gradient on the test specimen was to reach the maximum temperature difference of -12.3 ^{o}F at the top surface as specified in the AASHTO *Guide Specifications for Design and Construction of Segmental Concrete Bridges* (1999). The intent was to control the top surface temperature differential in the concrete specimen so that the nonlinear gradient would follow approximately that indicated by AASHTO. Application of the thermal gradient to the test specimen was intended to replicate the severe self-equilibrating tensile strain gradient that is developed in the SRB Bridge with the AASHTO negative thermal gradient.

Prestressing was applied to the concrete specimen to replicate the stress conditions in segmental bridge construction. Specimen prestressing also ensured that cracking did not occur immediately upon application of the thermal gradient. The uniform compressive prestress applied to the test specimens was the same as that found in the deck of the SRB Bridge.

18.2 SPECIMEN DESIGN

Each specimen tested in this study was a 4x8x28 in. prestressed concrete specimen as shown in Figure 195. The prestressed specimen was designed to use a central bar and anchors to induce a tensile stress condition and force cracking to occur at the specimen midsection under tensile loading. The specimen was designed such that each half, comprised of an anchor and confinement steel, applied a uniformly distributed stress at the mid-section of the specimen, which was unreinforced and where the stressed bar was debonded.

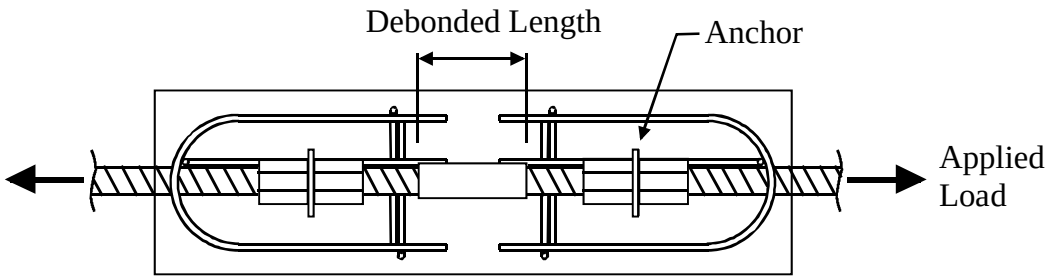

Figure 195: Prestressed concrete specimen schematic

The specimen design, shown in Figure 196, used a steel bar and hardware provided by Dywidag Systems International (DYWIDAG) to apply the prestressing and tensile loading. The steel bar was a 1-in. diameter DYWIDAG threaded bar with an ultimate strength of 150ksi and yield strength of 125ksi. Each anchor was created using two 1-in. diameter hex nuts on either side of a 1.125 in. diameter flat washer. Anchors were placed at the quarter points of the specimen, as measured from the outside face of the washers. The mid-section of the specimen was debonded from the DYWIDAG bar using a 4-in. length of 1-in. diameter PVC pipe. Confinement of the anchors was provided by #3 stirrups, which were tack welded in place as shown in Figure 197. The confinement reinforcement was attached to the anchors by a tack weld to the washer within each anchor.

To force cracking to occur at the midsection of the specimen, a 1.25 in. x 0.125 in. acrylic plate was placed vertically above and below the PVC and DYWIDAG bar as shown in Figure 198. The plate was sharpened along its edges to encourage crack initiation at this location. The acrylic plates were constructed from a 1.25 in. wide strip with a 1.25 in. diameter semi-circle cut out of the center, creating two halves with a half circle on each end. These two halves were then affixed to the PVC pipe with glue. Slots cut into each form prevented movement of the ends of the acrylic plates during concrete placement.

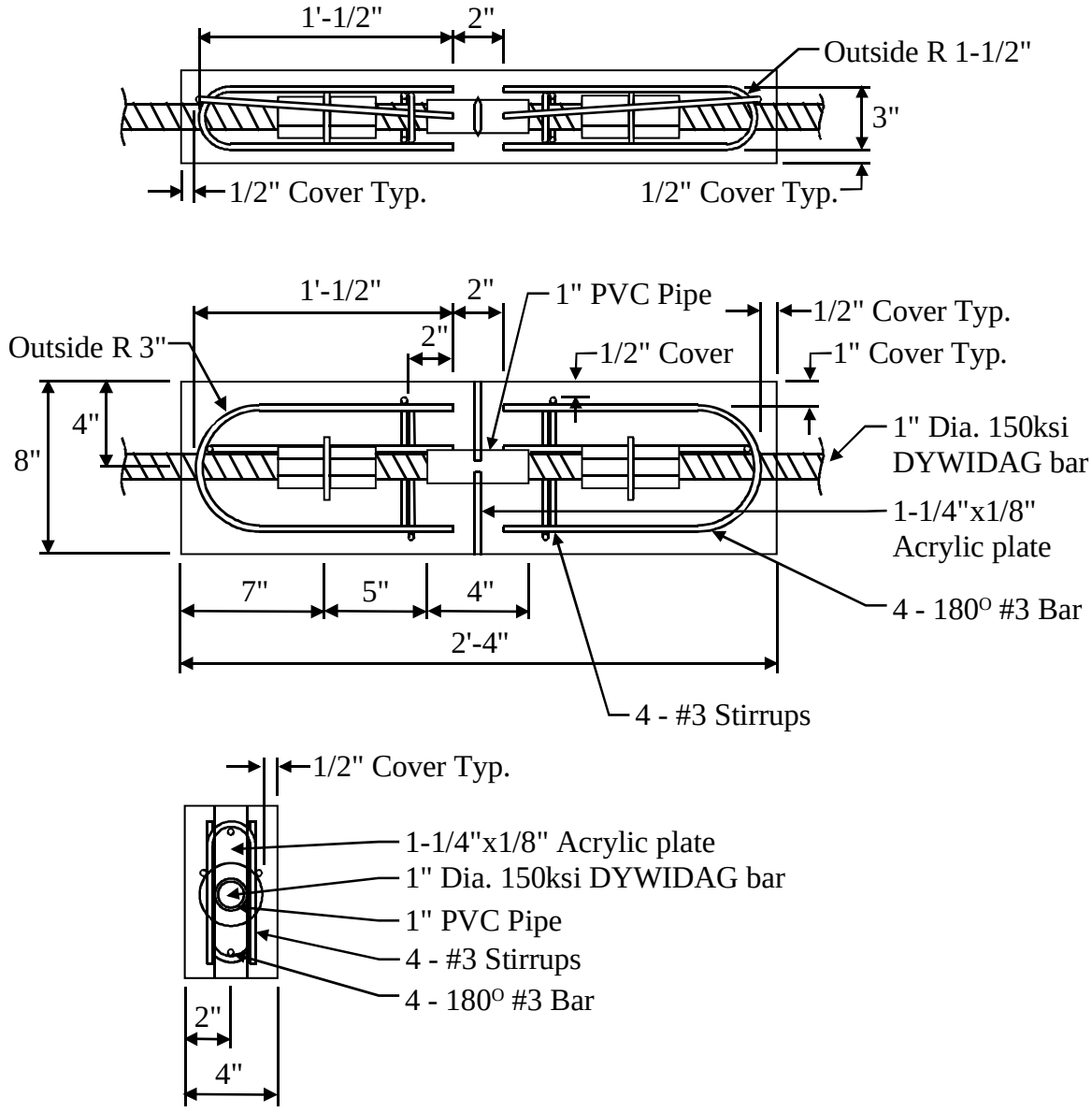

Figure 196: Prestressed specimen design

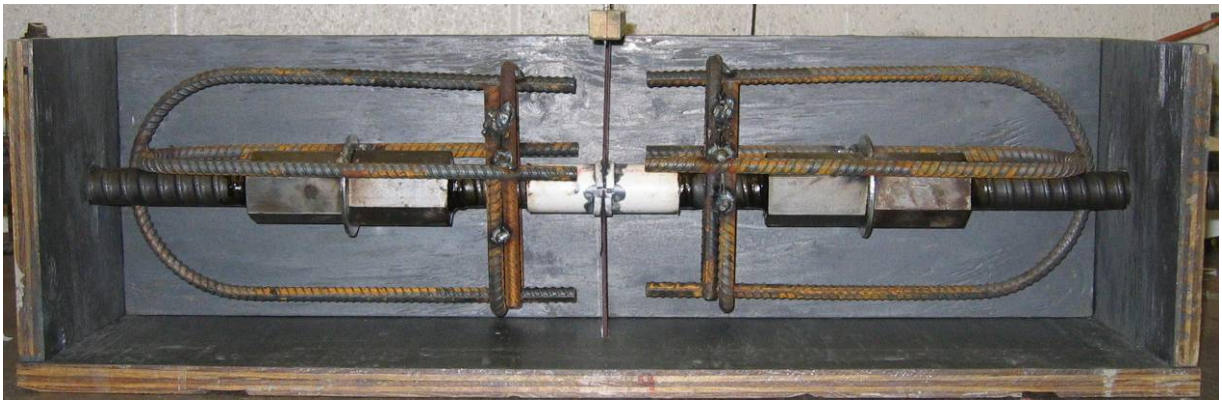

Figure 197: Prestressed specimen design

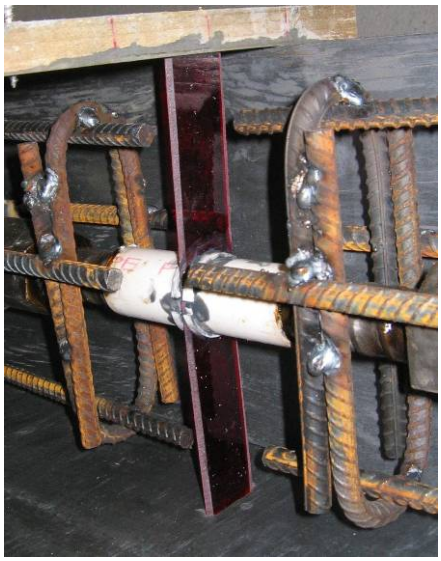

Figure 198: Acrylic plate installed in specimen

18.3 LOAD FRAME

The load frame assembly was comprised of a reaction frame, prestressing components, and instrumentation as shown in Figure 199 and Figure 200. The frame was designed to act as a stand-alone reaction frame and allow the test specimen to first be prestressed and then loaded in tension.

The reaction frame consisted of two short columns placed between built-up reaction beams. Each column was a rectangular tube section with welded end plates, each plate having a center hole for an all-thread bar. Each reaction beam was built-up from two C-channel sections placed back-to-back and spaced with a 1.5 in. gap using plain steel bar. The columns and beams of the reaction frame were held together by two 1 in. diameter all-thread rods placed through the center of the columns.

The specimen was placed in the center of the reaction frame with each end of the DYWIDAG bar extending through the reaction beams. At one end of the DYWIDAG bar, against the outside face of the reaction beam, was placed a load cell between two 1 in. thick DYWIDAG anchor plates and with one DYWIDAG anchor nut placed on the end. At the

opposite end of the DYWIDAG bar was placed a prestress locking seat, a hydraulic jack, and an anchor plate and nut on the end. The prestress locking seat was placed with a 1 in. thick plate between itself and the outside face of the reaction beam as shown in Figure 201. The 1 in. plate was used to minimize flexure of the channel flanges and the end plate of the prestress locking seat.

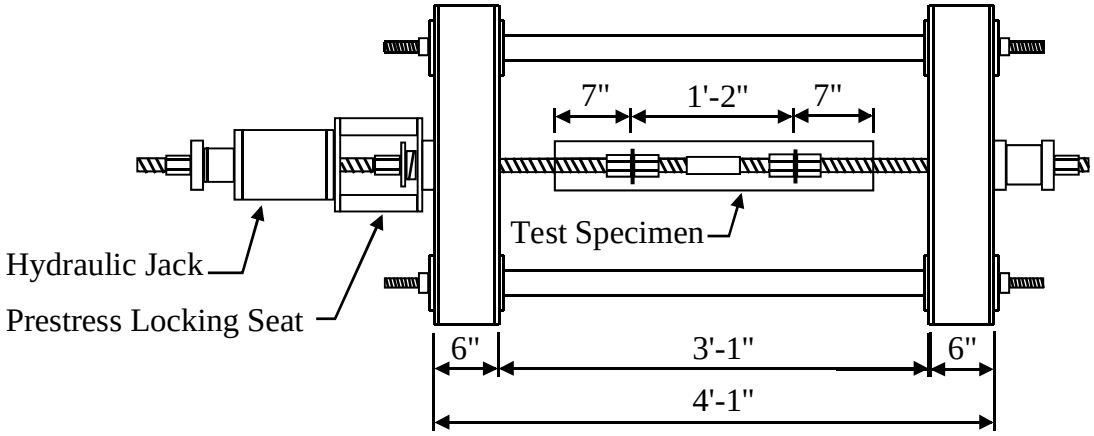

Figure 199: Load frame with specimen and instrumentation

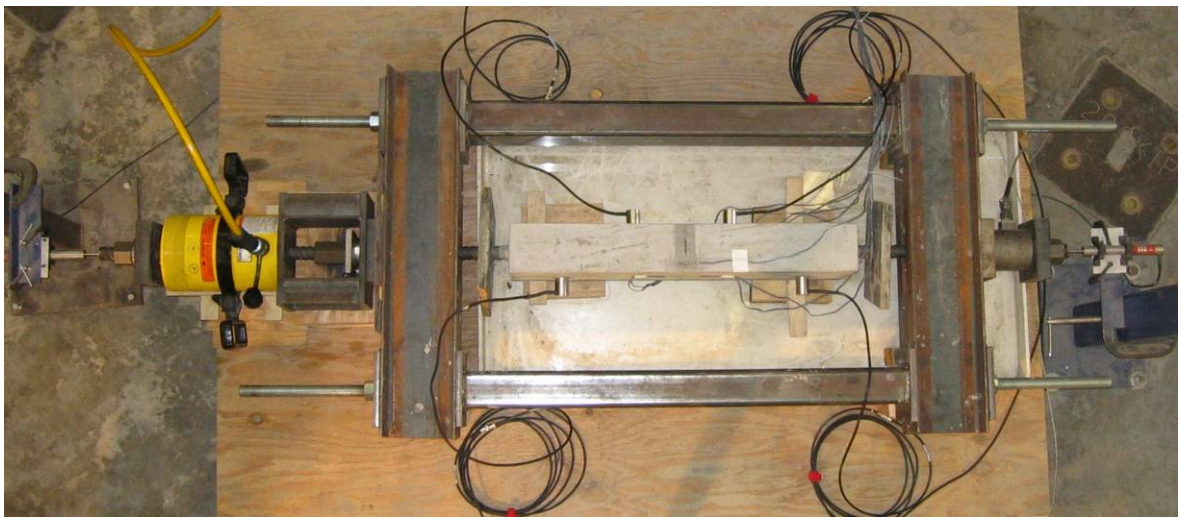

Figure 200: Test setup for prestress specimen

The prestress locking seat, shown in Figure 201, was designed to support the hydraulic jack during loading of the DYWIDAG bar and allow for the bar to be locked-off after prestressing. Over-size counter-oriented beveled washers, shown in Figure 201(b) were used to release the locking nut without requiring the application of additional load beyond the prestressing force. A single beveled washer was fixed and the other beveled washer free to slip. The over-size counter-oriented beveled washers allowed for slip in the washers around the DYWIDAG bar. When the free washer was displaced, the vertical slip of the washer reduced the horizontal distance between plates, relieving the locking nut of any load.

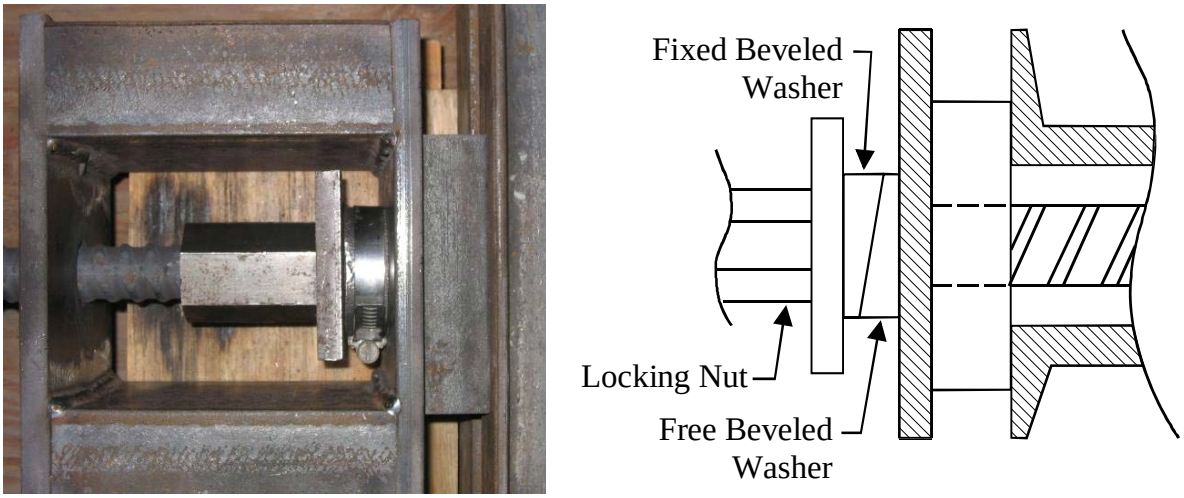

(a) (b)

Figure 201: (a) Top view of prestress locking seat with locking nut and washer setup

(b) Side view section of beveled washer and locking nut

18.4 APPLICATION OF THERMAL GRADIENT

To impose a nonlinear thermal gradient on a concrete specimen, an open-channel was constructed as shown in Figure 202 and Figure 203. The channel was placed on the top surface of the specimen and configured in a closed-loop flow system. The channel was constructed of 0.125 in. thick acrylic sheets with an inflow at one end and a flow spillway at the opposite end. The open channel flow of water was separated from the concrete specimen surface by a thin plastic sheet placed between the specimen and the channel. A silicone adhesive and sealant was used to seal the perimeter of the channel at the plastic sheet. A standard large cooler with a 0.625 in. diameter out flow pipe to a pump and valve was used as a constant-temperature water reservoir.

The nonlinear thermal gradient was imposed using a flow of chilled water over the top of the specimen (Figure 202). The water was carried by a closed loop system starting at a reservoir and pumped to the open channel inflow, over the specimen, over the flow spillway and returning to the reservoir by a shallow return channel. The flow was maintained at a depth of 0.5 in. to 0.75 in. above the surface of the specimen and at a flow of approximately 2.4 gallons per minute. The water in the reservoir was chilled 20°F colder than the initial average temperature of the specimen and maintained using ice. Water flow temperature in the open channel was recorded during testing by the placement of a single thermocouple at 0.25 in. above the top surface.

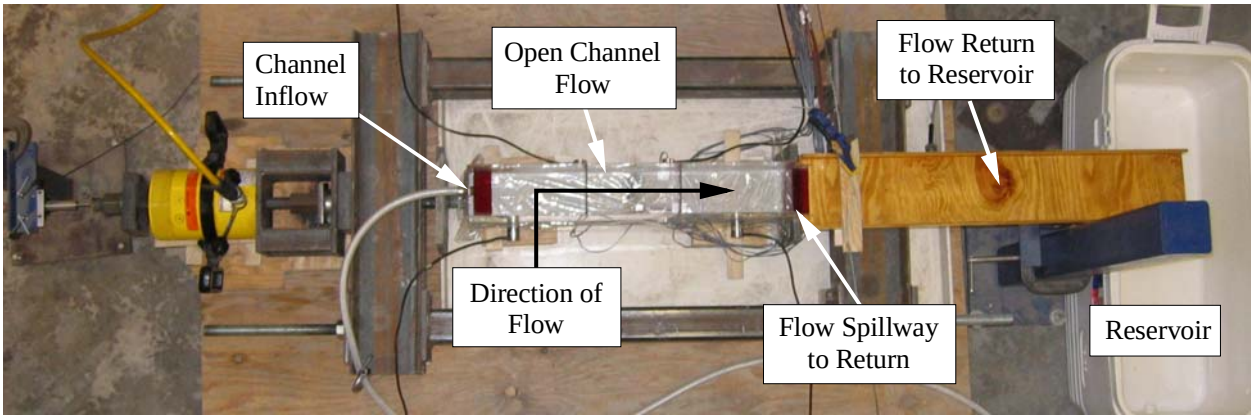

Figure 202: Load frame with thermal application setup

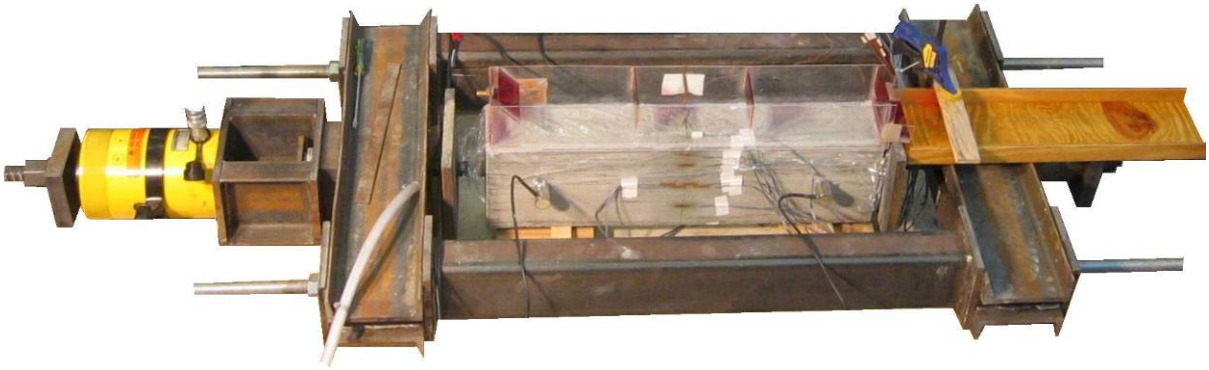

Figure 203: Load frame with open-channel on thermal test specimen

18.5 CONCRETE MIXTURE DESIGN

A concrete mixture design was developed to ensure a controlled and consistent mixture throughout testing. The mixture was designed as a high slump and high early strength concrete. Multiple test mixtures were performed prior to testing to ensure consistent concrete properties. The mixture was designed with a water-cement ratio of 0.40 and with a target slump of 9 in. to ensure adequate consolidation in the test specimen forms. A minimum compressive strength of 5000 psi at four days was used to allow for prestressing and testing of the concrete specimens within a single work week, or five day period.

Aggregates, cement, and admixtures were obtained from local vendors and concrete mixing was performed in the Civil Engineering materials lab at the University of Florida, Gainesville, FL. A 3/8 in. maximum diameter coarse aggregate (#89 granite) was obtained from Conrad Yelvington Distributors, Inc., Gainesville, FL. Concrete sand for fine aggregate was obtained from Florida Rock Industries, Inc., Gainesville, FL. The cement used was Type I/II portland cement. Micro-silica fume slurry, Force 10,000 from Grace Construction Products, was used to obtain a high early strength. When required, a high to mid-range water reducer was used to obtain the target slump. The water reducing admixture used was ADVA 140 of Grace Concrete Products. The mixture design properties are shown in Table 29 and the mixture design proportions are shown in Table 30. Results for the compressive strength and modulus of rupture tests performed for each test set are shown in Table 31.

Table 29: Concrete mix design properties

Property	ASTM	
Strength (psi)	C39	7000
W/C Ratio	--	0.40
Slump (in)	C143	9.0 ± 0.5
Plastic Unit Weight (lbs/cf)	C138	143.2 ± 2.0

Table 30: Concrete mix design proportions

Material	ASTM	Type	Proportion (lbs/cf)
Cement	C150	I/II	37.7
Cement	C618	Micro-Silica Slurry	0.36
Water	--	--	6.02
Fine Aggregate	C33	Sand	61.6
Aggregate	C33	#89 Granite	37.6
Admixture	C494	Water Reducer	Dosage rates vary

Table 31: Concrete mixture compressive strength and modulus of rupture

Compressive Strength (psi)	Test A	Test B	Test C	Test D	Test E	Test F
@ 4 days (testing)	5262	5183	5727	5448	5609	5463
@ 7 days	5863	6060	6044	6032	6398	6247
@ 28 days	6948	7594	7414	7319	7952	7547
Modulus of Rupture (psi) @ 4 days (testing)	749	705	767	703	685	650

19 INSTRUMENTATION

Each test included instrumentation for load, longitudinal displacement, strain, acoustic emission, and temperature (for thermal specimens). Placement of instrumentation for load, displacement, and acoustic emission (AE) is shown with the test setup in Figure 204.

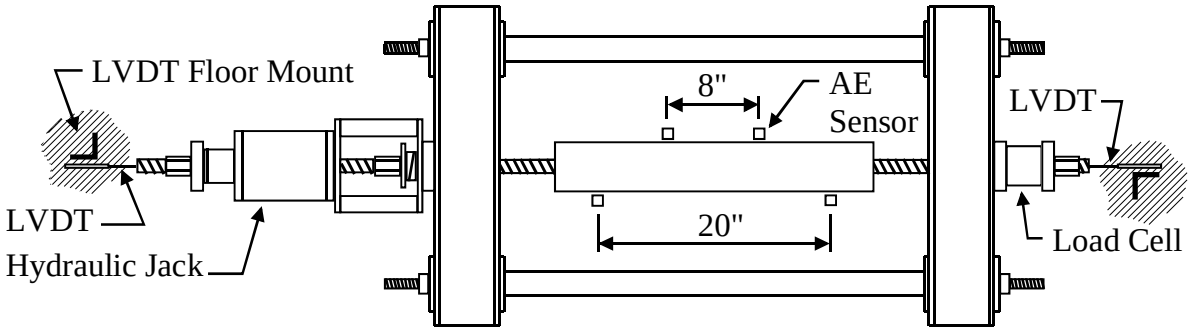

Figure 204: Instrumentation setup

19.1 ELECTRICAL RESISTANCE CONCRETE STRAIN GAUGES

Strain gauges were placed to capture both the strain profile and to capture cracking. Gauge locations and nomenclature for the thermal and non-thermal specimens are shown in Figure 205. Figure 206 shows the staggered placement of gauges R5 through R7 at mid-height of the section. This placement pattern was used to ensure that the primary crack would pass through at least one strain gauge. Nomenclature assigned to the strain gauges was associated with the four faces of the specimen: top, right, bottom, and left (e.g. TOP, R1, BOT, L1).

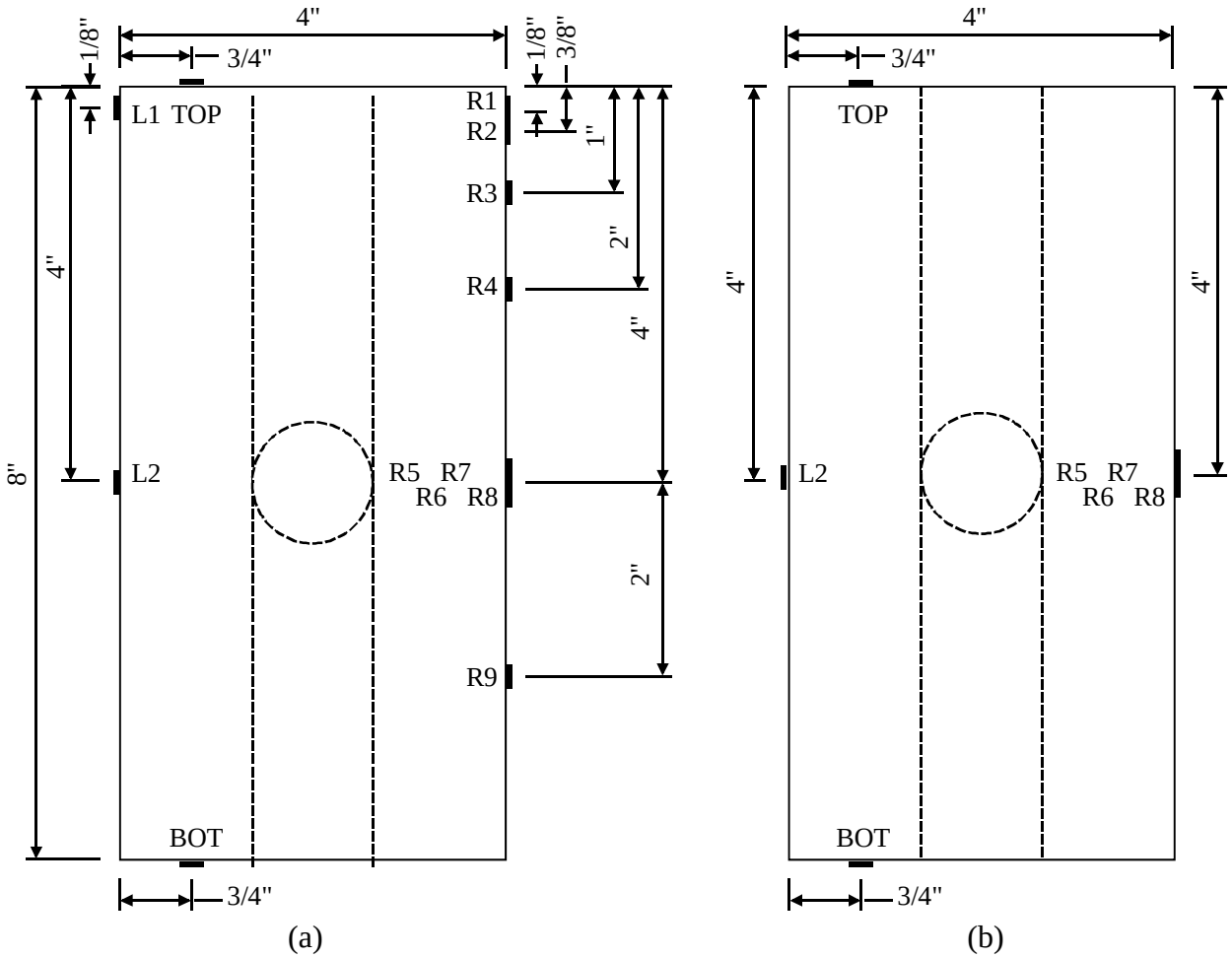

Figure 205: Strain gauge location and nomenclature for the (a) prestressed thermal specimen and (b) prestressed non-thermal specimen

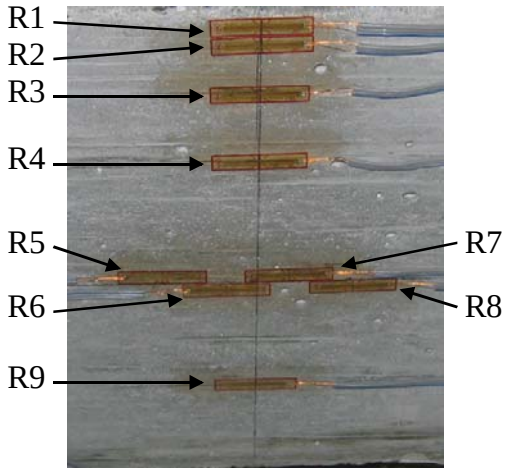

Figure 206: Strain gauge placement on right face of prestressed thermal specimen

Strain gauges used in this research were type PFL-20-11-3LT gauges produced by Tokyo Sokki Kenkyojo Co., Ltd. The gauges were foil type electrical resistance, self-temperature compensating (STC) strain gauges with a gauge length of 20mm and temperature compensation number of 11, corresponding to a coefficient of thermal expansion (CTE) of 11.8 x 10^{-6} /^{o}C (6.6 x 10^{-6} /^{o}F). Lead wires of the gauges were 3-wire temperature compensating to account for variation in lab temperature during testing.

Strain gauges were applied to the concrete specimen at the midsection prior to testing. The surface of the concrete at the location of the strain gauge was prepared by light grinding and/or sanding to remove concrete laitance. The area was then dusted with compressed air and cleaned with acetone. Each strain gauge was adhered to the concrete using Loctite 454 Instant Adhesive.

19.2 THERMOCOUPLES

Type T thermocouples were embedded in the concrete to measure the temperature profile at the midsection of the specimen as shown in Figure 207. Thermocouples were spaced through the depth of the specimen, as shown in Figure 208, to capture the nonlinear thermal gradient. Spacing ranged from 0.5 in. at the top, where the gradient was most severe, to 2 in. at the bottom. The thermocouple array was placed at 0.75 in. from the outside face of the specimen to avoid interference with the acrylic plate and steel bar. The Type T thermocouples used were Omega #FF-T-20-SLE.

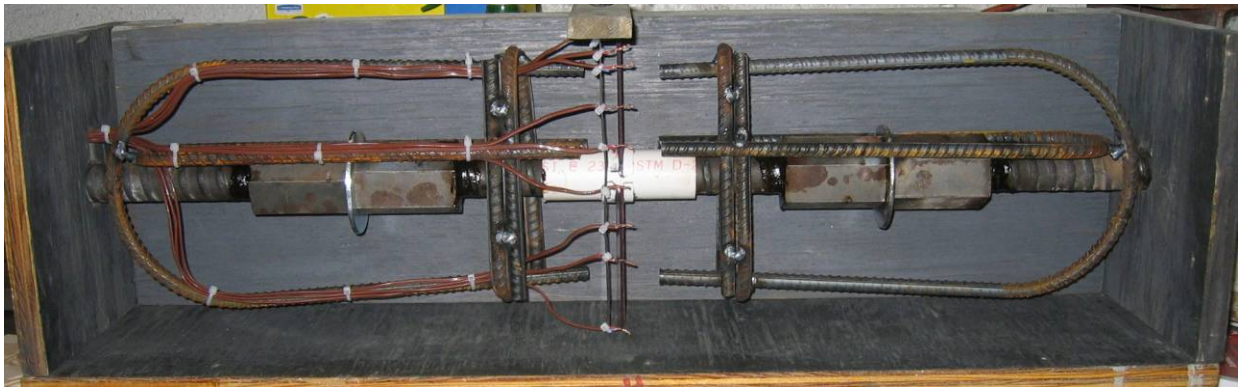

Figure 207: Prestressed thermal specimen assembled in formwork

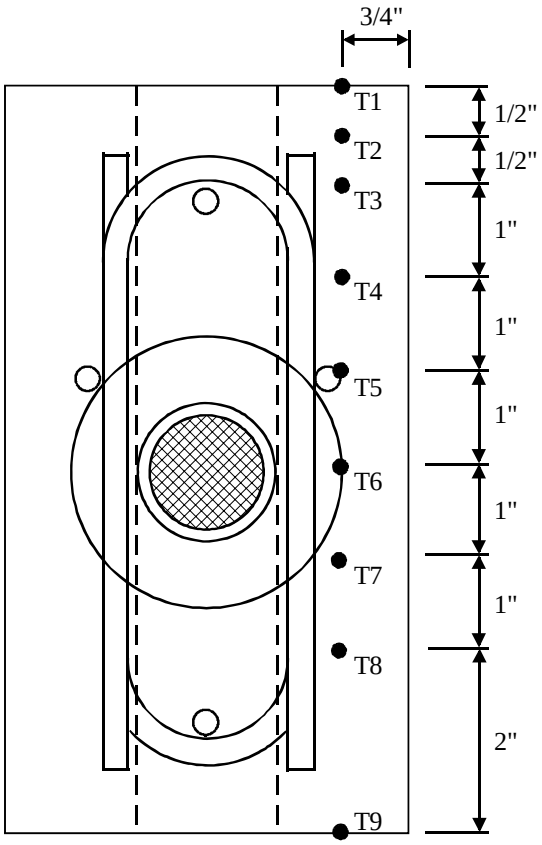

Figure 208: Thermocouple locations and nomenclature for prestressed thermal specimen

19.3 LOAD CELLS

A single load cell at one end of each load frame measured the load applied by the hydraulic jack to the DYWIDAG bar and specimen, as shown in Figure 209. Load cells used in this research were Houston Scientific 200 kip load cells. Load was applied using an Enerpac 60 ton hydraulic jack in combination with an Enerpac 10,000 psi hydraulic manual pump.

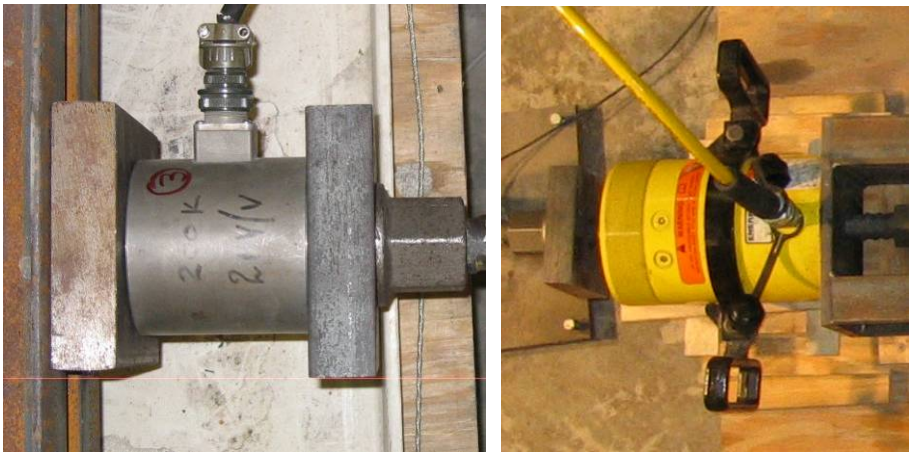

(a) (b)

Figure 209: Applied load measure by (a) load cell and applied by (b) hydraulic jack

19.4 Linear Variable Displacement Transducers

Linear variable displacement transducers (LVDTs) were placed on each end of the DYWIDAG bar. LVDTs were fixed to stands mounted on the floor to measure the longitudinal tip displacement at each end of the DYWIDAG bar (Figure 204). The difference in displacements was then used to calculate the net change in length of the bar. The LVDTs used in this research were of the DCTH Series produced by RDP Electrosense and had a displacement range of ±0.5 in.

19.5 Data Acquisition System

National Instruments model SCXI-1000DC Data acquisition (DAQ) System was used to acquire data from the instrumentation. The DAQ system recorded data from each strain gauge, thermocouple, LVDT, and load cell channel at a frequency of 10Hz. The load cell signal was split between the National Instruments DAQ system and the acoustic emissions DAQ to enable cross-platform synchronization.

19.6 Acoustic Emissions

This section provides background information on the nondestructive testing (NDT) approach of monitoring acoustic emission (AE) of a structural member. It also discusses the nature of the data measured, relevant terminology, and how AE data were used to assess damage progression in the prestressed concrete specimens tested in this research.

19.6.1 Background Information and Motivation

Acoustic emission (AE) techniques began in Germany in 1950 with testing of metals by J. Kaiser. AE technology was later modified to be used as a structural integrity monitoring device with concrete. The AE technique has been used as a nondestructive structural monitoring tool for plain concrete (Nielsen and Griffin 1977), reinforced, and prestressed concrete beams under flexural monotonic and cyclic loading conditions (Shield and Hearn 1997). Detection and location of microcracking and macrocracks has also been successfully completed under flexural loading (Labuz et al. 2001). AE signal characteristics have also been identified in order to classify the type of damage, microcracking or bond degradation between concrete and steel, that is occurring in reinforced concrete beams (Oh et al. 2000). The successful application of AE techniques to monitor concrete structural health was the motivation to utilize it as a tool for this research.

19.6.2 Introduction

An acoustic emission is produced when energy is released from a material under stress in the form of a transient stress wave. The cause of the energy release is a change of state of the material such as a crack forming in concrete or bond degradation between concrete and steel. The elastic wave travels through the specimen and is detected by mounted piezoelectric sensors that develop a voltage in response to mechanical stress, which is recorded with a data acquisition system. The output signal contain feature data; amplitude, energy, duration, rise time, and count associated with each “hit” recognized by the sensors. A hit occurs when the amplitude of the electromotive force generated by the sensor rises above a predetermined threshold. The threshold is set to eliminate noise caused by sources other than a structural defect, like electrical interference or ambient sound. A sample waveform from a hit is shown in Figure 210.

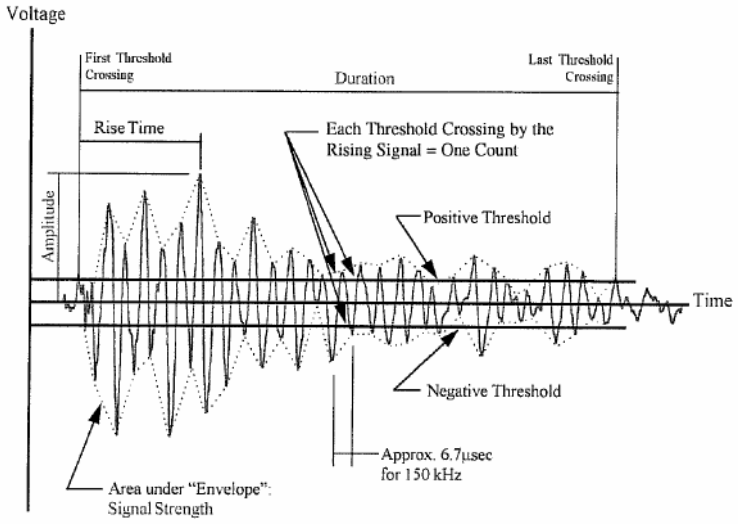

Figure 210: Waveform generated by a sensor "hit"

An "event" is defined as a local material change giving rise to acoustic emission (ASTM E-1316). An event is distinct from a "hit" which is simply the process of detecting and measuring an AE signal on a channel. To record events, hit data from at least two channels must be utilized. A location algorithm can be used to determine the source of an acoustic emission event using two or more sensors based on the time of arrival of the hit.

19.6.3 Structural Assessment Techniques

A key aspect in successfully using AE testing techniques involves identifying the appropriate parameters to focus on within the AE signal data. Energy analysis has previously been found to be a viable means of assessing AE signals for concrete bridge beams (Colombo et al. 2005) and compression of concrete (Puri and Weiss 2006). For the monotonically loaded concrete specimens tested in this research, focus was given to comparing cumulative event energy to applied load to gain insight regarding the damage progression of the prestressed concrete specimen.

19.6.4 Acoustic Emission Instrumentation

The AE equipment utilized in this research was the DISP-16 channel Acoustic Emission System designed by Physical Acoustics Corporation. The system is shown in Figure 211. The system features a Windows-based software package, AEWin, that allows acquisition and replay of collected AE data. The piezoelectric sensors used were model R31-AST with an integrated preamp (Figure 212). This sensor was engineered to attain high sensitivity and have the capability to drive long cables without the need for a separate preamplifier. The sensors also contained an integrated auto sensor test (AST) capability that allowed them to pulse elastic energy waves, as well as receive elastic energy waves. The AST feature permits verification of sensor coupling to the specimen of interest. Sensor coupling to the specimen was completed using hot glue as the adhesive. This sensor model is frequently used for structural health monitoring of small to medium concrete structures.

AE sensors were placed on each specimen at the intervals specified in Figure 204 and Figure 213. Sensors S1 and S2 were placed on the designated right face and sensors S3 and S4 on the opposite, or left, face of the specimen. The sensors were placed to allow for the capture and isolation of acoustic emission around both the anchors and the area of cracking at midsection of the specimen.

Figure 211: DISP-16 Channel Acoustic Emission System (O'Neill 2009)

Figure 212: R31-AST Piezoelectric Sensor (O'Neill 2009)

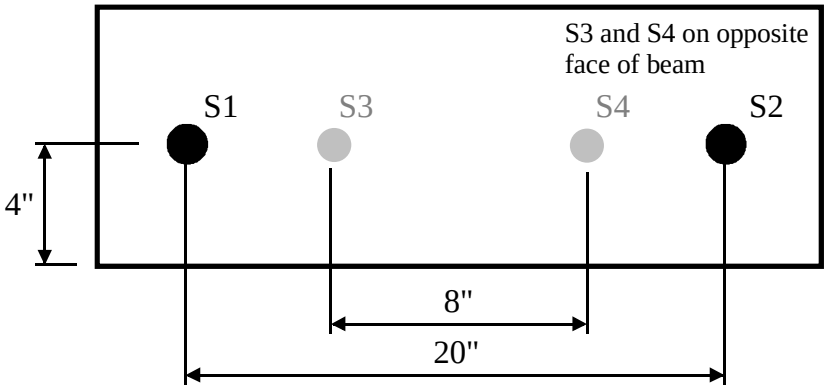

Figure 213: Acoustic Emissions sensor placement and nomenclature

20 TEST PROCEDURE

Specimen construction and testing extended over a period of several days and included prestressing, concrete mixing and placement, prestress transfer, thermal application, and finally direct tensile loading until cracking. Two identical load frames (Figure 214) were used in a single test set so that the same concrete mixture could be used in non-thermal and thermal testing scenarios. Non-thermal and thermal test results were then compared to determine the relative effect of the thermal gradient on cracking behavior.

The test procedure was designed to simulate the stress states in the top flange of a segmental box girder under prestressing, applied loads, and self-equilibrating thermal stresses. After the specimens were cast and prestressed, the resulting stress state is shown in Figure 215(a). This was intended to represent the precompressed tensile zone in the full scale SRB Bridge segment under prestress alone. To simulate tensile stresses caused by negative bending, the DYWIDAG bar was loaded in tension as shown in Figure 215(b) until the section cracked. For the specimen with the nonlinear thermal gradient imposed, the self-equilibrating stress profile shown in Figure 215(c) was also present. The combination of flexural tension and thermal stresses result in the stress state shown in Figure 215(d).

Figure 214: Load frame assembly prior to concrete placement

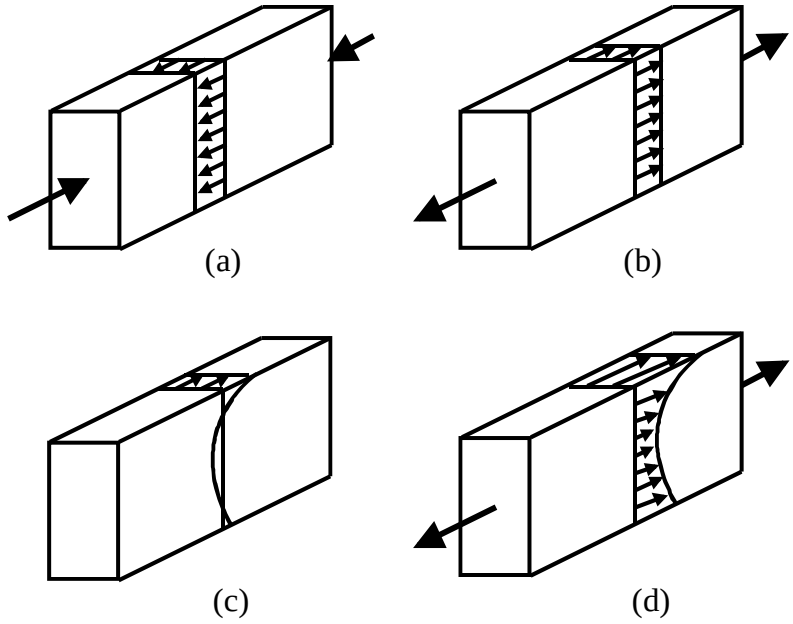

Figure 215: Stress state of each stage: (a) prestress, (b) direct tensile loading, (c) self-equilibrating thermal stress, and (d) combined thermal and direct tensile loading

20.1 PRESTRESSING

To prestress the specimen, the DYWIDAG bar was tensioned against the load frame before concrete placement. With the specimen formwork in place, the stressed bar was locked off using the prestress locking seat assembly. This allowed for the load frame with the specimen to be moved for concrete placement and maintain the prestress load during curing. Prestressing of the DYWIDAG bar was performed for two load frame assemblies. During stressing of the bar, data acquisition recorded the applied load and longitudinal displacement of the bar. These data were used to determine the initial prestress and prestress loss associated with locking off the bar.

20.2 CONCRETE PLACEMENT

For each test set, a single batch of concrete was mixed to ensure consistent mechanical and thermal properties between the non-thermal and thermal specimens. To ensure consistency, coarse aggregates were soaked in water for a 24hr period prior to mixing. The fully saturated aggregates were then removed from the water, allowed to drain for approximately 45 minutes, and then transferred and weighed in sealed buckets. Samples were taken and the aggregate moisture content obtained according to ASTM C566 (2004). During mixing of the concrete, a slump test was performed in accordance with ASTM C143 (2008) to ensure that target slump was reached. For further quality control, the unit weight of the mix was obtained in accordance with ASTM C138 (2009). Nine 4x8 in. cylinders were cast for compressive strength tests, ASTM C39 (2001). The 4x8 in. cylinders were used in lieu of 6x12 in. cylinders due to limited volume of the concrete mixer available. Three 4x4x14 in. beams were cast for the modulus of rupture test, ASTM C78 (2008). The compressive strength test and modulus of rupture test were performed immediately after testing of the non-thermal and thermal specimens were complete.

The concrete mixture was placed into the formwork for each specimen after prestressing of the bars. To provide adequate consolidation of the concrete, each load frame assembly with

the specimen was placed on a vibration table. Each specimen was moist cured by covering the specimen with moist cotton towels and plastic sheeting. The towels were moistened regularly while the specimen cured for 2 days before removing formwork.

20.3 NON-THERMAL TEST

Testing of the non-thermal specimen was conducted on day five as shown in the sequence of stages in Table 32. Data were acquired from all instrumentation during this entire test period including just before prestress transfer. The reading taken before prestressing constituted the zero strain reading.

Table 32: Sequence of stages for prestressed non-thermal specimen

Sequence of stages	Day performed	Duration
1. Tension DYWIDAG bar and lock-off	Day 1	5 minutes
2. Cast concrete in specimen forms	Day 1	1 hour
3. Remove formwork and apply strain gauges	Day 3	n/a
4. Begin data acquisition and take zero reading	Day 5	n/a
5. Unlock and release bar (prestress specimen)	Day 5	2 minutes
6. Apply tensile load to prestressed specimen until cracking observed	Day 5	5 minutes
7. Terminate data acquisition	Day 5	n/a
8. End Test	Day 5	n/a

During prestress transfer it was necessary to increase the bar force slightly to allow the beveled washer to be tapped out from under the locking nut and plate (Figure 201). This allowed the locking nut to be loosened and the prestress to be transferred to the concrete specimen. The increase in bar force caused a slight tension in the concrete section of approximately 25 microstrain. Careful observation during and after testing determined that this tensile strain was not significant enough to cause damage to the concrete.

Immediately after prestress transfer, tension was applied to the DYWIDAG bar at a rate of approximately 30 kips/min. When cracking of the specimen was visually observed, failure of the prestressed concrete specimen was considered to have occurred and the test was terminated.

20.4 THERMAL TEST

The thermal test procedure was similar in sequence to that of the non-thermal test, with the exception of additional stages for the thermal application (Table 33). The procedures for data acquisition, unlocking the stressed DYWIDAG bar, and prestressing of the concrete specimen were identical to that of the non-thermal test. After prestress transfer, a direct tensile load of approximately two-thirds the prestress was applied, which resulted in a net compressive stress in the concrete. At this point application of the nonlinear thermal gradient was initiated. After initiation of the thermal gradient, direct tensile loading continued such that cracking coincided with the complete development of the nonlinear thermal gradient. Failure of the specimen was considered to have occurred when visible cracking was observed. Upon cracking, the test was completed and data acquisition terminated. Crack pattern and location were then documented for the tested specimen.

Table 33: Sequence of stages for prestressed thermal specimen

Sequence of stages	Day performed	Duration
1. Tension DYWIDAG bar and lock-off	Day 1	5 minutes
2. Cast concrete in specimen forms	Day 1	1 hour
3. Remove formwork and apply strain gauges	Day 3	n/a
4. Begin data acquisition and take zero reading	Day 5	n/a
5. Unlock and release bar (prestress specimen)	Day 5	2 minutes
6. Apply tensile load to prestressed specimen to 2/3 of total prestress (preload specimen)	Day 5	1 minutes
7. Begin thermal loading	Day 5	2 minutes
8. Continue tensile loading of specimen until cracking observed	Day 5	2 – 3 minutes
9. Terminate data acquisition	Day 5	n/a
10. End Test	Day 5	n/a

21 RESULTS AND DISCUSSION

A series of six test sets, Test A through Test F, were conducted. The objective was to determine the effect of an applied nonlinear thermal gradient on the cracking behavior of the concrete specimen relative to a specimen that had no thermal gradient applied. This chapter presents and discusses the results of these tests.

21.1 THERMAL GRADIENT AND SELF-EQUILIBRATING STRAIN

Tests were conducted to match the upper portion of the AASHTO negative thermal gradient from the SRB Bridge with that of the tested concrete specimens. In these tests, the target temperature at the top surface was maintained at -12.3 ^{o}F (relative to the baseline specimen temperature) as the temperature gradient developed through the depth of the specimen to match the AASHTO gradient. The problem encountered with this approach was that the upper portion of the AASHTO negative thermal gradient on the test specimen resulted in lower self-equilibrating strains compared to those predicted in the SRB Bridge. This was due to the shallower test specimen and reduced temperature-profile nonlinearity. It was therefore determined that the target surface temperature of -12.3 ^{o}F would be obtained but that the target gradient would be based on the maximum self-equilibrating strain observed. The ability to reach the target gradient was assessed in preliminary testing and the time required to obtain the maximum self-equilibrating strain determined. The target gradient during production testing was then obtained by imposing the thermal application for a set period of time. Direct tensile loading then occurred simultaneously such that the estimated cracking load was reached in conjunction with formation of the target thermal gradient.

Figure 216 shows the temperature and strain results of the thermal gradient test. The top surface temperature differential obtained was -11.8 ^{o}F at 3.5 minutes and -12.5 ^{o}F at 5 minutes after initiating application of the thermal gradient. This compares well with the target AASHTO negative thermal gradient of -12.3 ^{o}F and was inline with the time required to load the specimen to cracking.

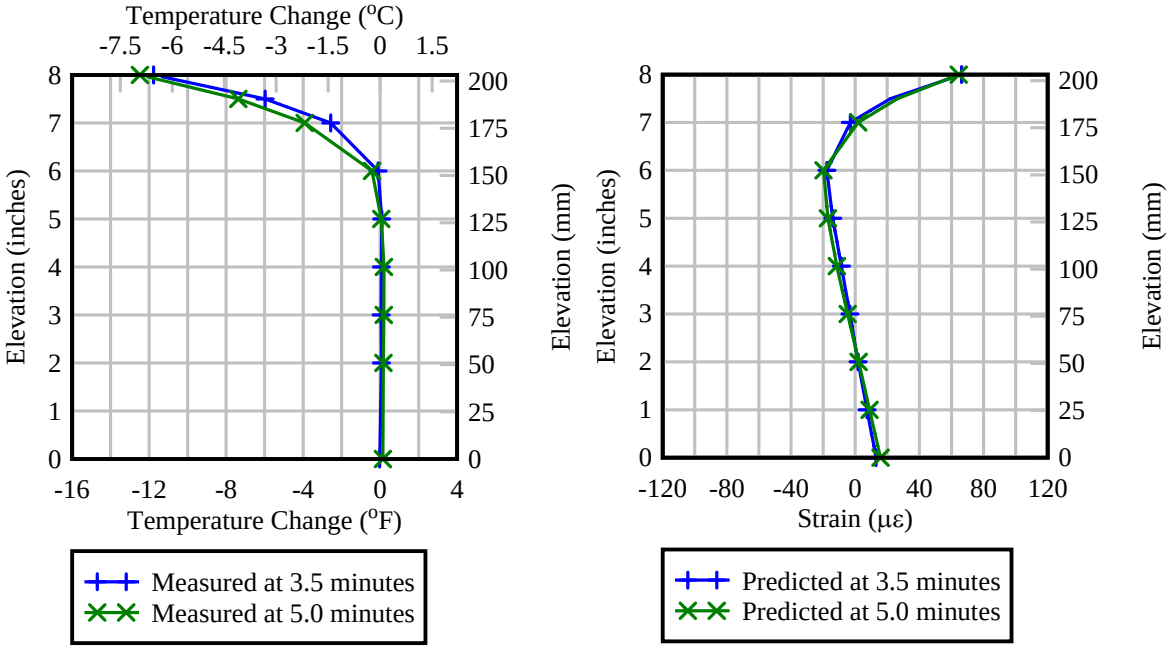

Figure 216: Test A – (a) measured thermal gradient and (b) calculated self-equilibrating strain gradient

The thermal gradient and self-equilibrating strain profile are shown through the elevation of the SRB Bridge in Figure 217. The test specimen gradients are shown overlaid in the top 8 in. of the profiles. The thermal gradient imposed during specimen testing resulted in a maximum self-equilibrating strain of 65 microstrain at the end of the test (Figure 216b) as compared to the SRB Bridge with the AASHTO negative thermal gradient having a calculated peak self-equilibrating strain of 44 microstrain.

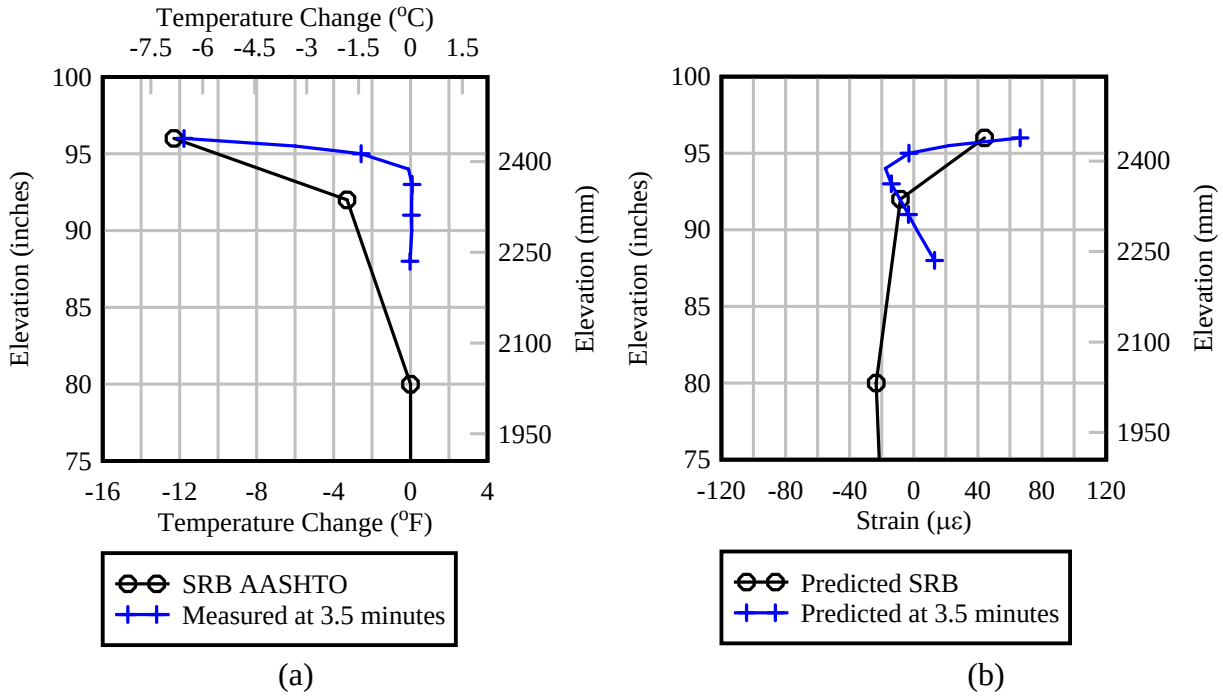

Figure 217: Test A and SRB comparison of (a) thermal gradients and (b) self-equilibrating strain gradients

Both the measured thermal gradient and resulting self-equilibrating strain gradient obtained on the test specimen were notably more severe than those calculated on the SRB Bridge from the AASHTO negative gradient. Although this is the case, the applied service load component, both in the SRB Bridge and experimental test specimen, is significantly greater than the thermal gradient component of the total strain gradient (Figure 192 and Figure 193). The total strain profile on the SRB Bridge is predominately a flexural gradient and the strain profile on the experimental test specimen is predominately uniform. The difference between a flexural strain profile and a uniform strain profile can be compared in the modulus of rupture test and the direct tensile test, respectively. Neville noted that the modulus of rupture test, a flexural strain gradient, overestimated the tensile strength of the concrete; the correct value being about 3/4 of the modulus of rupture (1995). There were four possible reasons given. The first is due to assumption based on the elastic beam theory, that the stress-strain relation is assumed linear. The tensile stress block, assumed to be triangular, is in actuality parabolic in shape under loads nearing failure; resulting in a lower maximum fiber tensile stress. Secondly, accidental eccentricity in a direct tensile strength test may result in a lower apparent tensile strength. A third explanation is that in a direct tensile test, the entire specimen volume is placed under the maximum stress, such that the probability of a weak element occurring is high; this is similar to the reasoning of a third-point loading arrangement in the modulus of rupture test. The fourth explanation is that the maximum fiber stress reached may be higher in flexure than in direct tension, this would be due to crack propagation being blocked by less stressed material nearer to the neutral axis of the section. (Neville 1995)

As such, it would be expected that the predicted tensile strength in the SRB Bridge would be greater than the measured tensile strength in the experimental test. The maximum fiber stress

measured in the experimental specimen would be 3/4 of the maximum fiber stress calculated in the SRB Bridge. The less severe gradient in the SRB Bridge will result in cracking at a higher applied stress than the stress profile applied to the experimental specimen. In addition, there is a 1/3 increase of maximum self-equilibrating tensile strain calculated in the experimental specimen compared to the predicted self-equilibrating strain in the SRB Bridge. Thus, the predominantly uniform total strain profile and increased self-equilibrating strain of the experimental specimen produce a harsher condition then those predicted in the SRB Bridge. If any effect was to be seen, it would be seen at a lower applied tensile stress as in the experimental testing.

Strains resulting from the applied mechanical load (prestress and applied tensile load) and strains resulting from the applied thermal gradient combined to form the total measured strain profile of the thermal specimen. Figure 218(a) shows the components of the total measured strain profile on the thermal specimen of Test A. The self-equilibrating strain is calculated from the measured differential temperature gradient. The applied mechanical strain is determined simply by removing the self-equilibrating strain from the total measured strain. This can be compared to the applied mechanical strain measured in the non-thermal specimen shown in Figure 218(b). There is an observed difference in magnitudes of the mechanical strain component between the thermal and non-thermal specimens of approximately 20 microstrain. One reason for this difference is flexural strain due to unintended bar eccentricity. Another is the presence of residual concrete drying shrinkage strains. These factors, which will be discussed in greater detail later, were not quantified and differences in these factors between specimens in each test set would be expected. The measured compressive strain in the top of the non-thermal specimen at initial cracking can also be associated with the effect of residual concrete drying shrinkage strains that result in a net residual tensile strain.

As discussed, Figure 218(a) shows that the self-equilibrating strain contribution to the total strain is significantly greater than that of the applied mechanical strain in the top portion of the specimen where the self-equilibrating strain profile is most severe. This contribution of self-equilibrating strain validates the reasoning behind needing to consider these strains in design. If the nonlinear thermal gradient does have an effect on the cracking behavior, it can be expected that the contribution from self-equilibrating strain would control over the mechanical strain contribution. To quantify the effect of the self-equilibrating strain contribution, the non-thermal and thermal specimens were compared.

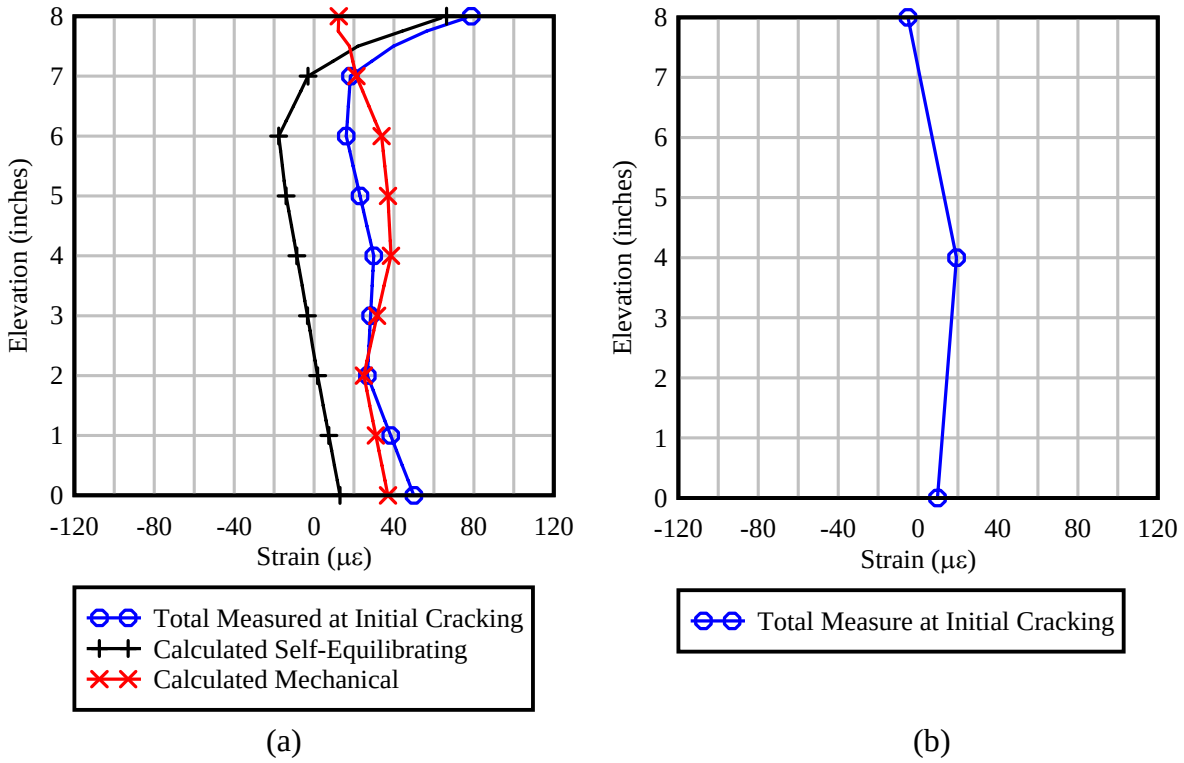

Figure 218: Test A measured strain components from (a) thermal specimen and (b) non-thermal specimen

21.2 Strain – Load Analysis

Strains measured during testing, and discussed below, required two analytical corrections. Although the strain gauges used in testing were self-temperature compensating (STC), an increased level of accuracy of strain measurement was achieved by applying two additional temperature corrections. The first correction accounted for a change in the gauge factor as the temperature deviated from the specified temperature at factory calibration. Murray and Miller (1992) explain that there is an apparent strain resulting from the thermal output associated with this temperature deviation. A factory specified equation for computing the apparent strain produced by this deviation is:

$$\varepsilon_{app} = \left[-2.97\times10^{1} + 2.73\times T^{1} - 7.23\times10^{-2}\times T^{2} + 5.30\times10^{-4}\times T^{3} - 1.40\times10^{-6}\times T^{4}\right](\mu\varepsilon)$$

Equation 33

where ε_{app} is the apparent strain from thermal output (με) and T is the temperature of material at the gauge (°C).

A gauge factor of 2.00 was assumed in Equation 33. The equation was adjusted to account for the actual gauge factor by applying the following ratio (Murray and Miller):

$$\varepsilon'_{app} = \frac{GF_1}{GF_2}\varepsilon_{app}$$

Equation 34

where ε'_{app} is the corrected apparent strain from thermal output, GF_1 is the gauge factor set for apparent strain (2.00), GF_2 is the gauge factor of strain gauge used, and ε_{app} is the calculated apparent strain from thermal output.

The second correction accounted for the difference in the coefficient of thermal expansion (CTE) between the gauge and concrete. The strain gauge was manufactured with a CTE of 11.8 x 10^{-6} /^{o}C (6.6 x 10^{-6} /^{o}F) and the concrete had an estimated CTE of 14.5 x 10^{-6} /^{o}C (8.0 x 10^{-6} /^{o}F). This final correction resulted in a total thermal output of:

$$\varepsilon_{TO} = \varepsilon'_{app} + (\alpha_2 - \alpha_1) \times 10^6 \times \Delta T \qquad \text{Equation 35}$$

where, ε_{TO} is the total thermal output correction ($\mu\varepsilon$), ε'_{app} is the corrected apparent strain from thermal output ($\mu\varepsilon$), α_1 is the specified CTE of the strain gauge (1/^{o}C), α_2 is the estimated concrete CTE (1/^{o}C), and ΔT is the change in temperature from the initial zeroed strain reading (Δ^{o}C).

The total thermal output correction strain from Equation 35 was added to the apparent measured strain to obtain the corrected measured strain. Temperature data used in Equation 33 and Equation 35 were obtained from thermocouples embedded in the specimen. The temperature gradient was assumed to be uniform through the width of the specimen. Where the elevation of a thermocouple (and therefore temperature data) did not match that of a strain gauge, the thermal output correction was linearly interpolated.

Data from the strain gauge designated “TOP” was not included in the strain profiles shown in Figure 218. This was due to uncertainty regarding the temperature of the gauge installed at the interface between the concrete and chilled water flow during thermal loading. An average of strains from the top most gauges on the right and left faces, R1 and L1, respectively, were taken as the top most reading as an alternative to the TOP strain gauge. Strain data on the top surface were linearly extrapolated from the two top most gauges.

21.3 BEHAVIOR

During each of the test sets performed, strain data and AE data were measured. A representative set of typical results (from Test A) are shown in Figure 219 and Figure 220. In these figures, the load axis indicates the tension load applied to the DYWIDAG bar. Recall that the concrete specimen was prestressed (i.e., precompressed) at the beginning of this load test. Throughout this discussion, the sign convention is such that applied tensile load is considered positive. Strain values are net measured strains relative to an initial reading taken with no prestress or applied load. The strain sign convention is such that tensile strain is positive and compressive strain is negative. Cumulative AE energy is also plotted. The AE feature event energy is the total elastic energy released by an emission event (ASTM E-1316 2006). The AE cumulative event energy is the sequential summation of energy from each event, starting at the onset of loading.

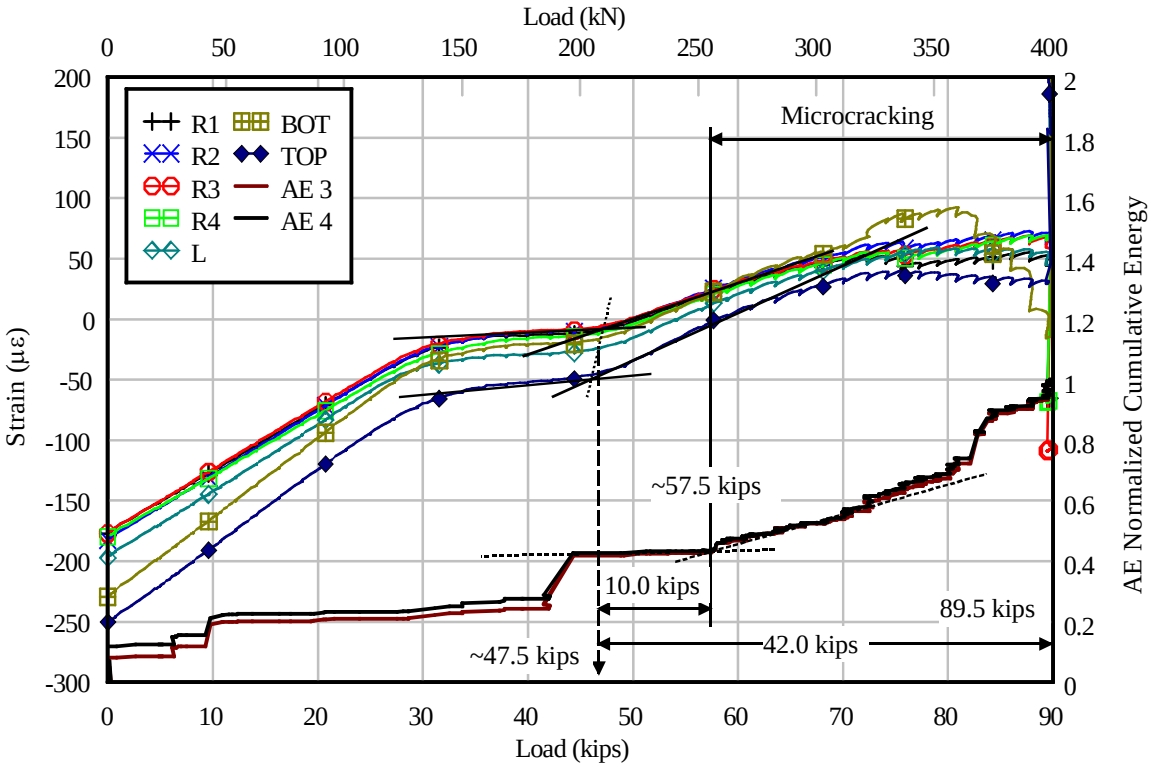

Figure 219: Test A - Non-thermal specimen

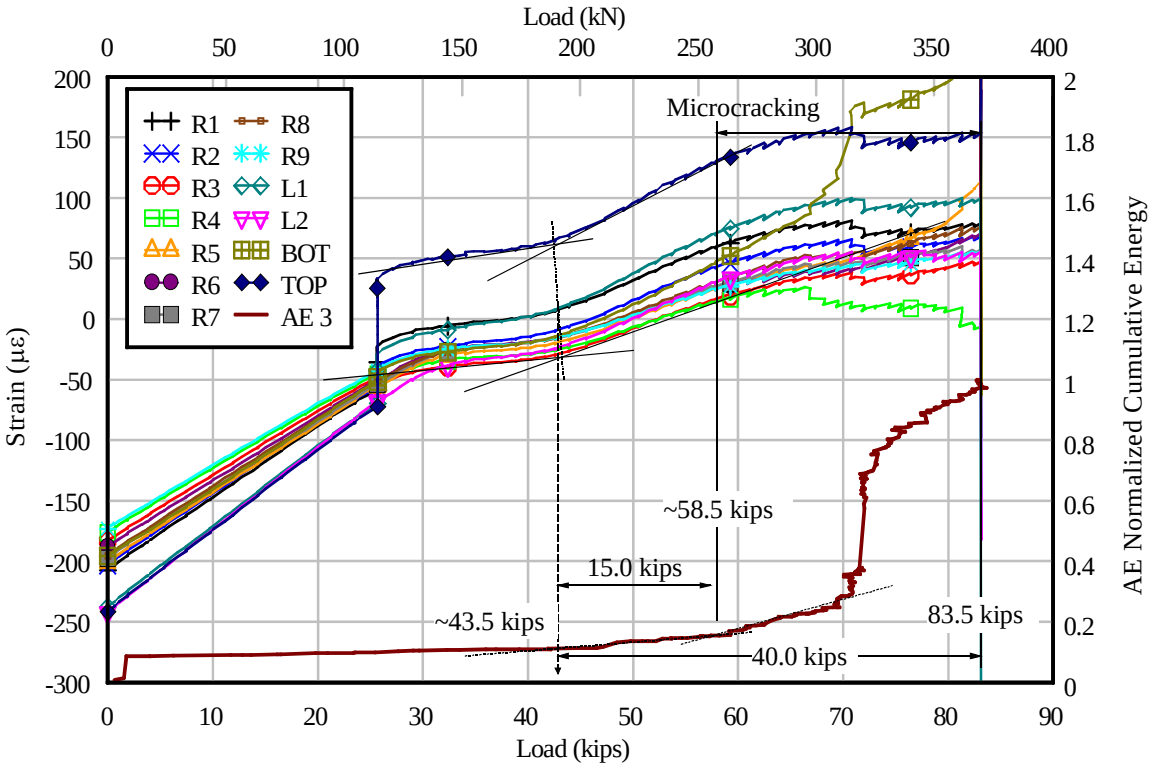

Figure 220: Test A - Thermal specimen

The initial measured strain of approximately -170 microstrain to -250 microstrain at zero applied tensile load is due to the prestress (Figure 219 and Figure 220). If the prestressing were applied uniaxially, then the strains in all of the gauges should be equal. Variation in the initial measured strain, however, indicates that the prestressing was applied with some eccentricity, which induced flexural strain. The flexural strain contribution to the measured strain varies with the location of each strain gauge in relation to the neutral axis of the section. Because the magnitude and distribution of the initial strain is similar between the thermal and non thermal specimens, it is likely that the DYWIDAG bar and internal anchors were not perfectly centered or parallel, resulting in induced flexure. Minimal out-of-straightness in the DYWIDAG bar while stressed prior to curing of the concrete specimen also may have contributed to the flexural strains when the specimen was prestressed.

As bar tension was increased from zero, the concrete specimen was decompressed. Each strain gauge indicated linear behavior as the strain approached zero with the slopes of the plots varying due to gauge location and eccentric prestressing. Strains in both thermal and non-thermal specimens reached a plateau at approximately 30 kips. In the thermal specimen the sharp increase in strain at approximately 25 kips was due to the application of the thermal gradient. The marked increase in strain, particularly in the top gauge, is associated with the self-equilibrating strains resulting from the nonlinear thermal gradient. No additional load was applied to the specimen for approximately 2 minutes as the thermal gradient was imposed.

The plateau in strain is associated with specimen stress moving from net compression to net tension. Ideally, the strain-load plot would continue from compression to tension without a change in slope. As the stress moved from compression to tension however, there was a small amount of “take up” in the anchorage. This take up was presumed to be the result of minute gaps formed between the anchor face and internal concrete surface from drying shrinkage of the concrete during curing. The anchor traversed this gap as it transitioned from applying a compressive stress on the specimen to applying a tensile stress on the specimen. Additional internal movement may have occurred due to crushing of the concrete at the face of the anchor and debonding of the DYWIDAG bar within the specimen.

Under ideal conditions the strain would have been zero over this transition between net compression and net tension. Drying shrinkage also resulted in residual shrinkage strains occurring from the fixed conditions between internal anchors. This contributed an initial tensile strain in the concrete before the strain gauges were applied and zeroed.

As loading continued beyond the strain plateau, the specimen was subjected to net tension. The initial tensile slope of the plots are linear over a range of about 10 kips in the non-thermal specimen and 15 kips in the thermal specimen. As loading continued beyond this point, the slope of the plot began to decrease. As noted in both the thermal and non-thermal plots, increased AE activity consistently occurred near this change in slope. While the decrease in slope would be indicative of stiffening, it is thought that this is the result of the reduced effectiveness of the strain gauge as microcracking begins.

Although the strain gauges appeared to indicate stiffening, in reality, the concrete is actually softening due to the microcracking. This is confirmed by the load displacement plot Figure 221, which shows the total load in the prestressing bar plotted against the bar elongation as measured at each end of the bar. The plot shows an overall decrease in specimen stiffness due to microcracking occurring in the concrete. This point is the same as that noted in the load strain plot. The displacement shown is the total elongation of the steel bar measured end-to-end of the total experimental system, including the composite specimen and steel bar extended from each

end (Figure 223b). The initial prestressing of the steel bar without concrete is shown to be linear in Figure 221. After curing and prestressing of the concrete specimen, loading of the specimen is shown to remain linear until initial microcracking occurs (determined using strain-load) and then the stiffness is reduced as cracking of the specimen progresses. The initial nonlinear portion to 15 kips can be associated with unmeasured initial deformations in the load frame.

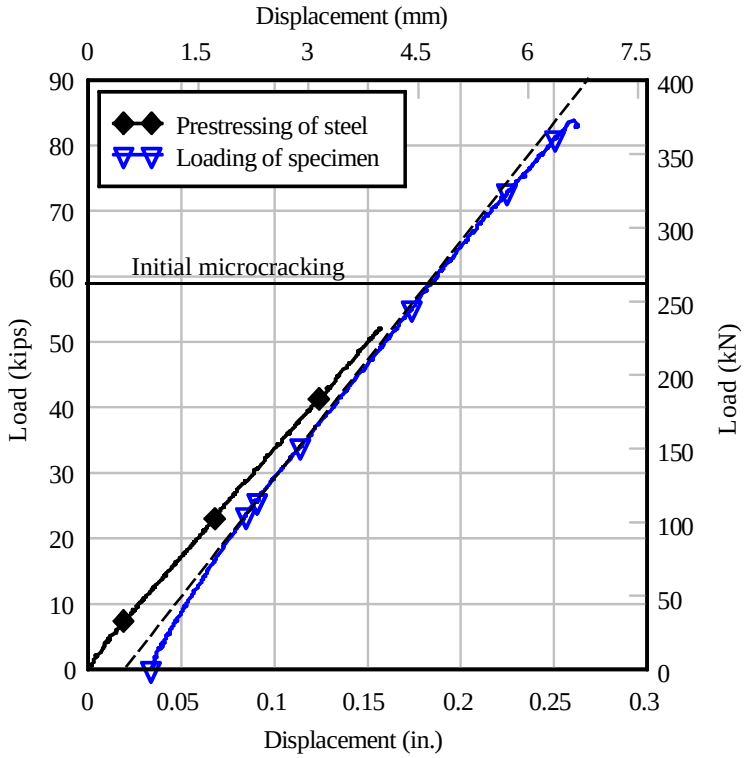

Figure 221: Test A Load-Displacement of Thermal specimen

The incremental rise and fall of strain evident in the plots resulted from the use of a manual hydraulic jack. After each stroke of the manual hydraulic jack, a slight loss of the applied direct tensile load, and thus strain, was observed on the specimen. This loading pattern did not appear to have any effect on the outcome of testing.

The slope change noted at the initiation of microcracking was typically dependent on the location of the final crack relative to the individual gauge. Generally, data from each strain gauge indicated an increase in axial stiffness when microcracking, and eventually macrocracking, occurred at the location of the gauge. In a few instances, the strain gauge data indicated a decrease in the apparent stiffness. This typically occurred when cracks formed in the vicinity of the gauge but not directly under the gauge. A few atypical instances where the strain gauge did not behave in this manner further indicate a reduced effectiveness of the strain gauge as microcracking begins. These instances may have occurred due to how debonding occurred at the surface interface of the gauge and concrete as microcracking occurred under and around the gauge.

The slope change continued until the microcracking coalesced into a single visible crack (Figure 222), which occurred at 89 kips and 83 kips for the non-thermal and thermal specimens, respectively. These macrocracks formed suddenly and were detected both visually and audibly. Ultimate failure of the specimen occurred when visible macrocracking and a sharp increase, or decrease, in strain was observed. At failure of the specimen, the minimal difference in the loads

between the thermal and non-thermal specimens was noted. Further analysis was performed on the tests to quantify the differences observed in cracking behavior between the thermal and non-thermal specimens.

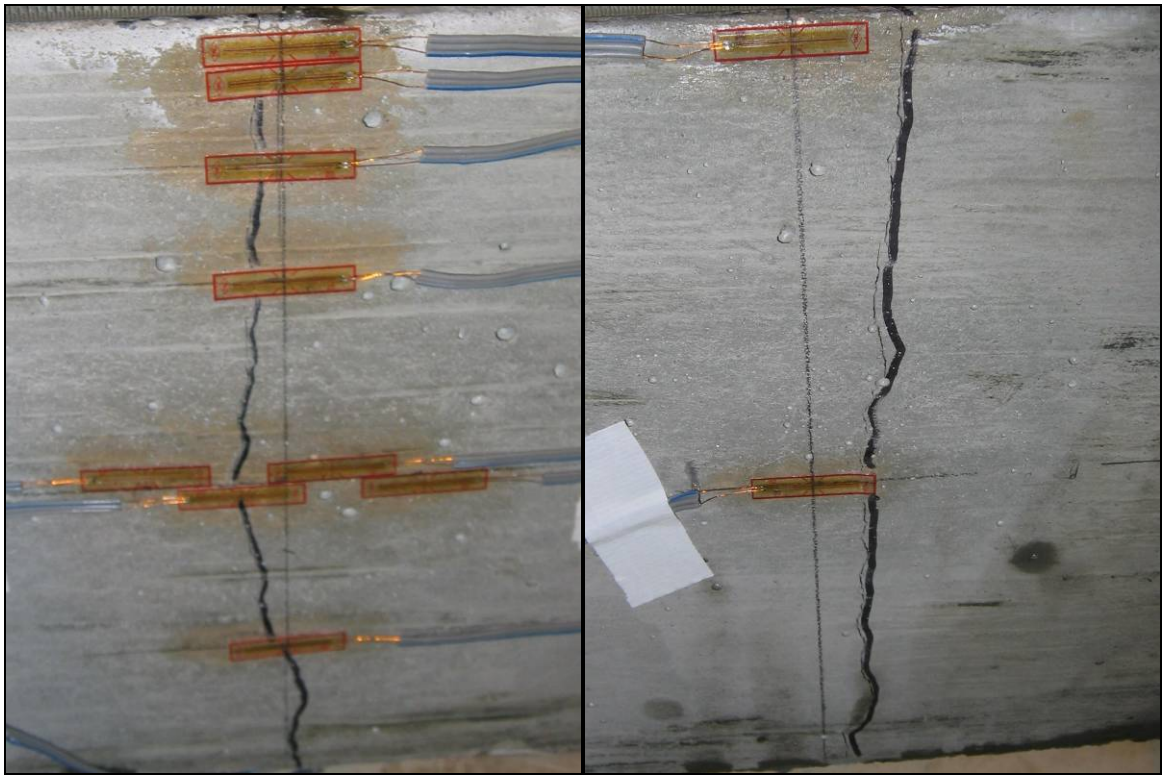

(a) (b)

Figure 222: Test A - Crack on (a) right face and (b) left face of thermal test specimen

21.4 ANALYSIS

To determine the share of the load carried by the concrete under net tension, the test specimen was modeled using a spring analogy. Figure 223a shows a model of the concrete section and steel bar between the anchors. If the gauge lengths of the concrete and steel bar are equal, then the relative stiffness is a function of the cross sectional area and modulus of elasticity. The total stiffness is the sum of the two stiffness terms. Using the section dimensions, a concrete modulus of elasticity of $57000\sqrt{f'_c}$, and a steel modulus of 29,000 ksi, it was determined that the concrete section comprises 83% of the total stiffness while the steel bar contributes 17%, which results in the concrete carrying most of the load applied to the bar.

To determine the net effect of the system stiffness on the overall load-displacement (Figure 221), the stiffness of the steel bar outside the anchors must be considered. Figure 223b shows the added spring element to account for this additional steel bar length. The calculated stiffness for this spring is 4% of the combined stiffness of the two parallel springs. The added bar length dominates the load deflection behavior because it is in series with the specimen and its stiffness is so much lower than that of the composite specimen. This explains the relatively small change in slope of the load-displacement plot when the concrete begins microcracking (Figure 221).

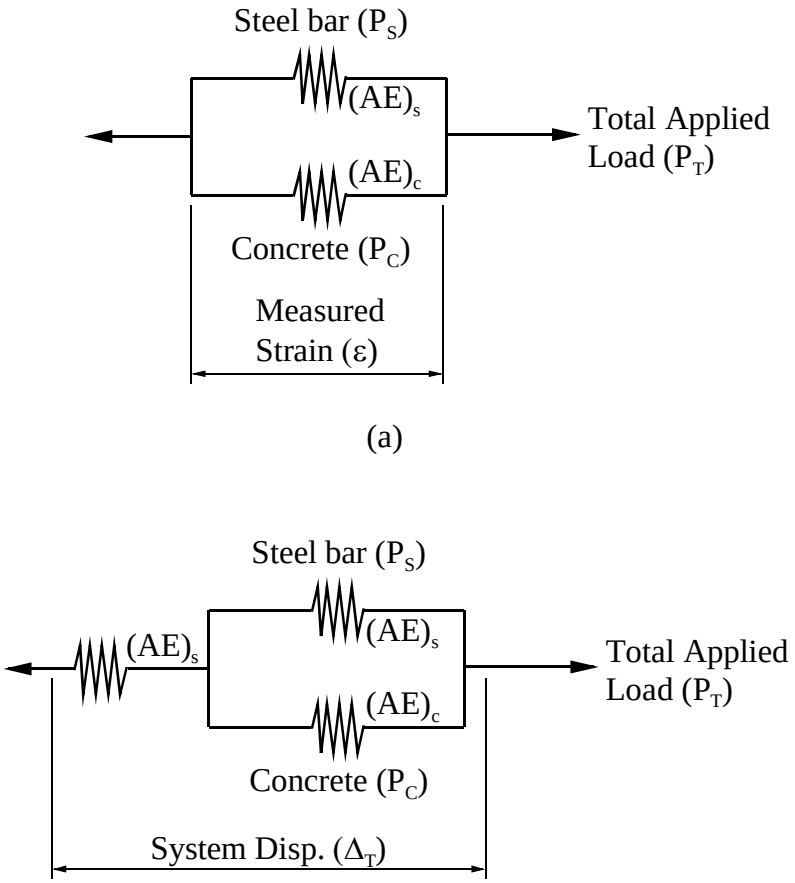

Figure 223: Axial stiffness of (a) specimen and (b) system

Figure 224 shows an idealized representation of the test data with measured strain plotted on the y-axis. The total bar load measured during the test was converted to stress using the portion of the load carried by the concrete as determined using the spring analogy model. This load was divided by the section area to obtain stress, which was offset by the known prestress. The net concrete stress, *f*, was normalized by the square root of the average cylinder compressive strength for the tested specimen.

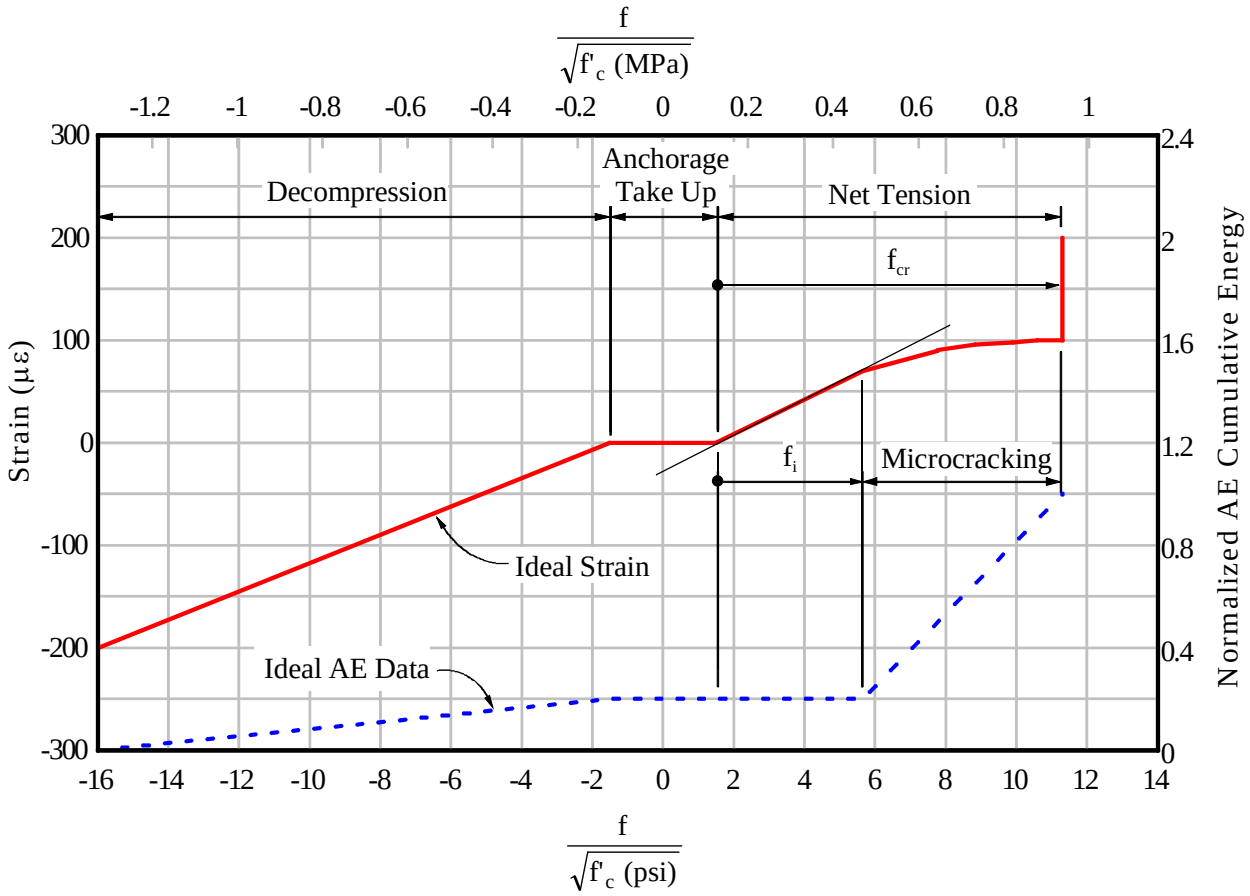

Figure 224: Idealized test data set and terminology

Decompression, anchorage take up, and net tension define the three distinctive regions of the stress strain curves for the specimen. Decompression is defined as the load range from the beginning of the test to the plateau associated with take up of the anchorage. Net tension began at the end of the anchorage take up, which is defined as the intersection point of the tangent lines occurring before and after the change in slope. The average of the strain gauges with the highest and lowest strain reading (shown connected by a small dashed line in Figure 219 and Figure 220) were used to establish the point at which net tension began. The tangent lines, points of intersection, and averages were all determined graphically.

Generally, the initial portion of the net tension curve was linear and as microcracking initiated in the concrete, the curve became nonlinear. The initiation of microcracking was also typically marked by a significant increase in AE cumulative event energy, which also indicates the occurrence of microcracking. The AE cumulative event energy assisted in quantitatively determining the onset of damage to the concrete specimen. It was observed that the rate of accumulation of AE event energy increased sharply at the onset of microcracking, corresponding to the change in apparent axial stiffness of the specimen. This point was determined, using AE data, as the intersection of a tangent line passing through data points that occurred during and after the take up of the anchorage, and a tangent line passing through data points following the sharp increase in accumulation of AE event energy. Accumulation of AE event energy that occurred prior to the tensile strain region was thought to be associated with events occurring at

the bond interface of the DYWIDAG bar and concrete. To eliminate extraneous AE events occurring from movement of the anchorage during loading, only the events occurring between AE sensors 3 and 4 in Figure 213 were used.

To evaluate the effect of the imposed self-equilibrating thermal stress on cracking behavior of the section, f_i and f_{cr} are defined. Stress f_i represents the average concrete net tensile stress at which microcracking begins, whereas f_{cr} is the average concrete net tensile stress required to form a visible crack. Both values are taken as a difference relative to the onset of the net tensile region as previously defined. Typical values of f_i and f_{cr}, defined earlier for an idealized data set in Figure 224, are presented for a typical test set in Figure 225 and Figure 226.

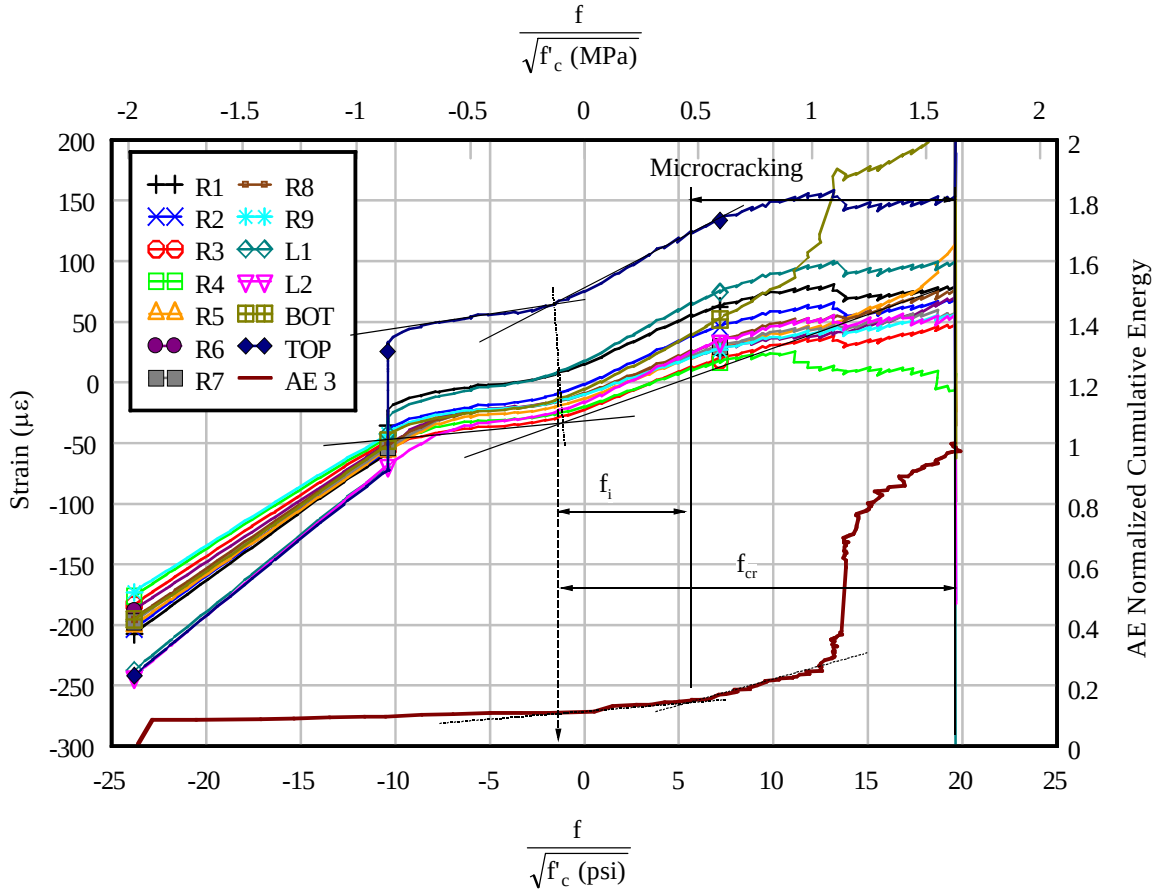

Figure 225: Test A - thermal specimen (stress ratio)

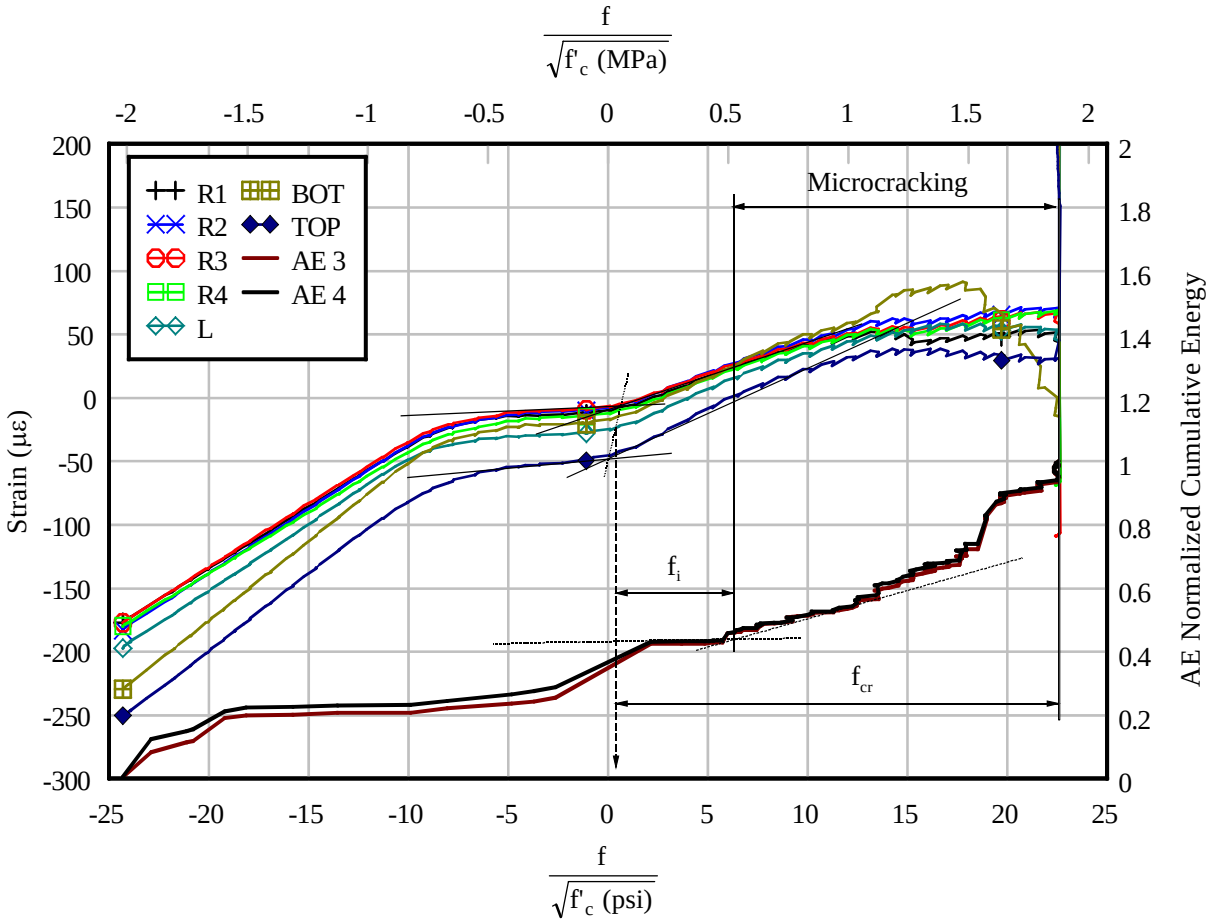

Figure 226: Test A non-thermal specimen (stress ratio)

21.5 CRACKING BEHAVIOR

To evaluate the effect of the imposed self-equilibrating thermal stress on cracking behavior of the section, the net tensile stress at initial microcracking, f_i, and the net tensile stress at visible cracking, f_{cr}, were compared for thermal and non-thermal specimen tests. By specifically investigating f_i for each thermal and non-thermal test, the effect of the nonlinear thermal gradient on the initiation of cracking behavior was determined. The net tensile stress values were normalized by the square root of the concrete compressive strength and compared. The results of f_i and f_{cr} are compared by showing the range of microcracking for each test set in Figure 227. Further numeric data represented in this figure can be found in Appendix H.

A direct comparison among non-thermal tests or among thermal tests was not considered due to concrete and test condition variability. The major factors contributing to the variability between tests were concrete material properties per batch (e.g. concrete compressive and tensile strength) and prestress force. As such, direct quantitative comparisons were considered only between the non-thermal and thermal specimens of a single test set.

In investigating the onset of cracking, it would be expected that the addition of a self-equilibrating tensile strain on a section, if significant, would result in a reduction in the applied net tensile load required to crack the specimen. This would result in a lower applied net tensile stress on the concrete. It can be observed in Figure 227 that the lower bound of microcracking, f_i,

of the thermal specimens show no such consistent decrease in applied net tensile stress when compared to the non-thermal specimens. The coefficient of variation for normalized values of f_i for all tests was 61%, with an average normalized value of f_i of 3.2 for all tests. This overall variation and the variation in f_i values for thermal specimens relative to non-thermal specimens reveal that there may be no significant effect that the nonlinear thermal gradient has on the initiation of cracking behavior.

For values of the normalized net tensile stress at cracking (f_{cr}), the coefficient of variation for all tests was 31% and the average value for all tests was 13.3. The observed differences in f_{cr} between non-thermal specimens and thermal specimens were not considered as critical in this investigation compared to the differences in f_i. The effect of a nonlinear thermal gradient on the serviceability, and thus the *onset* of damage to the concrete in the form of cracking, was the primary focus of this investigation.

The increased range of microcracking observed in Test A compared to other tests could be due to environmental conditions during concrete mixing and curing resulting in a difference in concrete properties (e.g. modulus of elasticity). Since test specimen results were compared within each test set, this was considered to be a minor factor in the results.

The normalized modulus of rupture for each test set, along with a value of 7.5 as reference, are shown in Figure 227. The averages for the upper and lower bounds of microcracking are shown for all tests, 3.2 and 13.3, respectively. This compares to the general cracking behavior of concrete previously discussed where it was noted that the normalized modulus of rupture could have a range between 5 and 12 (Popovics 1998). The comparable ranges and the variation in the upper and lower bounds indicate that the nonlinear thermal gradient had no discernable effect on the cracking behavior of concrete. It is postulated that the early microcracking changes the section properties and drastically curtails the influence of the severe gradient on the overall tension state in the concrete. This coupled with the variability associated with concrete in tension may explain why there is no apparent influence.

With both an observed decrease and increase, compared to an expected decrease, in the normalized net tensile stress at initial microcracking of the thermal specimen relative to the non-thermal specimen; and an observed average range of microcracking similar to that of the typical range for modulus of rupture in concrete; the influence of a nonlinear thermal gradient and the resulting self-equilibrating strains appear to be insignificant. Based on the tests conducted in this study, it has been determined that the self-equilibrating stresses from nonlinear negative thermal gradient had no discernable influence on the cracking behavior of concrete specimen tests in this research. As such, the consideration of a nonlinear thermal gradient and the structural response to such a gradient as outlined by AASHTO (1999) may not need to be considered for serviceability.

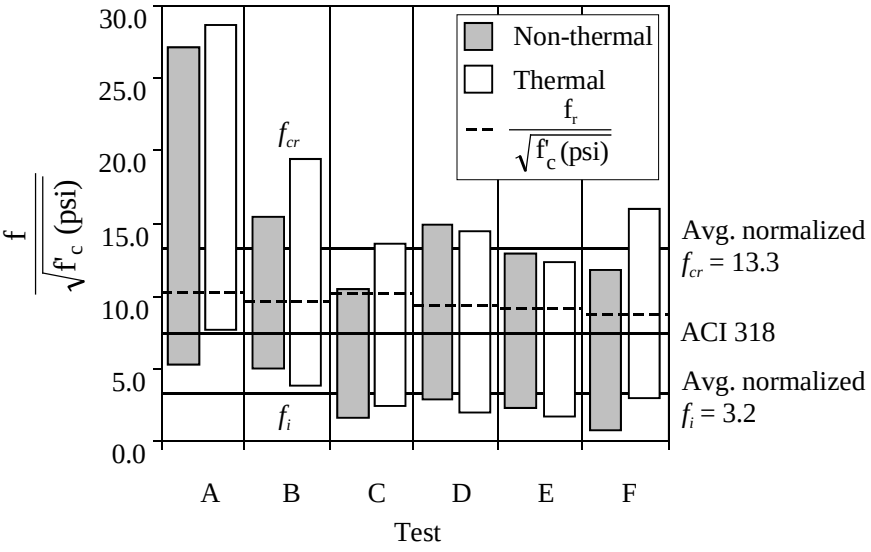

Figure 227: Stress ratio ranges of microcracking

22 CRACKING BEHAVIOR IN BEAM

A final test was performed on the Part One beam with the AASHTO negative thermal gradient imposed. The intent of this final test was to further investigate the effect of the AASHTO negative thermal gradient and resulting self-equilibrating stresses on cracking behavior in prestressed concrete. The following section describes the process of preparing the beam for testing, the procedure for testing, and a discussion of the results.

22.1 EPOXY OF JOINTS

To obtain the necessary flexural tensile stresses on the beam, the existing prestressed dry joint segmental beam was disassembled and epoxy applied to the joints. The post-tensioned bars were first detensioned and removed. Segments were separated and temporarily supported by wood blocks to allow for application of the epoxy (Figure 228). Segments 1, 3, and 4 were moved away from segment 2, which remained in position to be used as a point of reference when reassembled and to avoid disturbing the bearing.

Figure 228: Disassembled beam for application of epoxy

FDOT *Standard Specifications for Road and Bridge Construction*, Section 453, requires that the segmental joints be sandblasted before application of epoxy. To remain consistent with the field specifications, each of the match-cast faces were lightly sandblasted to remove concrete laitance and release agent from the match-cast. Plastic sheeting was taped to the edges of each face to protect instrumentation during application of the epoxy (Figure 229). The epoxy used was Pilgrim CBC 6, a slow-set epoxy for sealing and bonding of match-cast faces of joints between precast concrete segments in segmental bridge construction. Epoxy was mixed and applied to the match-cast faces of all three joints. The epoxy was prepared and applied professionally by a representative of the epoxy company used. Immediately following the application of epoxy, segments were reassembled and post-tension bars reinstalled along the length of the beam.

Figure 229: Epoxy applied to match-cast face at joint

22.2 PRESTRESSING

Immediately after application of the epoxy, the segments were moved as close as possible together and the prestressing bars were reinstalled. The bars were prestressed in tandem using identical hydraulic jacks that were connected through a manifold to ensure even application of pressure and force. P1 and P2 were stressed together followed by P3 and P4 (Figure 230). During the initial stressing operation, several inches of travel was required to squeeze out the excess epoxy and allow the joints to seat. The prestress forces both immediately after prestressing and just prior to testing are shown in Table 34. The change in prestress force observed in bar P2 and P4 may have been caused in lifting the tip of the beam slightly to remove a temporary support located at the tip of the cantilevered beam. This may have resulted in a shift of the beam and a loss of prestress force in P4. The total prestress force loss, however, was less than 2% of the original. The net horizontal eccentricity of the resultant prestress force from the beam centroid was less than 0.1 in. before testing. Vertical eccentricity was maintained at 1.5 in. below the centroid of the beam.

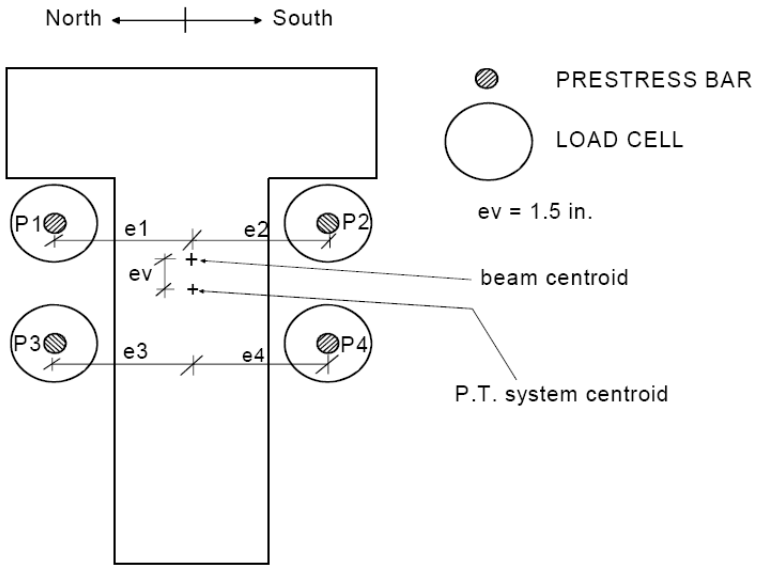

Figure 230: Post-tensioning bar designations and eccentricities

Table 34: Bar prestress force and eccentricity at prestressing

Bar	Force (kips)		Horizontal Eccentricity Designation	Horizontal Eccentricity (in.)
	After prestressing (4/28/2009)	Before testing (5/13/2009)		
P1	94.7	94.4	e1	8.5
P2	102.1	123.3	e2	8.5
P3	100.2	96.9	e3	8.5
P4	96.5	71.3	e4	8.5
Total	393.5	385.9		

22.3 MODIFIED TEST SETUP AND INSTRUMENTATION

The test setup and instrumentation used was identical to Part One tests except for a few minor changes. These modifications to the test setup and instrumentation were required for load tests on the epoxy-jointed segmental beam. The point of applied mechanical load was moved to 1.9 ft from the cantilevered end of the beam (Figure 231). This was required due to a change in the hydraulic jack and mechanism for mounting to the load frame. The hydraulic jack used to apply mechanical loads was a 60 ton manually pressurized jack, similar to the jack used in Part One testing but with a longer stroke.

Instrumentation used for this test is shown in Figure 232 through Figure 234. Fewer strain gauges were required than in Part One because the focus of the Part Two testing was on identifying the load and location at which cracking occurs. Strain gauges selected for monitoring were intended to capture the overall strain profile at mid-support and indicate crack location. A single strain gauge was selected at both Joint 1 (J1) and Joint 3 (J3) to detect cracking at these

locations. Additional strain gauges were applied, in series, to the top face of the beam at Joint 2 to capture cracking of the section at the predicted maximum tensile stress location over the mid-support (Figure 234 and Figure 235).

AE sensors were strategically placed on the flanges and top face of the beam to capture microcracking activity (Figure 232 through Figure 234). The AE sensors were placed around the mid-support where cracking was predicted to occur.

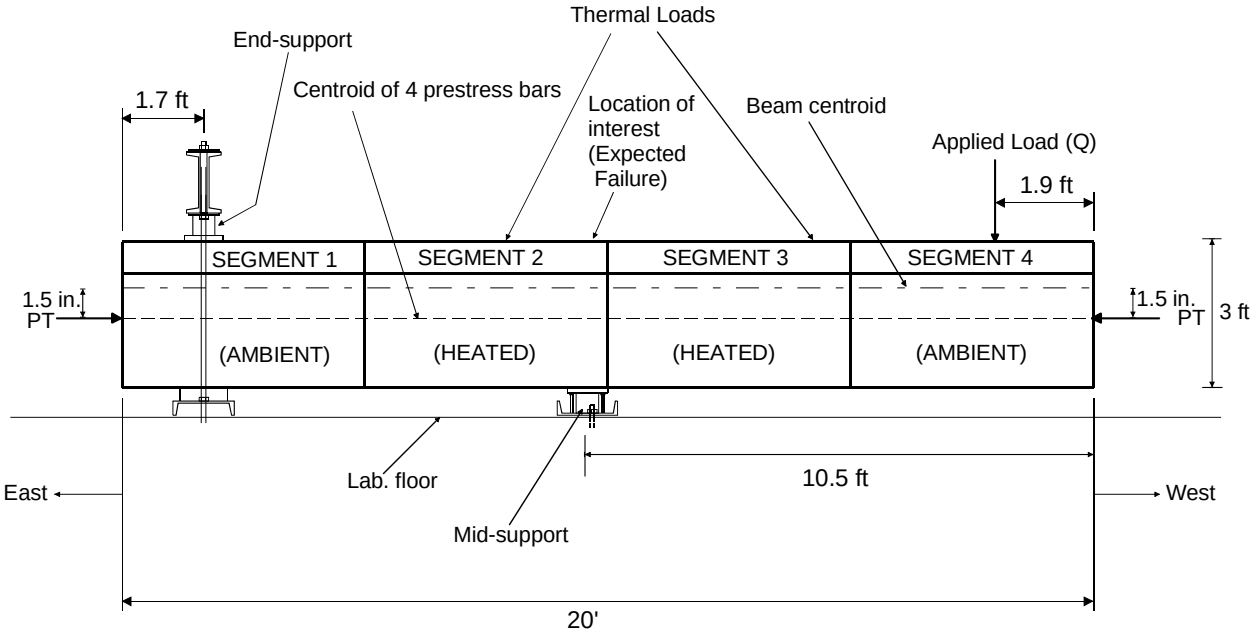

Figure 231: Modified test setup

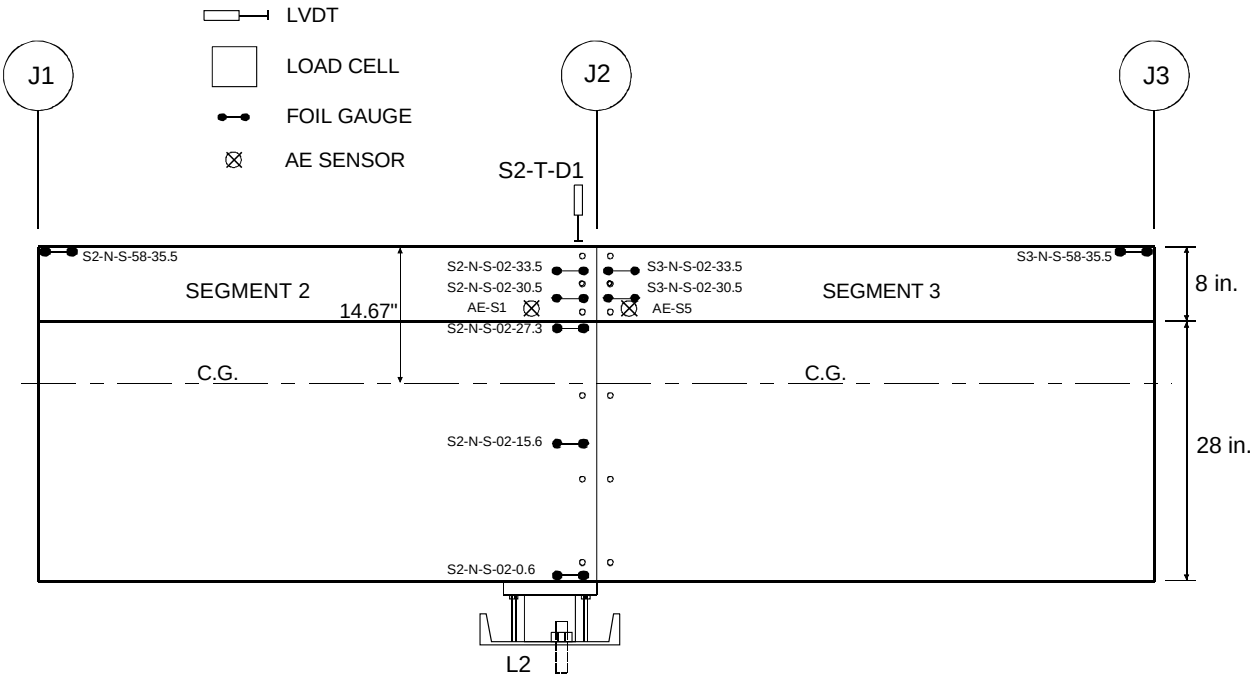

Figure 232: Modified instrumentation details (North side)

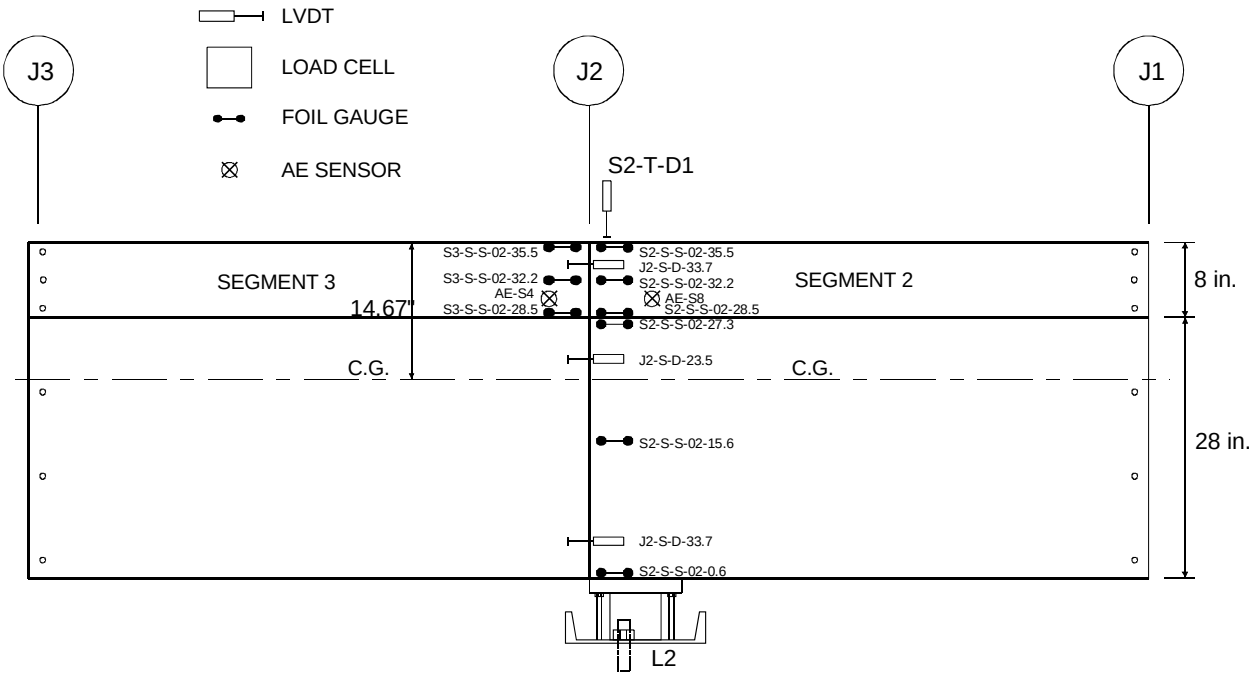

Figure 233: Modified instrumentation details (South side)

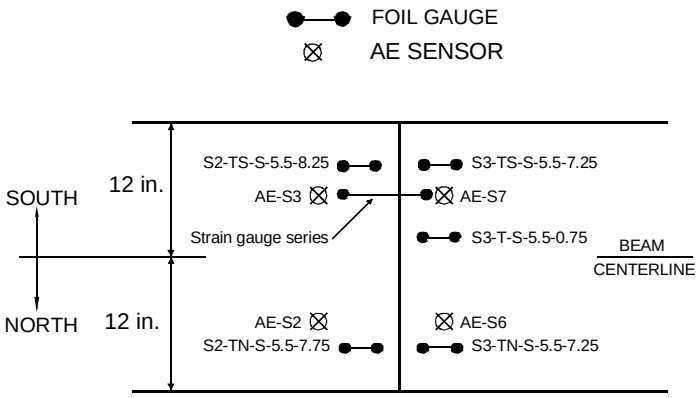

Figure 234: Modified instrumentation at midspan (top flange)

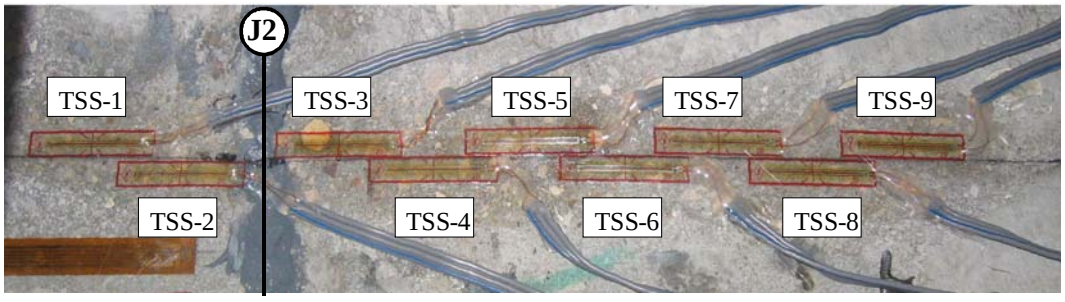

Figure 235: Strain gauge series for crack detection

22.4 TESTING PROCEDURE

The goal of this test was to determine the effect of the thermal gradient on cracking. A series of three load tests were conducted. The first load test was conducted with the AASHTO negative thermal gradient imposed. AE data were monitored in real-time as load was applied. The intent was to apply sufficient load to produce microcracking, but stop short of forming a crack. The second test was conducted with the segments at ambient uniform temperature. Load was applied with the intent to terminate the test when microcracking was detected using the real-time AE data. It was anticipated that the load required to reinitiate microcracking would be higher than that of the first test if the self-equilibrating stresses significantly affected the cracking behavior. The third, and final, test was conducted with the AASHTO negative thermal gradient imposed. The beam was loaded until visible cracks formed.

The AASHTO negative thermal gradient for the first and third load tests was imposed on the beam as in the Part One tests. The target thermal gradient was imposed on the heated segments prior to conducting the load test. Once the desired gradient was obtained, a mechanical load was applied to the beam.

To prevent loading past the initiation of cracking, AE sensors were monitored to detect cracking. The intent was to monitor the acoustic emission in real time during testing and to detect an increase in acoustic emission activity, typical at the initiation of cracking in concrete. A similar method utilizing the increase in acoustic emission energy was used successfully in the specimen tests (described earlier) to determine the initiation of cracking in post-test analysis. In monitoring the real-time acoustic emission during testing, an increase in acoustic emission was observed, typically indicative of cracking. Some difficulty was found in monitoring the real-time acoustic emission energy during testing and determining the initiation of cracking. As such, to further ensure detection of cracking, cyclical loading was performed. Cyclical loading allowed for the detection of previously induced damage, or cracking, in the beam. Cyclical loading of the beam produced a phenomenon known as the Kaiser Effect and damage was detected through what is known as the Felicity Effect.

The Kaiser Effect has been found to be an acoustic emission phenomena observed in some materials. ASTM defines it as follows; “Kaiser Effect [is] the absence of detectable acoustic emission at a fixed sensitivity level [threshold], until previous applied stress levels are exceeded,” (ASTM E 1316). This phenomenon facilitates an investigation of past loads applied to a structure.

The Felicity Effect is the breakdown of the Kaiser Effect. ASTM defines it as follows, “Felicity Effect [is] the presence of acoustic emission, detectable at a fixed predetermined sensitivity level [threshold] at stress levels below those previous applied,” (ASTM E 1316). The Felicity Ratio is the ratio between the load at the onset of acoustic emission during a reload and maximum load applied during the previous load cycle. Prior to breakdown of the Kaiser Effect, the Felicity Ratio is unity. If this ratio becomes less than unity, it is an indication that structural damage has occurred. Ridge and Ziehl (2006) found diminishing values of the Felicity Ratio as they applied cyclically increasing loads to strengthened reinforced concrete beams. This same effect was observed for reinforced and prestressed concrete beams (Shield and Hearn 1997).

Loading for the first test started at an initial loading to approximately 15 kips. The initial loading provided decompression in the extreme top fiber of the beam. Cyclical loading of the beam continued from this point, with each cycle beginning with a reduction of load by approximately 5 kips. The peak load applied increased by approximately 5 kips every cycle. This

cycle continued until evidence of initial cracking was observed in the acoustic emission by the Felicity Effect, at a load of 27 kips.

Loading for the second test was conducted in a similar manner. Initial loading of the beam went beyond the previous peak load by approximately 10 kips. Cyclical loading followed from this point. Again, cyclical loading continued by increasing the peak load for each cycle by approximately 5 kips until evidence of further cracking was observed by use of acoustic emission energy

The final load test was conducted with no cyclical loading and was loaded directly to failure of the beam. Microcracking and failure of the beam were detected using acoustic emission sensors and load-displacement data. Failure of the beam was confirmed by visual macrocracks. This completed the load test.

22.5 RESULTS

In total, three load tests were performed with the intent to reach ultimate failure of the beam on the final test. Further, it was the intent to stop loading in the first two tests at initial detection of microcracking through the use of acoustic emission energy. Although all three tests were performed, it appears, based on the data from the initial test, that structural cracking occurred during the initial loading. Consequently, only the first two tests are discussed.

Prior to the first load test the negative thermal gradient was imposed on the thermal segments. Temperature-controlled water was pumped through the pipes embedded in the thermal sections to impose and maintain the thermal gradient. This flow also caused significant spurious acoustic emissions that were detected by the AE equipment. As such, to avoid masking the acoustic emission from cracking, the water flow was terminated just prior to load application. Termination of flow, however, resulted in minor distortion of the thermal gradient, which became excessive after approximately 10 minutes. Figure 236 and Figure 237 show the slight distortion of the gradient over the 10-minute period following flow termination.

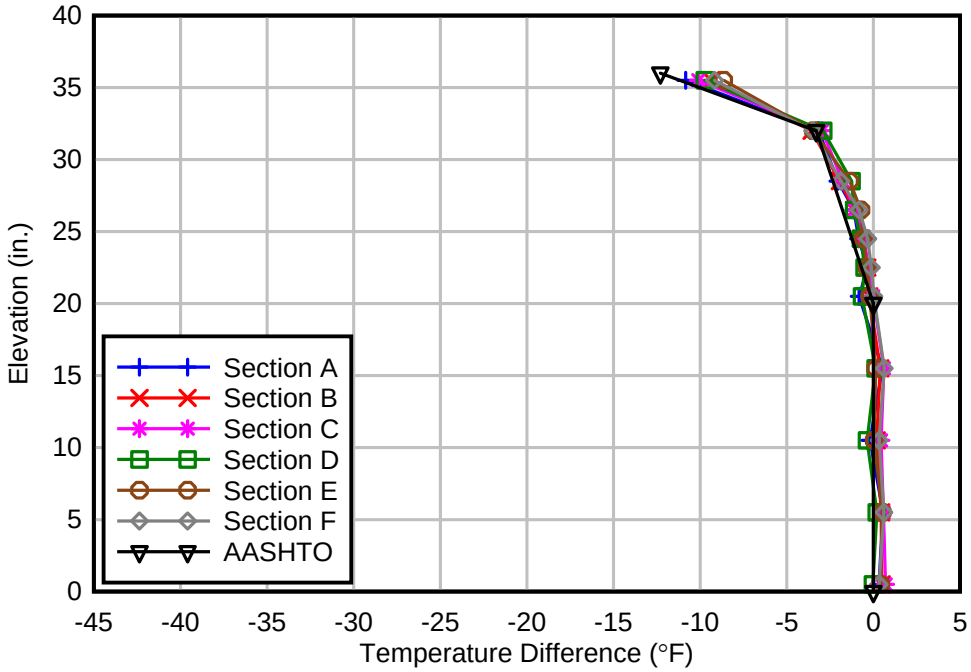

Figure 236: Laboratory imposed negative thermal gradient at load test initiation

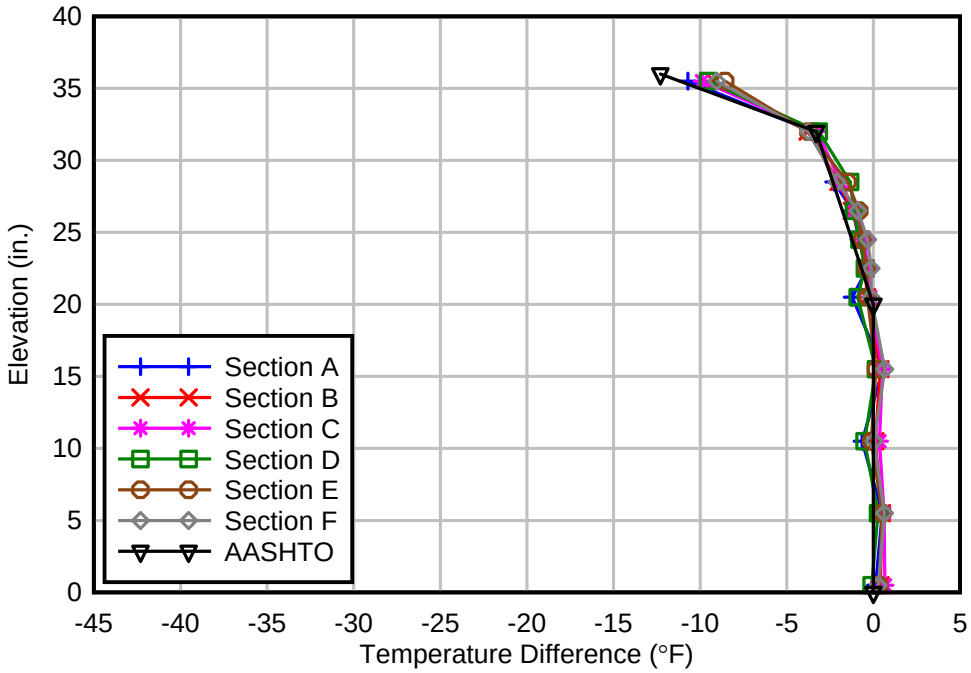

Figure 237: Laboratory imposed negative thermal gradient at estimated initial cracking (approximately 10 minutes after water flow was terminated).

The strains from the top strain gauges near Joint 2 are plotted against the applied load in Figure 238 and Figure 239. The predicted strain is shown for reference, assuming linear-elastic

behavior and accounting for self-equilibrating strain by assuming the target AASHTO negative thermal gradient. One of the top face strain gauges, *S3-TS-S-5.5-7.25*, shows linear behavior up to approximately 15 kips where the strain appears to plateau. Similarly, strain gauge *S2-TN-S-5.5-7.75* plateaus at approximately 25 kips indicating that macrocracking had propagated across the top. A similar plateau – which appears to be stiffening – was noted in the segment tests performed earlier in this research. The apparent stiffening of a strain gauge was noted to occur where cracking occurred in the vicinity of the strain gauge but not directly under it. This is further evident in observing the final macrocrack locations relative to the top strain gauges (Figure 240 and Figure 241). After investigating crack locations of the final test, it was noted that no visible cracking was observed under any strain gauge. Visible cracking was not investigated until the final test due to insulation requirements for maintaining the thermal gradient during testing.

Further evidence of cracking in the first load test is observed in the change in prestress force as loading was applied (Figure 242). The change in prestress force is linear as load is applied to the beam until approximately 15 kips and then becomes nonlinear as loading continues. This occurs at the previously noted point of initial microcracking.

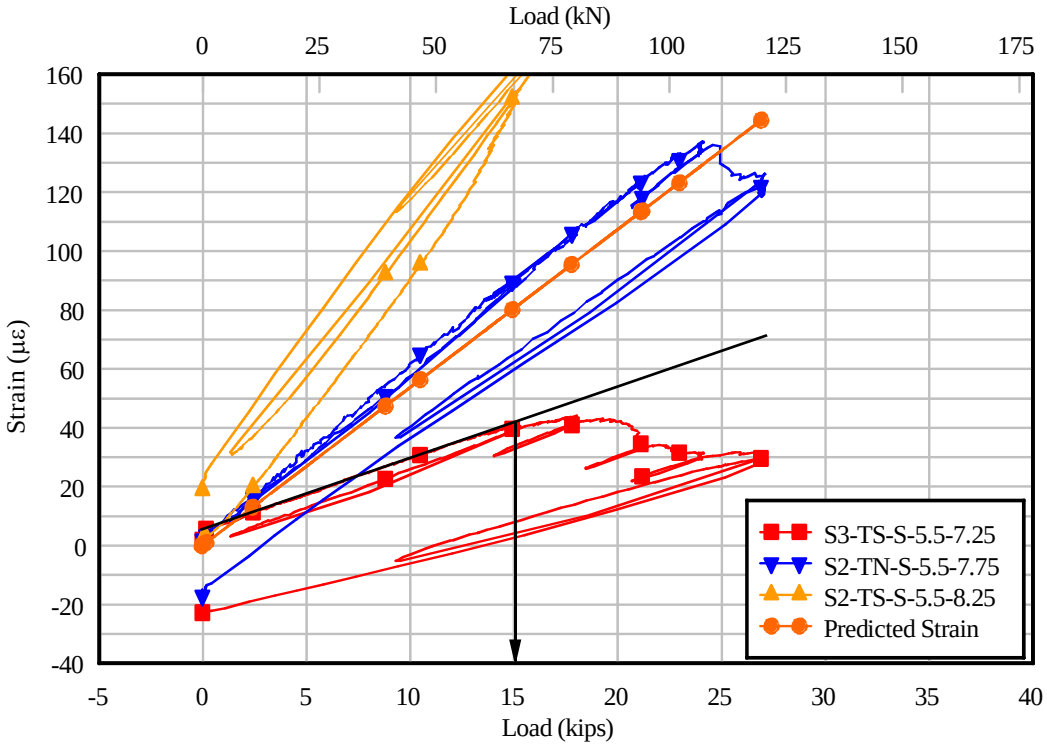

Figure 238: Thermal preload test – Top face strain gauges

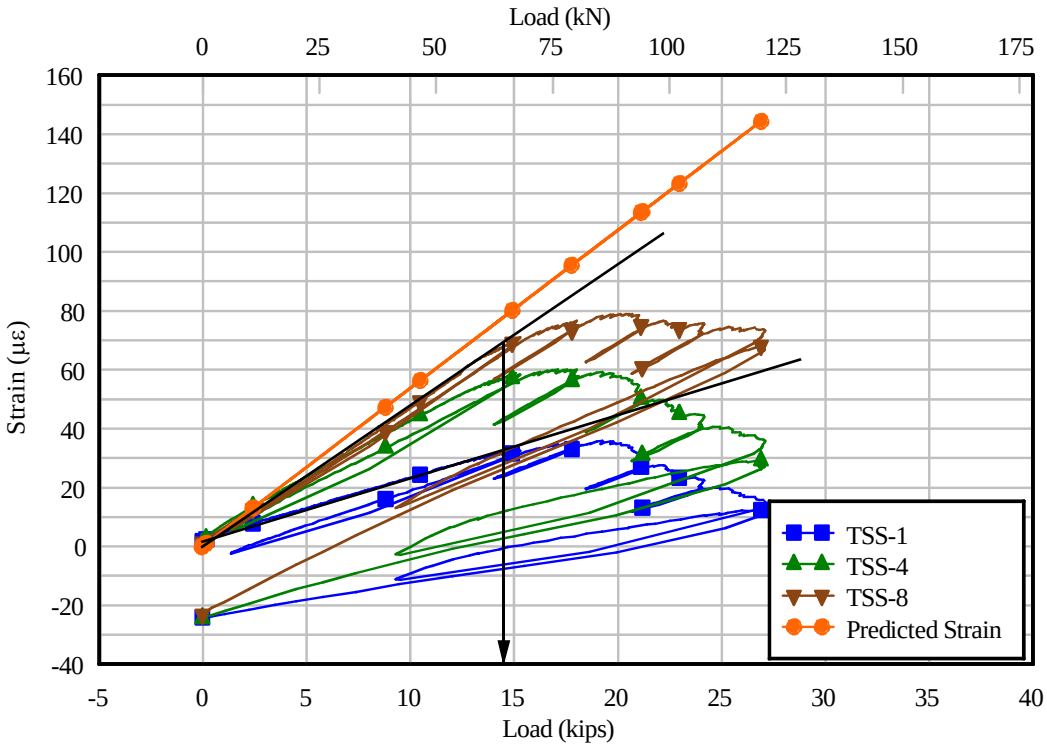

Figure 239: Thermal preload test – Cracking strain gauge series

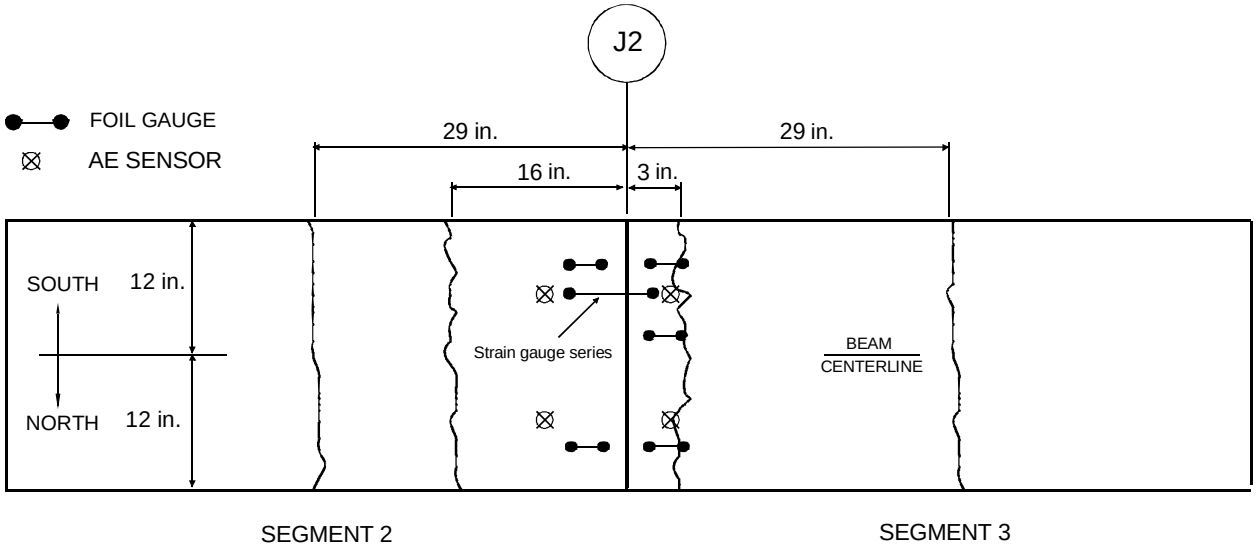

Figure 240: Visible crack locations - Top of beam

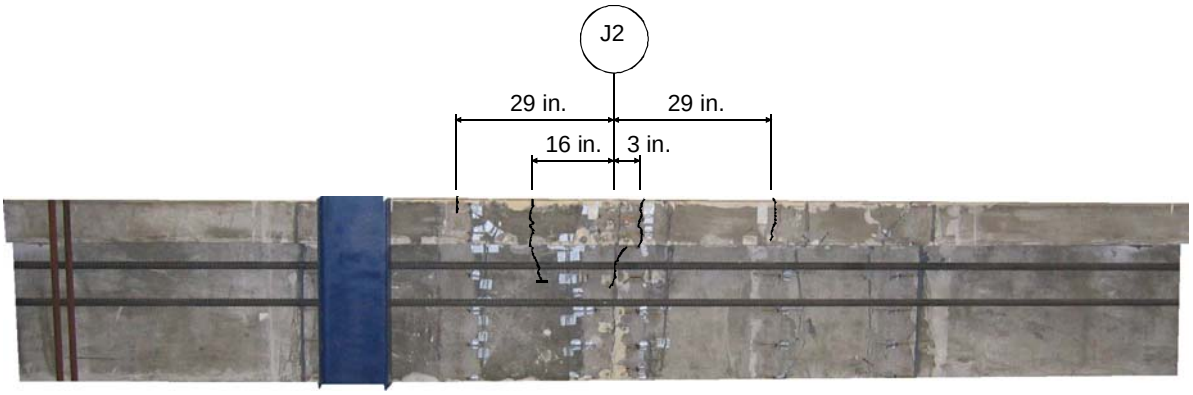

Figure 241: Visible crack locations - North side

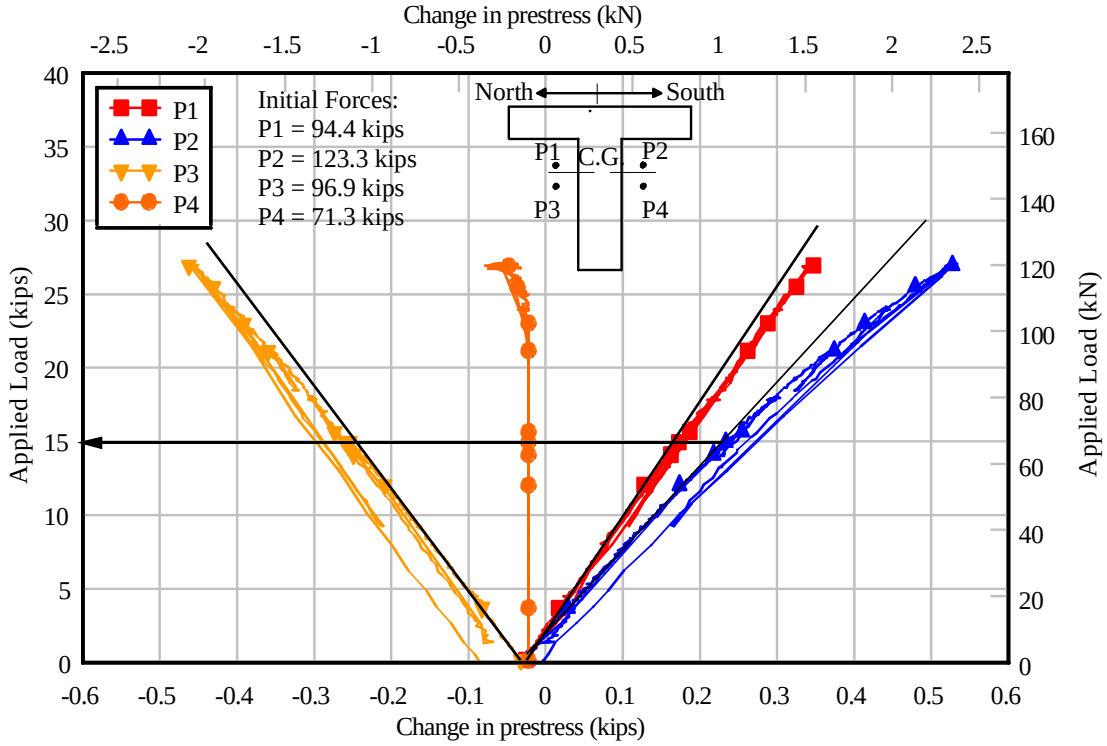

Figure 242: Thermal preload test – Change in prestress

Loading of the beam without a negative thermal gradient was the next scheduled test. At the time the test was conducted, the beam was thought to be uncracked based on acoustic emission observed in the previous test. Microcracking observed in the previous test was confirmed by similar strain behavior when the load reached to between 10 and 15 kips, approximately that measured in the previous test. The change in rate of additional strain, as before, can be observed in the strain-load plots shown in Figure 243 and Figure 244.

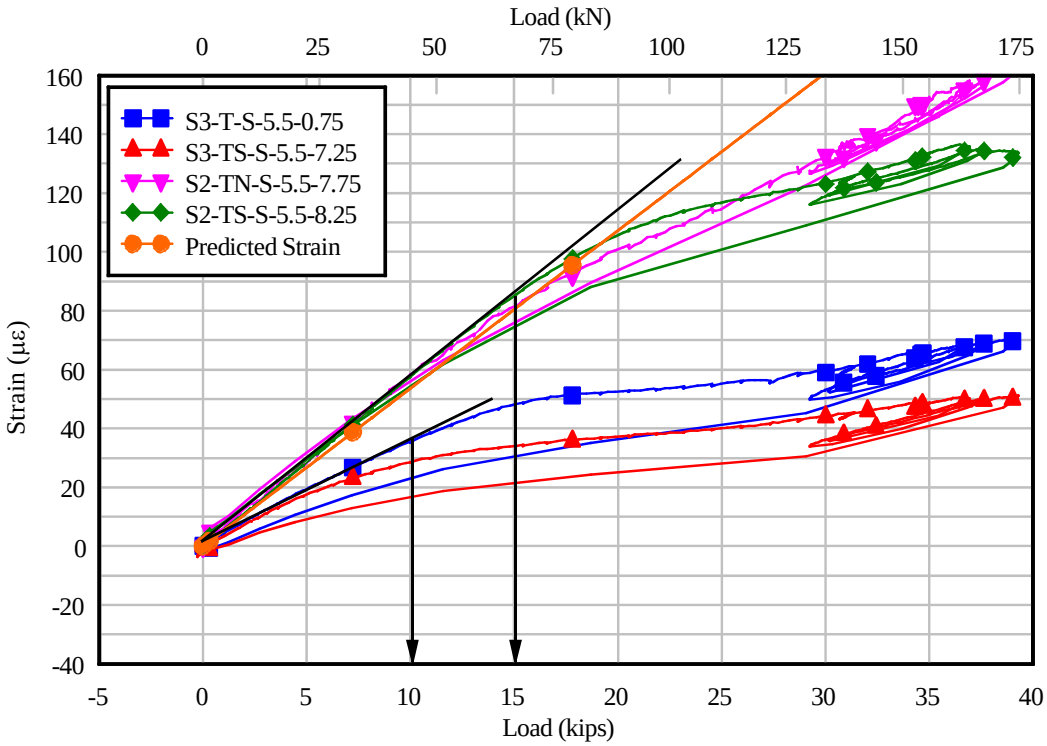

Figure 243: Non-thermal preload test - Top gauges

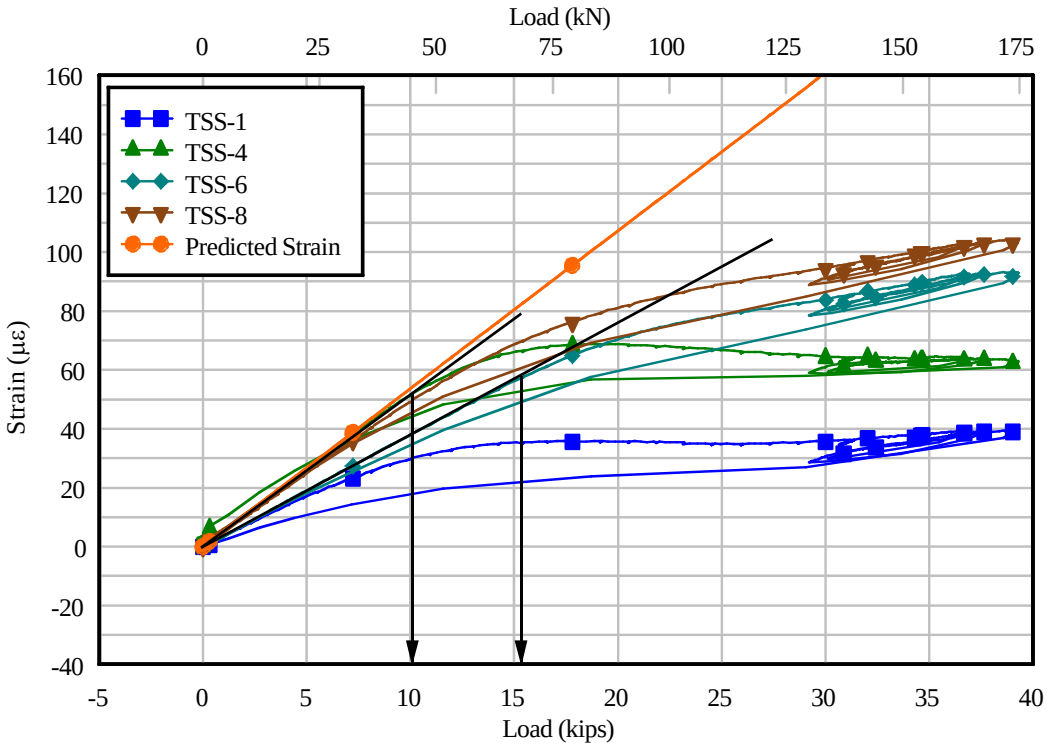

Figure 244: Non-thermal preload test - Cracking strain gauge series

A predicted applied load of 34 kips was expected at initial microcracking on the preloaded thermal test. The predicted applied load at microcracking was determined assuming $4\sqrt{f'_c\,(psi)}$ to be the maximum tensile stress at the extreme top fiber. Loading in the first test continued to 27 kips when an increase in acoustic emission energy was observed, corresponding to a predicted maximum tensile stress of $2.2\sqrt{f'_c\,(psi)}$. This compares to 15 kips, a predicted compressive stress in the extreme top fiber of $-0.8\sqrt{f'_c\,(psi)}$, at the observed initial microcracking.

The predicted compressive stress observed at the initial microcracking may have been due to several possibilities. It should first be noted that the beam had undergone several tests two years prior to the tests discussed in this chapter. These previous tests included mechanical loading and unloading, along with thermal loading. Damage to the beam may have occurred during these previous tests, resulting in cracks already existing prior to the tests discussed in this chapter. Another possibility is locked in tensile stresses due to drying shrinkage of the concrete segments may have contributed to a resulting lower applied tensile stress than predicted.

23 SUMMARY AND CONCLUSIONS – PART TWO

Six concrete specimen test sets were loaded to cracking both with and without temperature gradient, to investigate the effects of self-equilibrating tensile stress on cracking behavior. Each test set consisted of two identical prestressed specimens being loaded in direct tension until the concrete cracked. Each specimen had a steel bar through the center to apply a prestress and later a direct tensile force to the concrete. The specimen was constructed with confinement reinforcement around internal anchors on the steel bar at each end. At the center of the specimen, a 2 in. gauge length was left unreinforced. The prestressing bar was debonded at the same location to force cracking to occur in this gauge length. A load frame was instrumented with a load cell and LVDTs. Each specimen was instrumented with strain gauges and acoustic emission sensors. On one prestressed specimen from each test set, a nonlinear negative thermal gradient was imposed on the specimen by an open channel flow of chilled water over the top surface. This specimen was also instrumented with internal thermocouples to measure the temperature profile across the section.

The procedure for each test included, in sequence, stressing the steel bar in the load frame, casting the concrete specimen, prestressing the concrete specimen after curing, and loading the specimen in direct tension until failure of the concrete. The nonlinear thermal gradient was imposed during application of direct tensile loading for one specimen in each test set to determine the influence of the nonlinear thermal gradient on cracking.

The net tensile stress (or net tensile load) at the initiation of microcracking (f_i) and the net tensile stress at cracking (f_{cr}) were determined using measured strain data and cumulative acoustic emission energy. The net tensile stress at the initiation of microcracking and the net tensile stress at visible cracking were compared between specimens within each test set to determine the effect of the self-equilibrating stresses on the cracking behavior. The salient conclusions are as follows:

- With the influence of self-equilibrating tensile stress from a nonlinear negative thermal gradient, an expected decrease in normalized f_i values for thermal specimens relative to non-thermal specimens should occur. Rather, there was both an observed increase and decrease in normalized f_i values for thermal specimens relative to non-thermal specimens. This behavior reveals that there may be no significant effect that the nonlinear thermal gradient has on the initiation of cracking behavior.
- Average stress at which initiation of microcracking (f_i) was $3.2\sqrt{f'_c\,(psi)}$ and the average net tensile stress at cracking (f_{cr}) was $13.3\sqrt{f'_c\,(psi)}$ (Figure 227), with a coefficient of variation of 61% and 31%, respectively. The normalized stress range is similar to that of a typical range of the normalized modulus of rupture of concrete, 5 to 12. These similar ranges further reveal that there may be no significant effect that the nonlinear thermal gradient has on the cracking behavior of concrete. Cracking behavior influenced by any effect of a nonlinear thermal gradient is dominated by the influence of variability associated with concrete in tension.

A set of three tests were performed on the segmental beam to further investigate and quantify the effect of the AASHTO negative thermal gradient and resulting self-equilibrating stresses on cracking behavior of concrete in prestressed segmental bridge construction. The

segmental beam joints were sealed with epoxy and prestressed. The test setup and application of the AASHTO negative thermal gradient was similar to that of previous tests. The first test of three performed included an imposed AASHTO negative thermal gradient and was loaded to the initiation of microcracking as observed using acoustic emission energy. The second test was similar but did not include the imposed AASHTO negative thermal gradient. The third and final test included the imposed AASHTO negative thermal gradient and was loaded until visible cracking was observed in the beam. Based on recorded load, strain, and deflection data it is believed that cracking occurred during the first test with thermal gradient imposed. This could not be confirmed, however, because the thermal insulation surrounding the beam restricted visible inspection for cracking. Consequently, the effect of the AASHTO negative thermal gradient on cracking behavior of the segmental beam was unclear. Confirmation of microcracking occurring in first test was seen during the second test with an observed change in rate of additional strain as loading continued. This observed change occurs at a lower applied load range of approximately 10 kips to 15 kips, depending on the gauge used to make the assessment. The slightly lower load may be explained by the absence of the AASHTO negative thermal gradient and no additional self-equilibrating stress.

RECOMMENDATIONS

This research focused on two primary objectives. The first was to determine whether experimentally determined self-equilibrating thermal stresses caused by application of the AASHTO nonlinear thermal gradients match those predicted by analysis. Nonlinear thermal gradients can be divided into three components for analysis purposes (Figure 245):

- uniform temperature change
- linear temperature gradient
- non-linear temperature gradient

The uniform temperature component is typically specified separately as a seasonal variation of high and low temperature. Changes in temperature cause uniform expansion or contraction of the unrestrained superstructure. If the structure is restrained against this deformation, axial forces will develop. Generally, expansion joints and elastomeric bearings are used to accommodate movement due to this phenomenon.

A linear temperature gradient causes uniform curvature in the unrestrained superstructure. If the structure is restrained against curvature (restraints from vertical supports, e.g. bridge piers) then secondary moments develop as the result of a linear gradient.

A non-linear temperature gradient leads to the development of self-equilibrating stresses in the structure. The resultant axial force and moment caused by these stresses are both zero because the stresses are developed as the result of inter-fiber compatibility and are not associated with external forces and moments. These self-equilibrating stresses are the focus of this research.

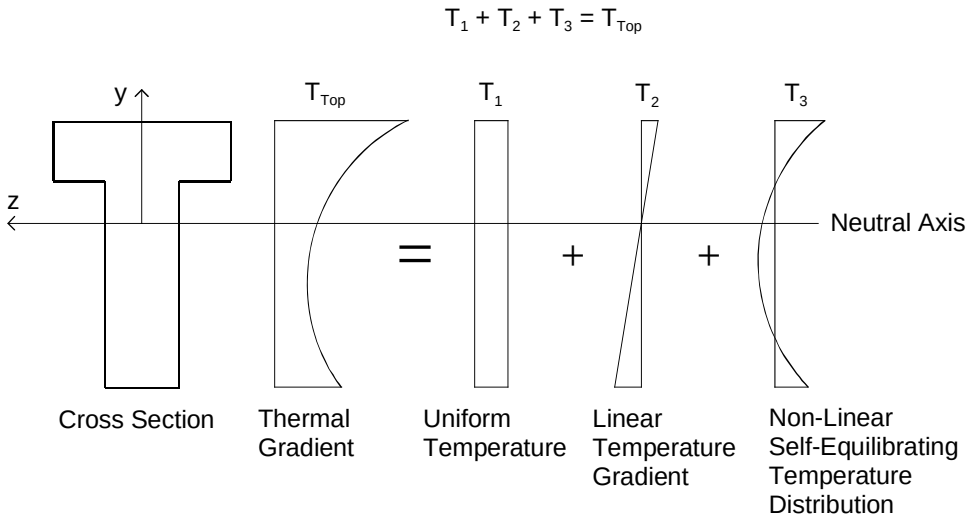

Figure 245 – Decomposition of a nonlinear thermal gradient

The essence of the experimental program to quantify self-equilibrating stresses is shown in Figure 246 and Figure 247. The first figure contains two graphs that show the self-equilibrating stresses measured during the application of the AASHTO specified positive non-linear thermal gradient for Florida. The second figure contains two similar graphs for the negative non-linear thermal gradient. These stresses were measured using two independent

methods. One set of stresses was determined directly by multiplying the measured mechanical strains by the experimentally determined elastic modulus. The other method extrapolated concrete stresses from the known (zero) stress state at the joint at the point of joint opening. The data from these two independent methods were in good agreement with each other and with self-equilibrating stresses calculated as prescribed by AASHTO.

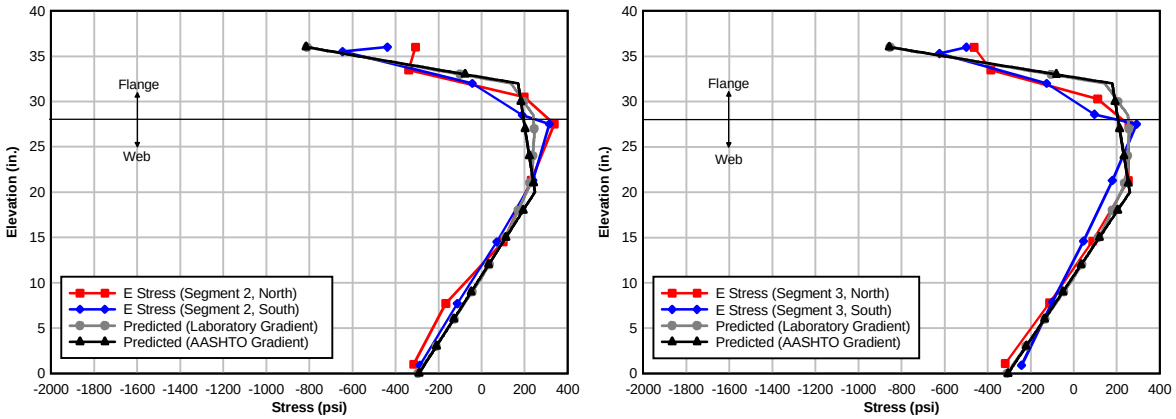

Figure 246 – Measured and predicted self-equilibrating stresses from the positive thermal gradient near joint J2 (a) Segment 2 and (b) Segment 3.

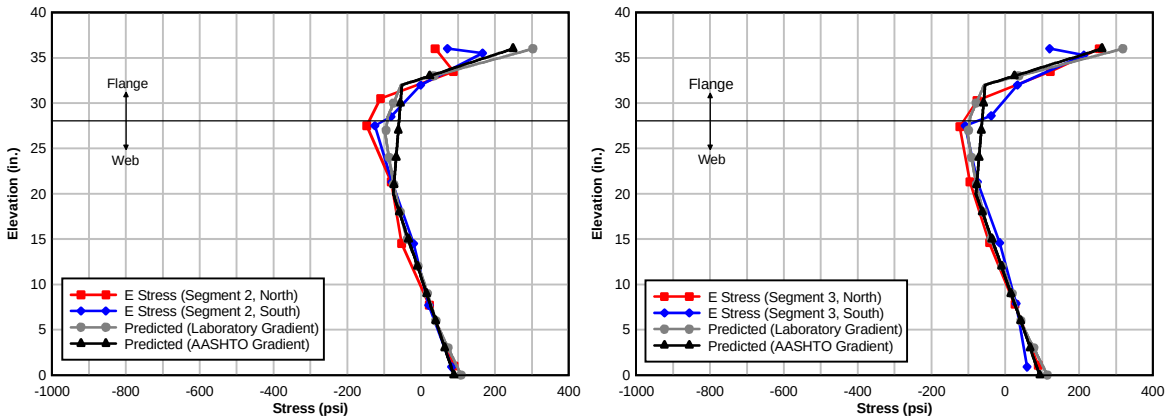

Figure 247 – Measured and predicted self-equilibrating stresses from the negative thermal gradient near joint J2 (a) Segment 2 and (b) Segment 3.

Initially, the design loads and thermal gradients of the SRB Bridge were investigated over the full height of the box section as shown in the Figure 249. Stress profile components of a simplified load combination for the SRB Bridge are shown in Figure 250 for the section immediately adjacent to the pier segment (under negative bending from live load). The stress profiles show the components of prestress, combined dead loads, superimposed service loads, and predicted self-equilibrating stress due to the nonlinear AASHTO negative thermal gradient. The locked-in stresses and stresses from the linear portion of the thermal gradient, however, are not included. The total stress gradient is shown with and without the predicted self-equilibrating stress. The self-equilibrating stresses create a severe tensile stress gradient in the upper four to six inches of the deck. Although not addressed in the AASHTO *Guide Specifications for Design and Construction of Segmental Concrete Bridges* (1999) it is likely that this stress state is

different in the deck away from the web due to shear lag. The deck slab at the tip of the cantilever or midway between the webs does not have the restraint offered by the web for the deck sections directly above the web. To satisfy the design requirements for serviceability, however, this severe self-equilibrating tensile stress gradient must be offset by prestressing ostensibly over the full width of the slab.

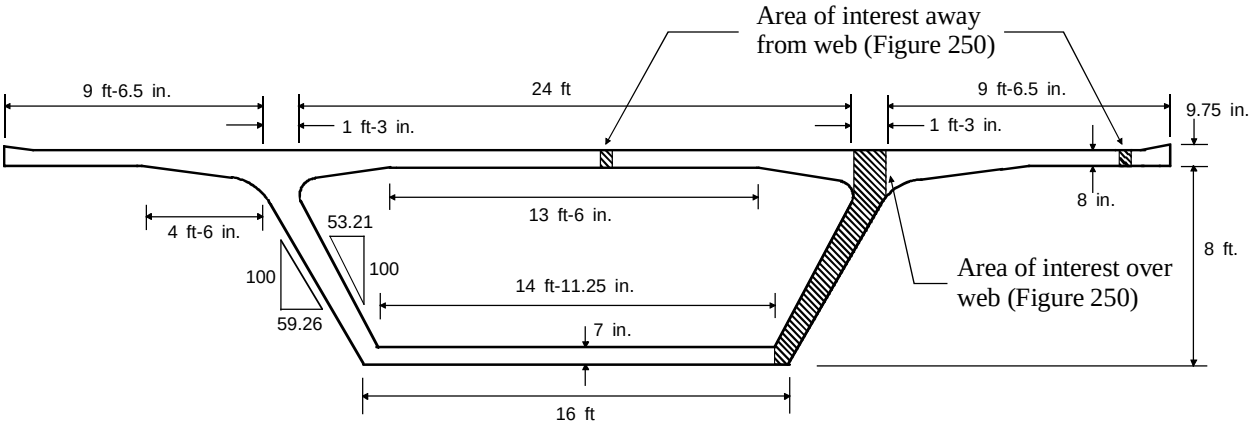

Figure 248: Typical cross section of Santa Rosa Bay Bridge

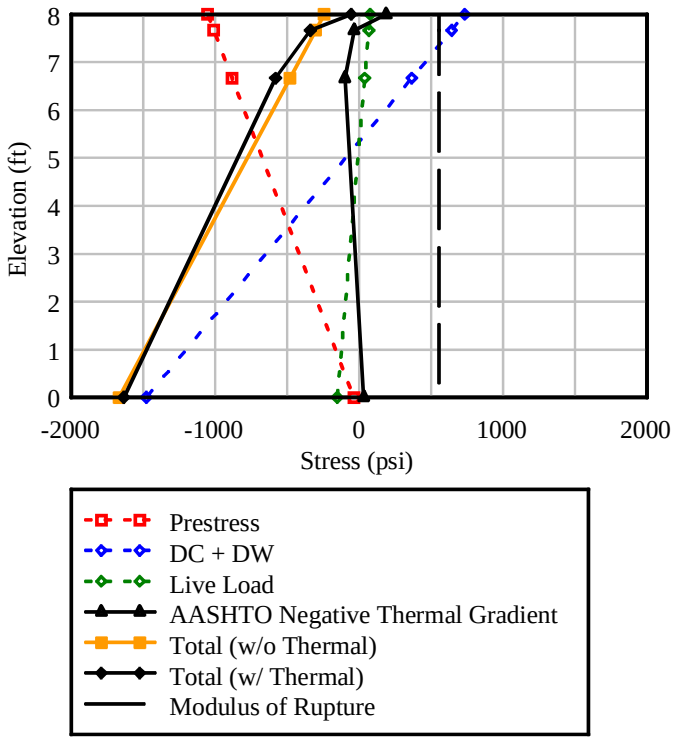

Figure 249: SRB Bridge stress profiles

Figure 250a shows the stress state in the deck over the web of the SRB Bridge prototype. Each stress block is plotted to scale relative to the zero stress datum and the modulus of rupture ($f_{r.}$). The self-equilibrating stresses were calculated with the negative design gradient applied

over the full depth of the box section. The service stresses include both the precompression and stresses from applied loads such that the sum of these stresses and the self-equilibrating stresses equal the modulus of rupture.

Figure 250b shows the stress state of the deck if it were completely unrestrained by the web under the negative design gradient. It has been assumed that the negative thermal gradient developed in the deck away from the web would be that specified by AASHTO *Guide Specifications for Design and Construction of Segmental Concrete Bridges* (1999), shown in Figure 5 with the depth "A" taken as 4 in. Although the Guide indicates that these provisions are intended for members over 24-in. deep, the self-equilibrating stresses for the thermal gradient are calculated for comparison to those determined for the full depth of the structure. Depending on the distance between webs, it is postulated that the deck sections away from the restraint of the webs will have self-equilibrating stress profiles that are more similar to Figure 250b rather than Figure 250a due to shear lag.

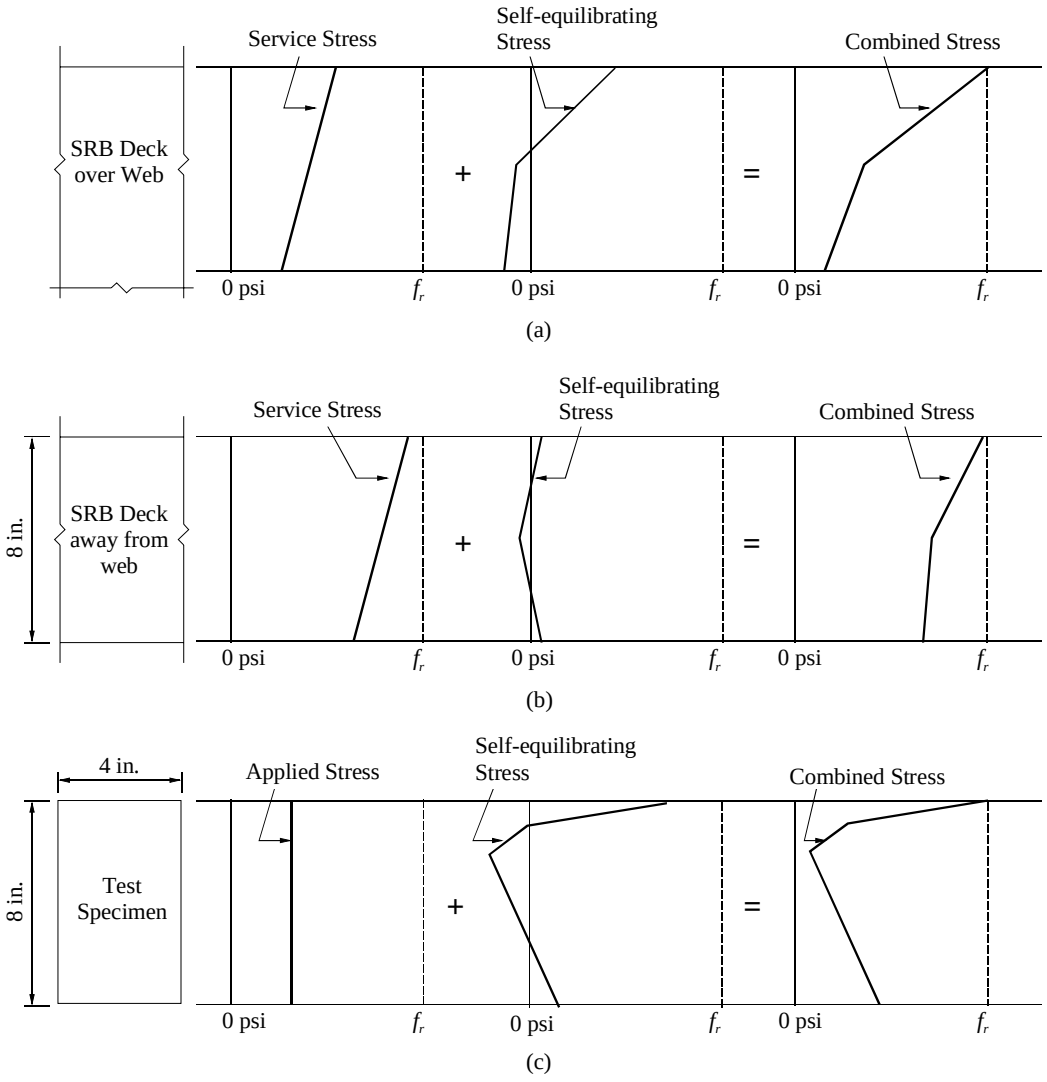

Figure 250: Stress profiles of (a) SRB Bridge over the web, (b) SRB Bridge away from the web, and (c) test specimen.

Ideally, multiple full scale models of the SRB Bridge would be constructed and tested with and without nonlinear thermal gradients under an applied mechanical load. This would capture the behavior illustrated in both Figure 250a and Figure 250b. Laboratory and budget constraints, however, restricted the size of the specimen. Consequently, a portion of the top flange of the box girder (Figure 250), where the self-equilibrating stress has a severe gradient relative to that of the imposed stresses, was isolated for use in component testing. Mechanically, the test specimen represents the unrestrained condition of the deck distant from the web. But in order to achieve the maximum tension stresses that occur in the prototype near the web (restrained), a more severe thermal gradient was used with the test specimen, which resulted in the self-equilibrating stresses shown in Figure 250c.

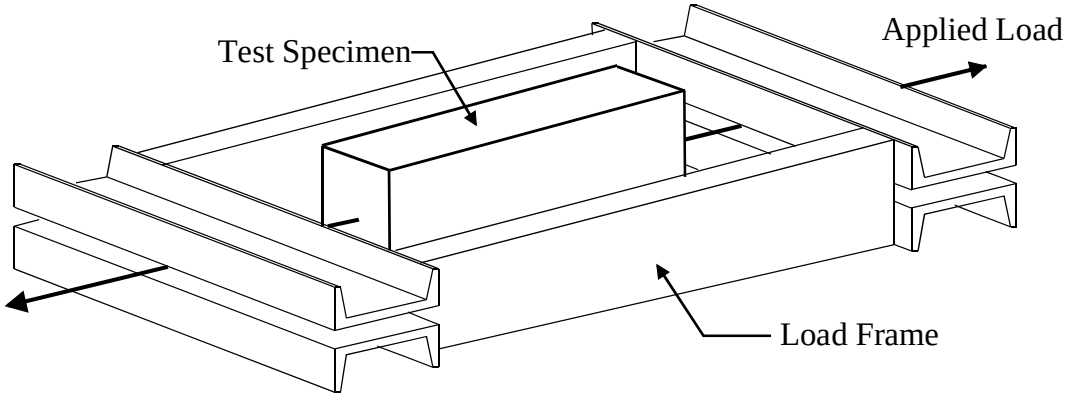

Figure 251: Load frame used to test concrete specimens

A summary of results from tests on the concrete specimens are shown in Figure 252. Each bar represents the range over which cracking is occurring, but has not yet formed a visible crack. The initiation of cracking (f_i) was determined using strain gage data corroborated with AE data. The cracking stress (f_{cr}) was the calculated stress at which the specimen was observed to crack (both visually and audibly). Note that the tensile stresses were normalized by the square root of the concrete compressive strength for comparison. To evaluate the effect of the imposed self-equilibrating thermal stress on cracking behavior of the concrete specimens, the stress ranges are compared for thermal and non-thermal specimen tests.

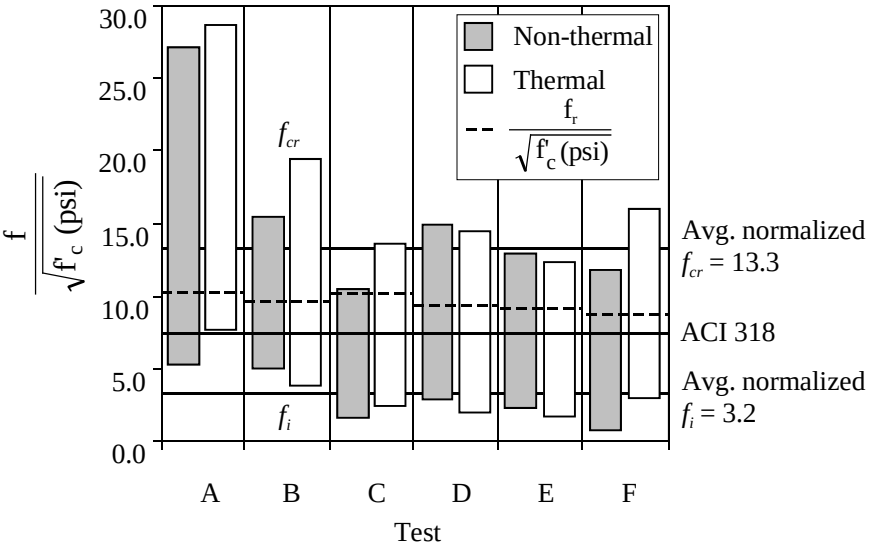

Figure 252: Stress ratio ranges of microcracking

The normalized modulus of rupture for each test set, along with a value of 7.5 as reference, are also shown in Figure 252. The averages for the upper and lower bounds of microcracking for all tests are 3.2 and 13.3, respectively. This compares to the general cracking behavior of concrete previously discussed where it was noted that the normalized modulus of rupture could have a range between 5 and 12 (Popovics 1998). The comparable ranges and the variation in the upper and lower bounds indicate that the nonlinear thermal gradient had no discernable effect on the cracking behavior of concrete. It is postulated that early microcracking changes the section properties and drastically curtails the influence of the severe gradient on the overall tension state in the concrete. This coupled with the variability of concrete tensile strength may explain why there is no apparent influence.

There are two major disadvantages when considering self-equilibrating stresses in the design of segmental bridges. The first is that the prestressing required to handle these stresses (but no other stress state) results in additional cost and generates additional creep and locked-in stresses. Second, consideration of the self-equilibrating stresses is not a trivial requirement either from the viewpoint of conceptual understanding or from a practical standpoint when it comes to implementing this check into the design process.

The results of these tests and the lack of anecdotal evidence or experimental research demonstrating that self-equilibrating stresses have caused serviceability or durability problems, indicates that the self-equilibrating stresses caused by the non-linear portion of the thermal gradient can be ignored in design. Indeed, the thermal gradient service stress state is already reduced by 50% for service checks when considered in conjunction with live load, with no rational basis. Stresses generated by structural redundancy in combination with the linear portion of the thermal gradient must be considered. Furthermore, axial movement caused by uniform temperature change must also be considered in the design process.

REFERENCES

AASHTO (1989a) "AASHTO Guide Specifications, Thermal Effects in Concrete Bridge Superstructures," Washington D.C.

AASHTO (1989b) "Guide Specifications for Design and Construction of Segmental Concrete Bridges," 1st Ed., Washington, D.C.

AASHTO (1994a) "AASHTO LRFD Bridge Design Specifications," Washington, D.C.

AASHTO (1994b) "Interim Specifications for the Guide Specifications for Design and Construction of Segmental Concrete Bridges," 1st Ed., Washington, D.C.

AASHTO (1998a) "AASHTO LRFD Bridge Design Specifications," Washington, D.C.

AASHTO (1998b) "Guide Specifications for Design and Construction of Segmental Concrete Bridges," Proposed 2nd Ed., Washington, D.C.

AASHTO (1999) "Guide Specifications for Design and Construction of Segmental Concrete Bridges," 2nd Ed., Washington, D.C.

AASHTO (2004) "AASHTO LRFD Bridge Design Specifications," 3rd Ed., Washington, D.C.

AASHTO (2007) "AASHTO LRFD Bridge Design Specifications," 4th Ed., Washington, D.C.

AASHTO TP 60-00 (2004), "Standard Method of Test for Coefficient of Thermal Expansion of Hydraulic Cement Concrete," Washington, D.C.

ACI Committee 318 (2002) "Building Code Requirements for Structural Concrete (318-02) and Commentary (318R-02)." American Concrete Institute, Farmington Hills, Michigan.

ASTM C 138 (2009) "Standard Test Method for Density (Unit Weight), Yield, and Air Content (Gravimetric) of Concrete," American Society of Testing and Materials, West Conshohocken, PA.

ASTM C143 (2008) "Standard Test Method for Slump of Hydraulic-Cement Concrete," American Society of Testing and Materials, West Conshohocken, PA.

ASTM C39 (2001) "Standard Test Method for Compressive Strength of Concrete Cylinders Cast in Place in Cylindrical Molds," American Society of Testing and Materials, West Conshohocken, PA.

ASTM C39 (2001) "Standard Test Method for Compressive Strength of Concrete Cylinders Cast in Place in Cylindrical Molds," American Society of Testing and Materials, West Conshohocken, PA.

ASTM C469 (1994) "Standard Test Method for Static Modulus of Elasticity and Poisson's Ratio of Concrete in Compression," American Society of Testing and Materials, West Conshohocken, PA.

ASTM C496 (2004) "Standard Test Method for Splitting Tensile Strength of Cylindrical Concrete Specimens," American Society of Testing and Materials, West Conshohocken, PA.

ASTM C566 (2004) "Standard Test Method for Total Evaporable Moisture Content of Aggregate by Drying," American Society of Testing and Materials, West Conshohocken, PA.

ASTM C78 (2008) "Standard Test Method for Flexural Strength of Concrete (Using Simple Beam with Third-Point Loading)," American Society of Testing and Materials, West Conshohocken, PA.

ASTM E1316 (2006) "Standard Terminology for Nondestructive Examinations," ASTM International, West Conshohocken, Pa., 33 pp.

British Standard BS 5400 (1978) "Steel, Concrete and Composite Bridges, Part I, General Statement." British Standards Institution. Crowthorne, Berkshire, England.

Colombo, S., Forde, M.C., Main, I.G., Halliday, J., and Shigeishi, M. (2005) "AE Energy Analysis on Concrete Bridge Beams," *Materials and Structures*, V. 38 No. 9, Nov., pp. 851-856.

Imbsen, R. A., Vandershof, D. E., Schamber, R. A., and Nutt, R.V. (1985) "Thermal Effects in Concrete Bridge Superstructures," NCHRP 276, Transportation Research Board, Washington, D.C.

Kaplan, M.F. (1963) "Strains and Stresses of Concrete at Initiation of Cracking and Near Failure," *ACI Journal*, V. 60, No. 7, July. pp. 853-860.

Labuz, J. F., Cattaneo, S., and Chen, L. (2001) "Acoustic Emission at Failure in Quasi-Brittle Materials," *Construction and Building Materials*, V. 15, No. 5-6, July-Sept., pp. 225-233.

Neville, A. M., 1995, *Properties of Concrete*, 4th Ed., Pearson Education Limited, London, England. pp. 289-600.

Nielsen, J. and Griffin, D.F., 1977, "Acoustic Emission of Plain Concrete," *Journal of Testing and Evaluation*, JTEVA, Vol. 5, No. 6, pp. 476-483.

Oh, B.H., Kim, K.S., and Kim, E.J. (2000) "Identification of Damages of Concrete Structures Using Acoustic Emission," *ACI Special Publication*, SP-193, pp. 195-210.

Popovics, S. (1998) *Strength and Related Properties of Concrete: A Quantitative Approach*, John Wiley & Sons, New York, NY. pp. 103-157.

Potgieter, I. C., and Gamble, W. L. (1983) "Response of Highway Bridges to Nonlinear Temperature Distributions," Rep. No. FHWA/IL/UI-201, University of Illinois at Urbana-Champaign, Urbana-Champaign, Ill.

Priestley, M. J. N. (1978) "Design of Concrete Bridges for Thermal Gradients," *ACI Journal*, V. 75, No. 5, pp. 209-217.

Puri, S. and Weiss, J. (2006) "Assessment of Localized Damage in Concrete under Compression Using Acoustic Emission," *ASCE Journal of Materials in Civil Engineering*, V. 18, No. 3, May-June, pp. 325-333.

Roberts, C. L., Breen, J. E., and Cawrse J. (2002) "Measurement of Thermal Gradients and their Effects on Segmental Concrete Bridge," *ASCE Journal of Bridge Engineering*, Vol. 7, No. 3, 166-174.

Roberts, C.L., Breen, J. E., and Kreger, M.E. (1993) "Measurement Based Revisions for Segmental Bridge Design and Construction Criteria," Research Rep. 1234-3F, Center for Transportation Research, Univ. of Texas at Austin, Austin, Texas.

Shield, C. K. and Hearn, S. W. (1997) "Acoustic Emission Monitoring as a Nondestructive Testing Technique in Reinforced Concrete," *ACI Materials Journal*, V. 94, No. 6, Nov.- Dec., pp. 510-519.

Shushkewich, K.W. (1998) "Design of Segmental Bridges for Thermal Gradient," *PCI Journal*, V. 43, No.4, pp. 120-137.

Thompson, M. K., Davis, R. T., Breen, J. E., and Kreger, M. E. (1998) "Measured Behavior of a Curved Precast Segmental Concrete Bridge Erected by Balanced Cantilevering," Research Rep. 1404-2, Center for Transportation Research, Univ. of Texas at Austin, Texas.

PART ONE APPENDICES

APPENDIX A – BEAM SHOP DRAWINGS

In this appendix, design plans for the construction of the laboratory segmental beam are presented. Steel reinforcement in prestress anchorage zones, thermocouple cages, copper tube locations, plans for the loading mechanism, and shear keys are shown.

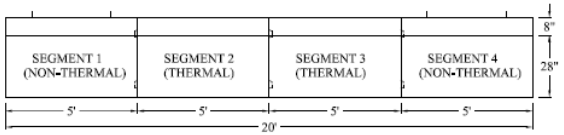

BEAM ELEVATION

SCALE ¼" = 1'-0"

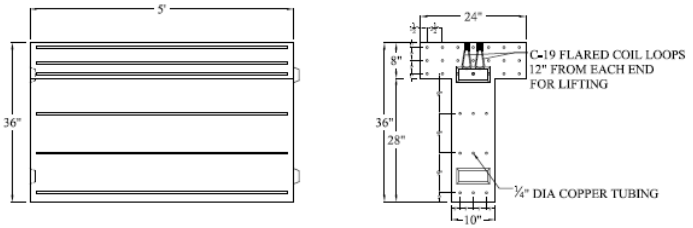

TUBING LAYOUT - SEGMENTS 2 & 3

SCALE : ½" = 1'-0"

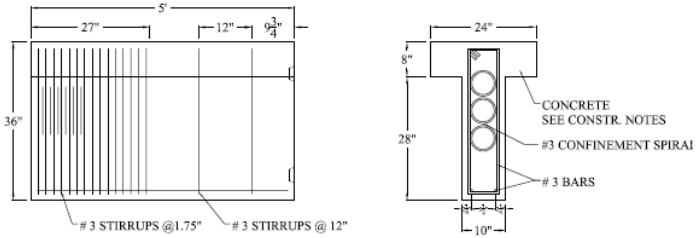

REINFORCEMENT LAYOUT - SEGMENT 1

SCALE : ½" = 1'-0"

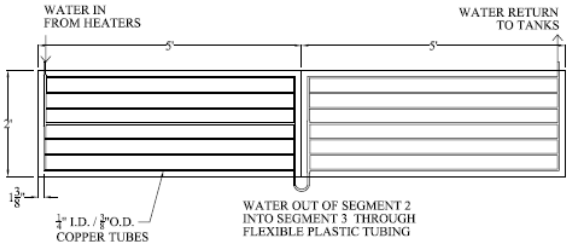

PLAN VIEW MANIFOLD SYSTEM - FLANGE

SCALE : ½" = 1'-0"

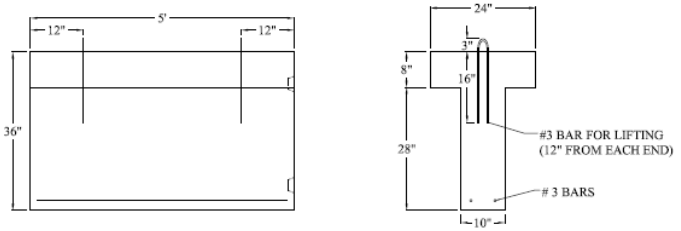

LIFTING REINFORCEMENT LAYOUT - SEGMENT 1

SCALE : ½" = 1'-0"

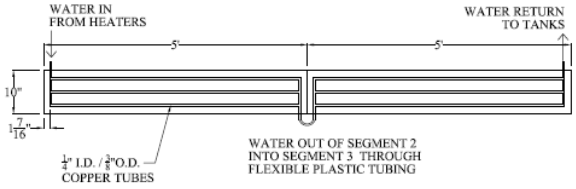

PLAN VIEW MANIFOLD SYSTEM - WEB

SCALE : ½" = 1'-0"

Scale : AS NOTED
Date : JULY 2005
Designed : F.M., D.W.
Drawn : D.W.
Checked : J.S.H.
CAD file :

SEAL

Date | Revision

PROPOSED TEST BEAM FOR
THERMAL GRADIENT RESEARCH
PROJECT PI's : H.R.H & G.R.C
RESEARCH TEAM: M.F., D.W., & C.A.

UNIVERSITY OF FLORIDA
STRUCTURES DEPARTMENT
GAINESVILLE, FL 32608
Voice: (352)392-9537
Fax: (352)392-3394
Web: www.ce.ufl.edu

Project # 029

Sheet 1 OF 3

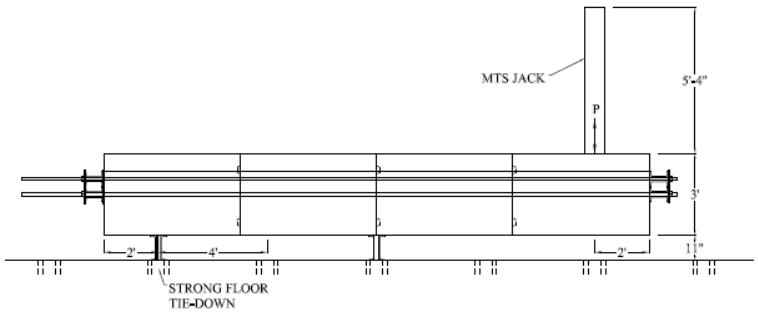

PRESTRESSING ELEVATION

SCALE ¼" = 1'-0"

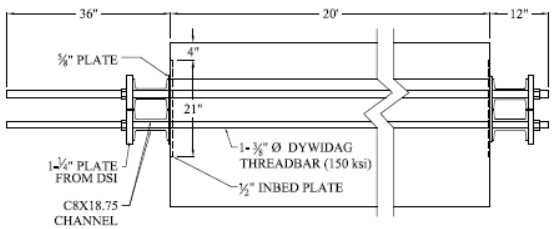

PRESTRESSING LAYOUT

SCALE : ½" = 1'-0"

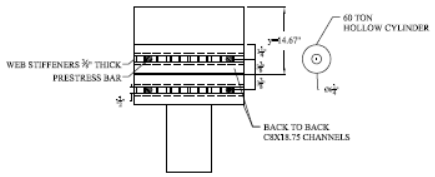

PRESTRESSING CROSS SECTION

SCALE : ¾" = 1'-0"

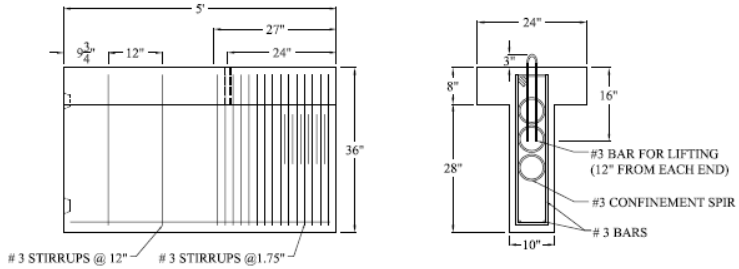

REINFORCEMENT LAYOUT - SEGMENT 4

SCALE : ½" = 1'-0"

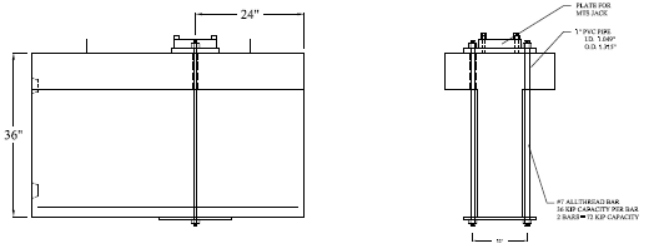

LOADING MECHANISM - SEGMENT 4

SCALE : ½" = 1'-0"

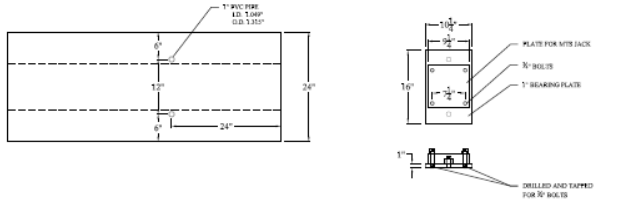

LOADING MECHANISM PLAN VIEW - SEGMENT 4

SCALE : ½" = 1'-0"

AS NOTED
JULY 2009
F.M. D.W.
D.W.
H.R.H
CAD File:

SEAL

Revision
Date

PROPOSED TEST BEAM FOR
THERMAL GRADIENT RESEARCH
PROJECT PI's : H.R.H & G.R.C
RESEARCH TEAM: M.F., D.W., & C.A.

UNIVERSITY OF FLORIDA
STRUCTURES DEPARTMENT
GAINESVILLE, FL 32608
Voice: (352)392-9537
Fax: (352)392-3394
Web: www.ce.ufl.edu

Project # 029

Sheet 2 OF 3

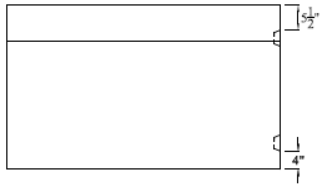

SHEAR KEY - SEGMENT 1

SCALE : ½" = 1'-0"

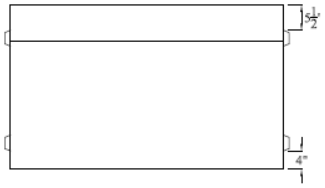

SHEAR KEY - SEGMENT 2

SCALE : ½" = 1'-0"

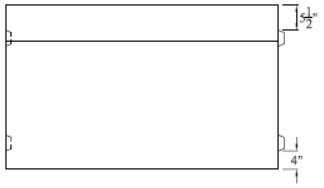

SHEAR KEY - SEGMENT 3

SCALE : ½" = 1'-0"

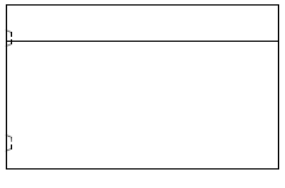

SHEAR KEY - SEGMENT 4

SCALE : ½" = 1'-0"

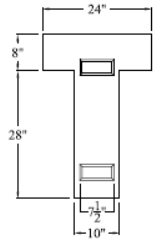

SHEAR KEY LAYOUT

SCALE : ½" = 1'-0"

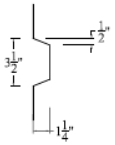

SHEAR KEY DETAIL

SCALE : 1-½" = 1'-0"

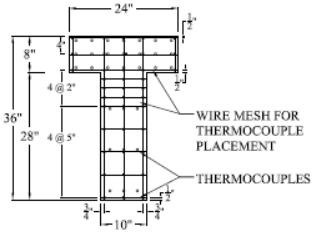

THERMOCOUPLE LAYOUT

SCALE : ½" = 1'-0"

NOTES

CONCRETE: ALL CONCRETE SHALL BE HIGH STRENGTH WITH A f 'c OF 5500 psi.
MIX TO BE PROVIDED BY FLORIDA ROCK INDUSTRIES OF TALLAHASSEE, FL
FORMWORK TO BE BUILT BY FDOT OF TALLAHASSEE.

STEEL: ALL STEEL INSIDE CONCRETE SHALL BE 60 KSI BAR.

PRESTRESS: PRESTRESS ALLTHREAD, PLATES, AND NUTS SHALL BE PROVIDED BY DSI.
EXTERNAL PRESTRESS SYSTEMS WILL BE BUILT BY UNIV. OF FL. MECHANICS

THERMOCOUPLES : THERMOCOUPLES SHALL BE MADE BY AND PLACED IN FORM BY THE U.F. RESEARCH TEAM.

COPPER TUBES : ALL TUBING SHALL BE CONSTRUCTED AND PLACED BY THE U.F. RESEARCH TEAM.

Scale: AS NOTED
Date: JULY 2009
Designed: F.M. D.W.
Drawn: D.W.
Checked: H.R.H.
CAD File:

Date | Revision

SEAL

PROPOSED TEST BEAM FOR
THERMAL GRADIENT RESEARCH
PROJECT PI's : H.R.H & G.R.C
RESEARCH TEAM: M.F., D.W., & C.A.

UNIVERSITY OF FLORIDA
STRUCTURES DEPARTMENT
GAINESVILLE, FL 32608
Voice (352)392-9537
Fax (352)392-3394
Web: www.ce.ufl.edu

Project # 029

Sheet 3 OF 3

APPENDIX B – CONCRETE MIX TICKETS

In this appendix, mix tickets for concrete used to cast each segment of the laboratory beam are shown.

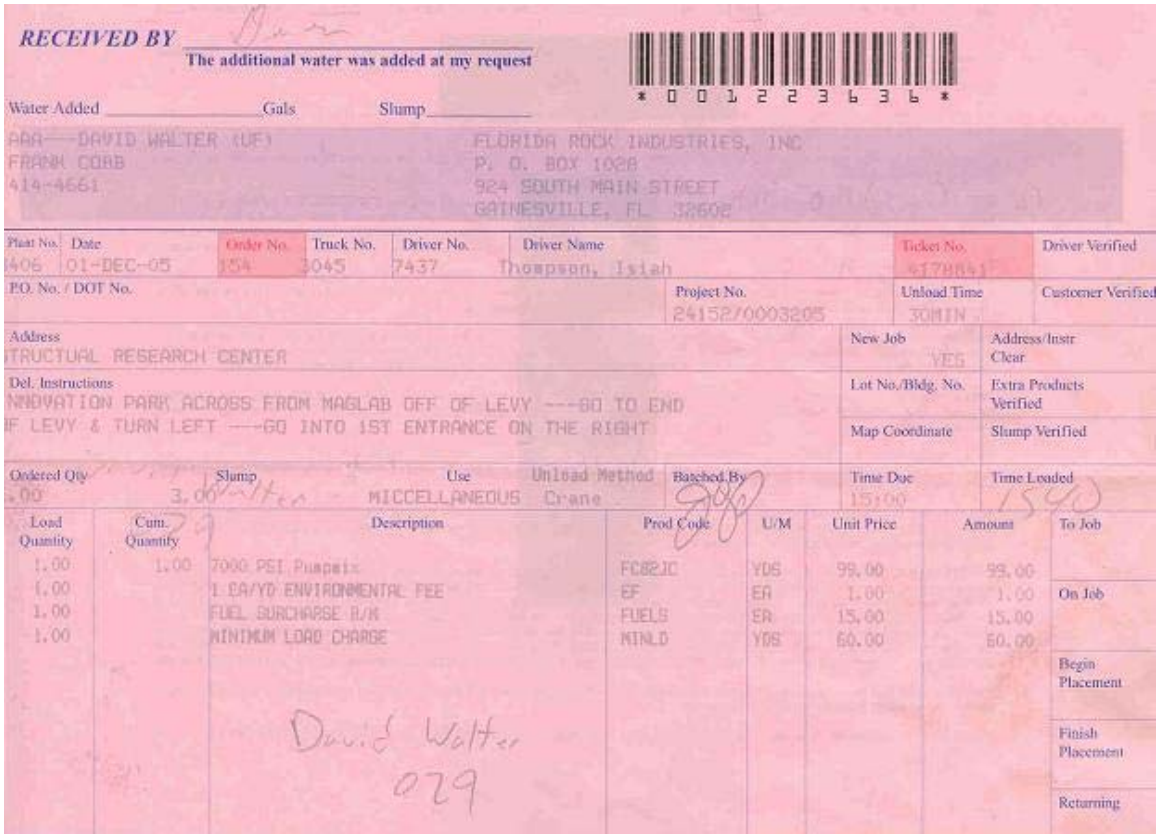

RECEIVED BY _____

The additional water was added at my request

Water Added _____ Gals Slump _____

AAA—DAVID WALTER (UF)
FRANK COBB
414-4661

FLORIDA ROCK INDUSTRIES, INC
P. O. BOX 1028
924 SOUTH MAIN STREET
GAINESVILLE, FL 32602

Plant No.	Date	Order No.	Truck No.	Driver No.	Driver Name	Ticket No.	Driver Verified
3406	01-DEC-05	154	3045	7437	Thompson, Isiah	4178841	

P.O. No. / DOT No.	Project No.	Unload Time	Customer Verified
	24152/0003205	30MIN	

Address	New Job	Address/Instr Clear
STRUCTURAL RESEARCH CENTER	YES	

Del. Instructions	Lot No./Bldg. No.	Extra Products Verified
NNOVATION PARK ACROSS FROM MAGLAB OFF OF LEVY ---GO TO END F LEVY & TURN LEFT ---GO INTO 1ST ENTRANCE ON THE RIGHT		
	Map Coordinate	Slump Verified

Ordered Qty	Slump	Use	Unload Method	Batched By	Time Due	Time Loaded
.00	3.00	MICCELLANEOUS	Crane		15:00	1340

Load Quantity	Cum. Quantity	Description	Prod Code	U/M	Unit Price	Amount	To Job
1.00	1.00	7000 PSI Pumpmix	FC82JC	YDS	99.00	99.00	
1.00		1 EA/YD ENVIRONMENTAL FEE	EF	EA	1.00	1.00	On Job
1.00		FUEL SURCHARGE R/M	FUELS	EA	15.00	15.00	
1.00		MINIMUM LOAD CHARGE	MINLD	YDS	60.00	60.00	
							Begin Placement
		David Walter 029					Finish Placement
							Returning

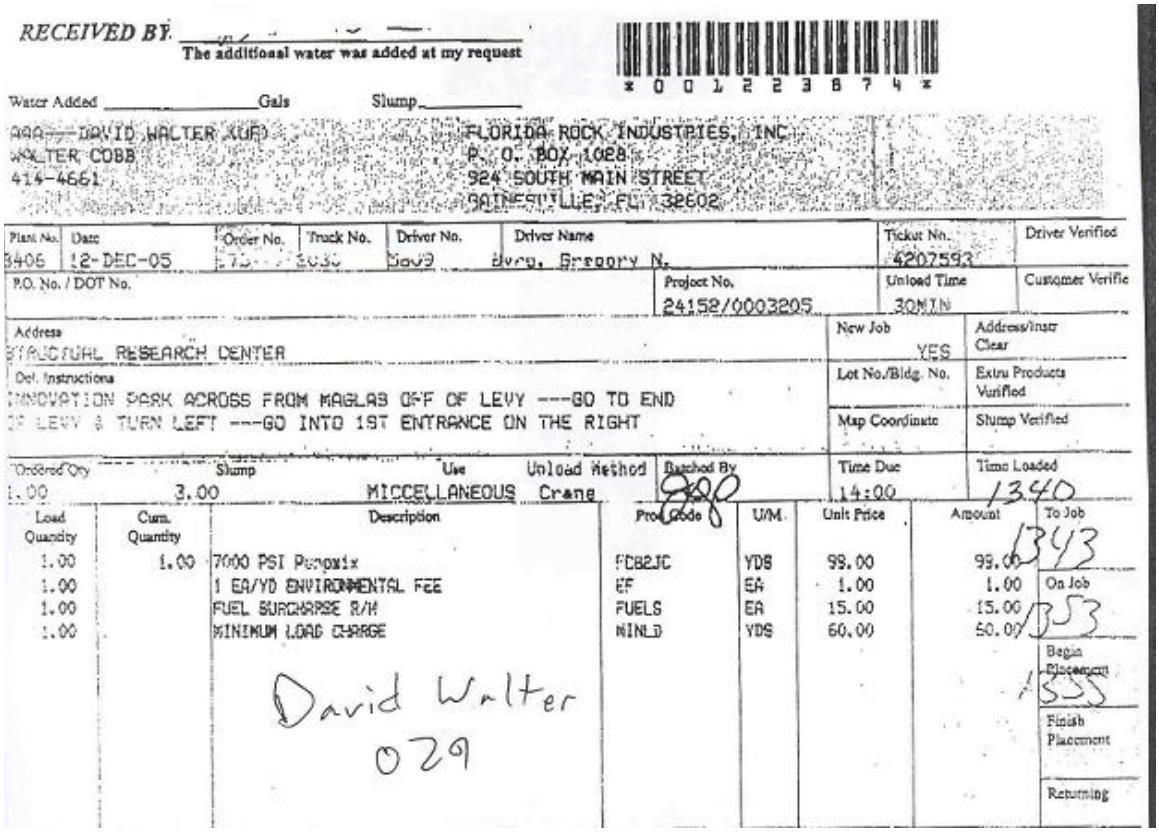

RECEIVED BY _____

The additional water was added at my request

Water Added _____ Gals Slump _____

AAA—DAVID WALTER (UF)
WALTER COBB
414-4661

FLORIDA ROCK INDUSTRIES, INC
P. O. BOX 1028
924 SOUTH MAIN STREET
GAINESVILLE, FL 32602

Plant No.	Date	Order No.	Truck No.	Driver No.	Driver Name	Ticket No.	Driver Verified
3406	12-DEC-05	[illegible]	[illegible]	3009	Avra, Gregory N.	4207593	

P.O. No. / DOT No.	Project No.	Unload Time	Customer Verific
	24152/0003205	30MIN	

Address	New Job	Address/Instr Clear
STRUCTURAL RESEARCH CENTER	YES	

Del. Instructions	Lot No./Bldg. No.	Extra Products Verified
INNOVATION PARK ACROSS FROM MAGLAB OFF OF LEVY ---GO TO END OF LEVY & TURN LEFT ---GO INTO 1ST ENTRANCE ON THE RIGHT		
	Map Coordinate	Slump Verified

Ordered Qty	Slump	Use	Unload Method	Batched By	Time Due	Time Loaded
1.00	3.00	MICCELLANEOUS	Crane		14:00	1340

Load Quantity	Cum. Quantity	Description	Prod Code	U/M	Unit Price	Amount	To Job
1.00	1.00	7000 PSI Pumpmix	FC82JC	YDS	99.00	99.00	1343
1.00		1 EA/YD ENVIRONMENTAL FEE	EF	EA	1.00	1.00	On Job
1.00		FUEL SURCHARGE R/M	FUELS	EA	15.00	15.00	1353
1.00		MINIMUM LOAD CHARGE	MINLD	YDS	60.00	60.00	
							Begin Placement 1355
		David Walter 029					Finish Placement
							Returning

RECEIVED BY _____
The additional water was added at my request

Water Added _____ Gals Slump Yes

0013233301

AAA---DAVID WALTER (UF)
FRANK COBB
414-4661

FLORIDA ROCK INDUSTRIES, INC
P. O. BOX 1028
924 SOUTH MAIN STREET
GAINESVILLE, FL 32602

Plant No.	Date	Order No.	Truck No.	Driver No.	Driver Name	Ticket No.	Driver Verified
406	19-JAN-06	139	51	7131	Boule, James A.	4314834	

P.O. No. / DOT No. | Project No. 24152/0003205 | Unload Time 30MIN | Customer Verified

Address: STRUCTUAL RESEARCH CENTER | New Job: YES | Address/Instr Clear

Del. Instructions: INNOVATION PARK ACROSS FROM MAGLAB OFF OF LEVY ---GO TO END OF LEVY & TURN LEFT ---GO INTO 1ST ENTRANCE ON THE RIGHT | Lot No./Bldg. No. | Extra Products Verified | Map Coordinate | Slump Verified

Ordered Qty	Slump	Use	Unload Method	Batched By	Time Due	Time Loaded
.00	3.00	MICCELLANEOUS	Crane	SC	14:00	1344

Load Quantity	Cum. Quantity	Description	Prod Code	U/M	Unit Price	Amount	To Job
1.00	1.00	7000 PSI Pumpmix	FC82JC	YDS	99.00	99.00	1.50
1.00		1 EA/YD ENVIRONMENTAL FEE	EF	EA	1.00	1.00	On Job
1.00		FUEL SURCHARGE R/M	FUELS	EA	10.00	10.00	2.00
1.00		MINIMUM LOAD CHARGE	MINLD	YDS	60.00	60.00	

Begin Placement | Finish Placement | Returning

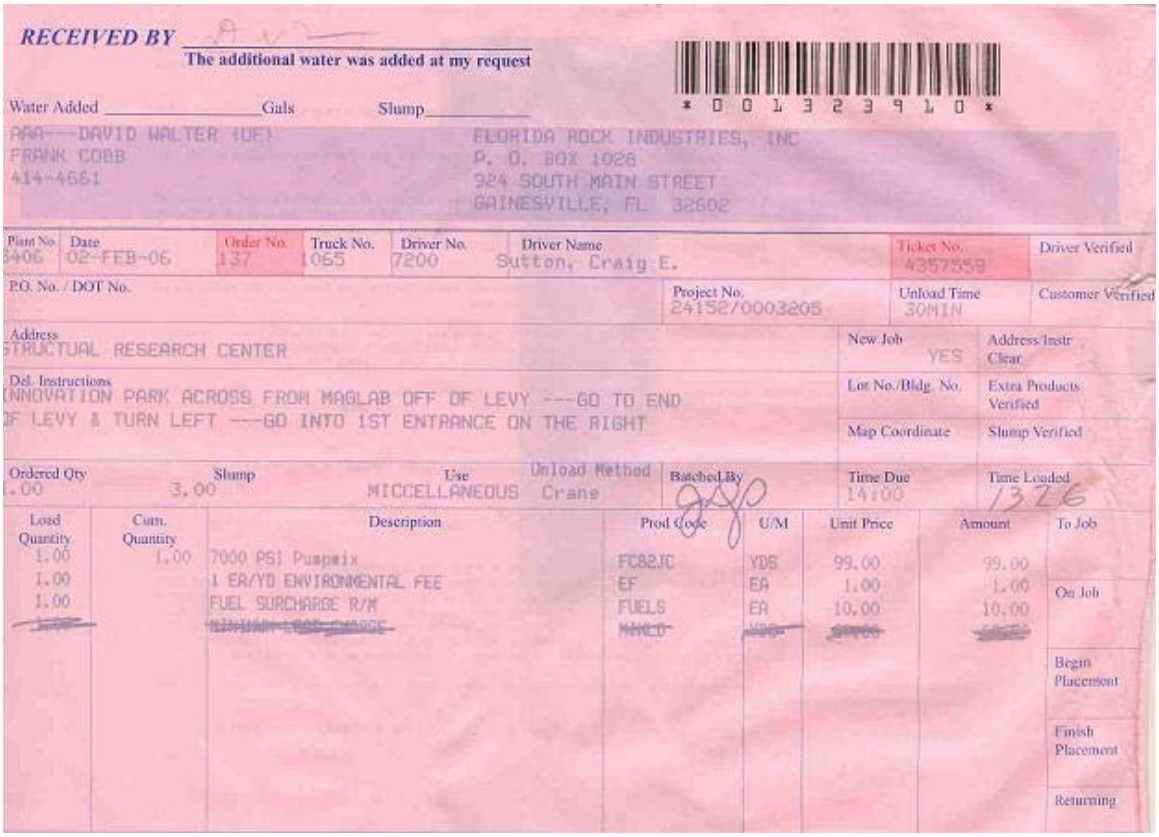

RECEIVED BY _____
The additional water was added at my request

Water Added _____ Gals Slump _____

0013239140

AAA---DAVID WALTER (UF)
FRANK COBB
414-4661

FLORIDA ROCK INDUSTRIES, INC
P. O. BOX 1028
924 SOUTH MAIN STREET
GAINESVILLE, FL 32602

Plant No.	Date	Order No.	Truck No.	Driver No.	Driver Name	Ticket No.	Driver Verified
3406	02-FEB-06	137	1065	7200	Sutton, Craig E.	4357559	

P.O. No. / DOT No. | Project No. 24152/0003205 | Unload Time 30MIN | Customer Verified

Address: STRUCTUAL RESEARCH CENTER | New Job: YES | Address/Instr Clear

Del. Instructions: INNOVATION PARK ACROSS FROM MAGLAB OFF OF LEVY ---GO TO END OF LEVY & TURN LEFT ---GO INTO 1ST ENTRANCE ON THE RIGHT | Lot No./Bldg. No. | Extra Products Verified | Map Coordinate | Slump Verified

Ordered Qty	Slump	Use	Unload Method	Batched By	Time Due	Time Loaded
1.00	3.00	MICCELLANEOUS	Crane	SP	14:00	1326

Load Quantity	Cum. Quantity	Description	Prod Code	U/M	Unit Price	Amount	To Job
1.00	1.00	7000 PSI Pumpmix	FC82JC	YDS	99.00	99.00	
1.00		1 EA/YD ENVIRONMENTAL FEE	EF	EA	1.00	1.00	On Job
1.00		FUEL SURCHARGE R/M	FUELS	EA	10.00	10.00	
[illegible]		[illegible]	MINLD	[illegible]	[illegible]	[illegible]	

Begin Placement | Finish Placement | Returning

APPENDIX C – LOADING FRAME DRAWINGS

Details of the loading frame which was used to apply mechanical loads at the cantilevered end of the test beam are shown in this appendix.

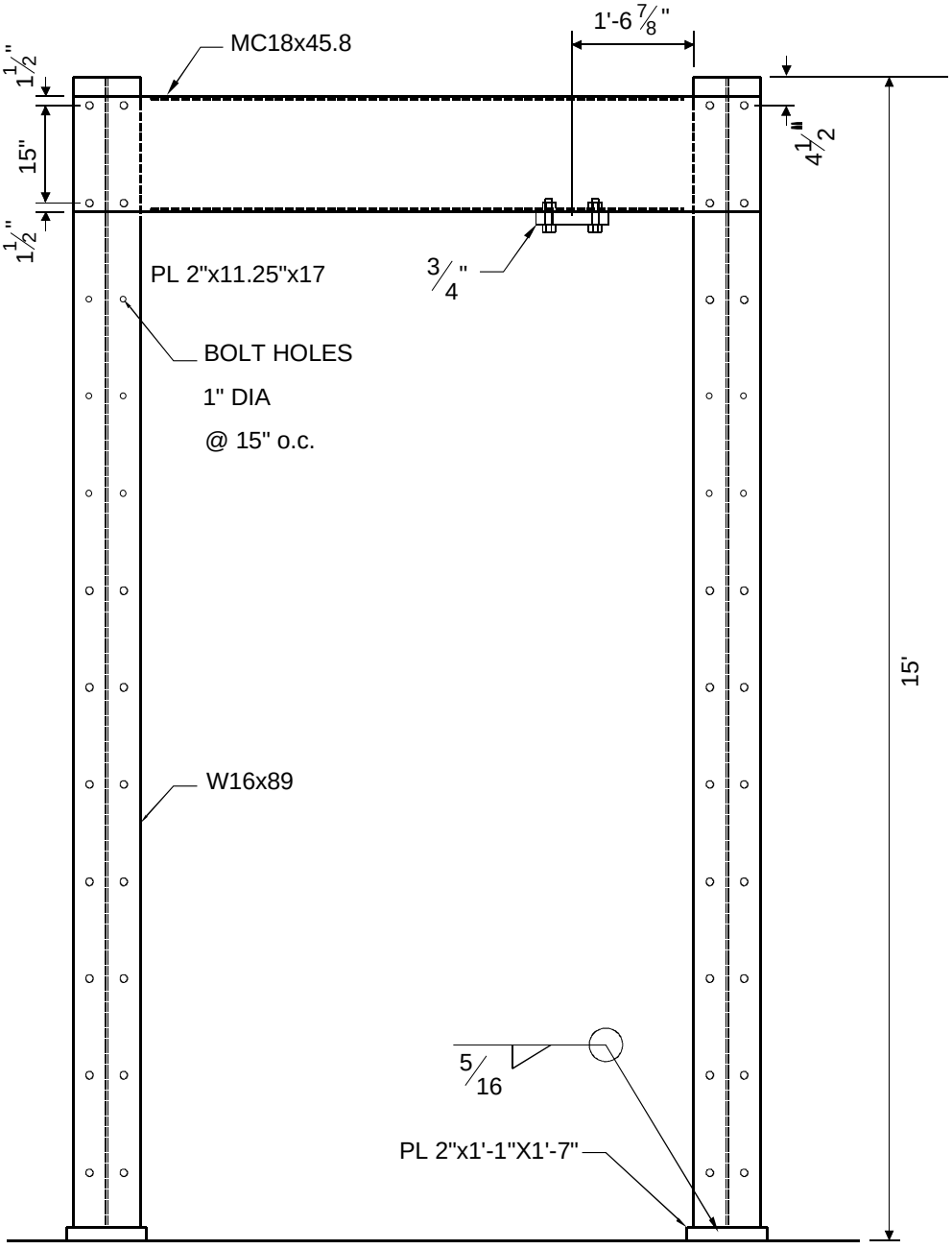
1'-6 7/8"
MC18x45.8
1 1/2"
15"
1 1/2"
4 1/2"
PL 2"x11.25"x17
3/4"
BOLT HOLES
1" DIA
@ 15" o.c.
15'
W16x89
5/16
PL 2"x1'-1"X1'-7"

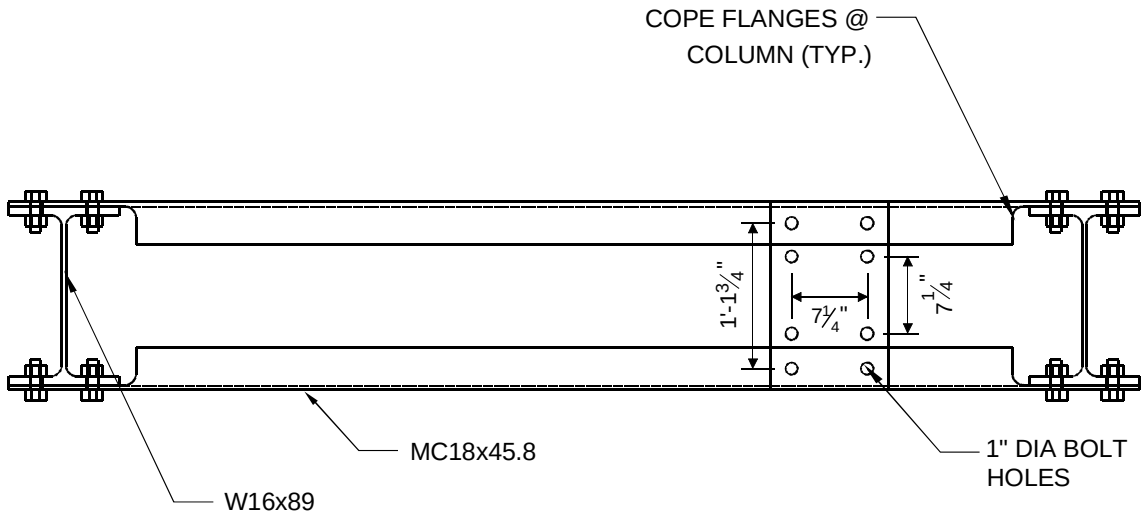
COPE FLANGES @
COLUMN (TYP.)
1'-1 3/4"
7 1/4"
1 1/4"
MC18x45.8
1" DIA BOLT
HOLES
W16x89

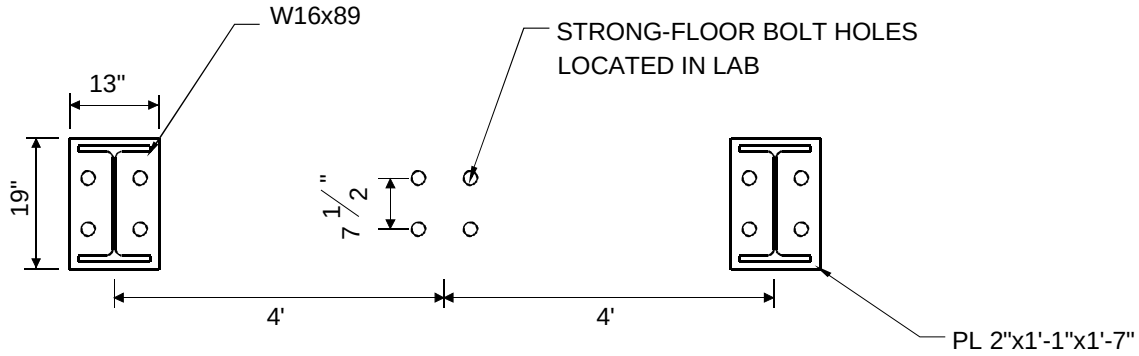
W16x89
STRONG-FLOOR BOLT HOLES
LOCATED IN LAB
13"
19"
7 1/2"
4'
4'
PL 2"x1'-1"x1'-7"

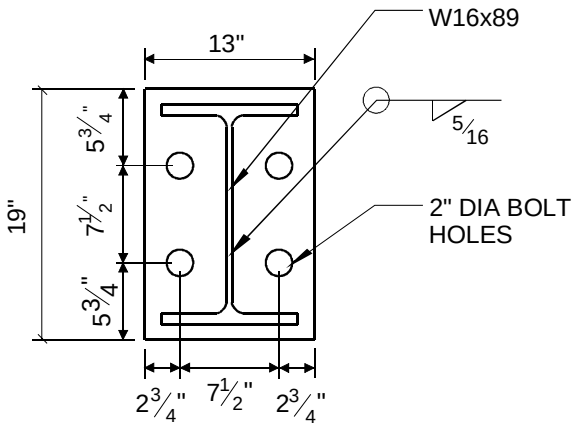
W16x89
13"
5 3/4"
7 1/2"
5 3/4"
19"
5/16
2" DIA BOLT
HOLES
2 3/4"
7 1/2"
2 3/4"

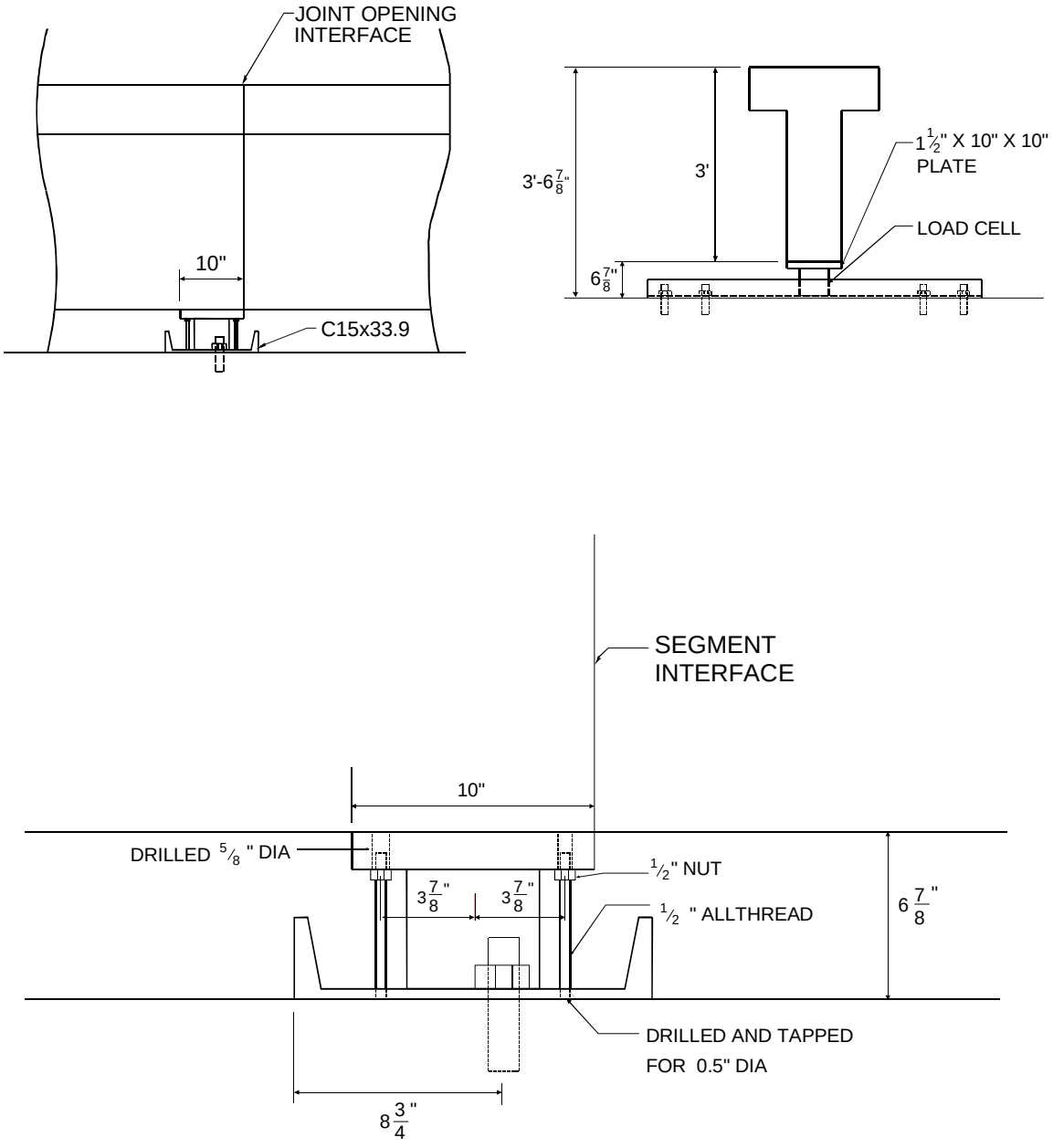
JOINT OPENING
INTERFACE
10"
C15x33.9
3'-6 7/8"
3'
6 7/8"
1 1/2" X 10" X 10"
PLATE
LOAD CELL
SEGMENT
INTERFACE
10"
DRILLED 5/8 " DIA
1/2" NUT
3 7/8"
3 7/8"
1/2 " ALLTHREAD
6 7/8 "
DRILLED AND TAPPED
FOR 0.5" DIA
8 3/4 "

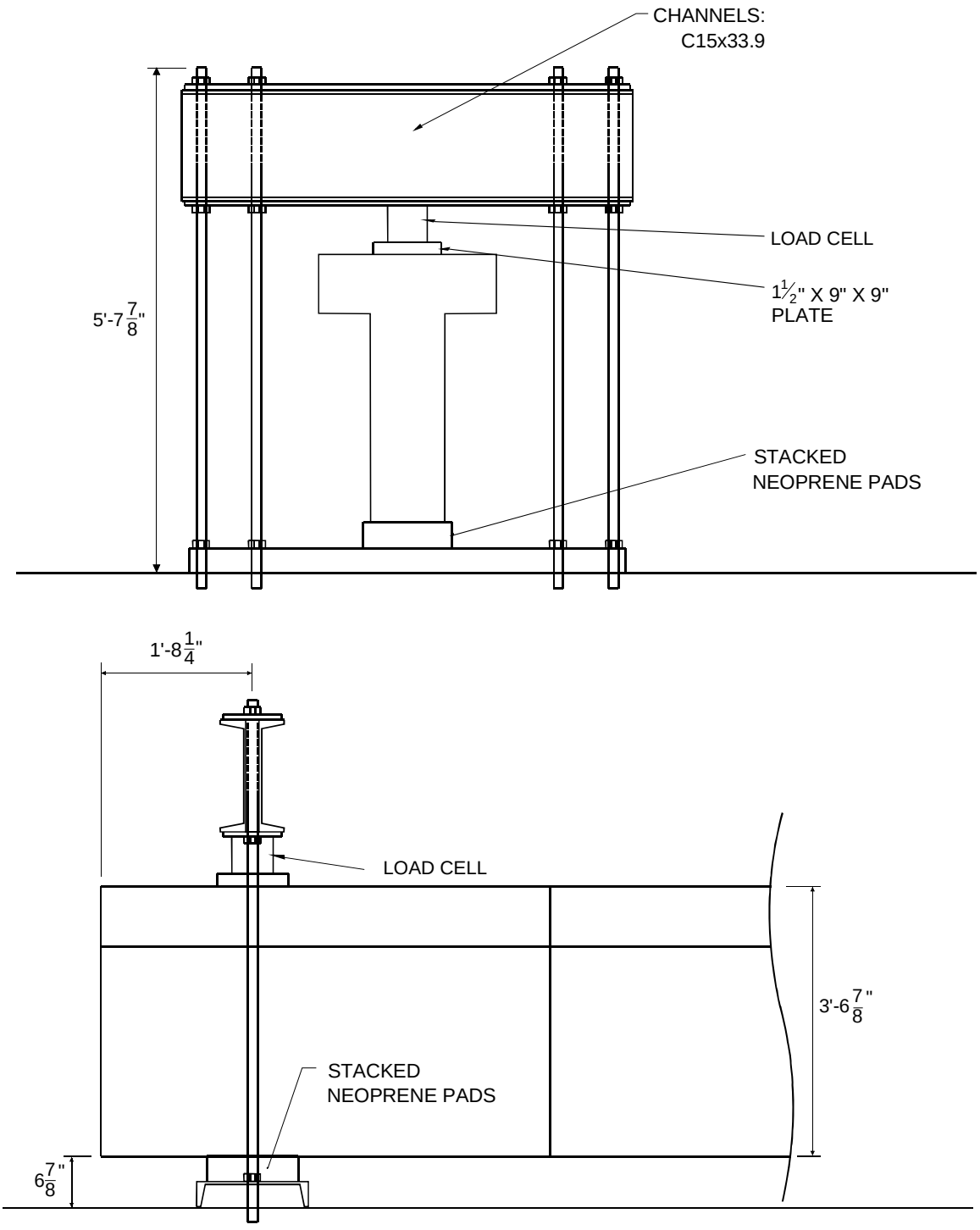
CHANNELS:
C15x33.9
LOAD CELL
1½" X 9" X 9"
PLATE
5'-7⅞"
STACKED
NEOPRENE PADS
1'-8¼"
LOAD CELL
3'-6⅞"
STACKED
NEOPRENE PADS
6⅞"

APPENDIX D – LOAD RESPONSE CURVES AT MIDSEGMENT (MECHANICAL LOADING)

In this appendix load versus strain response curves at the middle of Segment 2 and Segment 3 (30 in. away from joint J2) are presented.

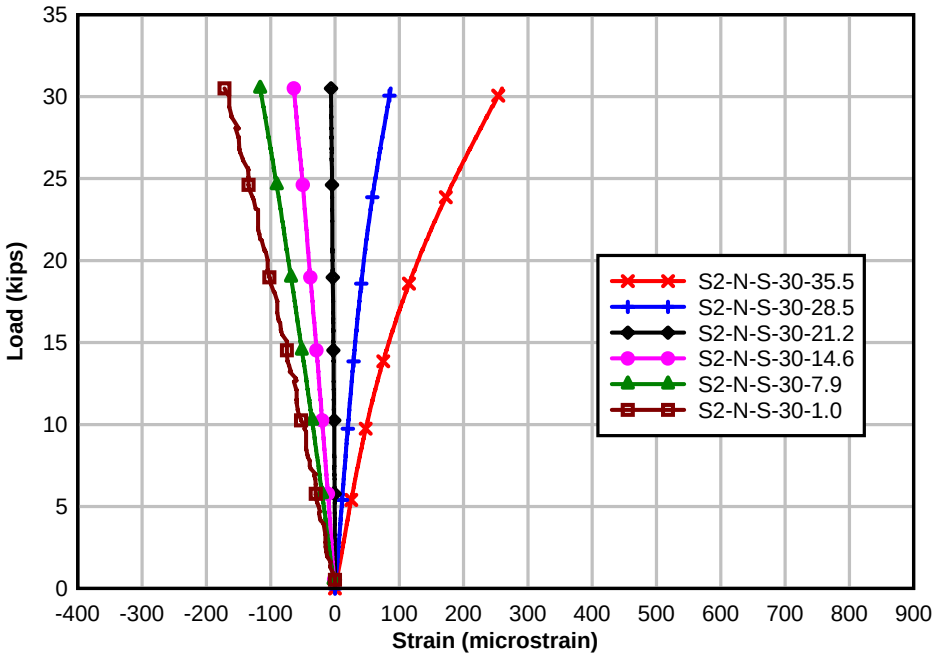

Figure 253 – Load vs. strain at middle of Segment 2 on North side

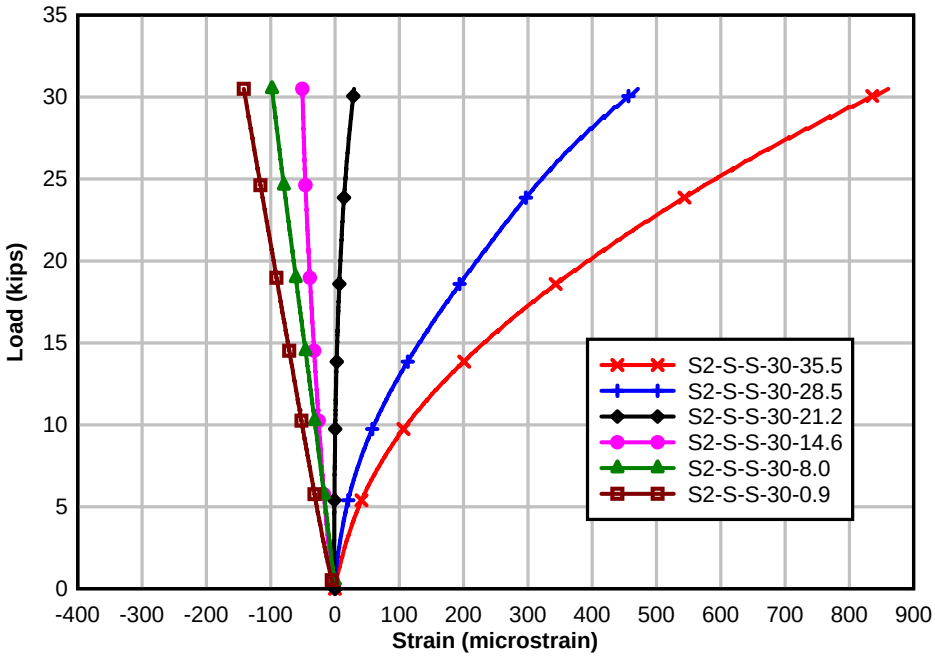

Figure 254 – Load vs. strain at middle of Segment 2 on South side

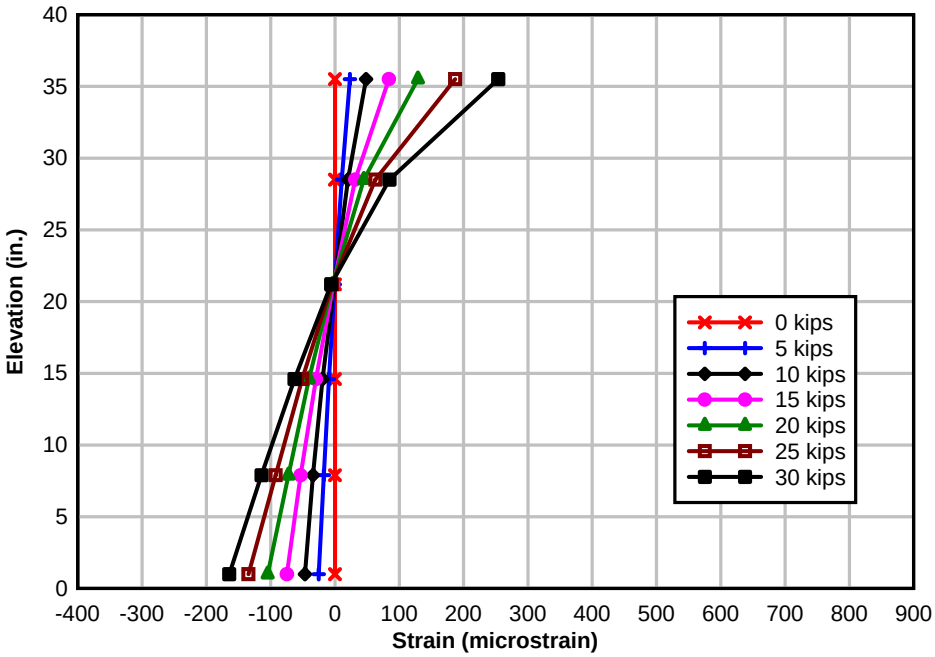

Figure 255 – Measured strain distributions at middle of Segment 2 on North side

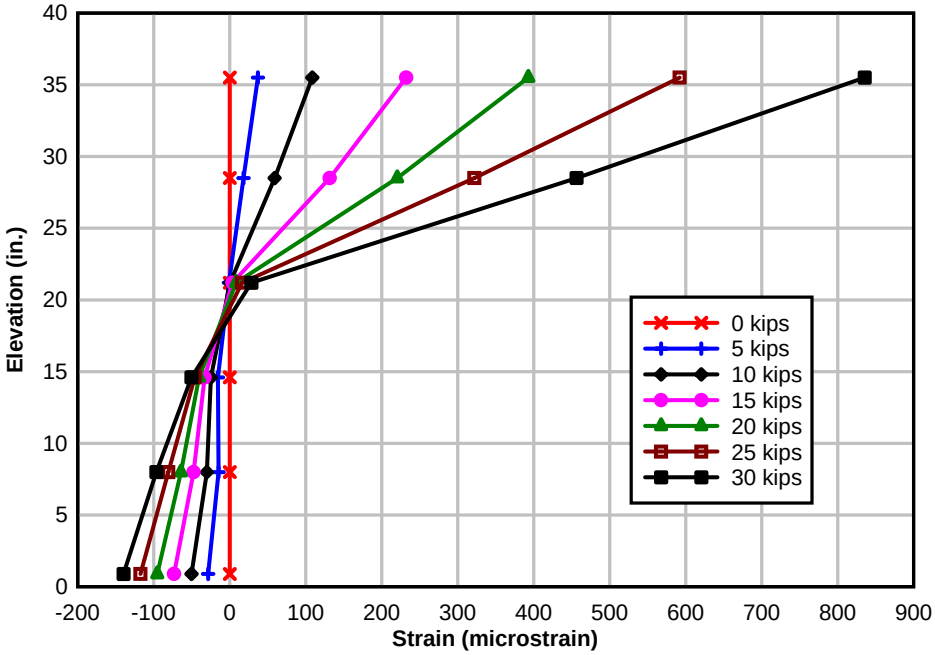

Figure 256 – Measured strain distributions at middle of Segment 2 on South side

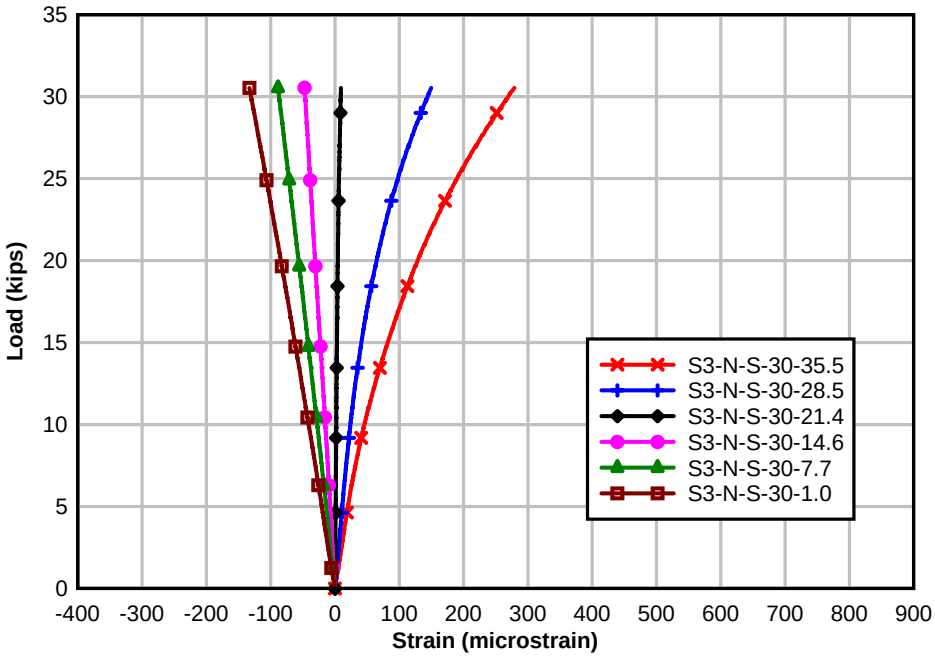

Figure 257 – Load vs. strain at middle of Segment 3 on North side

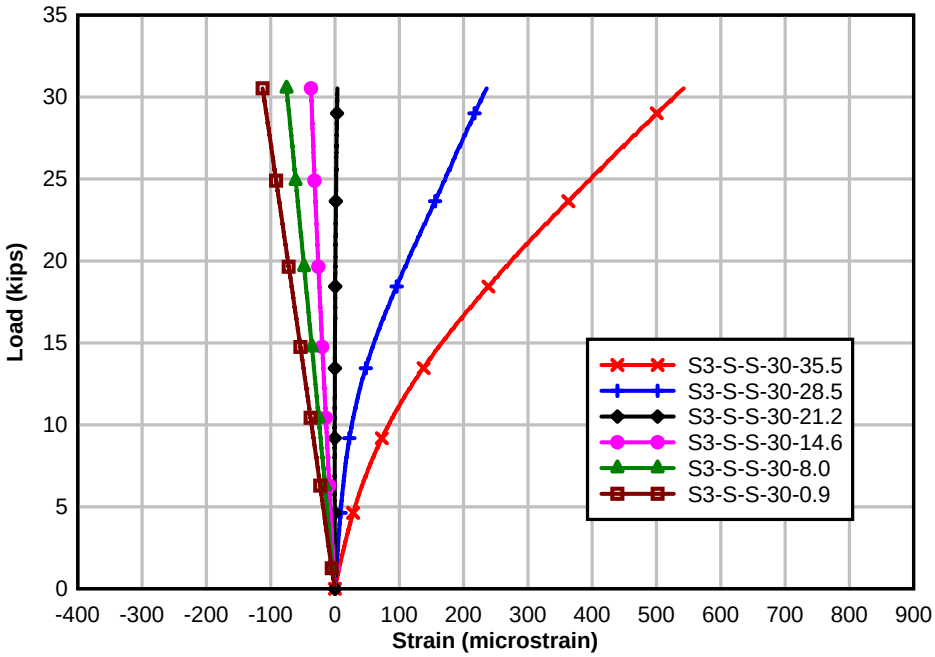

Figure 258 – Load vs. strain at middle of Segment 3 on South side

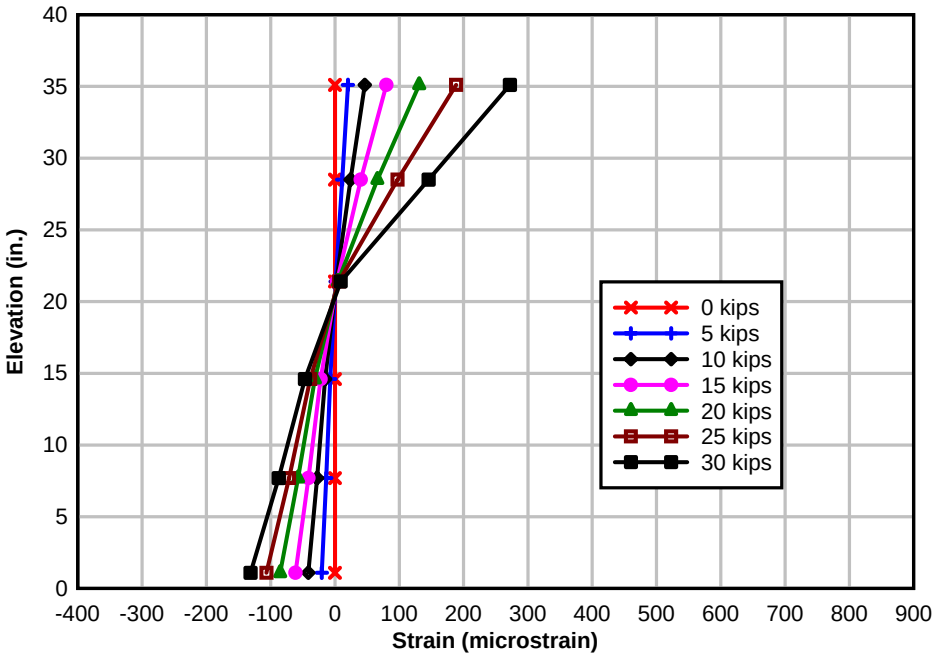

Figure 259 – Measured strain distributions at middle of Segment 3 on North side

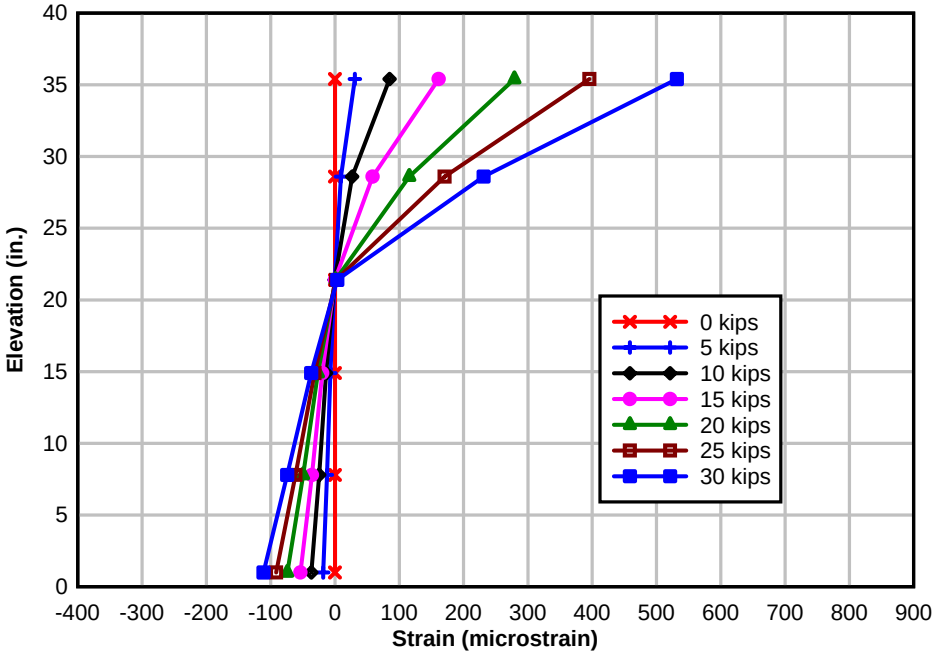

Figure 260 – Measured strain distributions at middle of Segment 3 on South side

APPENDIX E – LOAD RESPONSE CURVES (POSITIVE THERMAL GRADIENT)

Load vs. beam response curves which were derived from strain gauge and LVDT data are shown here. These curves were used to determine loads at which the joint at midspan (designated joint J2) opened. The curves were also used to determine effective concrete contact areas at joint J2, which were then used to quantify J stresses due to the AASHTO nonlinear positive thermal gradient.

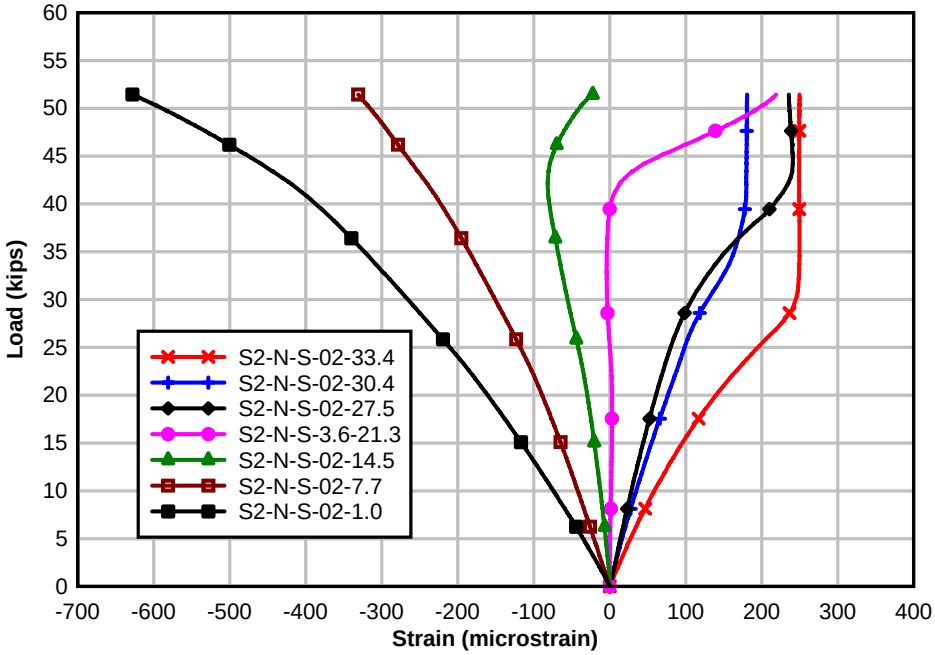

Figure 261 – Load vs. strain at reference temperature (Segment 2, North)

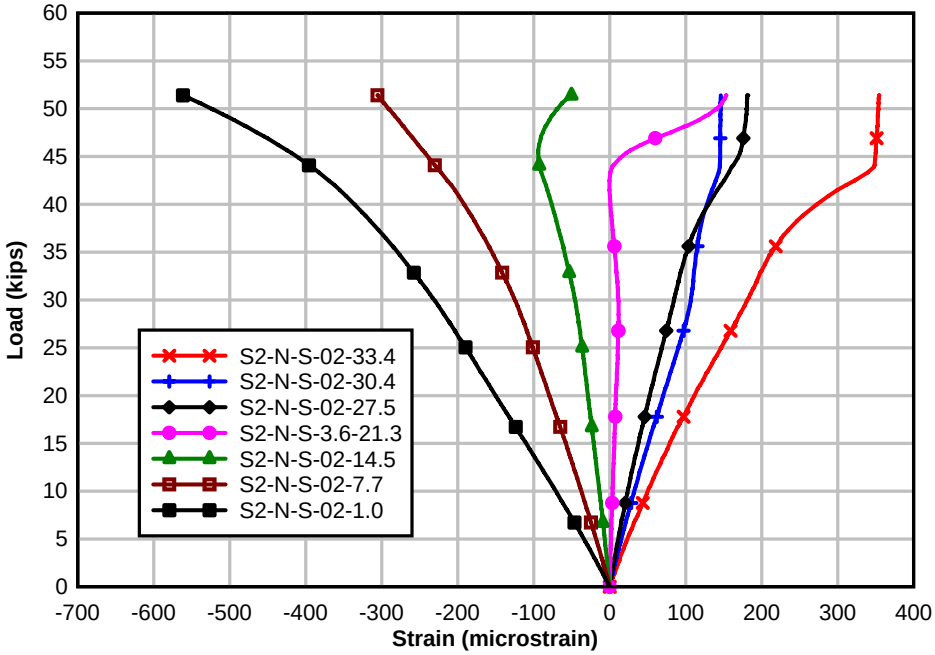

Figure 262 – Load vs. strain with positive thermal gradient (Segment 2, North)

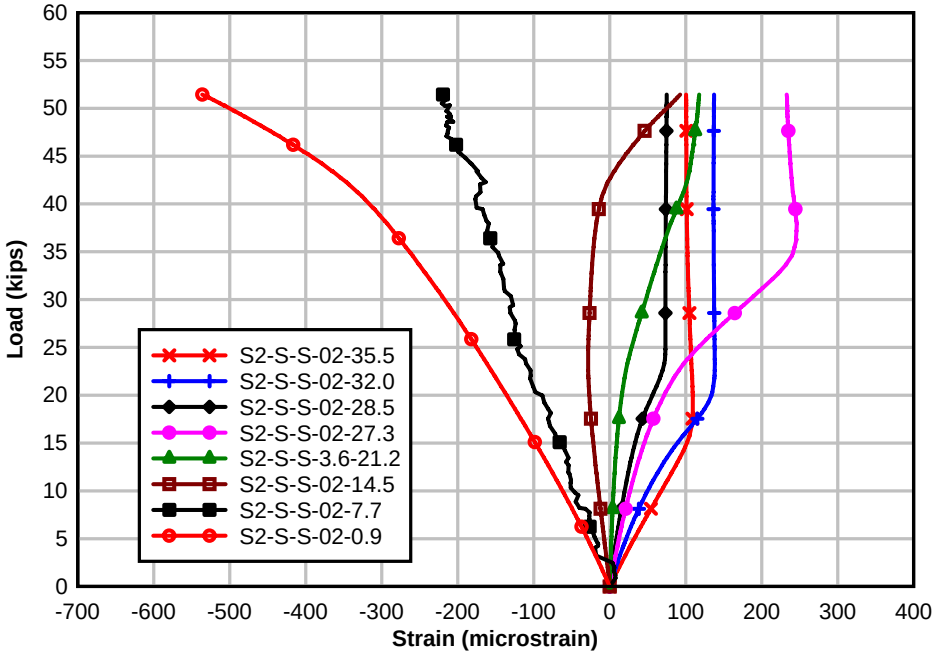

Figure 263 – Load vs. strain at reference temperature (Segment 2, South)

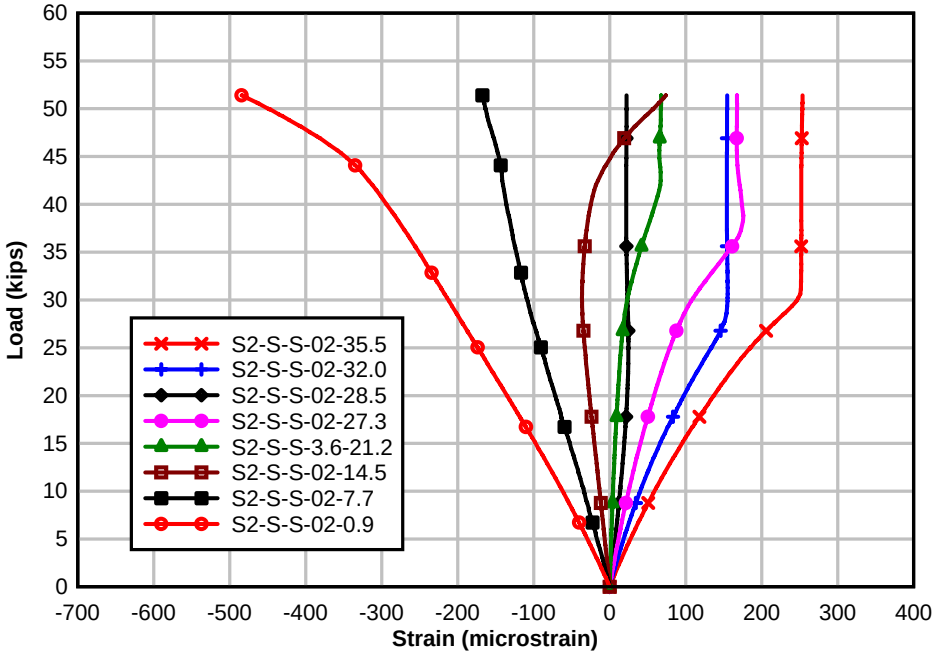

Figure 264 – Load vs. strain with positive thermal gradient (Segment 2, South)

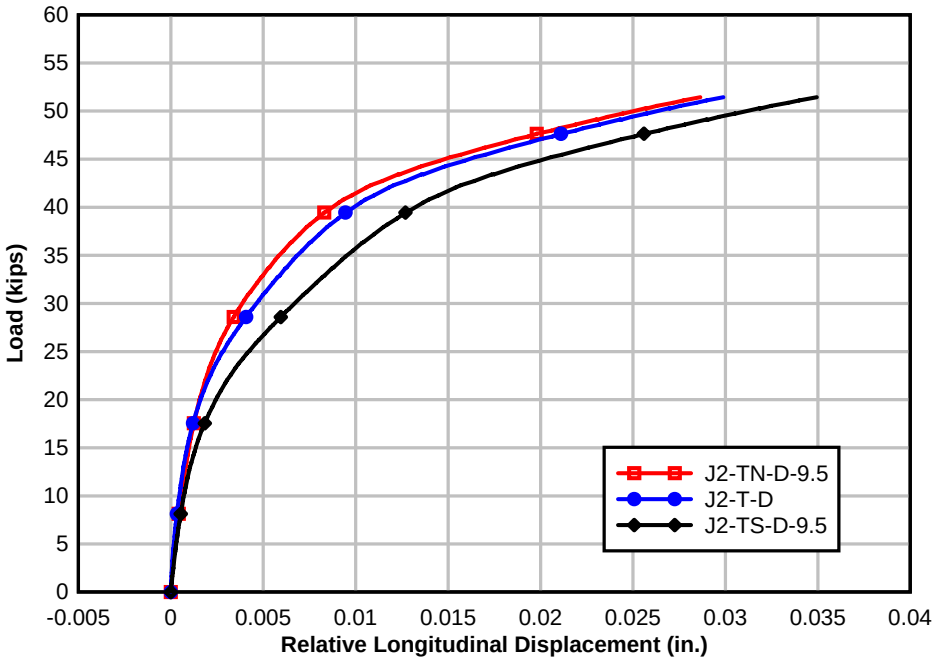

Figure 265 – Load vs. joint opening at reference temperature (Top flange)

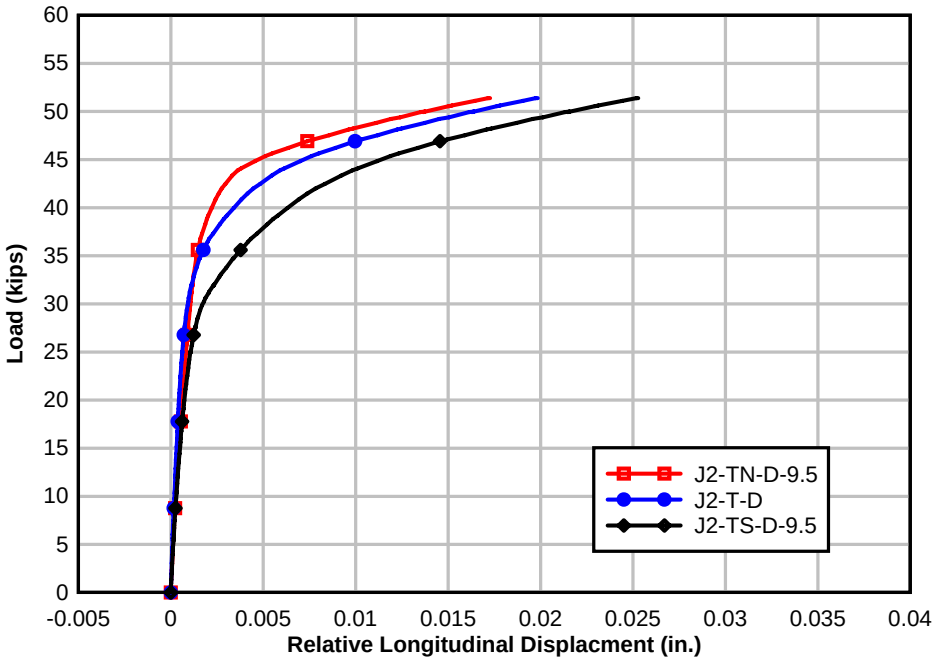

Figure 266 – Load vs. joint opening with positive thermal gradient (Top flange)

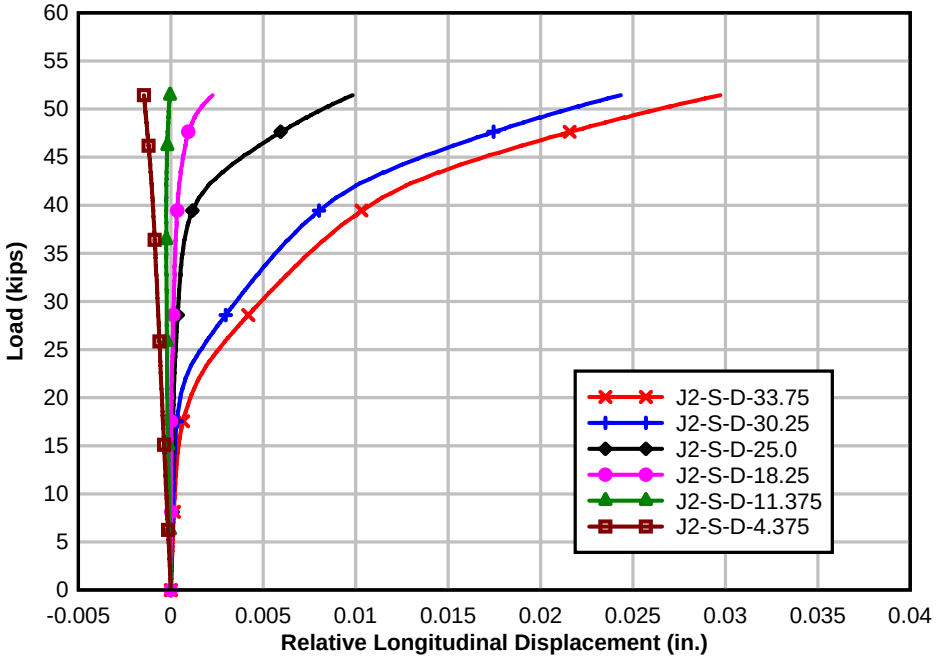

Figure 267 – Load vs. joint opening at reference temperature (South side)

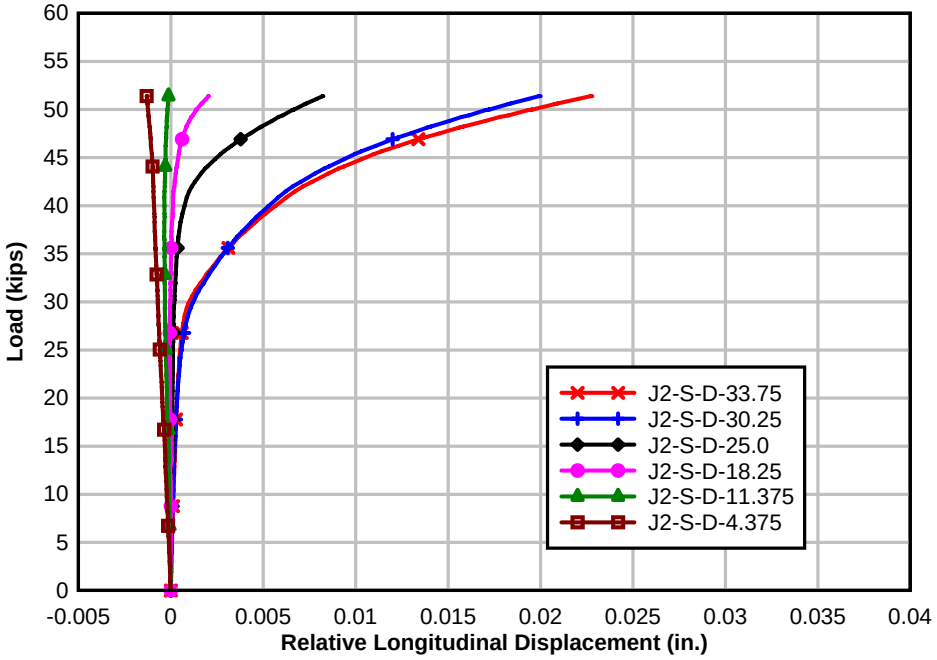

Figure 268 – Load vs. joint opening with positive thermal gradient (South side)

APPENDIX F – LOAD RESPONSE CURVES (NEGATIVE THERMAL GRADIENT)

Load vs. beam response curves which were derived from strain gauge and LVDT data are shown here. These curves were used to determine loads at which the joint at midspan (designated joint J2) opened. The curves were also used to determine effective concrete contact areas at joint J2, which were then used to quantify J stresses due to the AASHTO nonlinear negative thermal gradient.

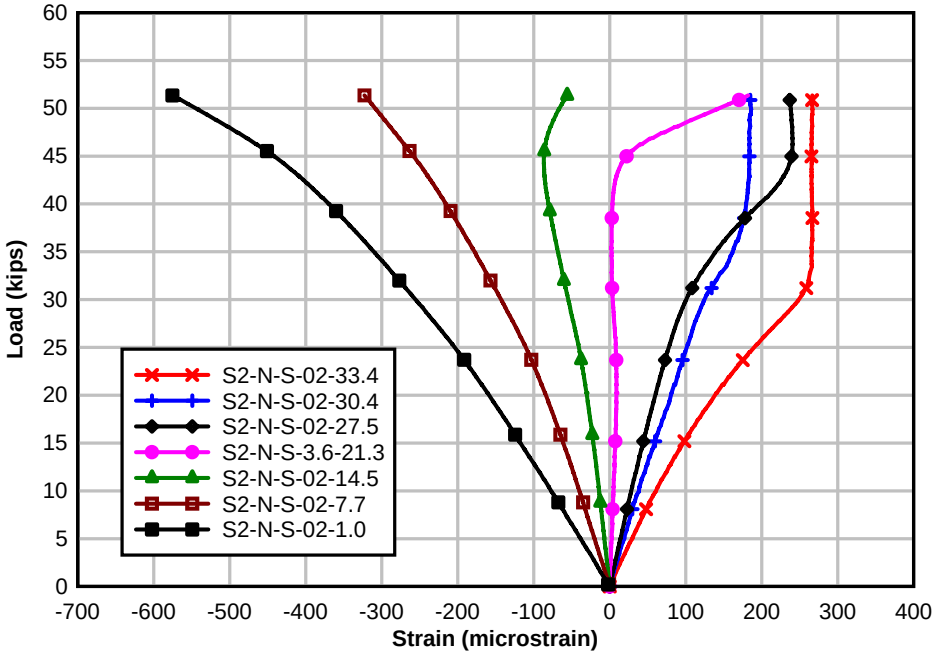

Figure 269 – Load vs. strain at reference temperature (Segment 2, North)

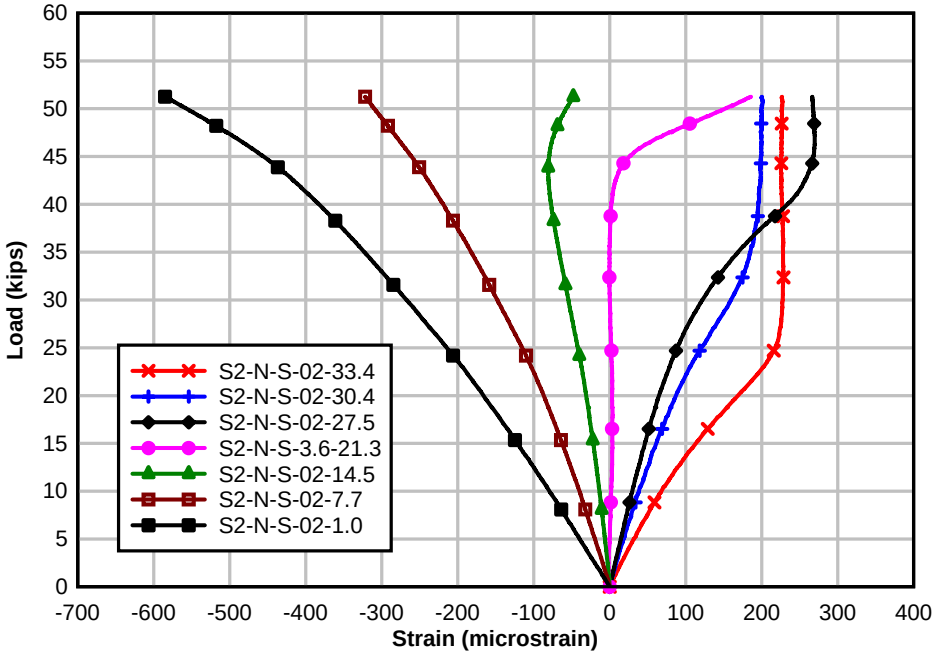

Figure 270 – Load vs. strain with negative thermal gradient (Segment 2, North)

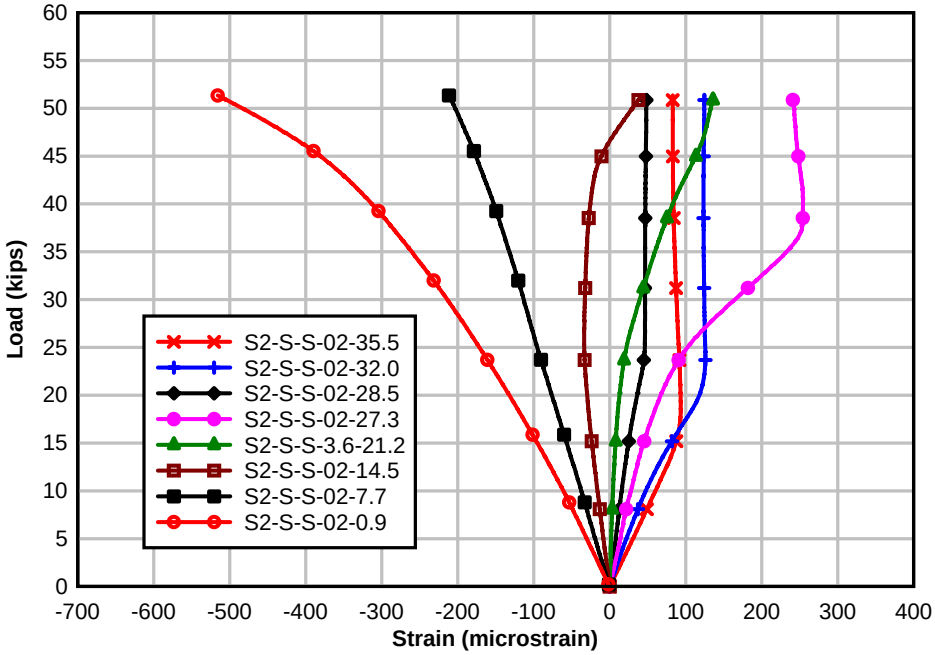

Figure 271 – Load vs. strain at reference temperature (Segment 2, South)

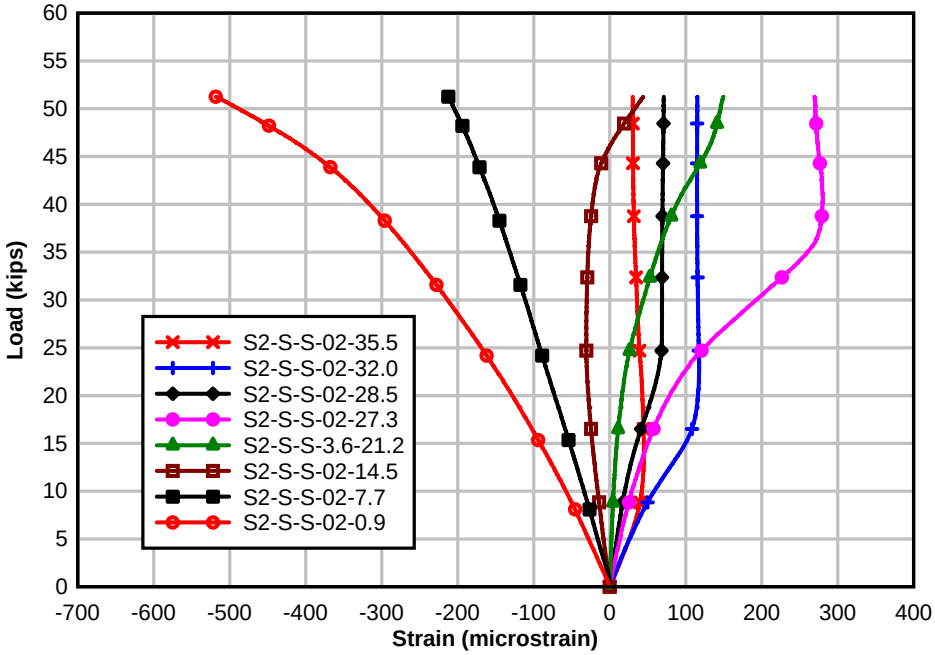

Figure 272 – Load vs. strain with negative thermal gradient (Segment 2, South)

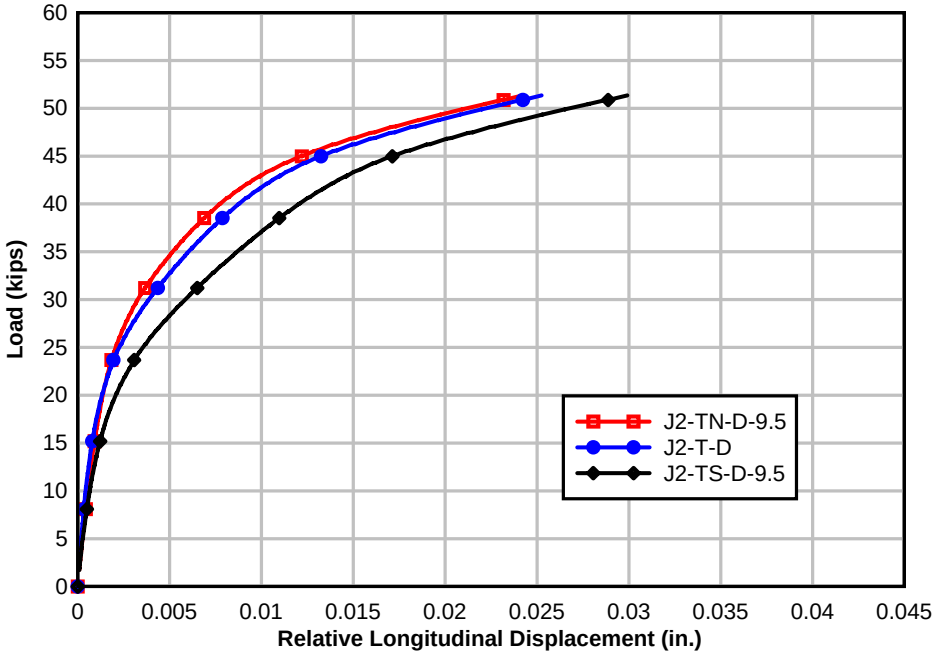

Figure 273 – Load vs. joint opening at reference temperature (Top flange)

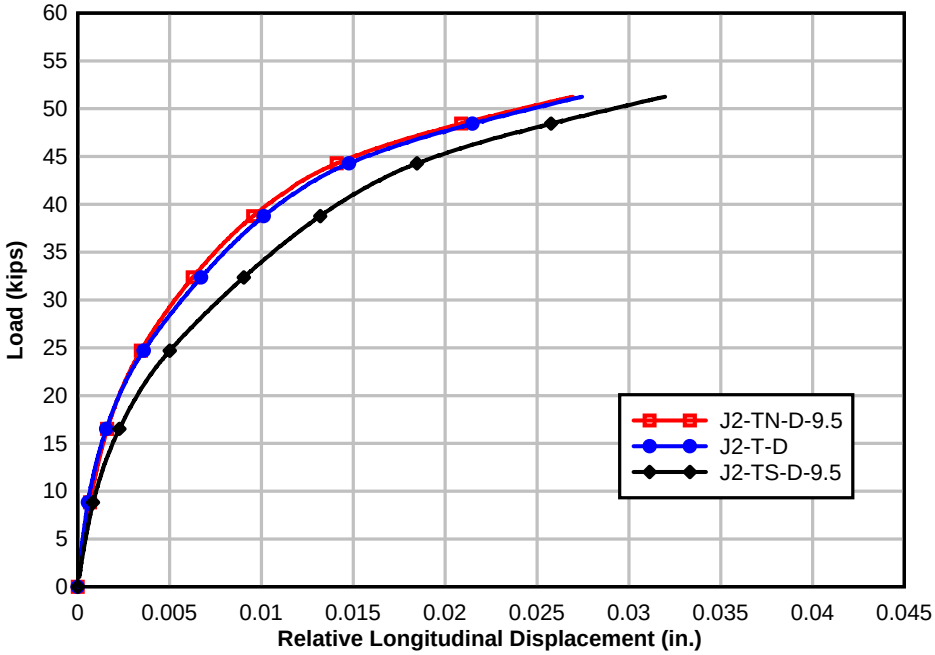

Figure 274 – Load vs. joint opening with negative thermal gradient (Top flange)

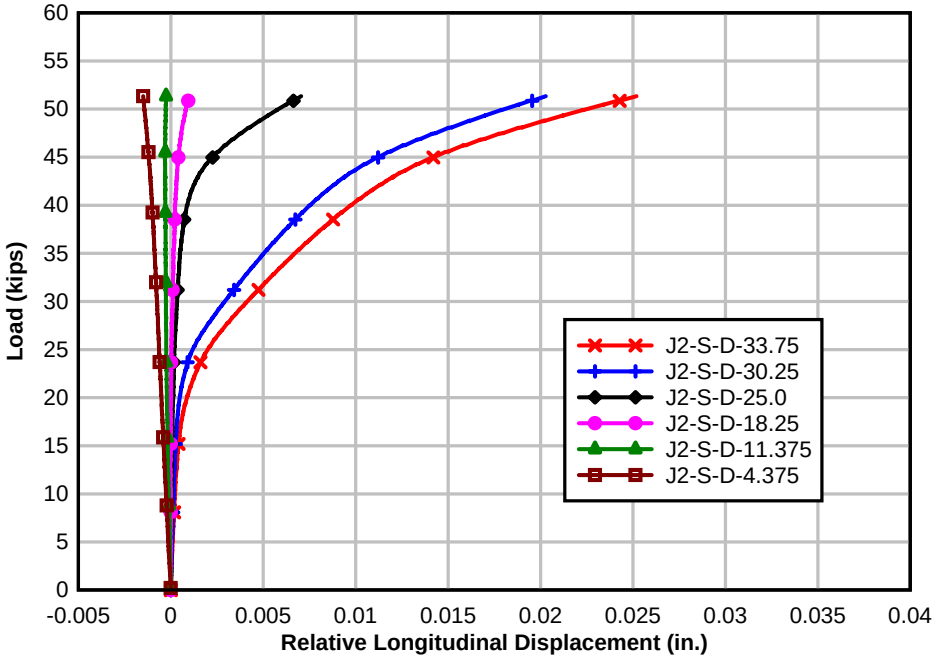

Figure 275 – Load vs. joint opening at reference temperature (South side)

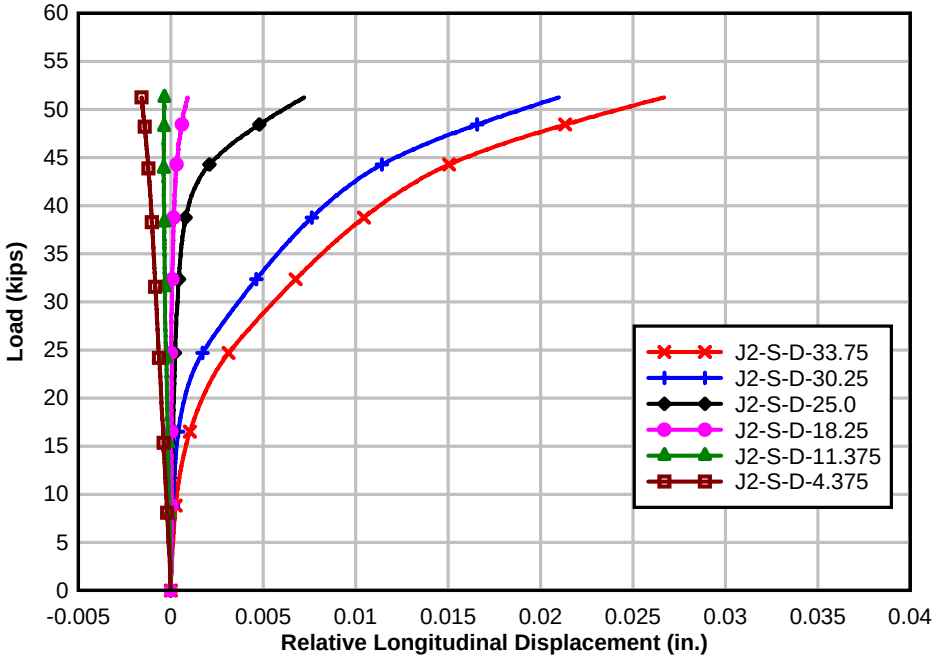

Figure 276 – Load vs. joint opening with negative thermal gradient (South side)

PART TWO APPENDICES

APPENDIX G - TEST RESULT FIGURES

This appendix includes results of Test A – Test F for the non-thermal and thermal specimens. Each includes strain-load on the primary x-axis and strain-stress on the secondary x-axis.

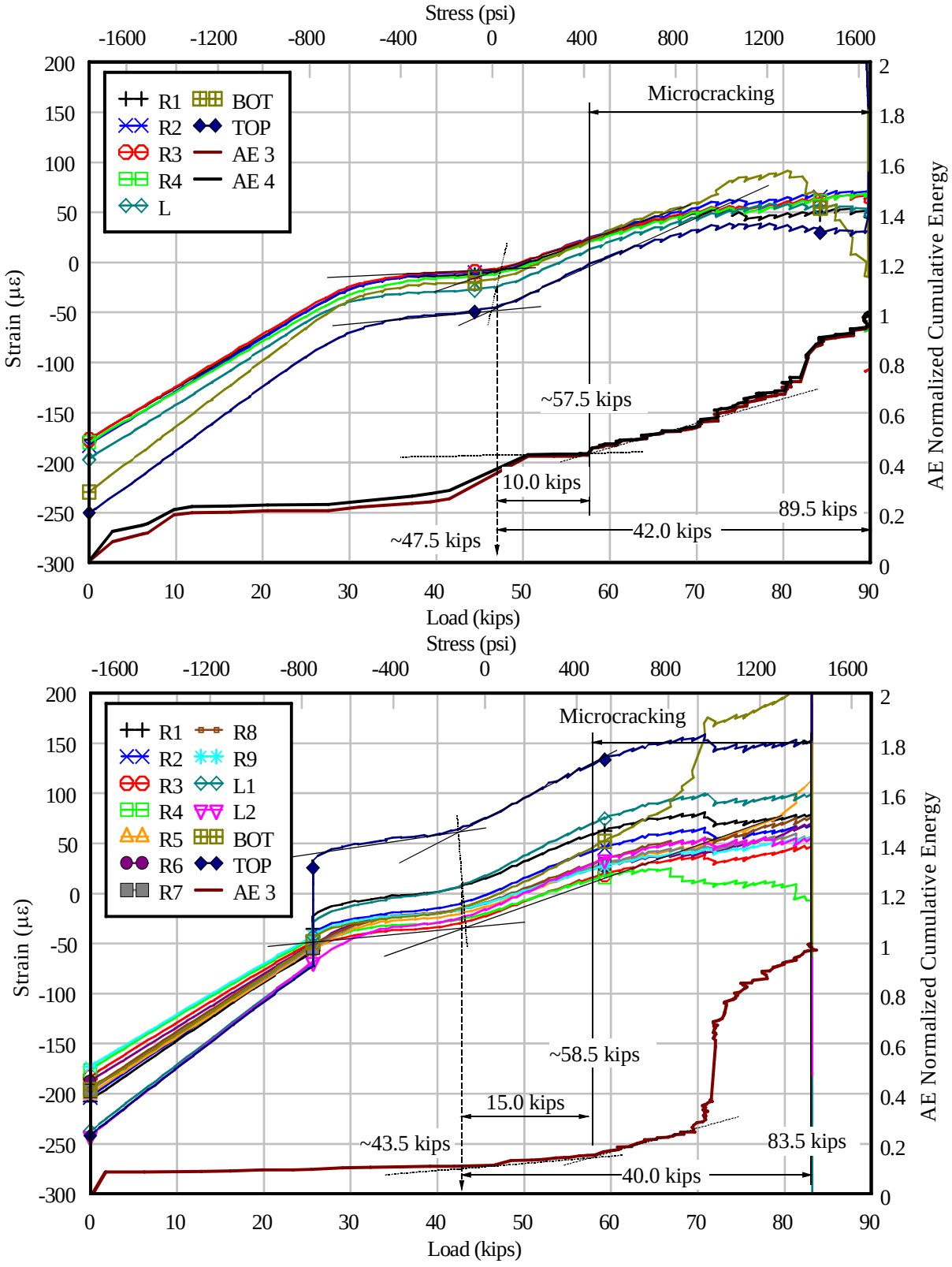

Figure 277: Test A results for non-thermal specimen (top) and thermal specimen (bottom)

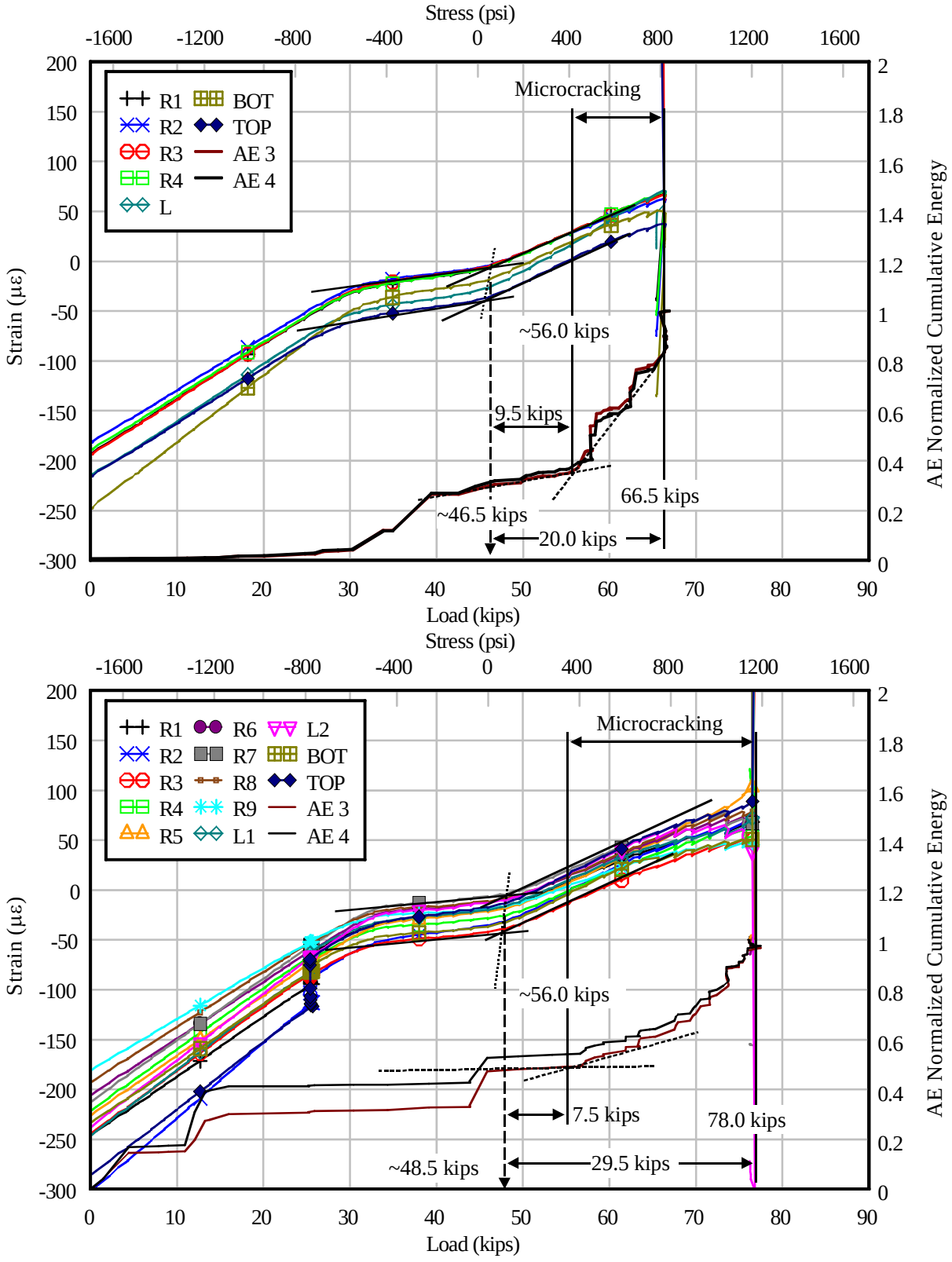

Figure 278: Test B results for non-thermal specimen (top) and thermal specimen (bottom)

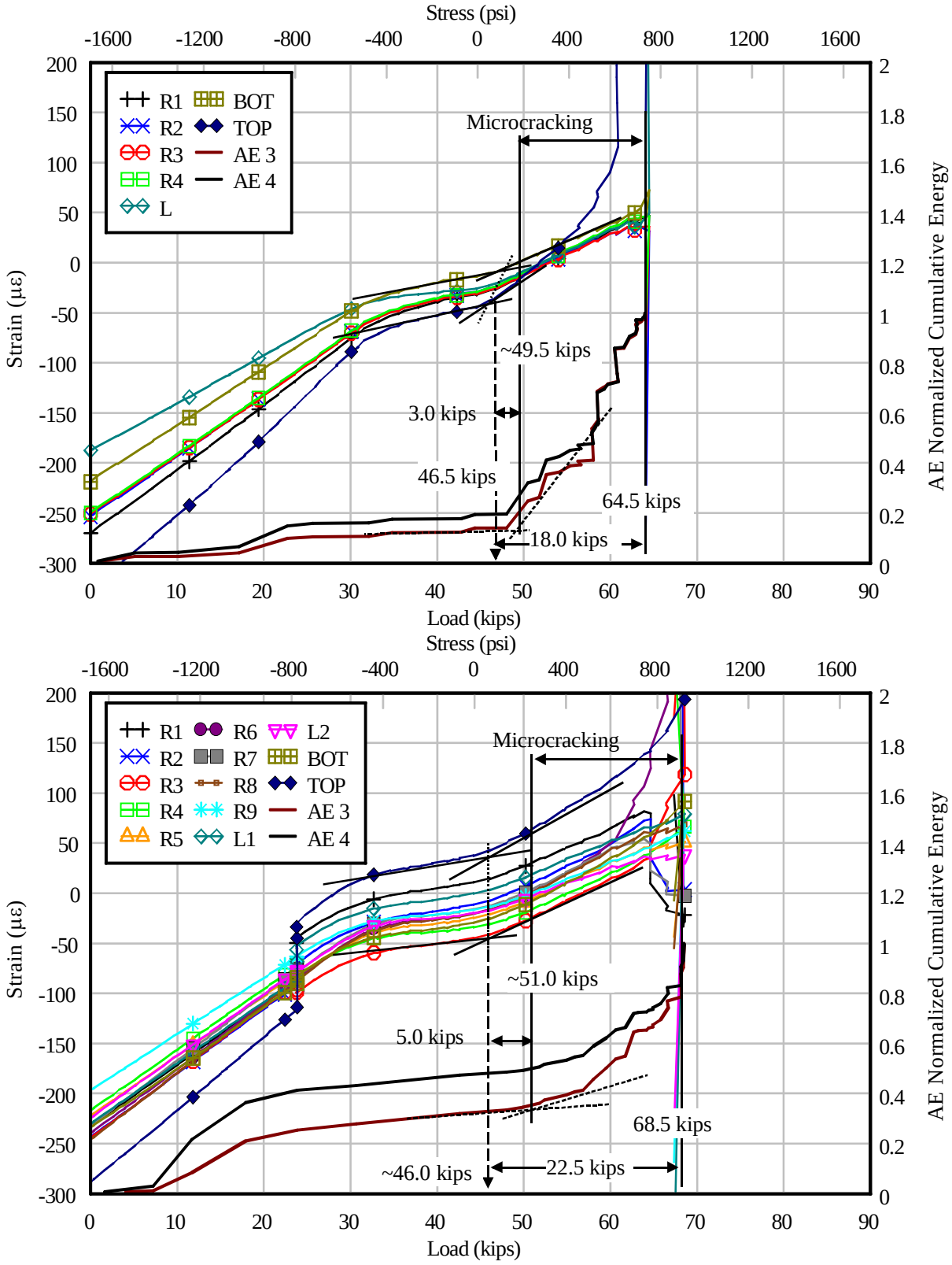

Figure 279: Test C results for non-thermal specimen (top) and thermal specimen (bottom)

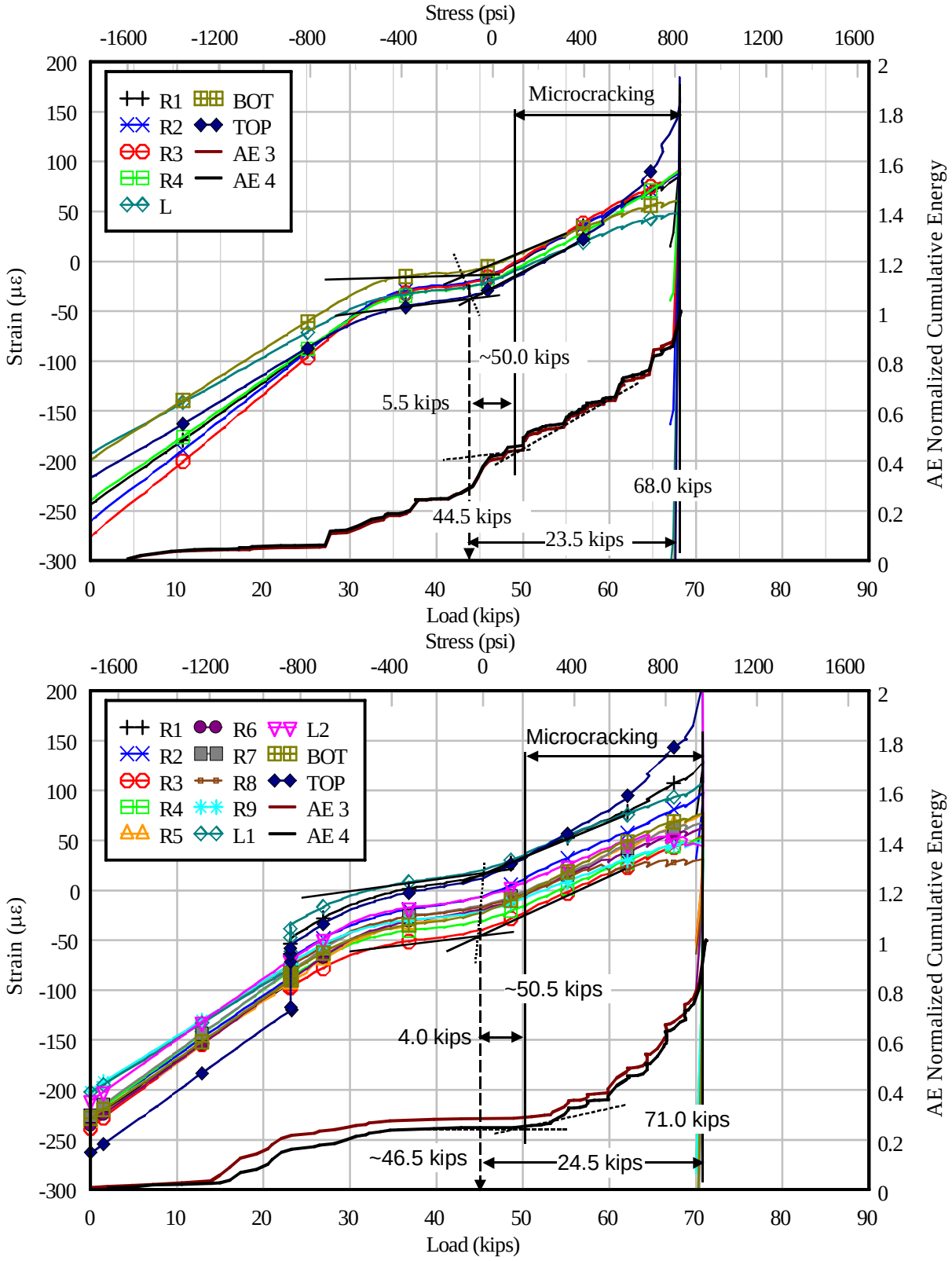

Figure 280: Test D results for non-thermal specimen (top) and thermal specimen (bottom)

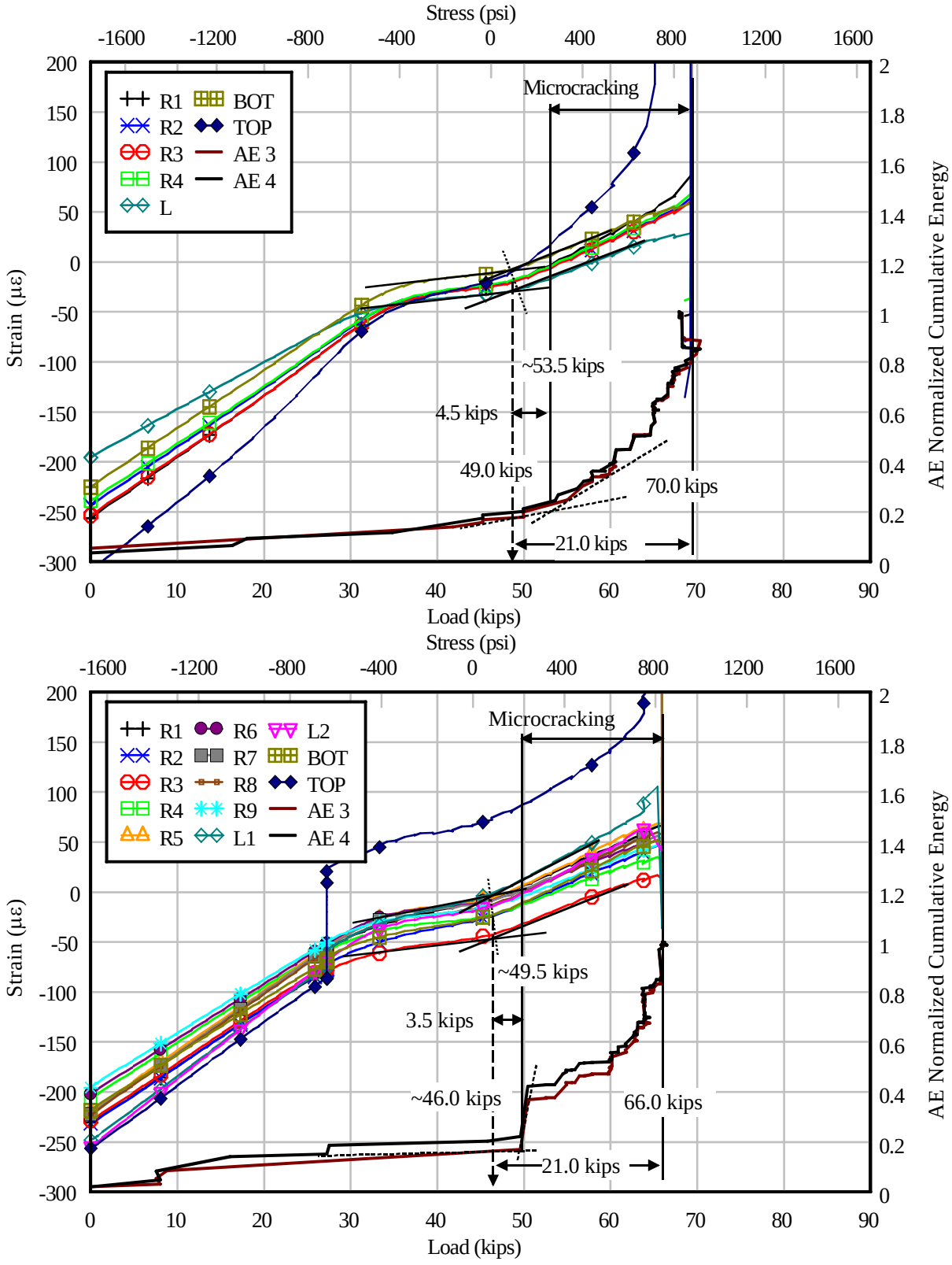

Figure 281: Test E results for non-thermal specimen (top) and thermal specimen (bottom)

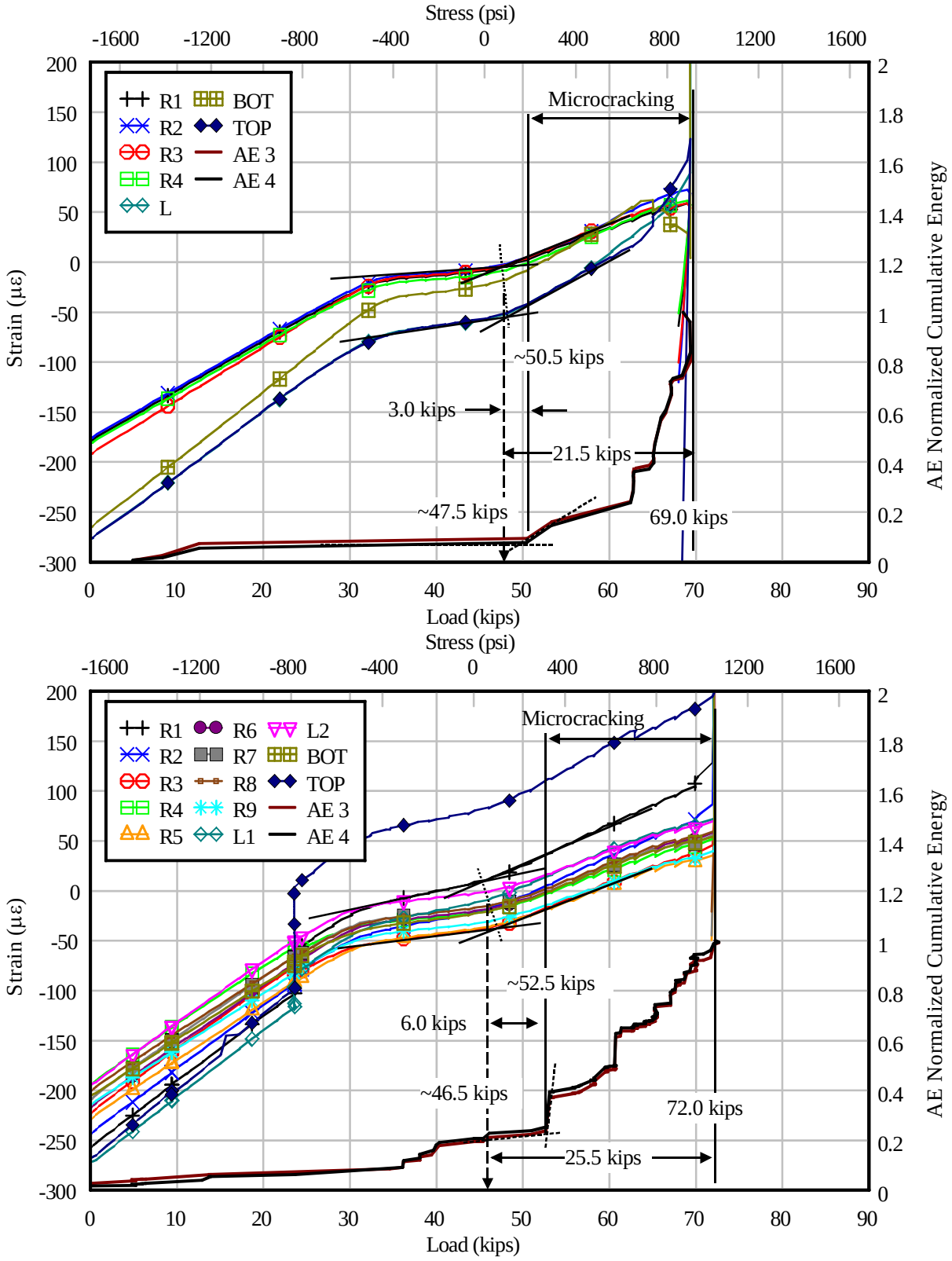

Figure 282: Test F results for non-thermal specimen (top) and thermal specimen (bottom)

APPENDIX H - TEST RESULT TABLES

Table 35: Net tensile load at initial microcracking for non-thermal and thermal tests

	P_i (kips)		P_i (kN)		Non-Thermal / Thermal
	Non-Thermal	Thermal	Non-Thermal	Thermal	
Test A	10.0	15.0	44.5	66.7	0.67
Test B	9.5	7.5	42.3	33.4	1.27
Test C	3.0	5.0	13.3	22.2	0.60
Test D	5.5	4.0	24.5	17.8	1.38
Test E	4.5	3.5	20.0	15.6	1.29
Test F	1.5	6.0	6.7	26.7	0.25

Table 36: Net tensile load at visible cracking for non-thermal and thermal tests

	P_{cr} (kips)		P_{cr} (kN)		Non-Thermal / Thermal
	Non-Thermal	Thermal	Non-Thermal	Thermal	
Test A	42.0	40.0	186.8	177.9	1.05
Test B	20.0	29.5	89.0	131.2	0.68
Test C	18.0	22.5	80.1	100.1	0.80
Test D	23.5	24.5	104.5	109.0	0.96
Test E	21.0	21.0	93.4	93.4	1.00
Test F	21.5	25.5	95.6	113.4	0.84

Table 37: Initial stress ratio for non-thermal and thermal tests

	$\frac{f_i}{\sqrt{f'_c\ (psi)}}$		$\frac{f_i}{\sqrt{f'_c\ (Mpa)}}$		$\frac{f_r}{\sqrt{f'_c\ (psi)}}$	$\frac{f_r}{\sqrt{f'_c\ (Mpa)}}$
	Non-Thermal	Thermal	Non-Thermal	Thermal		
Test A	5.2	7.8	0.43	0.65	10.3	0.86
Test B	5.0	3.9	0.42	0.33	9.8	0.81
Test C	1.5	2.5	0.12	0.21	10.1	0.84
Test D	2.8	2.1	0.23	0.17	9.5	0.79
Test E	2.3	1.8	0.19	0.15	9.1	0.76
Test F	0.8	3.1	0.06	0.26	8.8	0.73

Table 38: Final stress ratio for non-thermal and thermal tests

	$\frac{f_{cr}}{\sqrt{f'_c\ (psi)}}$		$\frac{f_{cr}}{\sqrt{f'_c\ (Mpa)}}$	
	Non-Thermal	Thermal	Non-Thermal	Thermal
Test A	21.9	20.9	1.82	1.73
Test B	10.5	15.5	0.87	1.29
Test C	9.0	11.3	0.75	0.94
Test D	12.1	12.6	1.00	1.04
Test E	10.6	10.6	0.88	0.88
Test F	11.0	13.1	0.92	1.09

APPENDIX I - LOAD FRAME SHOP DRAWINGS

This appendix includes the shop drawings used in fabrication of the load frame.

TOTAL ITEM LIST FOR FRAME CONSTRUCTION - (2)			
ITEM #	QUANTITY	ITEM	DIMENSIONS
1	4	C6X13	3'-0"
2	6	C6X13	0'-6"
3	4	HSS 5X3X1/4	3'-0"
4	9	PL 6X6X1/2	6x6x½ WITH 1⅜ DIA.
5	16	PL 6X6X1/2	6x6x½ WITH 1⅛ DIA.
6	6	PL 9X6X1/2	9x6x½ WITH 1⅜ DIA.
7	16	1½X1 BAR	1½x1x6

(2) - FRAME OVERVIEW

SCALE: NTS

University of Florida
Dept. of Civil and Coastal Engineering
Designer: Nathan Currier
Contact: 352-231-0465
Date: 02-27-08

SHEET: 1 OF 6

Figure 283: Frame overview

Figure 284: End frame detail

Figure 285: Column detail

ITEM LIST FOR PLATE WITH 1⅛" DIA - (8)			
ITEM #	QUANTITY	ITEM	DIMENSIONS
5	8	PL 6X6X1/2	6x6x½ WITH 1⅛ DIA.

(8) - PLATE WITH 1 1/8" DIA

SCALE: 3" = 1'-0"

University of Florida
Dept. of Civil and Coastal Engineering
Designer: Nathan Currier
Contact: 352-231-0465
Date: 02-27-08

SHEET: 4 OF 6

Figure 286: Plate detail 1

TOTAL ITEM LIST FOR PLATE WITH 1⅜" DIA - (9)			
ITEM #	QUANTITY	ITEM	DIMENSIONS
4	9	PL 6X6X1/2	6x6x½ WITH 1⅜ DIA.

(9) - PLATE WITH 1⅜" DIA

SCALE: 3" = 1'-0"

University of Florida
Dept. of Civil and Coastal Engineering
Designer: Nathan Currier
Contact: 352-231-0465
Date: 02-27-08

SHEET: 5 OF 6

Figure 287: Plate detail 2

ITEM LIST FOR PRESTRESS CHAIR - (3)			
ITEM #	QUANTITY	ITEM	DIMENSIONS
2	6	C6X13	0'-6"
6	6	PL 9X6X1/2	9x6x½ WITH 1⅜ DIA.

(3) - PRESTRESS CHAIR

SCALE: 1 ½ " = 1'-0"

University of Florida
Dept. of Civil and Coastal Engineering
Designer: Nathan Currier
Contact: 352-231-0465
Date: 02-27-08

SHEET: 6 OF 6

Figure 288: Prestress chair detail

APPENDIX J - SPECIMEN DESIGN AND TEST SETUP DRAWINGS

This appendix includes drawings for the fabrication of the test specimen.

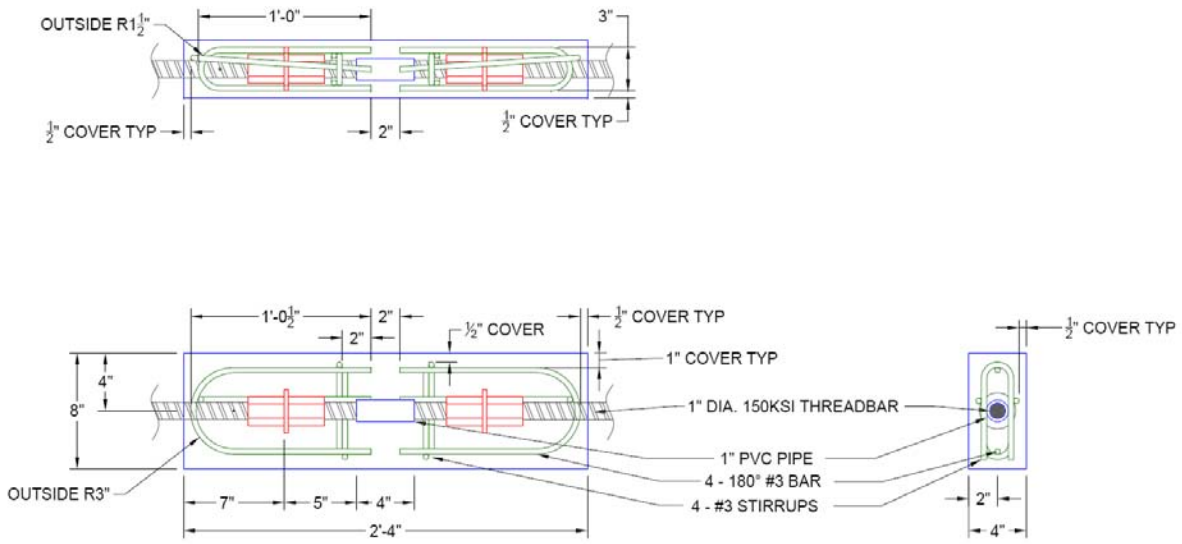

Figure 289: Specimen fabrication drawings

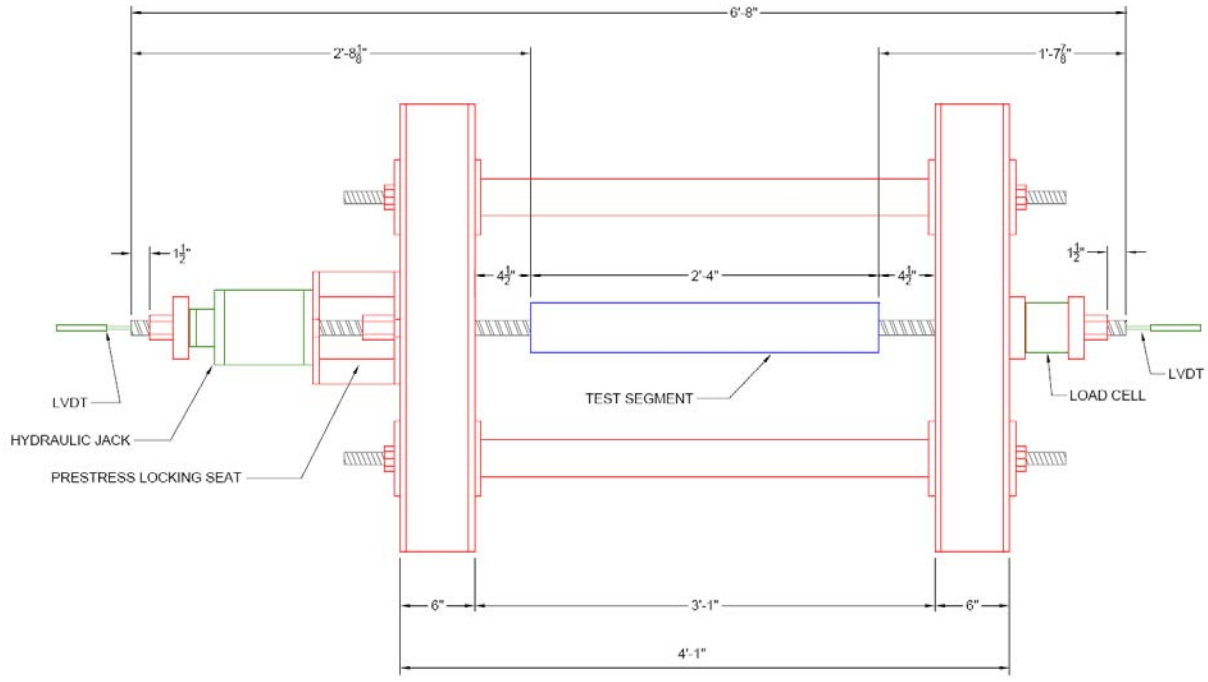

Figure 290: Test setup detail